FLOW VISUALISATION OF SEMI-CONFINED JET IMPINGEMENT

SHIRLEY ASHFORTH-FROST

A thesis submitted in partial fulfilment of the

requirements of The Nottingham Trent University

for the degree of Doctor of Philosophy.

This research programme was carried out in the

Department of Mechanical Engineering, Faculty of Engineering and Computing,

The Nottingham Trent University, Nottingham NG1 4BU, UK.

July 1994

CONTENTS

FLOW VISUALISATION OF SEMI-CONFINED JET IMPINGEMENT

by

Shirley Ashforth-Frost

ABSTRACT

The effect of near wall velocity and turbulence on surface heat transfer within the stagnation region of a semi-confined impinging jet has been studied. The single turbulent incompressible fully developed jet impinged perpendicularly onto a smooth surface.

New qualitative and quantitative experimental data of near wall velocity and Reynolds stress components have been obtained, using full field flow visualisation and laser-Doppler anemometry, at a Reynolds number of 20000 and nozzle to plate spacing (z/d) of two diameters, supported by some additional data for z/d=4 and z/d=6. The distribution of heat transfer coefficient has been obtained using a transient wall heating technique with liquid crystals as the temperature indicator. The heat transfer data has corroborated and extended existing data for the semi-confined case.

The influence of the semi-confinement and impingement plates on flow and heat transfer has been quantified. Both have the effect of extending the jet potential core. Heat transfer rates of typically 80% of the unconfined impinging jet are achieved with semi-confinement, which severely limits entrainment.

The experimental results have provided clear evidence of turbulent motions in the stagnation region which have a direct influence on heat transfer; the locations of the maxima in the turbulence components of the Reynolds stresses have been shown to coincide with the heat transfer maxima.

An instantaneous stagnation point was observed when $z/d \geq 6$ which was attributed to periodicity of the flow due to coherent turbulent structures generated at the jet exit.

The k-ϵ turbulence model, available in the commercial software PHOENICS, has been shown to predict the correct trends in mean axial and radial velocities, and in turbulent kinetic energy, k, downstream of the stagnation region ($r/d \geq 1$). Within the stagnation region, computed values of k were as large as nine times the experimental values. The predicted heat transfer was within 20% in the wall jet region where isotropy prevails and the magnitude of k compared well with experiment, but at the stagnation point where the flow has been shown to be anisotropic, the heat transfer was overpredicted by ~300%.

High average heat transfer rates are obtained when the impingement plate is placed within, and just at the end of, the potential core of the jet. These spacings, preferably without semi-confinement, are recommended for optimal performance not taking into account the required pumping power. At larger nozzle to plate spacings, jet impingement heat transfer becomes less effective.

ACKNOWLEDGEMENTS

I am grateful for all the support that I have received during the course of this work. In particular, I would like to thank the following persons: Dr Nath Jambunathan, my Director of Studies for his enthusiasm and tireless encouragement throughout this project and, on a more personal note, for his confidence in me in all aspects of my work; Professor Bryan L Button, my supervisor, for many useful and stimulating discussions; Mr Alan Crisp and Mr Eddie Edmonds, Principal Technicians, and their staff, for manufacturing, and providing help and support in the development of the experimental rigs; Mr Rob Potter for his encouragement, commitment and sterling work in carrying out some of the experimental tests.

Thanks are also due to Mr Jim Corlett for his help in obtaining much of the information used for this work, and to Mrs Doreen Corlett for maintaining up to date jet impingement and liquid crystal databases.

Special thanks are due to my colleagues, Mr Stuart Hartle and Mr Shabir Kapasi for their friendship and worthwhile discussions and who often induced the motivation to continue.

I take great pleasure in dedicating this work to those who are closest to me and have endured these recent years with me; my husband and parents. I would like to express my deep gratitude to my Mother who in recent years has offered overwhelming support, and my father, posthumously, who is always in my thoughts. I am indebted to my husband, Gary, for friendship, support and understanding during this busy period of our lives, which was mostly during his own demanding postgraduate education. The thanks I offer here hardly seems enough. Finally, to my three older brothers who have always believed in me and continue to show interest in my life and career.

I would like to acknowledge the National Advisory Body (NAB) for financial support during the period 1987-89, and The Nottingham Trent University for financial support thereafter, made possible by my then Head of Department and Dean, Professor Bryan L Button.

LIST OF PUBLICATIONS

Jambunathan K, Ashforth-Frost S and Button B L, 1990. Flow visualisation of a laminar jet impinging in a semi-confined space. In: *Proceedings of the Fifth International Symposium on Application of Laser Techniques to Fluid Mechanics*. Lisbon, Portugal, 9-12 July.

Thakker A, Frawley P, Jambunathan K and Ashforth-Frost S, 1991. An experimental study of the counter and tracker signal processors used in fluid measurements. In: *Proceedings of the Tenth International Congress on Applications of Lasers and Electro-optics*. San Jose, CA, USA, 60-9.

Ashforth-Frost S, Wang L S, Jambunathan K, Graham D P and Rhine J M, 1992. Application of image processing to liquid crystal thermography. In: *Proceedings of the IMechE Seminar Optical Methods and Data Processing in Heat and Fluid Flow*. City University, London, 2-3 April, 121-6.

Ashforth-Frost S and Jambunathan K, 1994. Effect of nozzle geometry and semi-confinement on the potential core of a turbulent axisymmetric jet. *Presented at The Tenth International Heat Transfer Conference*, Brighton, UK, 14-18 August, Paper no. 63.

LIST OF FIGURES

LIST OF APPENDICES

NOMENCLATURE

Symbol	Meaning
c_p	Specific heat at constant pressure
C_D, C_μ, C_1	Turbulence model constants
C_2, σ_ϵ, σ_k	Turbulence model constants
d	Nozzle diameter
f	Characteristic frequency
F_d	Doppler frequency
F_S	Frequency shift
h	Heat transfer coefficient; Grid spacing
h_p	Enthalpy at near wall node
h_w	Enthalpy at wall
k	Thermal conductivity; Turbulent kinetic energy.
L	Characteristic length scale
N	Number of data samples
Nu	Nusselt number
Nu_0	Stagnation Nusselt number
$\dot{q}$	Heat flux
r	Radial distance from the stagnation point
Re	Bulk Reynolds number
s	Skin friction factor
St	Stanton number
Str	Strouhal number
t	Time
T	Temperature
T_∞	Bulk fluid temperature
T_0	Initial temperature of plate
T_{aw}	Adiabatic wall temperature

T_{jet}	Jet temperature
Tu	Turbulence intensity
u	Normal or axial velocity component
u_b	Bulk velocity in the pipe
u_c	Centreline velocity
u_{max}	Maximum velocity in the pipe
u'	RMS normal velocity; component of normal Reynolds stress velocity component
$\tilde{u}$	Instantaneous normal velocity
v	Radial velocity component
v_p	Radial velocity at near wall node
v'	RMS radial velocity; component of normal Reynolds stress
$\tilde{v}$	Instantaneous radial velocity
$\overline{u'v'}$	Component of Reynolds shear stress
x	Distance into the plate
y	Distance from the plate surface
y_p	Distance from the plate to the near wall node
y^+	Non-dimensional distance from the plate
z	Nozzle to plate spacing

Greek symbols

α	Thermal diffusivity
δ_{ij}	Kronecka delta
ϵ	Dissipation rate of turbulent kinetic energy
η	Effectiveness, $\eta=(T_{aw}-T_\infty)/(T_{jet}-T_\infty)$
θ	Half laser beam intersection angle
κ	von Karman constant
λ	Wavelength of laser
μ	Dynamic viscosity

ν	Kinematic viscosity
μ_t	Turbulent dynamic viscosity
ν_t	Turbulent kinematic viscosity
ρ	Density
σ	Standard deviation
σ_l	Laminar Prandtl number
σ_t	Turbulent Prandtl number

CHAPTER 1

INTRODUCTION

This Chapter commences with an indication of the importance of impinging jets, and the usefulness of their numerical simulation, to industry. Current needs to enable further development of jet impingement processes and numerical models are then identified. Based on these needs, the specific aims are presented followed by the rationale and the objectives formulated to achieve these aims. The objectives are broken down into a series of questions which have been addressed through the course of the work and answered within the subsequent text of this thesis. Finally, an outline of the layout of the thesis is provided.

1.1 Background and statement of the problem

Jet impingement flows are frequently used in industrial practice for their high heat and mass transfer rates. Their employment is common but also diverse and typical applications include many heating, cooling and drying processes such as the manufacture of Printed Wiring Boards, printing processes, production of foodstuffs, de-icing of aircraft wings and the cooling of turbine airfoils. The high heat transfer rates are especially needed to achieve short processing times for product quality or due to temporal limitations of the process and/or for energy efficiency; an increasingly important factor in recent years, partly due to environmental implications. Another important consequence of jet impingement is that the non-uniform distribution of the heat transfer coefficient can lead to unwanted overheating due to hotspots. Consequently, the total design of a heating, drying or cooling system may critically depend on attainable heat or mass transfer rates as well as the required pumping power to achieve these rates. During the last three decades, the focus of jet impingement investigations has concentrated on obtaining correlations to describe the stagnation point, or average values of heat transfer. Reviewing the literature reveals that there are a large number of correlations available for surface heat transfer due to jet impingement, which include a range of physical quantities. In most cases these correlations include terms based

on jet exit conditions, despite early investigations which identified the importance of the local hydrodynamic phenomena, Gardon and Akfirat (1965). Due to the large number of physical quantities and possible geometric configurations there is no general agreement amongst these correlations, and universal guidelines have been provided to help the designer. In some cases these recommendations are inappropriate for the jet impingement configuration under design, such that an unsuitable nozzle to plate spacing is prescribed; the same heat transfer rates may be attainable at a different spacing which requires less pumping power. In order to establish the applicability of these correlations, or new correlations, it is clear that an increased physical understanding of the fluid flow/heat transfer phenomena is needed. The industrial designer can also use this information to move away from uneconomic, inefficient systems which have been designed by 'rule of thumb' or to further enhance a system by improving upon modifications based on 'in-situ' developments. An increased understanding of the fundamental physics of the flow can only be achieved by interpretation of detailed experimental measurements.

The fluid dynamic structure of such processes is an extremely complex problem, such that it is often reduced to that of a single impinging jet, which is complex in its own right. In practice, the flow field will be turbulent except at very low Reynolds numbers. Nevertheless, laminar solutions are useful in providing a starting point for a turbulent study or where they represent a particular problem.

Even when the practical application is simplified, the necessary experimental rigs can be complex and expensive, not to mention the time consuming data acquisition, validation and analysis. Numerical simulations are an alternative to the experimental approach and can provide a fast and economic solution which will describe the flow, or at least identify trends in the flow or heat transfer distribution. In this case, the designer needs to be aware of the

reliability and limitations of the numerical solutions for the particular geometry under investigation. An assessment of the model can only be obtained by comparison with experiment. Since numerical solutions are problem dependent there is a need for detailed experimental data specific to the jet impingement geometry. Indeed, despite much progress in the area of turbulence modelling over the past twenty years, there is not a universal turbulence model available which will allow reliable prediction of the flow field or heat transfer characteristics of all test geometries. The difficulty lies in the closure of the time averaged equations. Turbulence models are used to simulate the averaged character of real turbulence and, together with the mean flow equations, form a closed set thus enabling a numerical solution to be obtained. The further development of turbulence models warrants the provision of detailed experimental data as a bench mark test case. Jet impingement has been identified by other workers as a suitable vehicle for the development of turbulence models, since the flow characteristics are common to many engineering flow fields. There is therefore a further need for detailed reliable experimental data.

The determination of the mean flow characteristics and the measurement of turbulent quantities is thus of fundamental importance, both to the experimentalist and computationalist. The scarcity of turbulence data in this flow has been highlighted recently by several workers, for example, Gouldin et al. (1986), van den Berg (1990), Launder (1991) and McGuirk (1991), and has partially provided the motivation for this study. Such measurements have been performed and are supported with measurement of the associated heat transfer characteristics to enable interpretation of the results with direct reference to the heat transfer phenomena. Consideration of the required pumping power was beyond the scope of the present study. In addition, the performance of the widely used k-ϵ turbulence model has been assessed for the prediction of the above characteristics.

1.2. Aims and Objectives

1.2.1 Specific Aims

i) To seek a better understanding of the influence of near wall velocity and turbulence on surface heat transfer within the stagnation region of a single turbulent incompressible jet impinging in a semi-confined space perpendicularly onto a smooth surface at a single Reynolds number and low nozzle to plate spacing.

ii) To provide a benchmark for the future development of numerical methods and turbulence models.

iii) To assess the suitability of the kappa-epsilon (k-ϵ) turbulence model in predicting fluid flow and heat transfer characteristics of semi-confined jet impingement.

1.2.2 Rationale

A nozzle to plate spacing of 2d and Reynolds number of 20000 was selected for several reasons. These were

i) To retain a secondary peak in the distribution of heat transfer coefficient; the secondary maximum in heat transfer disappears at higher nozzle to plate spacings, and becomes less pronounced at lower Reynolds numbers.

ii) Review of the literature and communication with other research groups identified an urgent need for experimental data for this spacing and Reynolds number, for validation of new turbulence models.

iii) The k-ϵ turbulence model was developed for high Reynolds numbers. The k-ϵ model was selected for assessment in this study due to its wide use and availability in

industry and academia.

iv) Grid independence was more likely to be attained for a smaller nozzle to plate spacing.

v) Numerical predictions in the literature indicate only minor differences in the computed profiles of velocity and turbulence at higher Reynolds numbers.

vi) Limitations inherent to the LDA system restricted the levels of turbulence and mean velocity that could be obtained with confidence.

A semi-confined configuration was selected because

i) Despite the industrial relevance of this geometry, very few works were identified in the existing literature.

ii) The upper boundary simplifies the specification of the problem numerically; previous attempts to corroborate experimental data with computations by different authors had the downfall that the upper entrainment boundary had been specified in different ways in order to combat problems with convergence or due to mis-application.

1.2.3 Objectives

In order to complete these aims the following objectives were identified:

a Design, build and commission an airflow rig and traversing mechanism with associated instrumentation, to enable laser-Doppler anemometry measurements throughout a two dimensional vertical plane of the flow domain. The airflow rig will allow surface temperatures to be measured using Liquid Crystal Thermography (LCT) in order to evaluate heat transfer coefficients. Consider experimental

uncertainty during design. Develop software for the control of the instrumentation and efficient collection and analysis of the experimental data.

b Establish the range of geometric and fluid quantities for the experimental work, based on jet impingement applications, the characteristics of the LDA system, existing literature and preliminary measurements of velocity, turbulence and heat transfer.

c Obtain an insight into the flow characteristics of semi-confined jet impingement by using full field flow visualisation techniques.

d Identify data collection criteria to minimise experimental uncertainty. Validate the measurement of velocity and turbulence. Calibrate the liquid crystal temperatures.

e Obtain velocity and turbulence information for the test programme. Obtain heat transfer coefficient distributions using the same experimental arrangement and for the same conditions.

f Using an existing Computational Fluid Dynamics (CFD) package with the k-ϵ model of turbulence, with input of measured boundary conditions, predict the above characteristics. Compare results with existing work.

1.2.4 Breakdown of Objectives

Objective e was focused on obtaining detailed near-wall velocity and turbulence information since, as will be discussed in Chapter 2, it is the flow characteristics in this region that dominate the heat transfer process. The original objectives c to f were broken down into

the following questions:

Quality of results

Qualitative experimental results

What is a suitable seeding medium for flow visualisation? How can results be permanently recorded? How well does the seeding medium represent the fluid flow?

Quantitative experimental results

Can the LDA results be validated against other measurement techniques and other authors data? How does the output vary with seeding density and number of data samples? Is data correction necessary? What is the precision of the LDA system? What is the spatial resolution of the traverse mechanism? What is the most appropriate angle of rotation of the LDA optics for measuring the Reynolds stress components? How can near wall measurements be improved? What is the uncertainty propagated through the data reduction equations?

Should a steady-state or transient approach be used to evaluate heat transfer coefficients? What experimental working temperatures should be adopted? What is the spatial resolution of the temperature measurements? What is the temporal resolution? What is the thermal resolution? What is the overall uncertainty?

What is the uncertainty in the air supply? Is the jet axisymmetric? Are the test results repeatable?

Numerical results

What is the accuracy of the CFD package? Are the computations grid independent? Has satisfactory convergence been achieved?

Analysis of results

Qualitative experimental results

Are vortices generated/do coherent structures exist at the jet exit? Are vortices also generated at the impingement surface? Is the flow periodic? Can the mean flow be characterised?

Quantitative experimental results

Is the flow isotropic? What is the distribution of u, v, u', v' and $\overline{u'v'}$ in the stagnation region? Where does the maximum near wall (axial and radial) velocity and turbulence occur? Does transition of laminar to turbulent flow take place? If so, do these positions coincide with heat transfer maxima? Where do the maximum heat transfer coefficients occur? How does the heat transfer coefficient vary with radial distance and nozzle to plate spacing?

Is an overall assessment of the effect of near wall turbulent quantities on the heat transfer possible?

Numerical results

Is the mean flow field predicted well? How do the predictions of the turbulent quantities compare with the experimental? How well does the k-ϵ model predict the heat transfer distribution in the semi-confined case? How well does the k-ϵ model predict the turbulent kinetic energy in the stagnation region? Can this explain any differences in the modelling of heat transfer? Can recommendations for future work be proposed?

These questions have been answered through the course of the work and within the text of this thesis.

1.3 Outline of the investigation

This Chapter has provided a brief background to the study and statement of the problem. The aims, and objectives to achieve these aims, have been discussed in detail.

Relevant literature is reviewed in Chapter 2. The review commences with a description of the jet impingement flow field, its associated heat transfer characteristics and available correlations for the dependence of Nusselt number on Reynolds number. The effect of turbulence on heat transfer in stagnation flows is discussed, with particular attention paid to the axisymmetric impinging jet at low nozzle to plate spacings. Available works using full field flow visualisation techniques are also reviewed in order to gain an insight to the flow. The review of literature on the numerical prediction of jet impingement has focused on recent works which are considered the most reliable. Finally, a summary of the major outcomes of the survey is provided.

The experimental set-ups and procedures used for qualitative flow visualisation, laser-Doppler anemometry, and liquid crystal thermography are presented in Chapter 3. A discussion on the selection of experimental quantities in order to minimise uncertainty is included here and the validation of the measurement system.

The governing equations for flow and heat transfer, and their numerical solution, are presented in Chapter 4. Attention is paid to the grid dependence/numerical accuracy of the study (using the Richardson extrapolation technique) and convergence criteria. Details of the solution algorithm and commercial package PHOENICS (Parabolic, Hyperbolic or

Elliptic Numerical Integration Code Series) are not provided since they are well described in several texts.

The presentation and discussion of all experimental results is given in Chapter 5, while numerical results and their comparison with experiment are presented in Chapter 6. These Chapters concentrate on the characteristics of the semi-confined jet impingement flow field at a Reynolds number of 20000 and nozzle to plate spacing of 2d. Limited results at the same Reynolds number but nozzle to plate spacings of 4d, and 6d are included where they help to exemplify the characteristics of the 2d case. The turbulent characteristics of the flow field are compared with the associated distribution of the heat transfer coefficient.

Finally, in Chapter 7 a summary and conclusions from this study, practical applications of the results, and recommendations for further work are discussed.

CHAPTER 2

LITERATURE REVIEW

There are many variable quantities within the field of jet impingement and the classification of the many types of impingement often depends on the readers own interpretation. It therefore seems prudent to commence this Chapter by defining the various jet impingement geometries. These are illustrated in Figure 2.1. It is intended in this Chapter to concentrate on the works pertinent to the flow visualisation of fluid flow and heat transfer of a semi-confined axisymmetric impinging jet. The impingement of single unconfined axisymmetric (circular) and slot (two dimensional) jets, with uniform velocity profiles (flat), onto a flat surface have received the most attention. Because of the sparsity of results for the semi-confined case the unconfined axisymmetric case is also considered. Where the jet exit profile is not uniform or nearly uniform, specific reference is made to the geometry. The effect of nozzle geometry and semi-confinement is considered separately in Section 2.4.5.

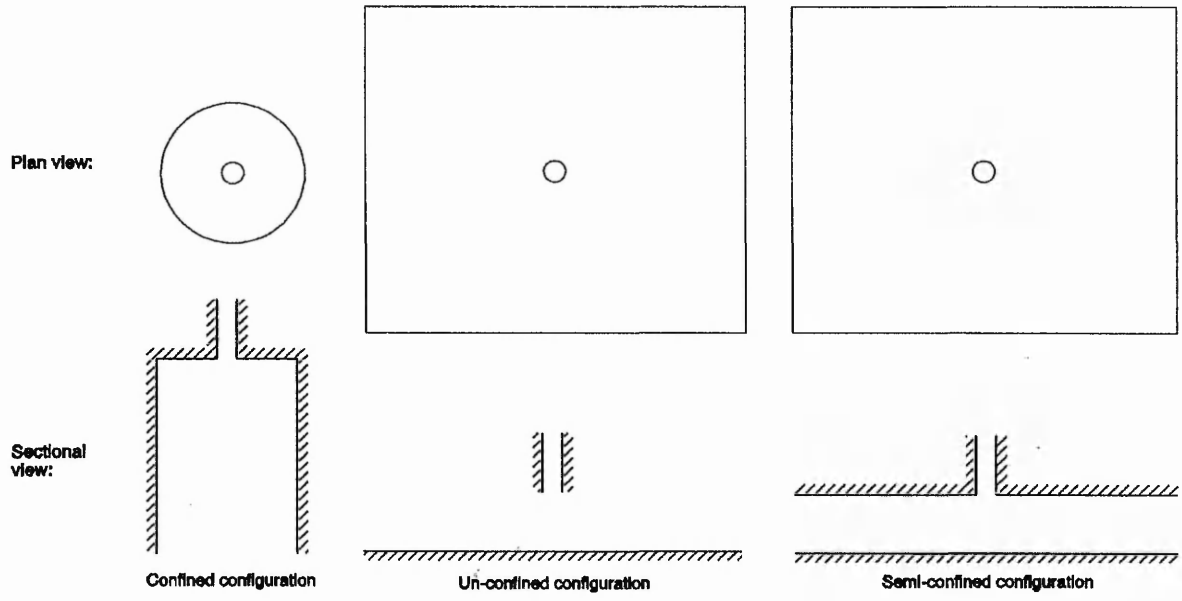

Figure 2.1. Definition of jet impingement geometries.

The literature survey is discussed in four parts. Firstly, an overview of existing literature reviews, which give information on a wide range of jet impingement configurations, is provided. The distinct flow regions of jet impingement are then characterised to provide a background to the problem. A discussion of heat transfer characteristics of jet impingement, and the effect of transport phenomena and geometry on heat transfer, forms the major part of this literature review, where a critical appraisal of relevant literature is provided. This Section includes both experimental and numerical works. Since it will be shown that turbulent jet impingement has a laminar-like dependence on Reynolds number in the stagnation region, literature on the laminar impinging jet will also be reviewed. Finally, the main points identified within the review are summarised at the end of the Chapter.

The focus of the survey is on low Reynolds number turbulent jets with $2<z/d<8$, for the region $0<r/d<4$. Since the object of this study is primarily to investigate the effects of velocity and turbulence on heat transfer, only the dependence of Reynolds number and turbulence are considered in the Nusselt number correlations.

2.1 Existing reviews

Jet impingement is a broad topic and there is consequently an extensive amount of archived literature. There are many variable quantities and several reviews on the subject are available. These include comprehensive lists of publications arranged in chronological order, such as Button and Wilcock (1978) and Button and Jambunathan (1989), or classified into various categories such as Arganbright and Resch (1971), Livingood and Hrycak (1973), Martin (1977) and Hrycak (1981) to succinct critical reviews. Some of these authors have included useful tabulated summaries of the experimental, theoretical and numerical work reviewed.

Martin (1977) provides a broad comprehensive survey which concentrates on the engineering applications of jet impingement. Both the fluid flow and heat/mass transfer characteristics of axisymmetric and plane jets are covered. With emphasis also on applications, Becko (1976) provides a review of heat transfer correlations for round and slot jets in single, lines and array configurations. Livingood and Hrycak (1973) and Hrycak (1981) summarise experimental and analytical heat transfer correlations for the same configurations and highlight the lack of knowledge of jet turbulence characteristics. Downs and James (1987) focus on the round impinging jet, only referring to other configurations where particularly relevant. Most recently, a critical review of heat transfer data for a single axisymmetric jet at small nozzle to surface distances can be found in Jambunathan et al. (1992).

Numerical works of flow and heat transfer characteristics of jet impingement are reviewed by Polat et al. (1989). Rodi (1980) critically reviewed mathematical models available at the time paying particular attention to the k-ϵ model, which was shown to predict a large range of geometries reasonably well. Persen (1986) addresses the application of various concepts to turbulence modelling and emphasizes the physical concepts involved. An excellent in-depth review of approaches to turbulence modelling is provided by Markatos (1986) who includes second-moment closures (Reynolds and Algebraic Stress Models) and Large Eddy Simulations (LES).

2.2 Description of the flow region

In the case of an impinging jet, three distinct flow regions can be characterised, illustrated in Figure 2.2; free jet, stagnation and wall jet regions.

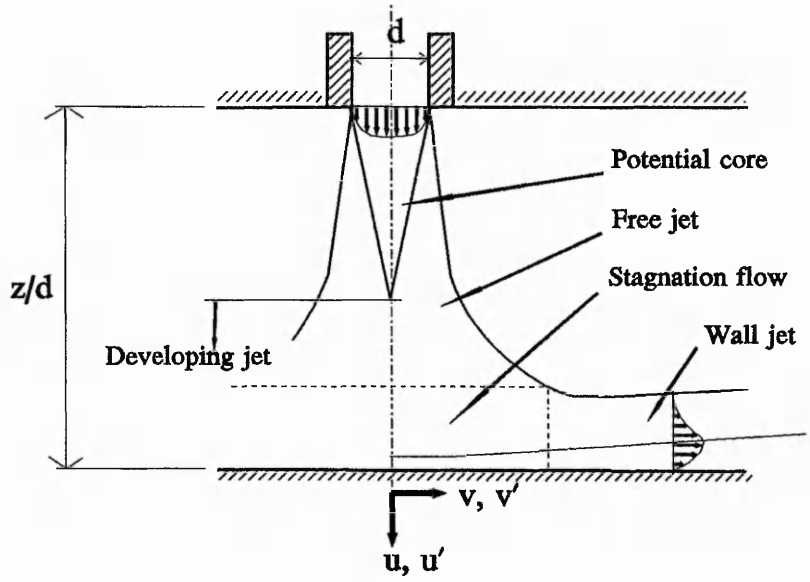

Figure 2.2 Schematic diagram of jet impingement flow field.

2.2.1 Free jet region

In the free jet region, the shear-driven mixing of the exiting jet and the ambient produces entrainment of mass, momentum and energy. This results in expansion of the jet, the development of a non-uniform radial velocity profile and modification of the jet temperature before impingement. According to Schrader (1961) this region extends from the nozzle exit up to 1.2d from the impingement surface.

The free jet can be subdivided into three separate regions; flow establishment or potential core region, developing and fully developed regions.

The potential core extends from the nozzle and is the central portion of the flow in which the velocity remains constant and equal to the jet exit velocity. It is formed as a result of turbulent mixing which originates near the nozzle exit. Turbulence is generated at the jet boundary and diffuses towards the axis such that the width of the mixing zone increases with

downstream distance, leaving the potential core region. Some authors state that the potential core length is dependent on Reynolds number while others state that it is independent of Reynolds number but dependent on the velocity profile. The latter view is supported by Abromavich (1963). The velocity profile on impingement will depend on the shape, velocity distribution and turbulence intensity at the nozzle exit. According to Gauntner et al. (1970) the length of the potential core generally lies in the region 4.7d to 7.7d.

The developing region is characterised by the axial velocity decay and additional entrainment of fluid. Schlicting (1968) shows that the jet half-width ($u=u_c/2$) is directly proportional to axial distance from the jet exit, at large distances.

After this region the velocity profile becomes fully developed. A Gaussian velocity distribution best fits experimental data in this region. The jet broadens and the axial velocity decays linearly (e.g. Schrader, 1961). Jet impingement in this region is not considered in the present study.

2.2.2 Stagnation region

In the stagnation region the axial flow strongly decelerates and radial flow accelerates producing an increase in static pressure. According to Schrader (1961) the stagnation flow region extends to 1.2d axially from the surface, and 1.1d radially from the stagnation point. Beltaos and Rajaratnam (1977) give 1.2d and 1.4d respectively. Giralt et al. (1977) agree with the axial extent of the stagnation zone. The accelerated stagnation flow transforms to the decelerated wall jet.

2.2.3 Wall jet region

The wall jet region is characterised by a bulk, decelerating flow in the radial direction. According to Abromavich (1963), for low nozzle to surface spacings, the maximum radial velocity occurs at approximately r/d=1.

2.3 Heat transfer characteristics of a laminar impinging jet

Most of the results available for laminar jet impingement have been obtained from theoretical or numerical investigations. According to Vickers (1959) and McNaughton and Sinclair (1966) an impinging jet is considered to be fully laminar when Re<1000. Sibulkin (1952) solved the boundary layer equations for laminar heat transfer to a body of revolution near the forward stagnation point and showed that the stagnation point Nusselt number was a function of $Re^{0.5}$. This same dependency has been derived by Scholtz and Trass (1970) for a parabolic impinging jet. In both studies a solution for the inviscid flow field was obtained. In the latter, this was utilised as a boundary condition for the viscous flow along the impingement plate.

For the laminar case, the full Navier-Stokes equations can be solved with appropriate boundary conditions. Saad et al. (1977) used a finite difference technique to model the semi-confined case for 1.5<z/d<12. The jet exit profile, parabolic or flat, was found to have a significant effect on the stagnation point heat transfer and corroborates the finding of Sibulkin (1952) that the radial velocity gradient determines the stagnation point heat transfer coefficient. For the flat velocity profile the dependence of Nusselt number on $Re^{0.5}$ was obtained as predicted by boundary layer theory. However, for a parabolic velocity profile a $Re^{0.36}$ dependence was obtained. This has not been substantiated by any other works for an axisymmetric jet and could be attributed to the coarse grid used close to the impingement plate. Deshpande and Vaishnev (1982, 1983) obtained numerical solutions for Re<1000

and z/d<5 using the unconfined geometry. Radial positions of maximum wall shear stress and pressure were investigated. The maximum pressure gradient was computed to be three times higher for a parabolic velocity profile than for a flat velocity profile. Jambunathan et al. (1989) carried out a parametric study using the semi-confined configuration. They corroborated the findings of Deshpande and Vaishnev (1982, 1983) and highlighted the substantial effect of varying the inlet velocity profile on the magnitude and radial location of the maximum friction factor.

2.4 Heat transfer characteristics of a turbulent impinging jet

The heat transfer distribution is determined by the hydrodynamics discussed in the previous Section. According to Chamberlain (1966) (see Gauntner, 1970) two different modes of heat transfer exist depending on the nozzle to plate spacing. When the surface is within the potential core the variation in heat transfer coefficient is attributed to turbulent fluctuations since the axial velocity is constant. The stagnation flow is laminar-like and the heat transfer rate compares well with that calculated by the laminar stagnation theory. When the surface is placed further downstream the turbulence is increased and both turbulence and velocity cause a variation. Investigations have shown that the heat transfer at the stagnation point reaches a maximum value when the impingement surface is placed just at the apex of the potential core. Gauntner (1970) and Sparrow et al. (1975) suggest a nozzle to surface spacing of 6.1d if the value is unknown. Beltaos and Rajaratnam (1977) recommend 6.1d to 6.3d.

2.4.1 Correlations for local Nusselt number

Many empirical correlations have been developed to allow the calculation of mean or local heat transfer distributions. A favoured method of correlation relates the Nusselt number to Reynolds number, Prandtl number, non-dimensional nozzle to plate spacing and radial

distance from the stagnation point: Nu=f(Re, Pr, z/d, r/d). Smirnov et al. (1961) gave a correlation Nu=f(d, Re, Pr, z/d), valid for $0.5<z/d<10$, $1600<Re<50000$ and $0.7<Pr<10$ where the Reynolds number exponent was 0.33. The dependence on the diameter has not been substantiated by any later works. The correlation was based partly on other authors data from as early as 1930 and the exact experimental conditions and geometries are not known. Huang (1963) measured the impact velocity at the stagnation point using a pressure probe for $1000<Re<10000$, $1<z/d<12$ and established a simpler correlation Nu=f(Re, Pr) where the Reynolds number exponent was 0.87. No other dependencies on the geometry or flow characteristics were reported. Subsequent works by other authors have indicated significant variations with change in geometry. Gardon and Cobonpue (1962) and Popiel and Boguslawski (1988) gave correlations for stagnation point heat transfer under an impinging jet as $Nu \sim f(Re^{0.5})$ for $z/d<5$. From the similar analyses of Sibulkin (1952) for the stagnating laminar flow on a cylinder, this suggests that the flow at the stagnation point of jet impingement at low nozzle to plate spacings is laminar even for a turbulent Reynolds number. According to Popiel and Boguslawski (1988), the Reynolds number exponent increased to 0.75 for $z/d>7$. Goldstein and Franchett (1988) proposed a correlation dependent on $Re^{0.7}$ and radial position, valid for $4<z/d<10$. The increase in the exponent with increasing axial and radial distance is not unexpected, since workers such as Rao and Trass (1964) have shown a dependence on $Re^{0.8}$ for fully developed turbulent wall jets. Most recently, and most relevant to this investigation, Yan et al. (1992) studied the impingement of a fully developed jet at Reynolds numbers of 23000, 50000 and 70000 for nozzle to plate spacings of 2d, 4d, 6d and 10d. Correlations give the exponent of the Reynolds number as 0.5, 0.56 and 0.58 for $z/d<2$, $z/d=6$ and $z/d=10$ respectively, thus confirming the appearance of a laminar boundary layer in the stagnation region at low nozzle to plate spacings (within the potential core) and the increase in the value of the exponent as the nozzle to plate spacing increases. They gave a value of 0.7 for the exponent

in the wall jet region. El-Genk et al. (1992) also show Nu to be strongly dependent on both z/d and r/d. Mohanty and Tawfek (1993) give correlations for impingement point heat transfer according to nozzle diameter in the form Nu=f(Re, z/d). The Reynolds number exponent varies between 0.67 and 0.71. Unfortunately, the data cannot be used to substantiate the dependence on diameter as reported by Smirnov et al. (1961), since different ranges of Re and z/d were considered for each nozzle.

These correlations did not include any dependence on local turbulence levels. Hoogendoorn (1977) however, established a correlation of $Nu/Re^{0.5} \sim f(Tu\ Re^{0.5})$ valid for $1<z/d<10$.

Jambunathan et al. (1992) reviewed extensively the correlations for Nusselt number dependence on Reynolds number obtained by various authors during the period 1967 to 1991, paying particular attention to the wall jet region. Linear regression was used to obtain the exponent of the Reynolds number in the relation $Nu \sim f(Re)$ for $1.2<z/d<10$ and $0<r/d<6$. Their findings supported the dependence on $Re^{0.5}$ at the stagnation point. A significant variation in the exponent was observed in the region $1<r/d<2.5$ which suggests that laminar to turbulent transition does occur in this region. They also demonstrate the trend for the exponent at the stagnation point to increase with increasing nozzle to plate spacing, and for the exponent to increase with increasing radial distance from the stagnation point, corroborating the findings of the previously cited authors.

2.4.2 Effect of turbulence on stagnation point heat transfer

Extensive studies have been carried out on the effect of turbulence on heat transfer at the stagnation point of a cylinder in a cross flow. Hoogendoorn (1977) compared the effect of turbulence on stagnation point heat transfer for cylinders in a free stream with that of jet impingement and concluded that the relative increase in heat transfer was the same. In the

direct vicinity of the stagnation point, jet impingement is considered to be analogous to this flow, and consequently these works are briefly reviewed.

Kestin et al. (1961a and 1961b) demonstrated the importance of the influence of turbulence on the heat transfer rate at the cylinder stagnation point at a high Reynolds number (>75000), stating that the largest heat transfer enhancement occurred at the lowest turbulence levels. They found that the local Nusselt number increased by 25%-50% when the turbulence intensity was increased from 0.5% to 2%. However, Lowery and Vachan (1975) reported a much lesser dependence of turbulence on heat transfer; at higher Reynolds numbers, they found that the heat transfer was enhanced as the turbulence intensity was increased to 14% but did not increase further for turbulence intensity >14%. Conversely, Sikmanovic et al. (1974) found that this augmentation of heat transfer for Tu<2% did not exist for low turbulent Reynolds numbers.

2.4.3 Effect of turbulence on jet impingement heat transfer

Extensive experimental studies on the influence of Reynolds number, turbulence and geometry on impingement heat transfer were first carried out by Gardon and Cobonpue (1962) and Gardon and Akfirat (1965). A short nozzle with rounded inlet was used. The heat transfer was augmented as z/d was increased from 0 to 5 due to the increasing level of turbulence at a constant axial velocity. The peaks in the heat transfer distributions occurred at r/d≈0.5 for z/d<4 with a secondary peak at r/d≈1.9. Below Re=14000 the secondary peak became less prominent and moved towards the axis while a slight tertiary peak emerged at r/d≈2.5. The magnitude of the heat transfer coefficient was reported by Gardon and Akfirat (1966) to be 40% too high in their earlier studies due to incorrect calibration of their transducer, although the heat transfer profiles were not affected. Koopman and Sparrow (1976) and Popiel and Boguslawski (1988) confirmed the existence of these three

peaks. The heat transfer beyond this point reduces due to the decelerating wall jet. At Reynolds numbers below 2500 the secondary peak disappeared entirely. Gardon and Akfirat (1965) concluded that since the inner peaks did not disappear then they were not caused by turbulence but by some other mechanism regardless of laminar or turbulent Reynolds number. The results therefore offered support to the theoretical finding of Kezios (1956) that at r/d=0.5 the boundary layer has a minimum thickness but was not supported by the experimental work of Hrycak et al. (1970). Gardon and Akfirat (1965) suggested two explanations for the outer peak

i) Penetration of turbulence into the boundary layer from the mixing layer of the jet

ii) Transition from laminar to a turbulent boundary layer flow.

Hall and Khan (1964) (see Cebeci and Bradshaw, 1984) demonstrated for pipe flow, that the thermal entry length diminishes with increasing Reynolds numbers because transition moves towards the pipe entry. If the latter explanation suggested by Gardon and Akfirat (1965) were the case, then as the jet Reynolds number increased, it might be expected that the secondary peak would move towards the stagnation point. However, the contrary was observed by Gardon and Akfirat; the secondary peak moved towards the stagnation point as the Reynolds number decreased.

At larger nozzle to plate spacings the secondary peaks disappeared to leave a bell shaped heat transfer profile. This is to be expected since transition from laminar to turbulent flow may not occur where the flow is fully turbulent on impact such as at large nozzle to plate spacings. Gardon and Akfirat (1965) suggested that the stagnation point heat transfer rate increases slightly beyond the apex of the potential core, but that the increase will only continue so long as the increase in turbulence compensates for the decrease in jet axial

velocity.

Schlünder and Gnielinski (1967) also showed that there was a qualitative agreement between turbulence intensity and heat transfer. They found that both the maximum turbulence and stagnation point heat transfer occurred at z/d=7.5 for Re>38000. Hoogendoorn (1977) obtained similar heat transfer profiles at z/d=2 and z/d=4. In addition to the convergent nozzle, Hoogendoorn (1977) also studied a jet issuing from a long pipe at the same Reynolds number for z/d=2. The heat transfer profile was identical for r/d>1 but instead of a maximum at r/d=0.5 the heat transfer continued to increase to a higher maximum value at the stagnation point. This could be expected due to the fully developed jet profile. Obot et al. (1979) found that for a contoured nozzle, the maximum stagnation point Nusselt number occurred at z/d=8. When this nozzle was replaced with a sharp edged inlet, the maximum Nusselt number had increased by ~25% and occurred at z/d=4. A similar investigation was made by Popiel and Boguslawski (1986). They found that for z/d<4, when the jet exit turbulence was increased from 0.75% to 1.8%, the heat transfer maxima were augmented by ≈40%.

Much of the heat transfer and fluid flow data obtained before the late 1980's had large or unknown uncertainties due to experimental errors such as heat conduction in the test plate, poor spatial resolution or inaccuracies inherent to the measuring technique. Although in general the trends in the data were modelled satisfactorily, such errors could substantially affect the heat transfer coefficient, especially near the stagnation point, and the measurement of turbulence near the impingement surface. With the development of new surface heaters and techniques such as liquid crystal thermography, a number of research groups have provided jet impingement heat transfer data which would appear to be less prone to such experimental errors. Goldstein and Franchett (1988) modelled jet

impingement due to discharge from a square edged orifice for nozzle to plate spacings of 4d, 6d and 10d at Reynolds numbers of 10000, 20000 and 30000 using a steady state liquid crystal technique with a 25 μm stainless steel shim heater. Gundappa et al. (1989) compared heat transfer distributions due to jets issuing from an orifice and a long pipe (l/d=10), evaluated using a Gardon heat flux gauge and thermocouples embedded in the surface. At z/d=7.8 the pipe exit produced the same trends as the orifice but a higher heat transfer at all radial positions. For smaller values of z/d, the different jets produced different profiles of heat transfer. Baughn and Shimizu (1989) and Baughn et al. (1991) used a similar technique but with a vacuum deposited gold coating to investigate the impingement of a fully developed jet. Baughn and Shimizu (1989) investigated an ambient jet at Re=23750 and nozzle to plate spacings of 2d, 6d, 10d and 14d. Baughn et al. (1991) studied the heated jet at Reynolds numbers of 23300 and 55000 for nozzle to plate spacings of 2d, 6d and 10d. The results agreed with previous studies and they confirmed that local heat transfer coefficients for an unheated jet can be used for a heated jet with entrainment if the heat transfer coefficient is defined in terms of the local adiabatic wall temperature. Baughn and Yan (1991) repeated the study of Baughn and Shimizu (1989) using a transient liquid crystal technique and obtained excellent agreement between the results. This study was extended in Yan et al. (1992), reported previously in Section 2.4.1.

In all of these investigations the experimental uncertainty was estimated to be less than 6%. Heat transfer results obtained by Baughn and Shimizu (1989) were used by Cooper et al. (1993) for comparison with near wall turbulence data obtained for the same geometry using hot-wire anemometry. The main objective of the investigation was to provide reliable data for turbulence model assessment. However, they identified a definite link between the near wall turbulence level and the heat transfer coefficient at r/d≈2 for a Reynolds number of 23000 and nozzle to plate spacings of 2d and 4d. This is the first experimental data to be

obtained very close to the impingement surface and will be used later for comparison with results from the present study.

2.4.4 Qualitative flow visualisation

Yokobori et al. (1979) attempted to visualise the role of turbulence in axisymmetric jet impingement heat transfer for $1000<Re<67000$ and $2<z/d<12$. Like several other authors, they identified the initiation of vortex structures at the jet exit. When the potential core region impinged directly onto the surface the laminar like stagnation flow was observed. They calculated auto-correlation coefficients based on stagnation pressure measurements and periodicity was clearly apparent. A Strouhal number was defined

$$Str = \frac{fd}{u_b}$$

At Re=16500 and z/d=3.3, Str=0.45. When the plate was positioned at $4<z/d<12$ large scale vortices, transported from the shear mixing region upstream, were present in the stagnation region. The vortices coalesced to produce small scale random turbulence at the jet axis and radial movement of the stagnation point was observed. This radial movement would conceal the existence of any secondary peak in the heat transfer measurements and could explain the mean bell-shaped distribution as previously reported. The periodicity had disappeared and for $z/d>7$ the stagnation flow field did not retain axisymmetry. They concluded that the flow field of the impinging jet should be considered an ensemble mean of unsteady random fluid motions in large scales. Kataoka et al. (1986, 1987) reported similar findings at z/d=6.7. They observed vortex rings at r/d=1 which broke up into large scale eddies at the end of the potential core region. Periodicity was observed for $r/d<4$. They defined a surface renewal parameter as the product of a turbulent Reynolds number and Strouhal number and concluded that enhancement of stagnation point heat transfer is mainly due to turbulent surface renewal by large scale eddies. Popiel and Boguslawski (1988) observed an intermediate maximum in heat transfer for $z/d\leq2$ at lower Reynolds

numbers which they attributed to vortices initiated at the jet exit striking the plate, as reported earlier in Popiel and Trass (1982).

2.4.5 Effect of nozzle geometry on heat transfer

Obot et al. (1979) carried out an extensive investigation into the effect of nozzle inlet shape and nozzle length to diameter ratio on unconfined impingement heat transfer. In all of their tests they reported similar shapes in the radial Nusselt number distribution but significant differences in their magnitudes. Nozzles with a sharp edged inlet produced much higher heat transfer than contoured nozzles and the difference was more pronounced the shorter the nozzle length. Although their investigation was extensive, the surface temperature was deduced from a series of rings concentric around the stagnation point which varied in width from 0.34 to 1.5 nozzle diameters, suggesting poor spatial resolution. Popiel and Trass (1991) proposed that the laminar boundary layer formed in the nozzle was responsible for the well defined structure of the vortices initiated there. When the nozzle boundary layer was disrupted, a much less distinct structure was observed. Yokobori et al. (1979) however, reported that a vortex structure was obtained when the boundary layer was turbulent. Lepicovsky (1989) discussed how the nozzle geometry affects the boundary layer thickness at the nozzle exit, which in turn controls the rate of jet mixing and spreading. Applying these findings to jet impingement, the jet mixing will affect the decay of the jet and the length of the potential core and consequently the heat transfer distribution. Lepicovsky (1989) demonstrated that a thin nozzle exit laminar boundary layer resulted in a shorter potential core than in the case of a thick turbulent nozzle exit boundary layer.

Obot et al. (1982) studied heat transfer distributions where the nozzle was an integral part of a flat surface parallel to the impingement surface (ie. semi-confined) for $18000<Re<50000$. Comparison with the unconfined case showed that semi-confinement

reduced the heat transfer, the most significant difference occurring for z/d=2 and the least difference occurring for z/d=6. Moreno et al. (1993) measured mass transfer coefficients for the semi-confined geometry and briefly addressed the effect of confinement. Although limited, their data indicated that the mass transfer was less dependent on Reynolds number in the semi-confined configuration.

2.4.6 Numerical investigations

Kim (1967) used Prandtl's hypothesis on eddy viscosity with a finite difference solution technique to predict axisymmetric jet impingement at high Reynolds numbers. For the low nozzle to plate spacings considered, he reported thinning of the wall boundary layer for small radial distances from the stagnation point with the minimum thickness occurring at r/d=0.7 which coincided with the position of maximum heat transfer. Bower et al. (1977) used a one equation model and found large discrepancies with experimental data of velocities and turbulent kinetic energy at low nozzle to plate spacings. Pamadi and Belov (1980) contradicted the theory of Gardon and Akfirat (1965) that a thinning of the boundary layer occurs at r/d≈0.5, and attributed the high heat transfer at this point to mixing induced turbulence. The outer peak was still attributed to transitional flow. These early investigations were restricted by the available turbulence models and the computing capabilities of the time.

The k-ϵ turbulence model has been widely used to simulate stagnation flows. Its use is not entirely justified since, as will be shown in this study, the impinging jet is an anisotropic flow and the basic assumption of the k-ϵ model, which employs the Boussinesq hypothesis, is local isotropy. Despite this fundamental drawback it has been, and still is, widely used due to its economy over Reynolds and Algebraic Stress Models and because it is readily available in various commercial packages. Studies using the Boussinesq hypothesis have had various

degrees of success and have shown significant variations between themselves and experimental data. In general the mean flow field and pressure distribution are predicted reasonably well regardless of which turbulence model is used. This can be explained by the fact that the flow in the stagnation region of an impinging jet is pressure driven. Vallis et al. (1979) used the standard k-ϵ model, Jones and Launder (1973), with wall function for low turbulent Reynolds numbers and nozzle to plate spacings >10d. Their results showed reasonable agreement with empirical data, but it is highly likely that the solution was not grid independent since the finest grid adopted was 16 x 14. Their computations were also restricted to the upwind finite difference technique. Chieng and Launder (1980) predicted stagnation point heat transfer rates approximately 500% larger than expected using a low-Reynolds number form of the k-ϵ model. Agarwal and Bower (1982) also used a low-Reynolds number k-ϵ model and showed that it performed better for jet impingement than the zero and one equation models but still led to over-prediction of turbulent kinetic energy along the jet axis. Amano (1983), and Amano and Brandt (1984) have studied the axisymmetric case at high Reynolds numbers (Re>100000) and in Amano and Neusen (1982) at lower Reynolds numbers for large nozzle to plate spacings. Amano (1983) used a hybrid finite difference technique with the same turbulence model. A 30 x 15 grid was used with local refinement near the jet axis. Comparison with experiment showed a 5% difference in computed velocities but 25% difference in skin friction coefficient. Amano and Jenson (1982) and Amano and Sugiyama (1985) used the k-ϵ model with three different models for the calculation of k and ϵ at the grid points nearest the wall. Reynolds numbers of 10000, 20000 and 40000 were studied at nozzle to plate spacings of 4d, 7d and 10d. A fully developed velocity profile was specified at the jet inlet. They observed a significant variation in results using the different models. Despite a reported 30% improvement in the prediction of the maximum heat transfer coefficient by fixing the value of ϵ at the wall as a function of k, the stagnation point heat transfer still showed considerable difference with

experiment.

The numerical errors associated with many of these simulations prevent any reliable assessment of the turbulence model accuracy. Barata et al. (1987, 1988, 1989, 1991) address in particular the problem of numerical accuracy by performing rigorous grid independence studies and introducing higher order discretisation schemes. For impinging jets in crossflow they have shown that the Reynolds shear stress is not predicted correctly by the k-ϵ model.

The importance of the jet impingement flow field has recently lead to liaison between a number of experimental and numerical research teams, e.g. ERCOFTAC (European Research Community on Flow Turbulence and Combustion) North Pilot Centre/SERC Community Club. At the 1991 Lyon/IAHR (International Association for Hydraulics Research) Workshop, the unconfined impinging jet case was adopted as a vehicle for comparison between various turbulence models and computational packages with experimental results at Re$\approx$23000 and z/d=2. This test case was further discussed at the 1991 seminar 'Turbulence Modelling for Impinging Flows' held at UMIST, Manchester and organised by Launder (1991). The upper boundary conditions were approximated. Several workers experienced problems with convergence due to this entrainment boundary and modified the conditions so as to attain convergence. The selection of a semi-confined geometry would simplify the specification of this boundary since the most straight forward boundary conditions correspond to the semi-confined geometry; without confinement the upper boundary can only be approximated. Results obtained using the k-ϵ and Reynolds Stress Models (RSM) models were compared with experimental results of heat transfer distribution, and limited velocity and turbulence results, within the stagnation region, and are reported by Brison and Brun (1991) and McGuirk (1991). No solutions using a modified k-ϵ or Algebraic Stress Models (ASM) were attempted. In general, numerical resolution was considered satisfactory, but significant differences between model/model and model/experiment were evident. The model/model differences could be

partly attributed to the different treatment of the entrainment boundary, different solution algorithms employed and the mis-application of boundary conditions. Comparison with experiment showed that in all of the computations the radial velocity profiles in the stagnation region were reasonably predicted but the Reynolds shear stress was underpredicted, the turbulent kinetic energy and heat transfer were overpredicted. The k-ϵ model showed the largest differences. The high levels of heat transfer were attributed to the overprediction of the turbulent kinetic energy within the stagnation region, which in turn result in too high entrainment rates of the free stream fluid. The most promising results were obtained using a Reynolds Stress Model with a new wall reflection model described by Craft and Launder (1991). However, this model is in early stages of development and its generality is unknown. McGuirk (1991) concludes that attention must be paid to the numerical treatment of the upper boundary and for future evaluations of numerical developments, experimental data of velocity, turbulence levels and Reynolds stresses are required within the impingement region. Van den Berg (1990), in an independent study of turbulent boundary layers, also concluded that the status of turbulence modelling is not satisfactory and that in order to support the development of semi-empirical models of acceptable accuracy, a more extensive base of reliable turbulence data is essential.

2.5 Concluding remarks

An overview of existing literature reviews has been provided for the general case of jet impingement and the classifications of jet impingement geometries have been clarified. The flow regions of jet impingement have been described, since the heat transfer distribution is dependent on the hydrodynamics of the flow. Works pertinent to the present configuration of semi-confined turbulent jet impingement at low nozzle to plate spacings have been discussed and the main outcomes are now summarised. It is interesting to note that much of the relevant work has only been completed over the last ten years.

Velocity and turbulence, particularly near the impingement surface, have a marked effect on the magnitude and distribution of the Nusselt number. The velocity and turbulence characteristics in the stagnation region are affected by nozzle geometry, confinement and the generation of upstream turbulence.

The early work of Gardon and Cobonpue (1962) and Gardon and Akfirat (1965, 1966) is some of the most relevant work on the effect of turbulence on jet impingement, and is still referred to by most workers, despite its inaccuracy in the magnitude of heat transfer coefficient. The trends in their data have been corroborated by more recent works, Koopman and Sparrow (1976), Obot et al. (1979), Goldstein and Franchett (1988) and Popiel and Boguslawski (1988). Although the stagnation heat transfer is high, the two major peaks in the heat transfer coefficient occur at $r/d \approx 0.5$ and $r/d \approx 2$.

The high heat transfer at the stagnation point has been attributed to high axial turbulence and velocity, Gardon and Akfirat (1965), Chamberlain (1966) (see Gauntner, 1970). The highest levels of heat transfer occur when the impingement plate is placed at the apex of the potential core where the maximum axial turbulence levels prevail, Gardon and Akfirat (1965). The length of the potential core, and consequently the level of turbulence, depends largely on the nozzle exit geometry, Obot et al. (1979) and Hoogendoorn (1977). When this length is unknown a value of $\sim 6.1d$ is recommended, Gauntner (1970), Sparrow et al. (1975) and Beltaos and Rajaratnam (1977). Increasing the level of turbulence in a stagnation flow has been shown to further augment the heat transfer, Kestin et al. (1961a & 1961b), Gardon and Akfirat (1965), Lowery and Vachon (1975), Hoogendoorn (1977), Obot et al. (1979), Popiel and Boguslawski (1986), Gundappa et al. (1989). According to Gardon and Akfirat (1965), the peak in heat transfer at $r/d \approx 0.5$ which occurs for both laminar and turbulent jets, cannot be attributed to the effects of turbulence but to some other mechanism related to

the radial velocity profile. This offers support to the theoretical finding of Kezios (1956) that the boundary layer has a minimum thickness at this location. Gardon and Akfirat (1965) further suggested two explanations for the secondary peaks in heat transfer at low nozzle to plate spacings; laminar to turbulent transition and diffusion of mixing induced turbulence into the boundary layer. Transition however, will only occur at low nozzle to plate spacings when the jet is arranged to give a laminar flow at the stagnation point. For larger values of z/d, or where the jet is fully developed on impact, laminar to turbulent transition may not take place. The second explanation is supported by the work of Yokobori (1979), Kataoka et al. (1987), Popiel and Trass (1982) and Popiel and Boguslawski (1988), who identified vortex structures within the vicinity of the plate, transported from the shear mixing region upstream. As well as these structures, vortices may be generated at the heat transfer surface, but as far as the author is aware, there is no evidence to confirm this possibility. The timely and excellent data of Cooper et al. (1993) on the unconfined jet has substantiated the higher levels of turbulence in this region. They have found that the near wall turbulence at the stagnation point continues to increase up to $r/d \approx 2$.

Only three works have been identified where a single semi-confined turbulent jet impingement configuration has been experimentally investigated, Obot et al. (1982), Lucas et al. (1992) and Moreno (1993). Although the mechanisms of heat transfer and trends in the heat transfer coefficient distribution appear similar, semi-confinement has the effect of reducing the heat transfer coefficient due to less mixing of the jet with the surrounding fluid, as a consequence of the semi-confinement. Obot et al. (1979) compared the effect of nozzle geometry on heat transfer, concluding that the greatest effects were encountered when a short nozzle was used and that a sharp inlet results in higher heat transfer rates. However, there is uncertainty as to the reliability of their data. This paper does at least highlight the difficulty in making direct comparisons of different authors data, since many workers neglect

the detailed specification of their nozzle geometry in publications. Only four research teams have been identified where a fully developed, or nearly fully developed, jet exit velocity profile was used, Hoogendoorn (1977), Gundappa et al. (1989), El-Genk et al. (1992) and Baughn and Shimizu (1989), Baughn and Yan (1992), Baughn et al. (1991) and Yan et al. (1992). For the very long nozzles (>50d) the highest heat transfer occurred at the stagnation point in all studies. However, the fully developed jets issuing from shorter nozzles (~25d), studied by Gundappa et al. (1989) and El-Genk et al. (1992) produced a local minimum at the stagnation point. For r/d>1, the heat transfer distributions exhibit similar characteristics to the flat velocity profile impinging jet.

There is plenty of evidence, Gardon and Cobonpue (1962), Hoogendoorn (1977), Popiel and Boguslawski (1988), Yan et al., 1992) to support the theory that at low nozzle to plate spacings the stagnation flow is laminar-like, even at turbulent Reynolds numbers, since the Nusselt number was found to have an $Re^{0.5}$ dependence, which agrees with the laminar stagnation theory of Sibulkin (1952). The exponent on Re increases with increasing z/d, Popiel and Boguslawski (1988), Yan et al. (1992), El-Genk et al. (1992) and Mohanty and Tawfek (1993) and with radial distance, Popiel and Boguslawski (1988), Goldstein and Franchett (1988), El-Genk et al. (1992), which supports the findings of Rao and Trass (1964) for a wall jet.

Numerical works on the impingement of axisymmetric jets have been reported from 1967 to the present day. The numerical errors associated with many of the early simulations have prevented any reliable assessment of turbulence model accuracy. During the last five years, jet impingement heat transfer has been used as a test case for numerical predictions and in particular the validation of turbulence models. The most relevant works have been contributions to the IAHR workshop in Lyon, 1991, reported in Brison and Brun (1991),

and discussed further in McGuirk (1991). The most recent contribution is by Craft et al. (1993). The k-ϵ model has been used successfully to predict many elliptic flow fields, yet its limitations for specific geometries is not fully appreciated. For the case of jet impingement, the k-ϵ model largely overpredicted the heat transfer coefficient and was attributed to the overprediction of the turbulent kinetic energy near the stagnation point which in turn leads to too much entrainment of the free stream fluid. Significant model/model differences were obtained which could be partly attributed to the varied specification of the upper entrainment boundary and the mis-application of boundary conditions.

Attempts to assess the relative merits of various computational approaches have been hindered by the lack of detailed experimental data and the varied specification of the flow field boundaries. Ideally, the same boundary conditions should be used for each case so that the differences can be linked directly to the turbulence model. To facilitate assessment, a better understanding of the near wall flow phenomena is essential. Cooper et al. (1993), reported earlier, have made a very recent, and relevant, contribution to this data, for the unconfined case. As far as the author is aware, this is the only work that has addressed the very near wall turbulence structure.

The explanation of local heat transfer maxima, the development of new turbulence models and validation of existing models warrants the provision of reliable and detailed experimental data as a benchmark test case, van den Berg (1990), Launder (1991) and McGuirk (1991).

CHAPTER 3

EXPERIMENTAL INVESTIGATION

Physical quantities need to be measured to within known uncertainty and, to obtain a better understanding of the physical phenomena, the uncertainty needs to be minimised. With the advent of computers over the past 20 years and their use for data acquisition and analysis, the measurement of engineering quantities, which involve the collection of mass amounts of data, has become more feasible and significantly reduced the possibility of human error. However, other uncertainties need to be addressed prior to the experimental tests, in the design and validation of the test facility and experimental procedures.

This Chapter covers the design, development and validation of the experimental rigs, the procedures adopted for the flow visualisation, laser-Doppler anemometry and liquid crystal thermography tests, and the corresponding data reduction equations. Detailed uncertainty analysis techniques have identified factors which influence the data and have allowed appropriate selection of the experimental procedures. The description of the test facilities and procedures will allow the data to be replicated by other workers.

For many random variables, the probability distribution is a specific curve known as the Gaussian or normal curve. The same simple model has been adopted for the LDA data analysis. As far as possible, where feasible, the data has been taken in random order. A series of tests were carried out to increase the precision of the experiments. Although factorial planning was not employed, the range of physical quantities measured were selected in order to obtain maximum information from a minimum number of experiments. The uncertainty has been estimated for all measured and evaluated physical quantities. The estimated uncertainties are given for the 95 per cent confidence intervals based on the arithmetic means. There are a number of methods of uncertainty analysis. A method described by Kline and McClintock (1953) and later for heat transfer measurements by

Moffat (1985), and in more detail by Coleman and Steele (1989), has been used to compute the experimental uncertainties in this study. Kapasi (1994), in a experimental study of jet impingement heat transfer, has demonstrated the use of the Monte Carlo simulation method.

Experimental results presented in this Chapter enable validation of the measurement system and an estimation of the associated uncertainties.

3.1 Air supply facility

It was initially intended to use a central compressed air supply for the experimental work. Prior to the commencement of the experimental programme the velocity at the nozzle exit was monitored over long time periods at 10 second intervals. There appeared to be a cyclic nature to the supply, which was difficult to discriminate on the rotameter and could not be entirely eliminated by the regulator. Consequently, a dedicated compressor was used. Air from the compressor passed through two filtering systems (25 μm and 5μm) followed by a high precision regulator. The air then passed through a plenum chamber manufactured from Perspex which included a sheet of honeycomb flow straighteners and turbulence eliminating screens. The contraction to the nozzle was designed with the aid of a BBC BASIC computer program described by Button and Leech (1972). The contraction area ratio, C, was 16:1 and the profile co-ordinates are presented in Appendix A. In general, variations in velocity are reduced axially by C^2 and laterally by $C^{1/2}$. According to Obot et al. (1979) a nozzle length greater than 20d is necessary to attain fully developed flow to within 5% and to ensure that the nozzle entry has a small influence on the jet exit velocity. The nozzle was a sharp-edged seamless stainless steel tube of internal diameter 20 mm and length of 22d. The nozzle was manufactured by parting off a long section of the tube followed by the removal of any burrs. In Figure 3.1 the jet exit profile is compared to that

computed from the empirical equation of Schlicting (1968):

$$\frac{u}{u_{max}} = \left(\frac{y}{R}\right)^{\frac{1}{n}}$$

where y is given as the distance from the pipe wall and n=6.5 at Re=20000. The maximum velocity (at the axis) was evaluated from

$$\frac{u_b}{u_{max}} = \frac{2n^2}{(n+1)(2n+1)}$$

The jet was fully developed to within ~5%.

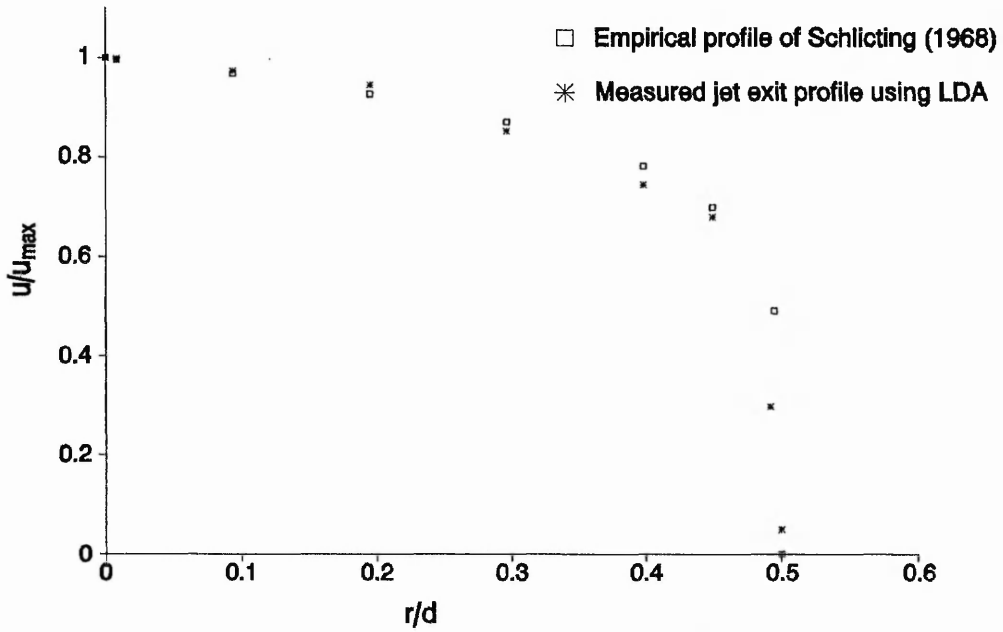

Figure 3.1 Comparison of jet exit profile with the empirical profile of Schlicting (1968).

The centreline jet exit velocity was found to be steady over long time periods after an initial warm-up period of one hour. The variations in the mean and fluctuating velocities over a typical continuous four hour period are shown in Figure 3.2. Maximum observed variations after the initial 1 hour period were 1% and 5% respectively.

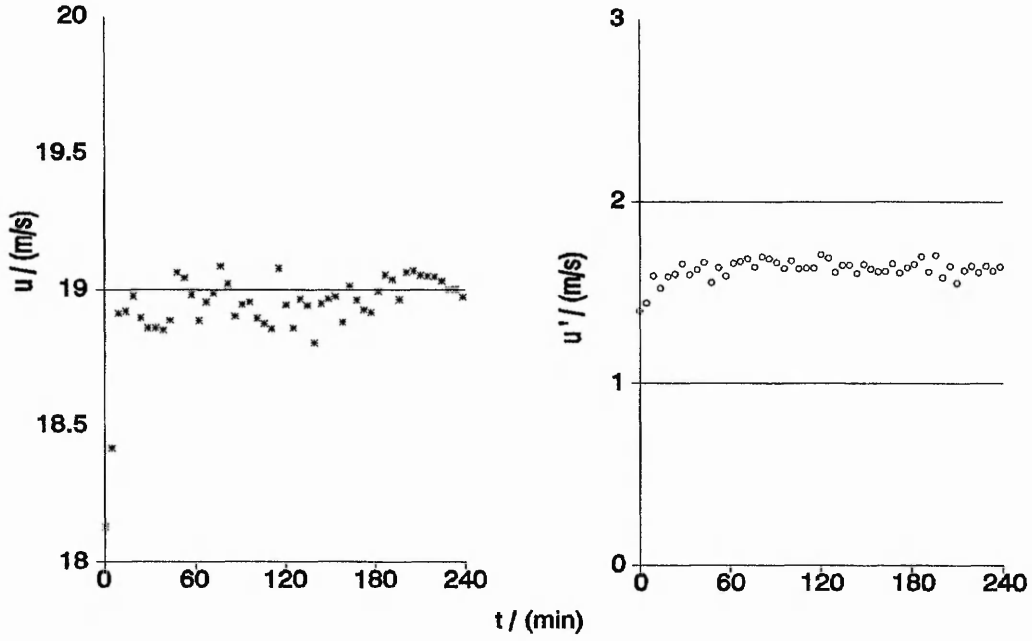

Figure 3.2 Jet exit velocity and rms velocity over continuous four hour period.

3.2 Qualitative flow visualisation

Prior to the detailed LDA measurements, visualisation studies were performed to provide a qualitative insight to the jet impingement flow. A simple lens arrangement, shown in Figure 3.3, was used to generate a thin light sheet (approximately 1 mm wide) by expanding a 10 mW HeNe laser beam in one plane between two matt black plates. The convex lens was positioned so that its focal length coincided with the cylindrical lens. The experiments were carried out in a dark room and results recorded, at 90° to the incident laser sheet, using a single lens reflex (SLR) camera and a 80-200 mm F4 zoom lens with a 1000 ASA red-sensitive film (Kodak 2475). The exposure time depended on the jet velocity and the region of the flow being photographed (aperture setting>5.6).

Oil smoke, cigarette smoke, water/glycerin particles, talc and hollow glass spheres were investigated as possible suitable seeding mediums.

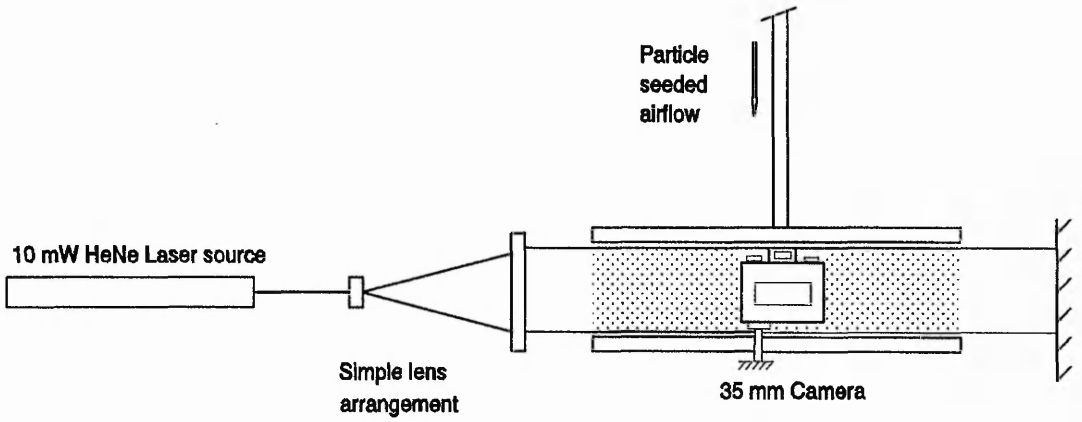

Figure 3.3 Experimental arrangement for flow visualisation

Limited tests were carried out using the oil smoke method only at low Reynolds numbers as the smoke rapidly mixed with the surrounding fluid preventing any clear results being recorded at higher nozzle exit velocities. The smoke was produced by vaporising Shell Ondina Oil 17 using a Fair Flow smoke generator manufactured by David Budworth Ltd. According to Merzkirch (1987) typical generators produce oil particles of 1 to 5 μm diameter and are assumed spherical.

Hollow glass spheres were selected for the majority of tests due to their superior light reflection properties and were introduced into the flow using a simple nebuliser arrangement. The seeding density was controlled by adjusting the height of the inlet pipe to the nebuliser. Electron scanning microscope photographs enabled the size distribution of the particles to be examined. The diameter of the glass spheres, which were spherical, ranged from 5 μm to 35 μm with an average wall thickness of 1.5 μm (Emerson and Cumming, Inc., 1977). The mean diameter was 11.5 μm with standard deviation of 4.5 μm. The density of the spheres was 228 kg/m^3, determined on a mass basis using Archimedes principle of fluid displacement.

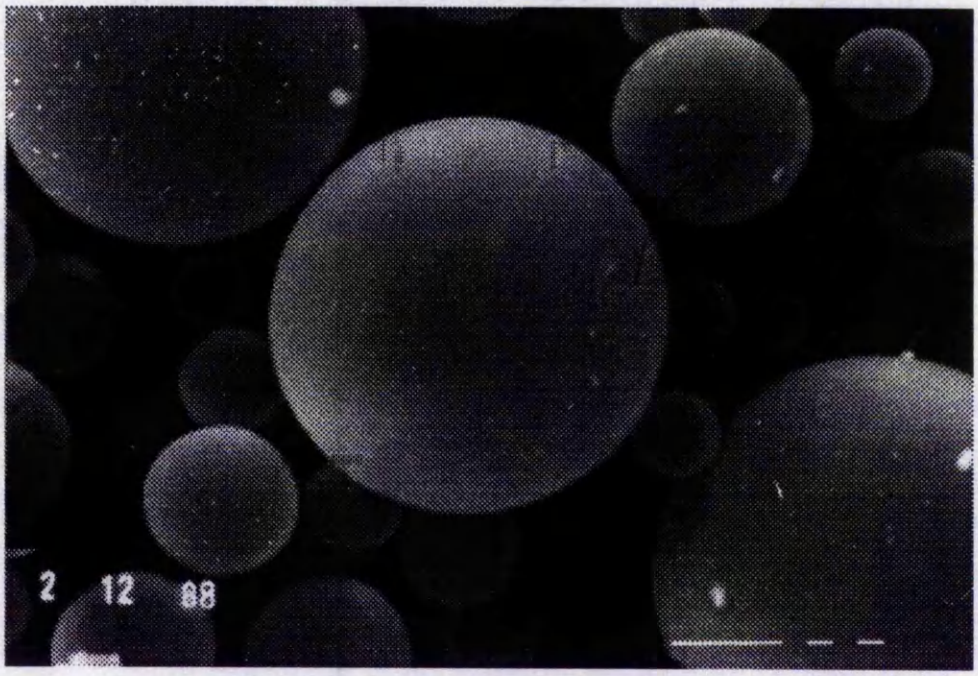

(a)

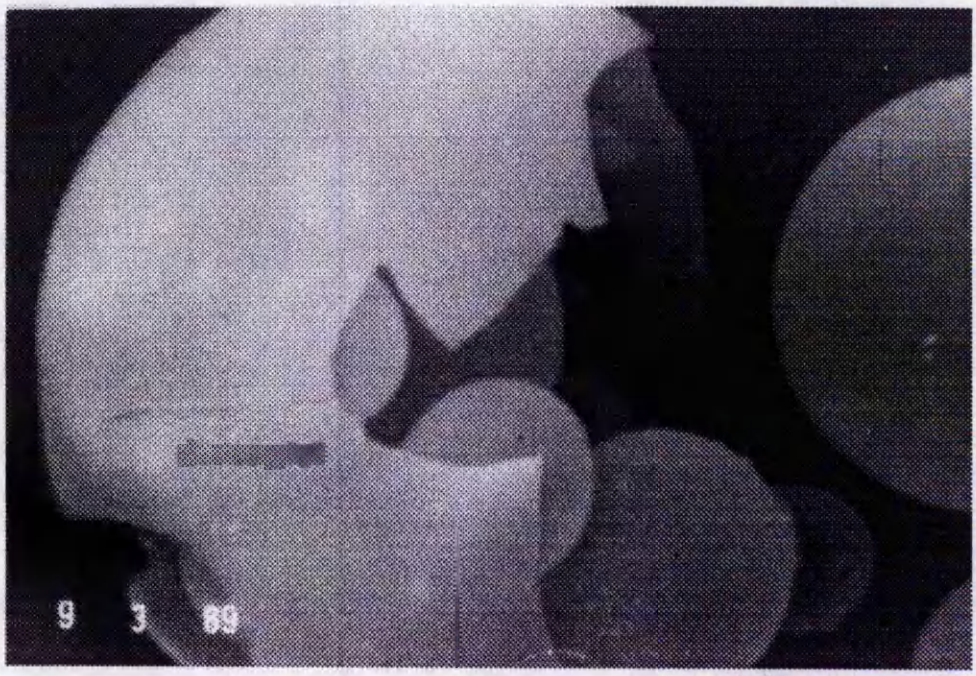

(b)

Figure 3.4. Glass microballoons; (a) before use, (b) after use.

Preliminary tests showed that the microballoons were prone to moisture contamination causing them to cluster, despite rigorous air filtering. Consequently, the microballoons were dried by placing them in an extractor oven for one hour at 100°C just prior to the tests. The jet emerged from a 10 mm nozzle, 22 diameters in length, after a smooth contraction, with a Reynolds number ranging from 600 to 20000. Nozzle to plate spacings of 2d, 4d and 8d were considered. Flow straightening was not employed to avoid damaging the microballoons. The results showed reasonable comparison with numerical simulations at Reynolds numbers below 2000, and are presented in Jambunathan et al. (1990). The results presented in Chapter 5 for the turbulent Reynolds numbers are only considered qualitatively and with reservation since it is not fully understood how well the microballoons follow the fluid flow. Photographs using the electron scanning microscope of samples taken of the microballoons, at the jet exit before impingement, and after impingement are shown in Figure 3.4. It is immediately apparent that some particles, especially the larger ones, have been damaged by the impact on the impingement plate.

Work in progress at the same time in other laboratories has subsequently been identified and offers support to the above. Yoshida et al. (1988) investigated jet impingement using hollow glass spheres of 48.9 μm mean diameter, standard deviation 8.7 μm suspended in air. The jet exit profile was also fully developed with a Reynolds number of 10000 based on a 10 mm round jet. By comparing LDA results of the development of the axial velocity profiles for the jet with and without the hollow glass spheres, they showed that particles rebound from the impingement plate to move upstream against the oncoming flow.

Obi et al. (1988) also considered larger particles in the range 69 to 148 μm concluding that the particles promote turbulence of the fluid in a flow with low turbulence and suppress turbulence in a strongly turbulent flow. This was substantiated by a detailed investigation

by Hetsroni (1988) on the effect of various seeding materials on turbulence of the main flow. He also showed that smoke particles of diameter less than 13 μm have little effect on the motion of the fluid.

3.3 Laser-Doppler Anemometry (LDA)

3.3.1 Principles of LDA and optical configuration

The principle of LDA consists of a particle crossing a beam of mono-chromatic (ie. single frequency) light which scatters light of a slightly different frequency due to the Doppler effect. When a particle crosses the intersection region of two mono-chromatic beams it will scatter light at two different Doppler shifted frequencies. Since the laser beams are also coherent (ie. in phase) these two frequencies will combine into a single Doppler difference frequency, which is directly proportional to the component of particle velocity in the plane of the two beams. Figure 3.5 gives a schematic diagram of the DANTEC single component laser-Doppler anemometer optics used in this investigation.

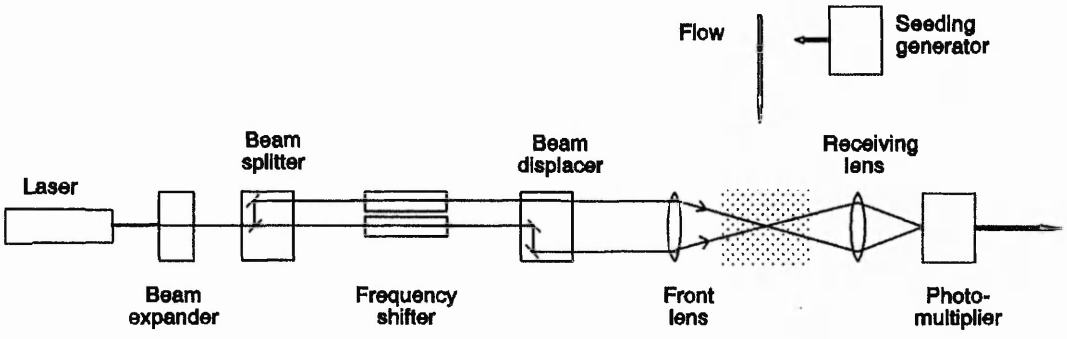

Figure 3.5 Schematic diagram of laser-Doppler anemometry optics.

Two laser beams from a single source are focused to intersect at their beam waists by the transmission optics, forming a series of interference fringes known as the measurement volume. The 3x beam expander has the effect of reducing the laser beam diameter at the

intersection point, thus reducing the size of the measurement volume (by a factor of 3) and increasing the relative light intensity (by a factor of 3^4). One of the beams has an optical frequency shift applied by a Bragg cell, which produces a moving fringe pattern enabling flow direction to be determined. A local frequency shift of 4 MHz was applied (by a DANTEC 55N10 frequency shift unit) as recommended by Tropea (1986). The other optical units, in the transmission stage, serve to displace and focus the laser beams into the flow of interest. Table 3.1 provides the characteristics of the LDA arrangement employed in this investigation.

Laser source	HeNe 10 mW
Laser beam diameter ($1/e^2$)	0.68 mm
Front lens focal length (f)	600 mm
Collection lens focal length	200 mm
Beam expansion factor	3
Optical frequency shift	40 MHz
Local frequency shift	4 MHz
Measurement volume size (dx,dy,dz)	0.24, 0.24, 4.7 mm
Effective measurement volume length	0.75 mm
Calibration factor	6.34 ms^{-1}/MHz
Pin-hole diameter	0.1 mm

Table 3.1. Characteristics of the LDA arrangement

As a seeding particle, which is assumed to follow the fluid flow, traverses the measurement volume it scatters light from the light and dark sections of the fringes. The measurement volume is imaged by a lens onto the cathode of a photomultiplier, which uses the principle of photo-electric transition to provide an electrical signal which is proportional to the frequency of scattering and hence to the velocity of the particles. A red narrow band interference filter was mounted in front of the photomultiplier to increase the signal to noise ratio by filtering ambient light. Forward scatter was used for light collection with the

photomultiplier placed approximately 22° off axis at f/3. This position corresponds to the secondary maximum of the light intensity scattered by an illuminated particle according to Mie theory (see Durst et al.,1981), and resulted in a reduced measurement volume length over which data was acquired. Johnson and Barlow (1989) highlighted the dependence of the Reynolds shear stress component in the near wall region on measurement volume length. Results obtained at the jet exit were the same for both forward scatter and off-axis collection. The signal processor extracts the Doppler frequency from the photomultiplier output. The signal processor used was a Dantec 55N20 frequency tracker. The principle of operation of this device is briefly described below. The incoming Doppler signal is amplified, filtered and compared with the output of a voltage controlled oscilloscope (VCO). After low-pass filtering, the error signal (phase difference between Doppler signal and VCO) is used to control the VCO to obtain a minimum phase difference. The VCO control voltage or frequency provides the flow information. The system is closed-loop such that if the frequency difference between the VCO and Doppler signal falls out of a certain range, then 'drop-out' occurs and the loop is opened. The last known signal is stored until a new one arrives. The tracker locks on to the instantaneous frequency as long as the loop stays locked. Consequently, a high particle seeding rate is required to ensure a continuous signal. The frequency tracking processor was developed jointly by DISA and AERE Harwell (Deighton and Sayle, 1971) and was first validated by Durst and Whitelaw (1971). The incoming signal and lock condition are monitored on an oscilloscope.

A microcomputer controlled two-dimensional X-Z traverse mechanism and instrumentation for the LDA system were designed to facilitate automatic data acquisition. To provide stability and vibration isolation the LDA optics were mounted onto the traverse mechanism which was fixed to a rigid frame supported by vibration isolation feet. This allowed measurements to be made in any vertical plane of the flow field. Calibration of the traverse

mechanism provided the positional resolution; the maximum backlash found was 0.01 mm in axis X and 0.05 mm in axis Z, positional errors varied between ±0.015 mm along axis X and ±0.085 mm along axis Z. A Linear Variable Differential Transducer (LVDT) was permanently installed to monitor the Z axis and thus reduce the positional errors in the Z direction to ±0.01 mm. The LVDT was calibrated against grade 0 gauge blocks which had been manufactured and calibrated according to BSS4311:1968.

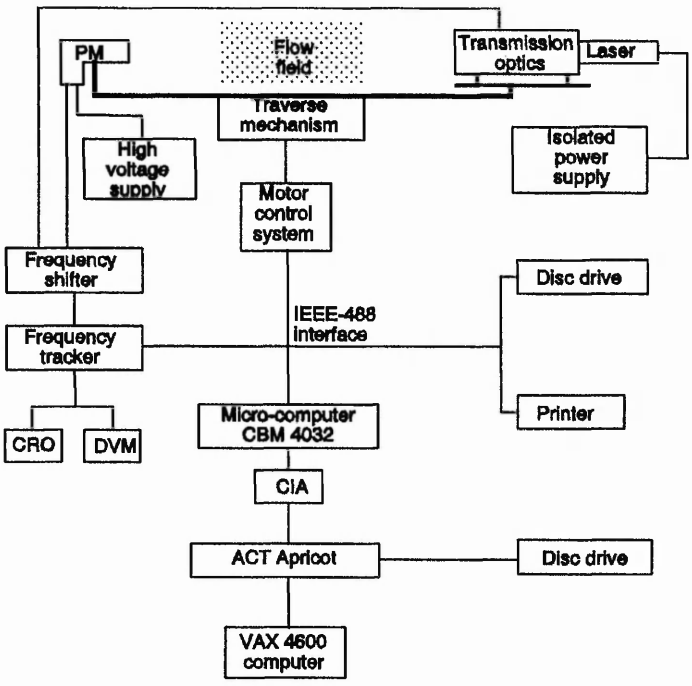

Figure 3.6 Schematic diagram of the complete measurement system.

A schematic arrangement of the complete measurement system is given in Figure 3.6. The computer was a Commodore 4032-PET micro-computer with the associated peripherals available such as disk drive, cassette player, plotter and paper printer. The operating system was BASIC 4.0. In order to use the IEEE-488 bus on the PET at maximum speed, it was necessary to use machine language rather than BASIC statements for data transfer. The computer controlled data acquisition from the tracker processor, movement of the traverse

and other peripherals, through the IEEE-488 interface and provided limited storage and data reduction capability. Floppy discs were used to provide real time storage of batches of experimental data. Data was transferred to a VAX 4600 computer for storage and rapid post processing, via a communications interface adapter (which converted IEEE-488 to RS-232) using poly-TRM/VT software to allow an ACT Apricot to emulate an ASCII terminal. Although the microcomputer is best restricted to data collection only, the on-line reduction and data analysis was used for a preliminary examination of the Doppler frequencies, enabling suitable range, filter settings and gain of the signal processor, and the BASIC software parameters to be set, since the accuracy of the measurement using LDA depends upon the correct choice of these parameters.

The development details of the traverse mechanism and the software for control, acquisition and analysis of data, formed a major part of the initial programme and are provided in Appendix B along with the machine language, BASIC program listing for the PET and FORTRAN coding for data analysis on the VAX 4600.

3.3.2 Initial position of the measurement volume

When the measurement volume is placed upon a surface, the surface provides a continuous signal equal to a zero mean velocity, which corresponds to the local shift frequency. In addition, since the laser beam has a Gaussian distribution, the signal has a maximum amplitude when the surface is in the centre of the measurement volume. This phenomenon was used to locate the measurement volume at the start of each test run. Prior to locating the measurement volume, a continuously seeded steady flow was used to obtain a maximum signal from the measurement volume, thus ensuring that the pin-hole receives a signal from the central region of the volume. A transparent prism 24.68 mm high, with a 18° apex, was used to locate the measurement volume at a known distance from the plate. The height of

this prism was measured to within 0.01 mm using an optical projector (Baty Shadowmaster). To determine the initial position in the radial direction, the measurement volume was positioned on the flat face of a transparent semi-cylinder, which was made a push fit into the jet nozzle. The principle of refraction was used to ensure that the laser beams passed through the centre of the cylinder face which corresponds to the centreline of the jet; if the laser beams, when at right angles to the face, do not pass through the centreline of the cylinder, then due to refraction, the beams would exit the semi-cylinder at an angle. The location of the measurement volume in the transverse radial direction was determined by identifying the maximum signal when the measurement volume was positioned on the flat face. The uncertainties in the axial, radial and transverse radial directions are estimated to be 25% of the effective measurement volume dimensions, leading to uncertainties of 0.05 mm, 0.05 mm, and 0.2 mm respectively. The radial positioning in the transverse direction was less accurate due to the length of the measurement volume.

3.3.3 Seeding of the flow field

A comprehensive account of the effect and requirements of seeding particles is given by Durst et al. (1981).For the LDA system to operate there must be light scattering particles contained within the flow field which are small enough to follow the fluid flow (typically 1-5 μm). When a seeding particle passes through the measurement volume, the full depth of modulation of the signal will only be achieved if the particle size is less than the fringe spacing. A particle size of half a fringe spacing is generally recommended for a good signal to noise ratio. In this investigation, a Dantec seeding generator has been employed to provide olive oil particles of 2-5 μm diameter, the fringe spacing being 6.34 μm.

Several workers (e.g. Durão and Whitelaw, 1974) have shown that careful seeding is necessary for jet flows to avoid biased measurements resulting from uneven particle

concentrations caused by unseeded entrained ambient air. In order to avoid this problem the jet arrangement has been surrounded by a large box (sufficiently far away from the geometry so as not to affect the flow field) and the seeded air supplied until the ambient air was considered sufficiently seeded before tests commenced.

The minimum number of particles required for a frequency tracker to provide a good representation of the true velocity characteristics depends on the scale size of the turbulence. There is no advantage in having an exceedingly high concentration, but if the seeding concentration is too low, at higher levels of turbulence the output from a frequency tracker will be biased towards the higher velocities, since more high speed than low speed particles will arrive in the measurement volume per unit time. The seeding concentration in this investigation was established by slowly increasing the amount of seeding to achieve a continuous signal.

3.3.4 Data acquisition and analysis

The instantaneous velocity ũ (the component normal to the fringes) measured at a given spatial location in the flow field was computed from (Durst et al., 1981),

$$\tilde{u} = \frac{\lambda(F_d - F_s)}{2\sin\theta} \tag{3.3}$$

and either stored in RAM for on-line data reduction or transferred to the VAX 4600 for postmeasurement analysis and the mean particle velocity u at that location computed from

$$u = \frac{1}{N}\sum_{i=1}^{N} \tilde{u} \tag{3.4}$$

The instantaneous velocity fluctuation u´, was given by

$$u' = \tilde{u} - u \tag{3.5}$$

and the root-mean-square values of the velocity fluctuations, or the standard deviation, σ, was determined from

$$\sigma = \left(\frac{1}{N} \sum_{i=1}^{N} u'^2 \right)^{0.5} \tag{3.6}$$

which is also a measure of the turbulence intensity at that location.

The third (skewness) and fourth (kurtosis, flatness or excess) statistical moments were computed as follows, Dietrich (1991):

$$\textit{Skewness} = \frac{1}{N} \sum_{i=1}^{N} \frac{(\tilde{u} - u)^3}{\sigma^3} \tag{3.7}$$

$$\textit{Kurtosis} = \frac{1}{N} \sum_{i=1}^{N} \frac{(\tilde{u} - u)^4}{\sigma^4} \tag{3.8}$$

The same equations apply to the direct measurement of radial velocity and turbulence components, v and v´.

In order to identify any fixed bias errors in the LDA system, the accuracy was assessed by comparing mean velocity results obtained at the exit of a fully-developed laminar pipe flow with the exact solution of the Navier-Stokes equations. For non-dimensional velocities greater than 0.1 a maximum deviation, from the parabolic form of the exact solution, of 0.3% was observed, shown in Figure 3.7. The larger discrepancies for lower velocities, at the edge of the jet, were attributed to mixing, since to gain access to the flow LDA measurements were made slightly downstream of the jet exit.

A minimum of 3000 data samples were acquired per measurement with a sampling rate of

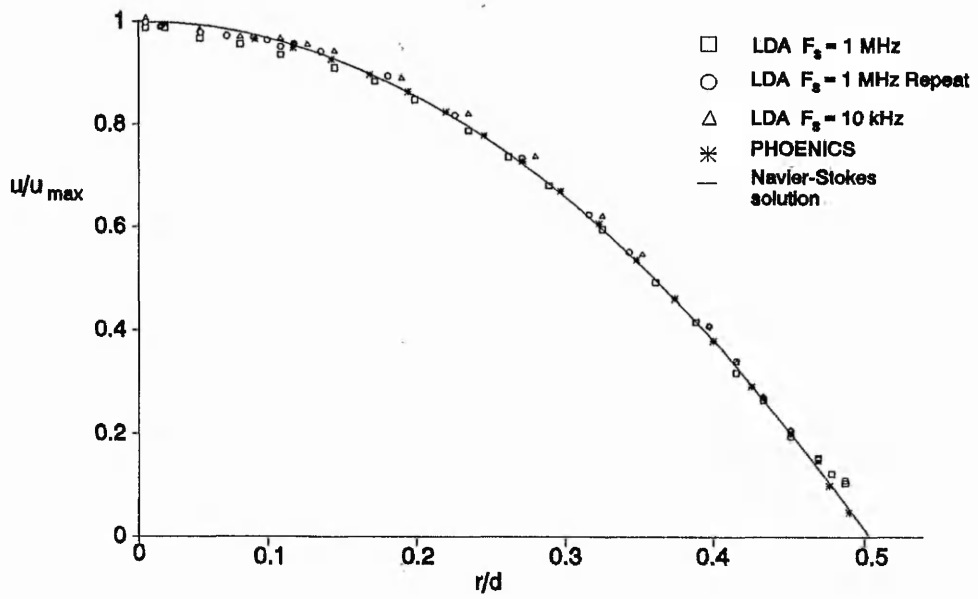

Figure 3.7 Laminar jet exit velocity profile.

100 Hz and an overall sampling period of 100s. Yanta and Smith (1973) suggested an approximation to determine how much data is necessary to obtain reliable statistical results. Their analysis assumed that the turbulence was Gaussian (ie. local isotropy) and reported that the number of data was dependent upon local turbulence intensity. Based on a 95% confidence level their formulae lead to

$$\epsilon_{mean}(\%) = \frac{196}{\sqrt{N}} \frac{\sqrt{\overline{u'^2}}}{u} \qquad (3.9)$$

$$\epsilon_{rms}(\%) = \frac{196}{\sqrt{2N}}$$

Bates and Hughes (1977) substantiated this finding concluding that all the statistical moments were dependent on sample size but weakly dependent on sampling rate. In the present investigation, to ensure that sufficient data had been collected to provide reliable velocity and turbulence measurement, the variation in the four statistical moments measured

at r/d=1, y/d=0.04 were compared for an increasing number of samples. The effect of sample size is shown Figure 3.8. There are no appreciable variations in the velocity and turbulence intensity curves. The scatter in the skewness and kurtosis, however, only converges with a sufficiently large sample size; N>2000 and N>2500 respectively. A minimum sample size of 3000 is therefore considered satisfactory. At the above station using a 95% confidence interval results in variations of mean velocity and turbulence intensity not exceeding ±0.5%, ±2% respectively (precision error). The calculated errors using equation (3.9) are $\epsilon_{mean} = 3.58\sqrt{\overline{u}^{'2}}/u = 0.46\%$ and $\epsilon_{rms} = 2.53\%$. Combined with the bias error of 4% quoted by the manufacturer and supported by Durst and Whitelaw (1971) for the frequency tracker, this leads to an overall uncertainty of ~4% and ~4.5% in the directly measured velocity and turbulence components respectively, based on the root-sum-square combination method.

In flows dominated by large scales, such as jet impingement, high seeding densities can bias the distributions towards the higher velocities. The selected sampling time was expected to minimise the velocity bias problem.

Since this investigation was mainly concerned with the measurement of near wall turbulent quantities, particular attention has been focused on the associated bias errors. When making LDA measurements within a boundary layer, bias can be caused by shift bias, due to the light scattering measurement volume being close to the wall, where a non-valid coherent signal can be recorded due to specular reflections, and by gradient bias due to the finite dimensions of the measurement volume. The effects of the latter have been minimised by using beam expansion to reduce the size of the measurement volume and by adjusting the focal length of the collection optics to reduce the data collection 'window'. Shift bias arises due to the use of frequency shift (which is required to measure velocity

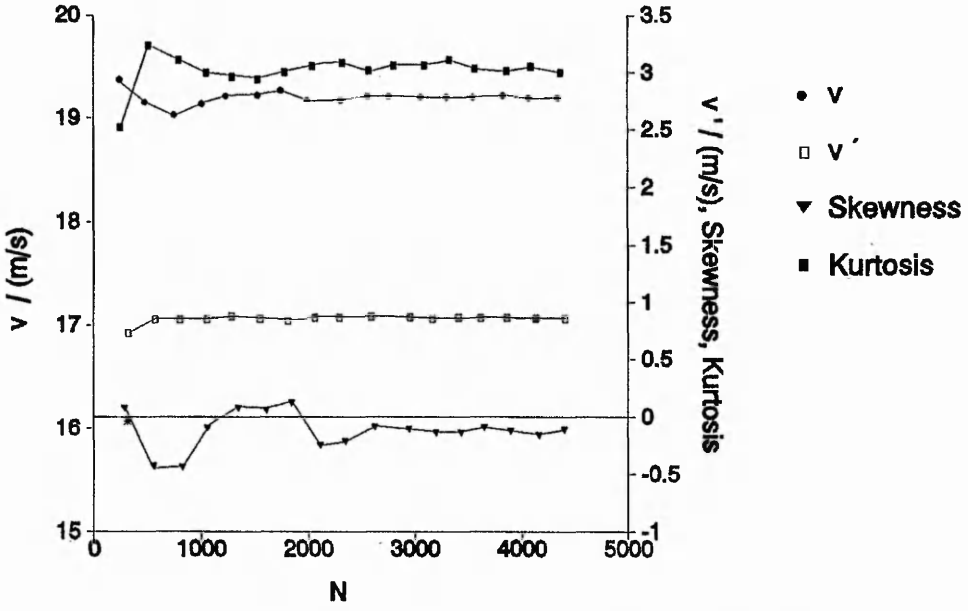

Figure 3.8 Effect of sample size on statistical moments.

direction and turbulence). As recommended by Tropea (1986), to reduce fringe bias, a frequency shift as high as twice the Doppler frequency, but at least equal to the Doppler frequency, is required. The 4 MHz shift used in this study corresponds to $1.7u_b$. The first four non-dimensional statistical moments, that is to say, radial velocity profiles, turbulence intensity, skewness and kurtosis (flatness) at various radial locations have been examined as the wall is approached. Erroneous values in the third and fourth moments were observed at the points closest to the wall. Similar trends were observed at all radial locations. Further examination of the data obtained in this region by plotting the velocity probability density functions shown in Figure 3.9, revealed that a secondary peak appears around the local shift frequency, which results in slightly lower mean velocity values and higher turbulence intensities.

At r/d=3, for y/d>0.01 the two distributions are detached and a cut off frequency was introduced into the data collection software which corresponds to the local shift frequency.

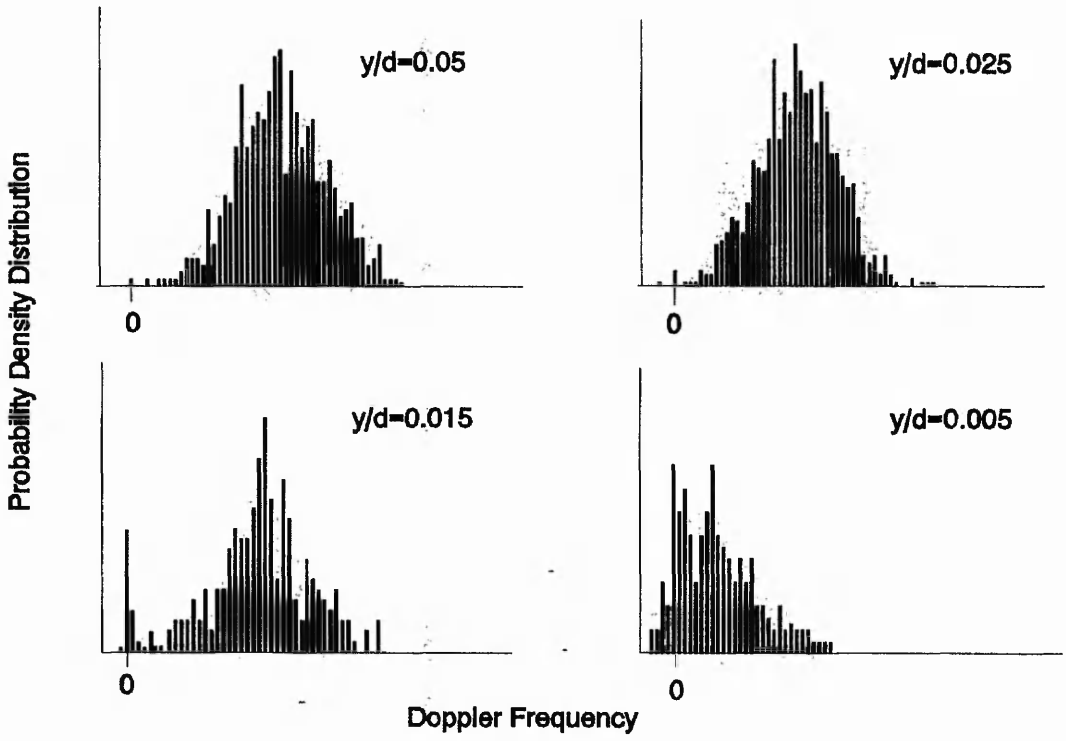

Figure 3.9. Velocity probability density functions as the wall is approached.

However for y/d<0.01 the distributions could not be separated and consequently results obtained within this region are not considered reliable.

A comparison of results before and after correction in Figure 3.10 shows the slight improvement in velocity and turbulence data. A skewness factor of about zero exists in the boundary layer except very close to the wall where a positive skew indicates the existence of low velocities with high probability to be measured. The increase in kurtosis close to the wall for r/d=3 suggests a decreasing intermittency factor.

The assumed Gaussian distribution will not provide a true representation of a skewed pdf found, for example, in the shear layer region of the jet and indicated by the skewness

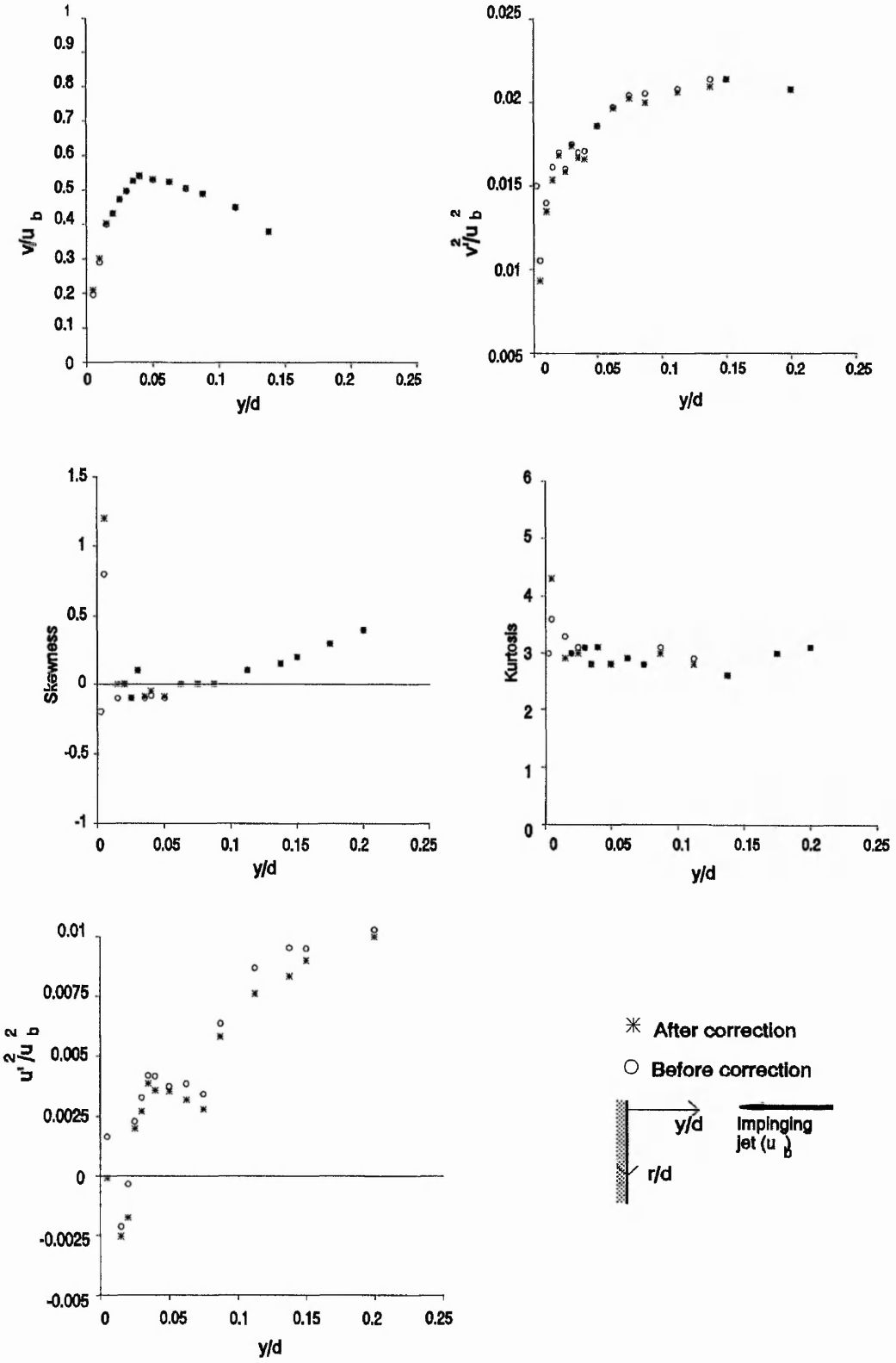

Figure 3.10 Near wall results before and after correction.

factors. However, Ribeiro and Whitelaw (see Durst et al., 1981) compared results using Gaussian and non Gaussian models at a turbulence intensity level of 50% and skewness factor of 0.5. They reported differences in the mean velocities and turbulence intensity of 4% and 2% respectively. The differences were considerably smaller for lower levels of turbulence and skewness.

Nearly 30% of all measurements were repeated and compared with each other. All measurements were found to be repeatable within the uncertainty intervals.

3.3.5 Measurement of the Reynolds stress components

Reynolds stresses can be measured using a one component laser-Doppler anemometry system by rotating the LDA transmission optics relative to the principal directions but in the same plane, Durst and Whitelaw (1971), Durst and Tropea (1981). However, having low uncertainties in the measurement of v and v´ does not necessarily lead to a small uncertainty in the results for Reynolds stresses. A general uncertainty analysis was performed prior to the experimental programme to investigate the response of the result to uncertainties in the measured variables and the choice of the angle of rotation. Figure 3.11 gives the angles of rotation of the LDA transmission optics, as employed in this investigation, where x is the axial, and y the radial, directions of flow and three components of velocity v, $v_{\theta+}$ and $v_{\theta-}$ are measured directly.

By resolving parallel to the measured velocity components $v_{\theta+}$ and $v_{\theta-}$ at θ_+ and θ_-, equations for the principal velocities and Reynolds stress components can be shown (see Appendix C) to be given by

$$v = \textit{direct measurement} \tag{3.10}$$

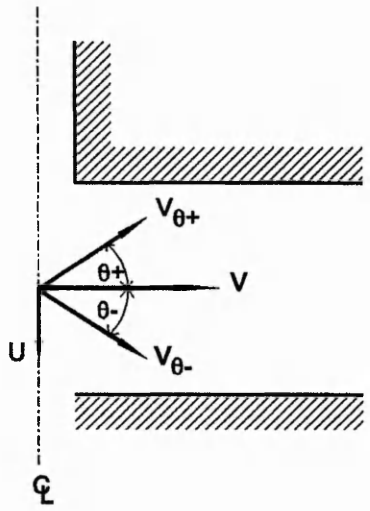

Figure 3.11. Angles of rotation of LDA system.

$$\overline{v'^2} = \textit{direct measurement} \tag{3.11}$$

$$u = \frac{v_{\theta^+} - v_{\theta^-}}{2\sin\theta} \tag{3.12}$$

$$\overline{u'^2} = \frac{\overline{v'^2_{\theta^+}} + \overline{v'^2_{\theta^-}} - 2\overline{v'^2}\cos^2\theta}{2\sin^2\theta} \tag{3.13}$$

$$\overline{u'v'} = \frac{\overline{v'^2_{\theta^+}} - \overline{v'^2_{\theta^-}}}{4\cos\theta\ \sin\theta} \tag{3.14}$$

Two of the stress components are inferred from the measured quantities and it is therefore necessary to compute the resulting uncertainty propagated through these data reduction equations. Kline and McClintock (1953) showed that the uncertainty interval of a result $r=f(x_1,x_2.....x_n)$ is given by

$$\delta r = \left[\left(\frac{\partial r}{\partial x_1}\delta x_1\right)^2 + \left(\frac{\partial r}{\partial x_1}\delta x_1\right)^2 + ...\left(\frac{\partial r}{\partial x_1}\delta x_n\right)^2\right]^{0.5} \tag{3.15}$$

where δx_i are the uncertainties in the measured variables x_i.

Applying this procedure to Equations (3.13) and (3.14) leads to equations from which the uncertainties in the indirectly measured Reynolds stress components can be evaluated based on directly measured components (see Appendix C):

$$(\delta\overline{u'v'})^2 = (\delta\overline{v'^2})^2\frac{1}{8\cos^2\theta\sin^2\theta} + \left(\overline{u'v'}\frac{\cos 2\theta}{\cos\theta\sin\theta}\delta\theta\right)^2 \tag{3.16}$$

$$(\delta\overline{u'^2})^2 = \frac{(\delta\overline{v'^2})^2(1+2\cos^4\theta)}{2\sin^4\theta} + \left(\frac{2(\overline{v'^2}-\overline{u'^2})\delta\theta}{\tan\theta}\right)^2 \tag{3.17}$$

Inspection of these equations reveals that both uncertainties depend on the value of the turbulent fluctuations themselves. The last term in Equations (3.16) and (3.17) can be considered small compared to the other terms. In Figure 3.12 the coefficients of the remaining terms are plotted as a function of θ. Referring to Figure 3.12, in order to extend the measurements close to the impingement surface a small value of θ was preferred to avoid rotation of the optics by a large angle in the transverse direction, which would be necessary to maintain the laser beams parallel to the surface. For the shear stress term the minimum uncertainty is obtained when θ=45° and in addition the $\delta\theta$ term goes to zero (see Equation (3.16)). As expected for the normal stress term the ideal value of θ is 90°, and angles less than ~35° should be avoided. The cross-over point of the two curves shown in Figure 3.12 indicates that an angle of 63° is the most appropriate for the measurement of both quantities. However, in this investigation, a compromise of θ=45° was chosen to minimise rotation of the optics out of plane. This leads to uncertainty estimates for the

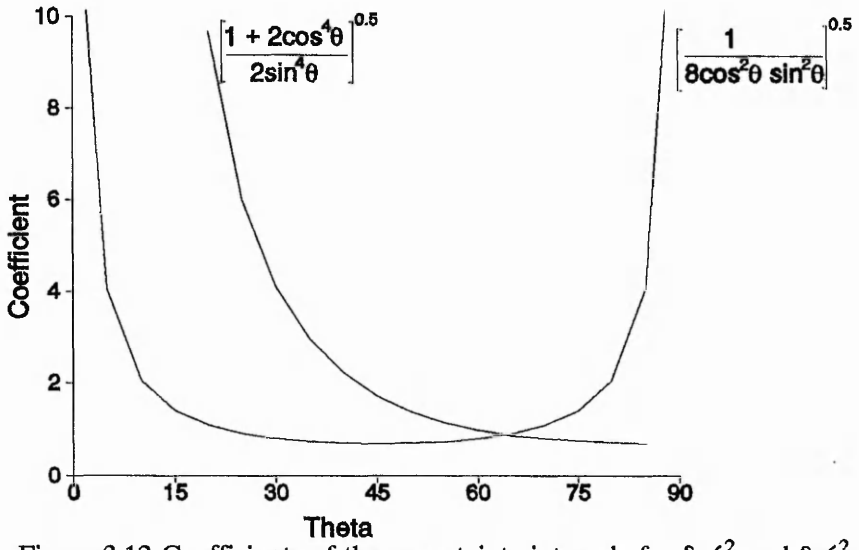

Figure 3.12 Coefficients of the uncertainty intervals for $\delta u'^2$ and $\delta v'^2$.

inferred Reynolds stress terms of

$$(\delta\overline{u'v'})^2 = \frac{1}{2}(\delta\overline{v'^2})^2 \qquad \textit{and} \qquad (\delta\overline{u'^2})^2 = 3(\delta\overline{v'^2})^2 \tag{3.18}$$

Finally, in order to measure the near wall Reynolds stress components, the measurement volume was tilted by ϕ=2° relative to the wall. Although the mean velocity in the ϕ direction is zero at all locations due to axisymmetry, the v components will receive a contribution from the ϕ direction turbulent fluctuation. This contribution cannot be determined without having full knowledge of the turbulent field. Since the angle is very small the uncertainty is expected to be negligible, such that a correction has not been made and the fluctuation values have been assumed to represent the v components.

The redundant measurement of v (from the ±45° measurement) agreed with the directly measured profiles to within 5% at all radial planes examined. These are presented in Figure

3.13 for r/d=0.5, 1 and 3. The deviations are attributed to the cumulative effects of errors due to positioning, flow stability, precision of the measurement system and statistical uncertainty. Excluding spatial uncertainties, the overall uncertainties in the measurement of the mean radial velocity, mean normal velocity, radial component of turbulence, normal component of turbulence and the shear stress component are estimated to be less than 6%, 8%, 7%, 15% and 7% respectively, when the laser beams are angled at 45° to the impingement plate.

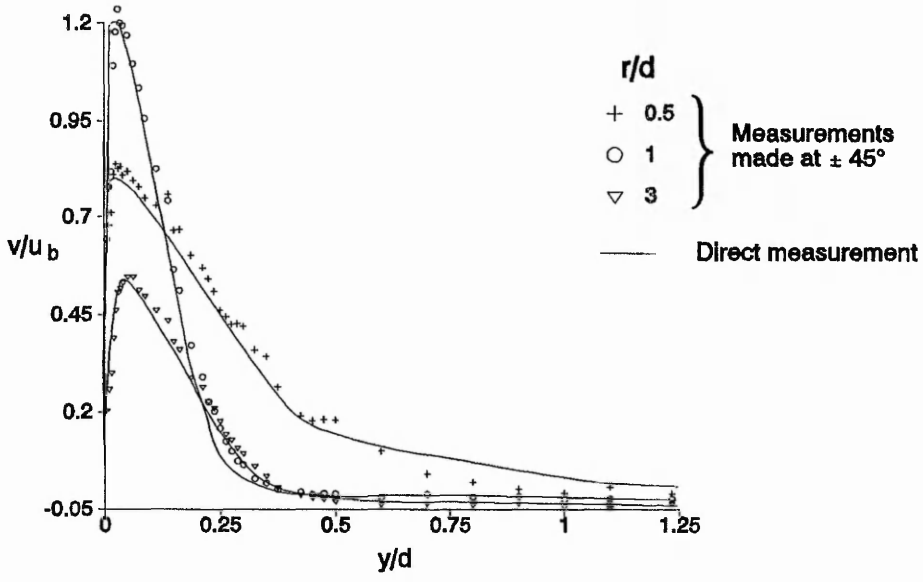

Figure 3.13. Comparison of direct measurement of radial velocity and turbulence profiles with those inferred from measurements made at ±45°.

3.4 Liquid crystal thermography

3.4.1 Thermochromic liquid crystals

Cholesteric liquid crystals reflect light at a specific wavelength (colour) for a given temperature. They have been used extensively for surface temperature (leading to heat transfer) measurement. The application of liquid crystals to fluid mechanics and heat transfer has been reviewed by Yianneskis (1988) and by Kasagi et al. (1989), who also provide a detailed discussion of chromatic interpretation. More recently, Lin et al. (1994) have compiled a database of liquid crystal references for various applications. Jones et al. (1992) describe the physical phenomena that render the liquid crystals suitable for heat transfer testing and also review the methods of analysis using video systems.

A typical narrow band liquid crystal formulation changes colour through the whole spectrum over a specified bandwidth and is colourless below and above this range. The microencapsulated liquid crystal used in this investigation was type BM/R39C0.8W/C17-10 (manufactured by Hallcrest Inc., Poole, England) which had a claimed red start temperature of 39°C and bandwidth of 0.8°C. The liquid crystals were calibrated in-situ to within 0.1°C using fast response thermocouples, and their time response is reported by Ireland and Jones (1987) to be of the order of a few milliseconds. The in-situ calibration during each test avoided any change in the colour play of the liquid crystals with temperature, due to degradation. The BM/R39C0.8W liquid crystals were mixed with BM/R20C5W. The latter formulation had colour play between 20°C and 25°C and was used to indicate when the impingement plate had returned to uniform ambient temperature.

3.4.2 Selection of the experimental technique

From the literature survey, over the range of physical quantities being considered, the maximum heat transfer coefficient was predicted to be less than 200 W/m^2K, Gardon and Akfirat (1965) and Baughn and Shimizu (1989). In order to achieve minimal experimental uncertainty, a direct comparison of the uncertainties associated with both the steady state and transient experimental approaches was carried out. This procedure is described in detail by Moffat (1985) and Coleman and Steele (1989). The uncertainty in h, δh, increases as h decreases for the steady state technique due to reducing power requirements for decreasing h, but δh decreases as h decreases for the transient technique due to the increase in elapsed time of the test, the uncertainties being approximately equal when $h \approx 200$ W/m^2K.

The temperature mismatch between the jet temperature and ambient was also considered at this stage. The heat transfer distribution for an isothermal jet only reflects the effects of velocity variations whilst for a heated jet, both velocity variation and thermal entrainment are important. Hollworth and Gero (1985) showed that the thermal effect depends strongly on z/d since it is due to thermal mixing which occurs upstream. For a temperature mismatch of 30°C, they showed that the heat transfer profiles were the same at the stagnation point for $z/d \leq 2$. Heat transfer within the region $0 < r/d < 3$ at $z/d = 2$ is the focus of the present study. Although the profiles followed the same trends the difference between them increased with z/d and r/d. For illustration, in the $z/d = 2$ case at $r/d = 4$ there was a 10% difference. However, the difference is expected to be considerably less for the present study for two reasons. Firstly, a semi-confined configuration leads to lower entrainment rates and secondly, the fully developed jet exit profile will result in a lower shear at the edge of the jet which will reduce initial entrainment of the ambient air. The recent findings of Baughn et al. (1991) and Lucas et al. (1992) support this conjecture. For axisymmetric jet impingement, Goldstein et al. (1990) and Baughn et al. (1991) demonstrated that local heat

transfer data for an unheated jet can be used for a heated jet if the local heat transfer coefficient is defined in terms of the adiabatic wall temperature. In order to compare stagnation point heat transfer data at larger nozzle to plate spacings with that of other authors who have used ambient jets, the adiabatic wall temperature at the stagnation point was measured. Kataoka (1985) considered the effect of the temperature difference on the development of the jet and correlated the potential core length as a function of the Reynolds number and the density ratio. The effects only became significant at much larger temperature differences than in the present study (typically up to 300°C).

The buoyancy parameter was negligible over most of the impingement plate, which justifies the assumption that forced convective heat transfer due to the impinging jet dominated the flow so that results could be corroborated with LDA data.

Based on the above considerations (lower uncertainty, minimal thermal effects at z/d=2 and negligible buoyancy) the transient experimental technique was selected for this investigation.

3.4.3 The transient technique

The transient technique is based upon the surface temperature transient as a measure of the heat transfer coefficient when a surface is exposed to a fluid temperature change. Several methods have been utilised to achieve the change in fluid temperature relative to the surface. Clifford et al. (1983), Ireland and Jones (1985, 1986), Metzger and Larson (1986) and Metzger et al. (1991) use switching valves to raise the temperature of their flow relative to an ambient temperature surface. O'Brien et al. (1986), Jones and Hippensteele (1987), Baughn and Yan (1991), and Yan et al. (1992) use a preheated surface and expose it to a

cool flow field. For jet impingement, Baughn and Yan (1991) and Yan et al. (1992) remove an insulating shield blocking a heated flat surface from the impinging jet whereas Metzger et al. (1991) used an ambient temperature wall and suddenly raised the temperature of the flow using a ball diverter valve. They applied a correction to the jet temperature to account for losses due to transient heating of their nozzle. A similar method has been used in this study, but the transient change in jet temperature has been avoided by pre-heating the nozzle assembly.

3.4.4 Analysis of transient wall heating

The technique requires measurement of the elapsed time to increase the surface temperature of the coated test specimen from a known initial temperature to a predetermined value. The rate of heating is recorded by monitoring the colour change patterns of the liquid crystal with respect to time. Ireland and Jones (1985, 1986) and Ireland (1987) describe in detail the principles of the technique. If the specimen is made from a material with low thermal diffusivity and chosen to be sufficiently thick, then the heat transfer process can be considered to be one-dimensional into a semi-infinite medium. Schultz and Jones (1973) provided a guideline for the minimum thickness according to

$$x > 4\sqrt{\alpha t} \tag{3.19}$$

Numerical or analytical techniques can be used to solve the one-dimensional transient conduction equation:

$$\frac{\partial T}{\partial t} = \alpha \frac{\partial^2 T}{\partial x^2} \tag{3.20}$$

where temperature T is a function of distance x from the surface (through the thickness of the specimen) and time t, ie. T(x,t). Edwards (1987) replaced the above equation with finite difference equations and used an explicit numerical solution method. The main

disadvantage of the explicit approach is that each nodal equation must satisfy a stability criteria. The discretised equations are based on a truncated Taylor Series which leads to a source of numerical error in the subsequent computations. Using the implicit numerical method would remove the stability criteria but this would involve solving a set of algebraic equations simultaneously. In addition, although the truncation error would be reduced and would lead to a more accurate solution, the implicit technique is still not as accurate as the exact analytical solution. Kreith and Black (1980) demonstrated the inferiority of the numerical techniques. For these reasons, the analytical solution as used by Ireland and Jones (1985) has been preferred in this investigation.

The surface was subjected to an airflow of temperature T_∞ and a heat transfer coefficient of h. The following boundary conditions are used in the analysis:

Initial condition $$T(x,0) = T_0 \tag{3.21}$$

Semi-infinite assumption $$T(\infty,t) = T_0 \tag{3.22}$$

Heat flux condition at surface $$q = h[T_\infty - T(0,t)] = -k\left(\frac{\partial T}{\partial x}\right)\Big|_{x=0} \tag{3.23}$$

The solution to Equation (3.20) subject to the initial and boundary conditions is (Kreith and Black, 1980):

$$\frac{T(x,t)-T_0}{T_\infty - T_0} = 1 - erf\xi - e^{Bi+\eta}(1 - erf(\xi + \sqrt{\eta})) \tag{3.24}$$

$$\textit{where} \quad \xi = \sqrt{\frac{x^2}{4\alpha t}}, \quad Bi = \frac{hx}{k} \quad \textit{and} \quad \eta = \frac{h^2\alpha t}{k^2} = \frac{h^2 t}{k\rho c} \tag{3.25}$$

At the surface, x=0 so that ξ=Bi=0 , and the equation reduces to

$$\frac{T(0,t)-T_0}{T_\infty-T_0} = \theta = 1 - e^{\eta}\,(1 + erf\sqrt{\eta}) \tag{3.26}$$

The exact values of the Gauss error function, *erf*, are available from tables. Herein, a series expansion for the error function has been employed:

$$erf\sqrt{\eta} = \frac{2}{\sqrt{\pi}}\left(\sqrt{\eta} - \frac{1}{3}\sqrt{\eta}^{\,3} + \frac{1}{5(2!)}\sqrt{\eta}^{\,5} - \frac{1}{7(3!)}\sqrt{\eta}^{\,7} \pm \ldots.\right) \tag{3.27}$$

A simple FORTRAN program has been developed (see Appendix D) to obtain heat transfer coefficients using the above analysis and incorporating the series expansion for the Gauss error function up to the $(\sqrt{\eta})^{17}$ term. A radiation correction has not been applied to h due to the uncertainty in the emissivity of the test surface, which according to Baughn et al. (1989) varies with the thickness of the liquid crystal layer. However, based on their findings the radiation would amount to a maximum of 6% of the convective heat transfer.

The partial differentiation of the terms of Equation (3.26) and the propagation of the uncertainty in each measured variable through this equation is demonstrated in Appendix E. Inspection of the resulting expression for δh enables the experimental test conditions to be selected in order to minimise δh:

$$\frac{\delta h}{h} = \left[\left(\frac{\delta t}{2t}\right)^2 + \left(\frac{\delta(\sqrt{\rho ck})}{\sqrt{\rho ck}}\right)^2 + \left(\frac{1}{\beta(T_\infty - T_0)}\right)^2\left(\delta T_{(0,t)}^2 + (\theta - 1)^2\delta T_0^2 + \theta^2\delta T_\infty^2\right)\right]^{0.5} \tag{3.28}$$

$$\textit{where}\quad \beta = 2\sqrt{\eta}\left(\pi^{-0.5} - \sqrt{\eta}(1 - \theta)\right)$$

The uncertainty in h due to δt/2t diminishes as t increases and is a maximum for higher values of h. Its contribution to the overall uncertainty is small compared to the influence of the thermal properties of Perspex and temperature measurement. The uncertainty in k has been determined in Appendix F and is not a function of the experimental test

conditions. It does however make a significant contribution to the overall uncertainty. The fractional uncertainty in h due to uncertainty in temperature measurement is a minimum when $\beta(T_\infty - T_0)$ is large. For typical test conditions, large values of β occur when $0.3<\theta<0.5$. Since δT_0 and δT_∞ are equal, the minimum effect of these quantities occurs when $\theta=0.5$. A choice of $\theta\approx0.5$ is therefore the most suitable situation. Selection of the test conditions as described leads to a typical overall uncertainty in h of ~8%.

3.4.5 Preparation of the test specimens

A sheet of Perspex, 20 mm thick, was used as the impingement plate and was slightly roughened using a fine scourer, to improve adhesion of the liquid crystals, while maintaining its transparency. A 10 mm grid was scribed onto the plate directly beneath the liquid crystals. The liquid crystals were supplied in a water based emulsion which when sprayed onto a surface dries as a paint. The emulsion was mixed two parts to one part distilled water. Two thin coats of the combined mixture were applied to the substrate using an artists air brush with approximately 45 minutes allowed for drying between coats. The thickness of the layer was estimated to be 30 μm, based on the size of the liquid crystal encapsulations. A thin layer of soluble black paint was then applied to improve the colour resolution by absorbing unreflected light. The thickness of the total layer was estimated to be less than 40 μm. Bonnett (1989) showed that the thermal conductivity and diffusivity of chiral nematic liquid crystals are similar to those of Perspex, so that effects due to a different thermal resistance have been considered negligible.

Two fast response type T foil (5 μm thick) thermocouples were flush mounted directly on the Perspex substrate at r/d=1 and r/d=3, beneath the liquid crystals using thin strips of flexible polypropylene double-sided adhesive tape (0.075 mm). These thermocouples were used for continuous calibration of the liquid crystals. An additional thermocouple was

mounted at the stagnation point to measure the adiabatic wall temperature. The response time quoted by the manufacturers for the thermocouples was 5 ms. The thermocouples were calibrated to within 0.1°C against a primary standard mercury-in-glass thermometer using an ice point reference (Delristor Ltd. Icell MkII). Thermocouple theory and practice is described in detail by Moffat (1990). A further 'stick-on' thermocouple was placed on the underside of the impingement plate which measured the initial plate temperature (ambient) and validated the semi-infinite assumption.

3.4.6 Experimental set-up and recording procedure

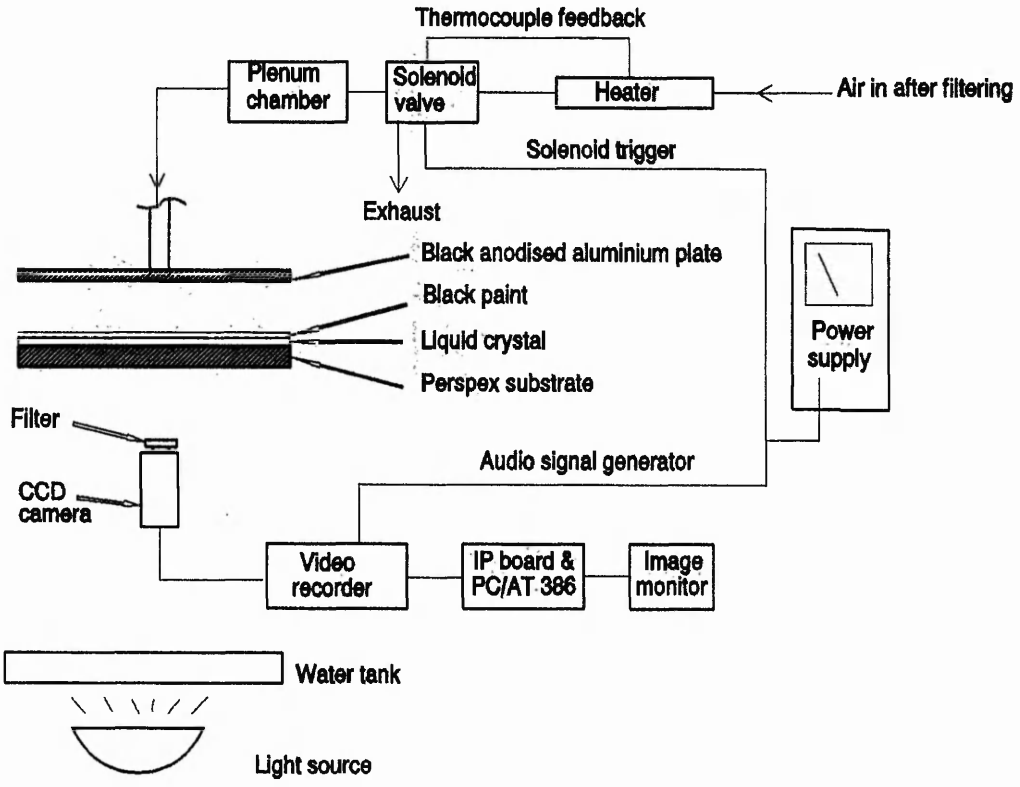

Figure 3.14 Experimental set-up for the heat transfer investigation.

Figure 3.14 shows the experimental set-up for the heat transfer investigation. A Sylvania hot air nozzle and fast response solenoid valve preceded the air supply configuration

described in Section 3.1. The required jet temperature was input at the controller and a thermocouple feedback loop was employed to maintain a steady air flow temperature. Approximately 30 minutes were allowed to ensure steady conditions. The solenoid valve was energised from a DC power supply. An audio signal was generated on the video recorder to mark the start time of the test. This was achieved by a simple electrical circuit which sends a low voltage signal to the audio input channel of the video recorder at the start of the test. The voltage was supplied from the solenoid circuit so that the switching of the solenoid and the generation of the audio signal were synchronised. The time to energise the solenoid valve was quoted by the manufacturers as 16 ms which was far less than the 40 ms frame speed of the camera and the duration of the test. The warm air was passed through the nozzle configuration and the jet exit temperature was allowed to stabilise, which minimised errors due to transient changes in the jet temperature caused by losses to the nozzle and plenum chamber. All pipework, and the plenum chamber were insulated to minimise heat losses. The axial exit velocity of the jet was monitored using a Pitot-static tube manufactured to BS1042:1983 connected to a micromanometer, allowing measurement of the dynamic pressure to within 0.1 Pa. The warm air was then diverted by the solenoid to the exhaust position and the impingement plate at ambient temperature quickly positioned in place. Without delay, the solenoid was again energised to start the test, and the liquid crystal isotherms recorded on U-matic video. Thermocouple temperature readings were recorded as part of the test image using a Keithley 2001 High Speed Digital Multimeter which allowed 180 readings per second directly in °C. The response time of the temperature measurement system after the start of the test was of the order of 100 Hz, which ensured a correct temperature recording on consecutive images which were recorded at 25 frames/s. The recovery factor of the thermocouple was neglected due to the very low velocity in the plenum chamber.

The CCD mono-chrome video camera (756 x 581 resolution, 0.5 lux sensitivity) fitted with a mono-chrome narrow band filter (5286 Å, half bandwidth 73 Å), was positioned to record the liquid crystal thermographs from the underside of the test specimen, through the Perspex, which provided a viewing angle which was normal to the heat transfer surface. The use of narrow band filters in temperature measurement and calibration is described by Akino et al. (1989). Illumination was provided by a 300 W Quartz Halogen lamp placed behind, and slightly above, the camera. To avoid erroneous results caused by infra-red heating from the light source, the light was filtered by placing a water tank in front of the lamp. Both the illumination and viewing angles were fixed during calibration and experiment.

After the tests the video was replayed and an image processing system, described by Ashforth-Frost et al. (1992), used to analyse the recorded images. Briefly, the facility employs an IBM compatible 386 personal computer with a Data Translation® (1989) on board arithmetic frame grabber and associated software, and an A/D card to facilitate detection of the audio signal. The audio signal was generated by incorporating a simple electrical circuit to send a low voltage signal to the audio input channel of the video recorder, at the start of the test. On replaying the video during data analysis the A/D convertor detects the presence of the low voltage. A monitor connected to the video camera allowed focusing and monitoring during the tests and a high resolution monitor was used to carry out spatial calibration. Calibration was performed for each test by positioning the liquid crystal isotherm over the tip of the fast response thermocouple and recording the temperature displayed by the multimeter. Having thermocouples at different radial positions allowed the change of calibration due to degradation with radial position to be accounted for. However, changes in calibration due to position were shown to be negligible since they could not be discriminated during a single test. Video frames can be analysed at intervals

of 40 ms, determined by the video rate of the camera.

3.5 Concluding remarks

The design, development and validation of the experimental rigs, the procedures adopted for flow visualisation, laser-Doppler anemometry and liquid crystal thermography have been described. The data reduction equations have been derived and uncertainty analyses undertaken to allow appropriate selection of the experimental procedures. The principles of laser-Doppler anemometry, necessary seeding, accurate positioning of the measurement volume within the flow field and the measurement of the Reynolds stress components have received particular attention. Except in the low velocity intermittent region near the bottom edge of the jet (see Section 5.2.1 later), the uncertainties in the mean radial velocity, mean normal velocity, radial component of turbulence, normal component of turbulence and the shear stress component are estimated to be less than 6%, 8%, 7%, 15% and 7% respectively, when the laser beams are angled at 45° to the impingement plate. The transient wall heating technique was selected for the liquid crystal tests based on experimental uncertainty analysis. This technique has been described along with the careful preparation of the test specimens and the experimental set-up and recording procedures using a mono-chrome image processing system. The uncertainty in the measured heat transfer coefficient is estimated to be less than 8%. The above estimates do not include spatial uncertainty which is estimated as less than 1% of the nozzle diameter in all directions.

CHAPTER 4

NUMERICAL INVESTIGATION

In this Chapter the governing equations of motion are presented, and the closure of the time averaged equations using the k-ϵ turbulence model are discussed. The first order solution procedure is briefly described. Particular attention is paid to numerical accuracy by selecting an independent grid, based on findings obtained using Richardsons extrapolation technique, by careful application of boundary conditions and by ensuring a converged solution.

4.1 The governing equations of motion

The flow geometry can be described by the full Navier-Stokes equations and the continuity equation. For an incompressible, steady, two-dimensional, axisymmetric flow, the governing equations in cylindrical coordinates read (Bird et al., 1960):

Axial equation of motion:

$$\rho\tilde{u}\frac{\partial\tilde{u}}{\partial x} + \rho\tilde{v}\frac{\partial\tilde{u}}{\partial r} = -\frac{\partial\tilde{p}}{\partial x} + \frac{\partial}{\partial x}\left(2\mu\frac{\partial\tilde{u}}{\partial x}\right) + \frac{1}{r}\frac{\partial}{\partial r}\left(r\mu\left(\frac{\partial\tilde{u}}{\partial r}+\frac{\partial\tilde{v}}{\partial x}\right)\right) \tag{4.1}$$

Radial equation of motion:

$$\rho\tilde{u}\frac{\partial\tilde{v}}{\partial x} + \rho\tilde{v}\frac{\partial\tilde{v}}{\partial r} = -\frac{\partial\tilde{p}}{\partial r} + \frac{\partial}{\partial x}\left(\mu\left(\frac{\partial\tilde{v}}{\partial x} + \frac{\partial\tilde{u}}{\partial r}\right)\right) + \frac{1}{r}\frac{\partial}{\partial r}\left(2r\mu\frac{\partial\tilde{v}}{\partial r}\right) - \frac{2\mu\tilde{v}}{r^2} \tag{4.2}$$

Continuity equation:

$$\frac{\partial}{\partial x}(\rho\tilde{u}) + \frac{1}{r}\frac{\partial}{\partial r}(\rho r\tilde{v}) = 0 \tag{4.3}$$

These are exact equations and form a closed set describing all the details of the fluid motion where the variables represent instantaneous values. To describe turbulent flow a statistical approach is used where the instantaneous values of a variable are replaced by the sum of the mean value and a fluctuating value

$$\tilde{u} = u + u' \; ; \qquad \tilde{v} = v + v' \; ; \qquad \tilde{p} = p + p'$$

Averaging of the equations results in:

Axial equation of motion:

$$\rho u\frac{\partial u}{\partial x}+\rho v\frac{\partial u}{\partial r} = -\frac{\partial p}{\partial x}+\frac{\partial}{\partial x}\left(2\mu\frac{\partial u}{\partial x}\right)+\frac{1}{r}\frac{\partial}{\partial r}\left(r\mu\left(\frac{\partial u}{\partial r}+\frac{\partial v}{\partial x}\right)\right)-\frac{\partial}{\partial x}\overline{\rho u'^2}+\frac{1}{r}\frac{\partial}{\partial r}\rho r\overline{u'v'} \tag{4.4}$$

Radial equation of motion:

$$\rho u\frac{\partial v}{\partial x}+\rho v\frac{\partial v}{\partial r} = -\frac{\partial p}{\partial r}+\frac{\partial}{\partial x}\left(\mu\left(\frac{\partial v}{\partial x}+\frac{\partial u}{\partial r}\right)\right)+\frac{1}{r}\frac{\partial}{\partial r}\left(2r\mu\frac{\partial v}{\partial r}\right)-\frac{2\mu v}{r^2}-\frac{\partial}{\partial x}\overline{\rho u'v'} +\frac{1}{r}\frac{\partial}{\partial r}\rho r\overline{v'^2}-\rho\frac{\overline{v_\theta'^2}}{r} \tag{4.5}$$

Continuity equation:

$$\frac{\partial}{\partial x}(\rho u)+\frac{1}{r}\frac{\partial}{\partial r}(\rho r v)=0 \tag{4.6}$$

The averaging process has introduced unknown correlations between fluctuating velocities. Physically, these quantities represent the transport of momentum by turbulent motion and act as a stress on the fluid. They are called the Reynolds stresses. The equations no longer form a closed set and can only be solved when these turbulent quantities are known.

4.2 Closure of the averaged equations

In analogy with viscous stresses in laminar flow, the Reynolds stresses can be related to the mean rate of strain by Boussinesq's eddy-viscosity concept:

$$-\rho\overline{u_i'u_j'} = \mu_t\left(\frac{\partial u_i}{\partial x_j}+\frac{\partial u_j}{\partial x_i}\right)-\frac{2}{3}\rho k\delta_{ij} \tag{4.7}$$

where μ_t is the turbulent or eddy viscosity and k is the kinetic energy of turbulent fluctuations

$$k = \frac{1}{2}\overline{u_i'u_i'} \tag{4.8}$$

Determination of the turbulent viscosity now becomes the main problem. Kolmomogorov (1942) suggested that the turbulent viscosity could be evaluated from

$$\mu_t = \rho C_\mu' k^{1/2} L \tag{4.9}$$

where $k^{1/2}$ is a velocity scale for the large scale turbulent motion and L a characteristic length scale, usually modelled by the expression

$$L = \frac{C_D k^{\frac{3}{2}}}{\epsilon} \qquad \textit{where} \qquad \epsilon = \nu_t \overline{\frac{\partial u_i'}{\partial x_j} \frac{\partial u_i'}{\partial x_j}} \tag{4.10}$$

ϵ is the rate of dissipation of the turbulent kinetic energy, C_μ' and C_D are empirical constants. Substituting for L in Equation (4.9), the turbulent viscosity can then be defined as

$$\mu_t = \frac{C_\mu \rho k^2}{\epsilon} \qquad \textit{where} \qquad C_\mu = C_\mu' C_D \tag{4.11}$$

and the quantities k and ϵ now need to be found. The two equation k-ϵ model of turbulence solves transport equations for k and ϵ which can be deduced from the Navier-Stokes equations (see Tennekes and Lumley, 1972). For this flow geometry, they read (Rodi, 1980):

$$\rho u \frac{\partial k}{\partial x} + \rho v \frac{\partial k}{\partial r} = \frac{\partial}{\partial x}\left(\frac{\mu_t}{\sigma_k}\frac{\partial k}{\partial x}\right) + \frac{1}{r}\frac{\partial}{\partial r}\left(r\frac{\mu_t}{\sigma_k}\frac{\partial k}{\partial r}\right) + S_k \tag{4.12}$$

$$\rho u \frac{\partial \epsilon}{\partial x} + \rho v \frac{\partial \epsilon}{\partial r} = \frac{\partial}{\partial x}\left(\frac{\mu_t}{\sigma_k}\frac{\partial \epsilon}{\partial x}\right) + \frac{1}{r}\frac{\partial}{\partial r}\left(r\frac{\mu_t}{\sigma_\epsilon}\frac{\partial \epsilon}{\partial r}\right) + S_\epsilon \tag{4.13}$$

$$S_k = P_k - \rho\epsilon \tag{4.14}$$

$$S_\epsilon = C_1 \frac{\epsilon}{k} P_k - C_2 \rho \frac{\epsilon^2}{k} \tag{4.15}$$

$$P_k = \mu_t\left(2\left(\left(\frac{\partial u}{\partial x}\right)^2+\left(\frac{\partial v}{\partial r}\right)^2+\left(\frac{v}{r}\right)^2\right)+\left(\frac{\partial u}{\partial r}+\frac{\partial v}{\partial x}\right)^2\right) \tag{4.16}$$

σ_k, σ_ϵ, C_μ, C_1 and C_2 are further empirical constants. Viscous dissipation has been neglected and is considered negligible at high Reynolds numbers, Tennekes and Lumley (1972). The standard version of the *k*-ϵ model proposed by Launder and Spalding (1972) has been employed in this investigation. The turbulence model constants used have been found to give good agreement with a range of free turbulent flows and wall flows and have the following values, Launder and Spalding (1974): σ_k=1.0, σ_ϵ=1.314, $C_\mu{}'$=0.5478, C_D=0.1643, $C_\mu = C_\mu{}' C_D$=0.09, C_1=1.44 and C_2=1.92.

4.3 The energy equation

For a two-dimensional axisymmetric flow the energy equation reads

$$\rho u\frac{\partial \tilde{h}}{\partial x}+\rho v\frac{\partial \tilde{h}}{\partial r}=\frac{\partial}{\partial x}\left(\frac{\lambda}{c_p}\frac{\partial \tilde{h}}{\partial x}\right)+\frac{1}{r}\frac{\partial}{\partial r}\left(r\frac{\lambda}{c_p}\frac{\partial \tilde{h}}{\partial r}\right) \tag{4.17}$$

where $\tilde{h}$ is the instantaneous value of enthalpy. The time averaged energy equation becomes

$$\rho u\frac{\partial h}{\partial x}+\rho v\frac{\partial h}{\partial r}=\frac{\partial}{\partial x}\left(\frac{\lambda}{c_p}\frac{\partial h}{\partial x}-\rho\overline{u'h'}\right)+\frac{1}{r}\frac{\partial}{\partial r}\left(r\frac{\lambda}{c_p}\frac{\partial h}{\partial r}-\rho\overline{v'h'}\right) \tag{4.18}$$

In direct analogy to the turbulent momentum transport, the turbulent heat transport is assumed to be related to the enthalpy gradient

$$-\rho\overline{u_i'h'}=\frac{\lambda_t}{C_p}\left(\frac{\partial h}{\partial x_i}\right) \tag{4.19}$$

where $\lambda_t/\rho c_p$ is turbulent diffusivity of heat Γ which is related to the turbulent viscosity by a turbulent Prandtl number,

$$\Gamma=\frac{\lambda_t}{\rho c_p}=\frac{\nu_t}{\sigma_t}=\frac{\mu_t}{\rho\sigma_t} \tag{4.20}$$

4.4 The wall function and calculation of Nusselt number

In the immediate vicinity of the impingement and confinement plates where the local Reynolds number is low, viscous effects are influential so that a wall function is often used to bridge this area. The logarithmic law of the wall was used to compute the skin friction factor, s, which is used to determine the Stanton number, St. For turbulent flow, this assumes a logarithmic dependence of the radial velocity on the normal coordinate to the wall and that the production of turbulent kinetic energy is equal to the dissipation in the log-law region. The implementation of this wall function into PHOENICS is described by Rosten and Worrell (1988) and in further detail by Ludwig et el. (1989). PHOENICS does not output any heat transfer information as a standard option but does allow the skin friction, Stanton number and other computed variables, to be extracted during its execution by using appropriate GROUND coding. In PHOENICS, when the local Reynolds number, Re>132.5, the skin friction is given by

$$s = \left(\frac{\kappa}{\ln(1.01 + 9\ \mathrm{Re}\ s^{0.5})} \right)^2 \tag{4.21}$$

where κ is the von Karman constant and the local Reynolds number, Re, is defined as

$$\mathrm{Re} = \frac{y_p v_p}{\nu} \tag{4.22}$$

Otherwise

$$s = \frac{1}{\mathrm{Re}} \tag{4.23}$$

The Stanton number is then computed from

$$\mathrm{St} = \frac{s}{\sigma_t(1 + Ps^{0.5})} \tag{4.24}$$

where

$$P = 9\left(\frac{\sigma_l}{\sigma_t} - 1\right)\left(\frac{\sigma_t}{\sigma_l}\right)^{0.25} \tag{4.25}$$

The development of this equation is described by Jayatilleke (1969). The Stanton number is based on the enthalpies at the near wall node and at the wall. To facilitate a direct comparison with experiment St is used to obtain the heat flux to the wall such that the Nusselt number can be calculated according to the definition given in Chapter 3. Having extracted St and v_p from PHOENICS using the GROUND coding provided in Appendix G, the heat flux to the wall can be obtained using

$$St = \frac{-\dot{q}}{(h_p - h_w)\rho v_p} \tag{4.26}$$

where h_p and h_w denote the computed enthalpies at the near wall node and the wall respectively, which are easily extracted from GROUND.

4.5 Solution procedure

Detailed descriptions of the most common discretisation procedures, convection-diffusion schemes and solution algorithms are provided in several texts; Patankar (1980), Fletcher (1988a), Fletcher (1988b), Ludwig et al. (1989). The solution procedure used in this investigation is based on a finite volume discretisation, on a staggered grid, of the governing equations. It was introduced by Patankar and Spalding (1972) and described in detail by Patankar (1980) and thus only the pertinent features of the procedure are described below. The solution procedure commences with the derivation of the finite difference form of the governing equations which are formulated by integrating the time averaged equations over a small control volume surrounding each grid point, along with suitable assumptions about the distribution of the dependent variables between the grid points. The computations were carried out using the commercially available PHOENICS computer code version 1.6.2 based on this conventional finite volume method, employing a staggered grid arrangement to avoid oscillatory pressure and velocity fields. The scalar variables are stored at the grid points and the velocities at the face of the grid cells. A hybrid upwind interpolation scheme was

specified to handle the combined effects of convection and diffusion. This scheme cuts off diffusion when the cell Peclet number (Pe) exceeds 2.0 ie. central differencing is used when Pe<2 and upwind differencing when Pe≥2 (Patankar, 1980). In practice, the upwind scheme is invoked over most of the flow domain. PHOENICS uses the SIMPLEST (Semi-Implicit Method for Pressure Linked Equations ShorTened) solution algorithm of Spalding (1980) to enforce continuity and solves the discretised equations iteratively using the TDMA (TriDiagonal-Matrix Algorithm) line solver, described by Patankar (1980).

4.6 Grid specification

An axisymmetric polar grid was used with the z-axis aligned with the nozzle centreline and the y-axis being radial. The final grid was adopted after comparing results obtained with various mesh densities and near wall cell sizes. The predicted radial profiles of velocity and velocity gradient at a plane close to the impingement plate were used to test the grid dependency of the computations. The nodes were concentrated in regions of large gradients; namely, close to the impingement surface and at the edge of the jet (shear layer). The grid refinements were guided by considering the effect of varying the mesh density of grids using the Richardson extrapolation technique, described in detail by Caruso et al. (1985). This procedure identifies areas of the solution domain needing grid refinement based on local error estimates. The method is based on Taylor series expansion of the solution error e_h, defined as the difference between the exact solution ϕ and the numerical solution ϕ_h, calculated on a grid spacing of h. e_h is given by

$$e_h = \phi - \phi_h = a_1 h + a_2 h^2 + ... \tag{4.27}$$

Similarly, another solution using a coarser grid with spacing $2h$ leads to

$$e_{2h} = \phi - \phi_{2h} = a_1 2h + a_2 4h^2 + ... \tag{4.28}$$

Subtraction of Equation (4.27) from Equation (4.28) yields

$$\phi_h - \phi_{2h} = a_1 h + a_2 3h^2 + ... \tag{4.29}$$

In this investigation, the values of h are small, typically 0.005 m or smaller in the stagnation and shear layer regions, such that the value of h^2 (and higher orders of h) can be neglected. Inspection of Equations (4.27) and (4.29) leads to

$$e_h = \phi - \phi_h \approx \phi_h - \phi_{2h} \tag{4.30}$$

Hence the difference in solutions of the fine grid and coarse grid provide an estimate of the solution error e_h associated with the fine grid, at the grid points of the coarse grid.

Since the storage locations of the variables for the fine and coarse grids do not coincide, it is necessary to interpolate the fine grid solution before applying the above error analysis. Simple FORTRAN procedures for the bi-linear interpolation and error calculation are provided in Appendix G with a listing of the GROUND subroutine used to obtain the required data from the PHOENICS solver. The grid refinement study commenced with the comparison of two grids comprising 70 x 26 and 140 x 52 cells in the radial and axial directions respectively, for the z/d=4 case as an extension to the work described in Jambunathan et al. (1990).

The effect of the length of the solution domain, shown in Figure 4.1, was examined to ensure that the outflow boundary did not lie within a recirculation region. As a result, the impingement and confinement plates were extended to 15d. The coarse grid is shown in Figure 4.2. The grids are cartesian and non-uniform with a higher concentration near the centre of the jet and the impingement surface. Figure 4.2 also shows the contour plots for the solution errors of the finer grid, for the pressure field and two mean velocity

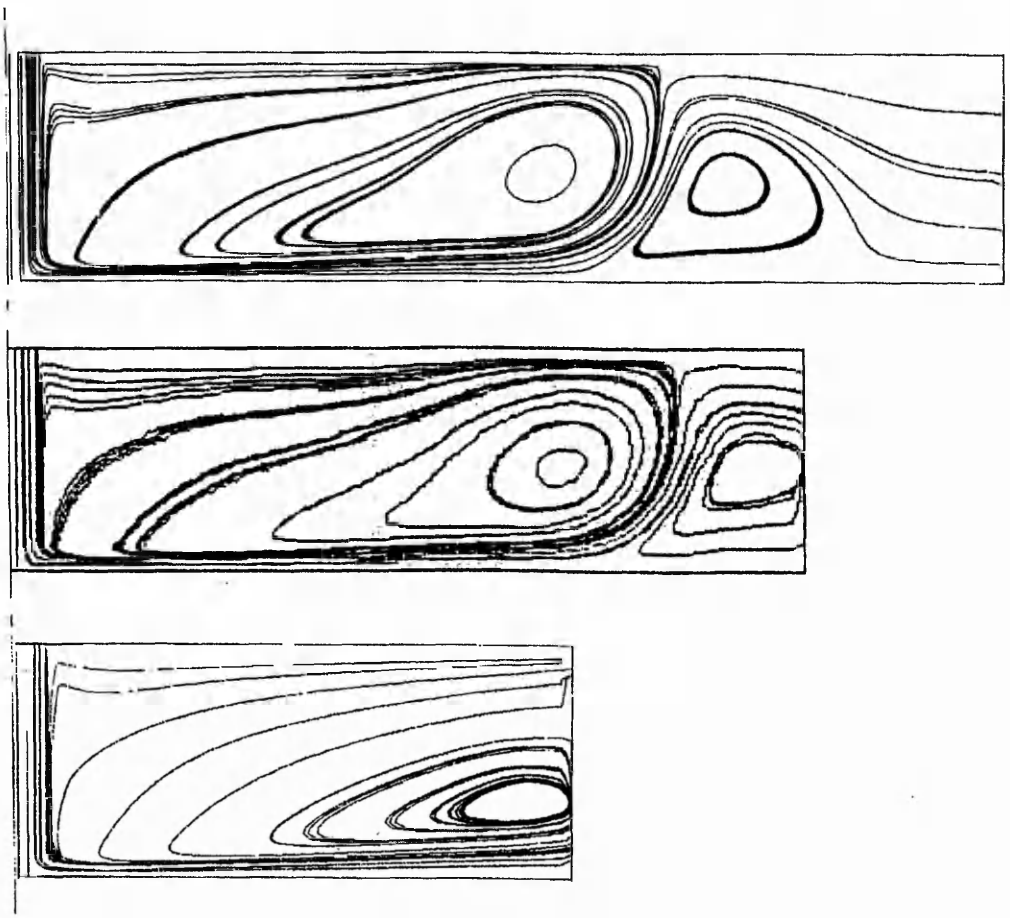

Figure 4.1. Radial extent of solution domain.

components. The pressure contours show maximum errors which exceed 50% within the stagnation region. The solution error of the radial velocity component shows local areas of high error up to 10% in the shear layer region, and over 50% within the stagnation region and the boundary layer. Similar errors occur for the axial velocity component. These large errors can be attributed to the high velocity gradients in these regions. The errors obtained with these relatively coarse grids highlight the lack of numerical accuracy associated with many of the early numerical works cited in Chapter 2. The numerical errors for the turbulent quantities were substantially higher than those for the mean velocities. It was therefore apparent that an exceptionally fine grid would be necessary to obtain a grid independent solution for nozzle to plate spacings of 4d or larger.

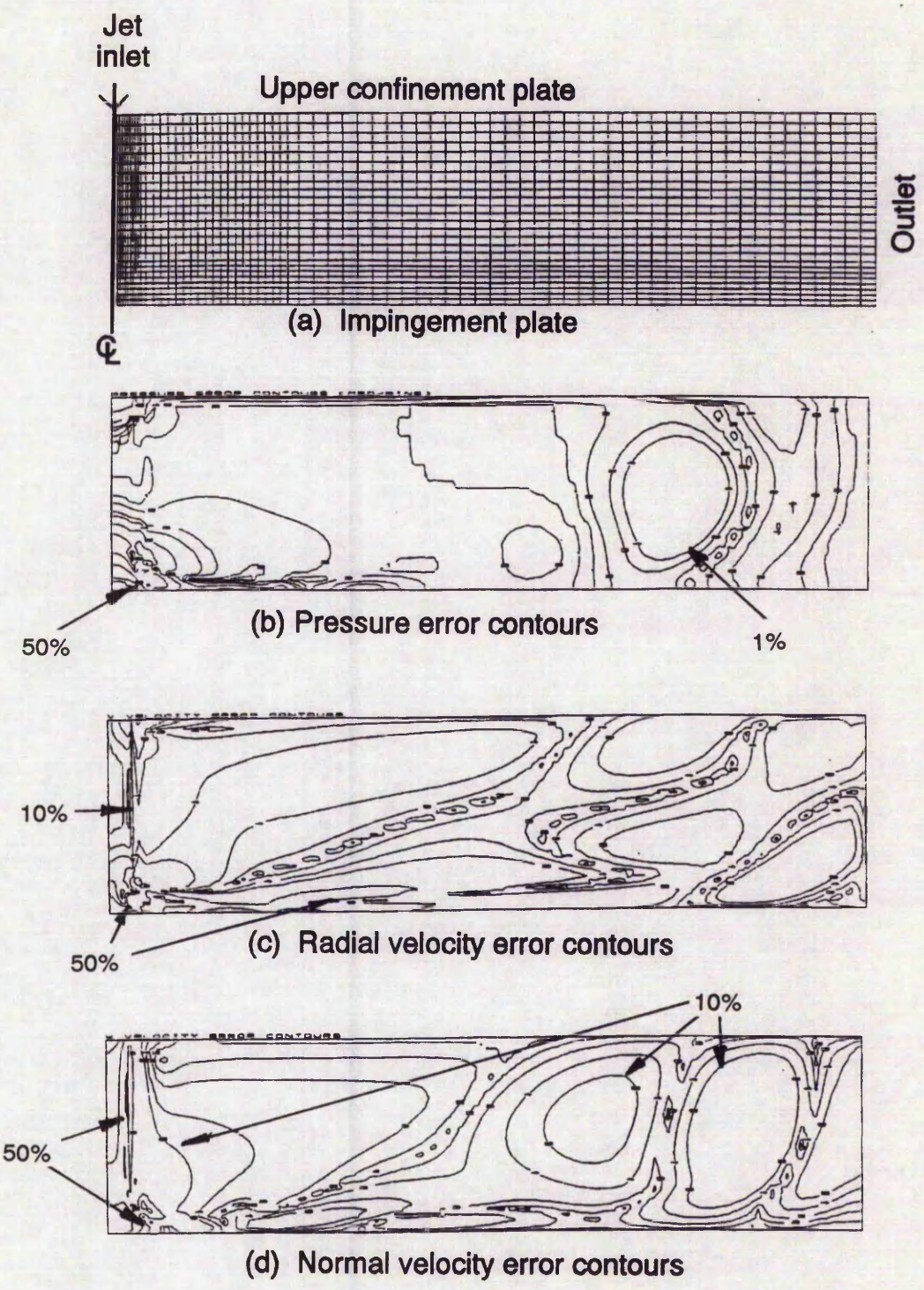

Figure 4.2 Assessment of numerical errors: (a) 70 x 26 grid, (b) pressure error contours, (c) radial velocity error contours, (d) normal velocity error contours.

Having gained an insight into the required grid density for jet impingement flow fields the attention was focused on the z/d=2 case. For the remainder of the grid dependency study, a higher concentration of grid cells was applied within the shear layer and boundary layer regions. In particular, the size of the grid cells (ranging from 0.0025d to 0.05d) within a region 0.1d from the impingement surface were addressed. Figure 4.3 shows the dependence of velocity and velocity gradient on the size of the near wall grid size. Results corresponding to the 0.0025d grid are not shown since they were indistinguishable from those of the 0.005d grid.

The development of the axial velocity as the impingement plate was approached showed little dependence on the near wall cell sizes. The radial velocity profiles however show a significant dependence at small radial distances from the jet axis, due to the large velocity gradients in this region. The change in the computed velocity gradient with near wall cell size is given in Table 4.1, where the percentage differences have been obtained with reference to the finest cell size of 0.0025d. A near wall cell size of 0.02d was selected for two reasons. The improvement obtained with the 0.005d or 0.01d grid was not substantial when compared to the economy of the 0.02d grid. In addition, the activated wall function presumes that the near wall grid cell lies within a turbulent region. Calculation of the non-dimensional distance from the wall y^+, based on the computations, indicated that a near wall cell size of 0.02d (ie. a y^+ of 0.01d) would satisfy this criterion in the stagnation region.

Near wall cell size	% difference with finest grid cell
0.05d	50
0.02d	10
0.01d	3
0.005d	<1

Table 4.1. Percentage error associated with near wall cell sizes.

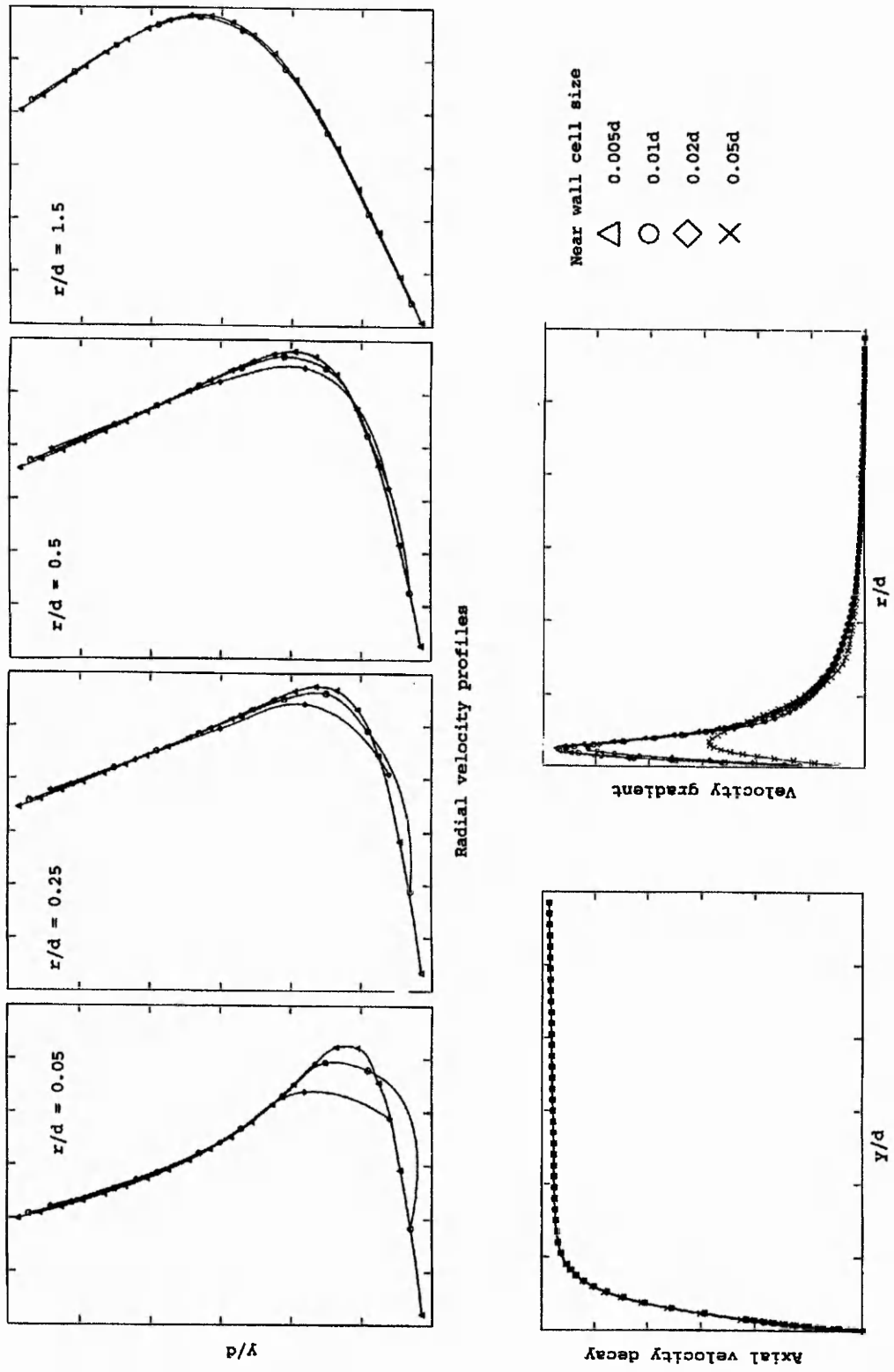

Figure 4.3. Grid dependency study.

Figure 4.4. 120 x 68 grid used for z/d = 2 computations.

A 120 x 68 grid was finally adopted, which corresponded to a mesh density approximately twice that of the fine grid used for the z/d=4 computations, and is shown in Figure 4.4. In order to compute the errors associated with this grid a solution was also obtained for a grid with half the number of grid cells. The near wall turbulent kinetic energy and radial velocity profiles for the 60 x 34 and 120 x 68 grids are shown in Figure 4.5. The difference between these values indicates the error in the fine grid according to Richardsons extrapolation technique as previously discussed. The calculated errors between the grid systems were a maximum for the turbulent quantities giving errors for turbulent kinetic energy of the order of 10% in the stagnation region.

4.7 Boundary and initial conditions

The elliptic nature of the flow field requires that boundary conditions be specified on all sides of the solution domain. Measured values of velocity and turbulence intensity, obtained using laser-Doppler anemometry and presented in Chapter 5, were specified at the jet exit. The dissipation was deduced from $\epsilon=C_{\mu}^{3/4}k^{3/2}/L$, CHAM Ltd. (1990), where L was estimated to be 5% of the inlet diameter. Zero velocities were specified at the solid surfaces and a logarithmic wall function activated, described in detail by Launder and Spalding (1974). A floating zero pressure was specified at the outlet boundary and the computed pressures are relative to it. The use of the PHOENICS Input Language (PIL) command SAME ensured that any inflowing mass brings in the same value of the variable as already

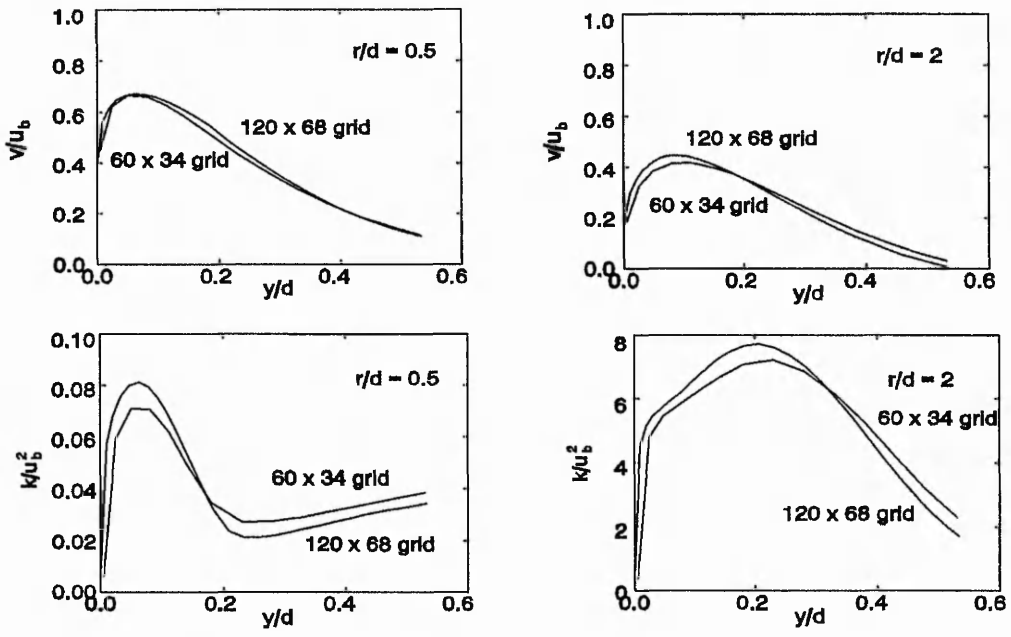

Figure 4.5 Near wall turbulent kinetic energy and radial velocity profiles for a 120 x 68 grid and a 60 x 34 grid.

prevails in the cell. A constant temperature was prescribed at the wall which simulates the experimental boundary condition and the heat transfer coefficient was obtained as described in Section 4.4. Viscosity, thermal conductivity, specific heat and density were modelled as being independent of temperature. The PHOENICS data input file, Q1.dat and the GROUND coding necessary to obtain heat transfer data are provided, fully commented, in Appendix G.

4.8 Accuracy of the numerical procedure

Before performing the computations for comparison with experiment, the accuracy of the numerical procedure was demonstrated by comparing the exact solution of the Navier-Stokes equation for fully developed laminar pipe flow with the PHOENICS solution using similar grid independence and convergence criteria. A maximum difference of 1% was reported, and shown graphically in Figure 3.7. The PHOENICS solution to laminar jet impingement

was compared to flow visualisation results and qualitative measurements of velocity using laser-Doppler anemometry, Jambunathan et al. (1990). Reasonable qualitative agreement was obtained for the mean flow. The radial velocities agreed with the LDA measurements to within 10%. More recently, the numerical results have been corroborated by Moreno et al. (1993), using a commercial finite element program called FIDAP.

4.9 Convergence

For the turbulent jet impingement case, convergence was not readily achieved, and proved considerably more difficult at this Reynolds number than the lower Reynolds numbers investigated in Jambunathan et al. (1990). To assist convergence, the pressure and velocity fields were solved to provide reasonable initial fields before activating the k-ϵ turbulence model. Linear and false-time-step under-relaxation were also applied to pressure and the other variables respectively to help procure convergence. Relaxation was not applied to the enthalpy equation since the temperature changes are small enough so as not to contribute any significant effect to the transport properties. In addition, the enthalpy equation was only solved when convergence of the other variables had been achieved. The amount of relaxation varied as the solution progressed (pressure: 0.8 - 0.2, velocities and other scalars: locally dependent on grid size and in-cell value), the greater relaxation being applied to the turbulent quantities. Only when local relaxation was applied to the velocity and turbulent quantities, implemented using the PIL PATCH command with PHASEM and SAME, was a converged solution achieved. The local values of false time step were obtained, based on the LDA data for velocities and preliminary computations for the turbulent quantities, by dividing a characteristic length by a characteristic velocity. For the velocities, the cell size and local velocity were used whereas for the turbulent kinetic energy the turbulent kinetic energy divided by the energy dissipation rate was used. Maximum and minimum values for the variables and initial values were also specified according to the jet inlet conditions. The

sums of the absolute residuals of the continuity and momentum equations were used to monitor convergence. Typically 3500 sweeps were necessary to procure convergence which used approximately 3 hours cpu time on the VAX 4600 computer.

4.10 Concluding remarks

The governing equations of motion and equations for the k-ϵ turbulence model have been described. The established Richardson extrapolation technique has been used to obtain a grid independent solution for a single jet impinging in a semi-confined space at a nozzle to plate spacing of 2d and Reynolds number of 20000.

The discretisation methods are shown to require very fine meshes to yield sufficiently small solution errors. It has been demonstrated that the numerical solutions can contain considerable numerical errors even when very fine grids, with a high density of cells in critical regions, are used. The numerical errors for the turbulent quantities can be substantially higher than those for the mean quantities, which must be kept in mind when comparing with experiment. By careful consideration of the numerical grid density, an uncertainty interval of 10% in the turbulent kinetic energy, computed using the k-ϵ turbulence model, within the stagnation region was obtained, using a grid density of 120 cells in the radial direction and 68 cells in the axial direction.

CHAPTER 5

PRESENTATION AND DISCUSSION OF EXPERIMENTAL RESULTS

The effect of near wall velocity and turbulence on the distribution of heat transfer coefficient beneath a semi-confined impinging jet, at a single Reynolds number of 20000 and nozzle to plate spacing of two diameters, has been studied. Some insight into the flow structure of the impinging jet was first obtained by performing full field qualitative flow visualisation at a range of Reynolds numbers and nozzle to plate spacings. A selection of these results are presented as appropriate. New experimental data of near wall velocity and turbulence at z/d=2, and some data at z/d=4 and z/d=6, has been obtained using laser-Doppler anemometry. The larger nozzle to plate spacings were investigated to gain as deeper understanding as possible into the structure of the turbulent flow and its effect on the heat transfer mechanism, and to substantiate the results. In order to relate the flow field data directly to the heat transfer mechanism, the surface heat transfer coefficient was determined for the same geometry, using liquid crystal thermography on the same experimental rig. In this Chapter these experimental results are presented and discussed, focused on the z/d=2 case. The results are presented in four sections. The first three sections present results obtained using flow visualisation, laser-Doppler anemometry and liquid crystal thermography, respectively. Concluding remarks are provided in the fourth section.

The data is non-dimensionalised with the mean bulk velocity at the jet exit, u_b, unless otherwise stated. The velocity components of the Reynolds stresses are presented as u'/u_b, v'/u_b for the normal components and $\overline{u'v'}/u_b^2$ for the shear component. Probability density distributions of velocity are considered with the corresponding skewness and kurtosis (flatness or excess) factors and the significance of these factors explained. The axial and radial velocity and turbulence profiles are considered with particular attention paid to the near wall characteristics. Finally, comparisons are made to relate the characteristics of these

distributions to the local maxima in the convective surface heat transfer coefficient. Wherever possible, data is compared with that of other authors. A very relevant piece of work was completed recently by Cooper et al. (1993) but for the unconfined case, using hot-wire anemometry. The present work corroborates their data qualitatively, the quantitative differences being attributed to the difference in geometry.

5.1 Qualitative flow visualisation

Preliminary results obtained using oil smoke as the seeding medium are shown in Figure 5.1(a) for a Reynolds number of 1200 at a z/d of 8. The potential core of the jet is shown and the considerable deflection close to the impingement plate. Wall eddies are formed which stretch and diverge in the radial direction. Further downstream the flow begins to resemble that of a wall jet. Although not clear from the Figure, a larger scale recirculation then forms with imposed finer turbulence as the wall jet rolls back with complete direction reversal, defining the separation point. Popiel and Trass (1982), as a result of smoke-wire tests, partly attributed these wall eddies to vortices initiated at the jet exit and developed in the mixing region of the approaching jet, for the unconfined jet impingement case at a Reynolds number of 3500 with a flat velocity profile. More recently, Popiel and Trass (1991) confirmed that a similar phenomenon occurred for the case of semi-confined jet impingement up to Reynolds numbers of 20000. This phenomenon was not evident in Figure 5.1(a) nor in the higher Reynolds numbers considered. Popiel and Trass (1991) further suggested that the flow was periodic in the impingement region at turbulent Reynolds numbers. Kataoka (1986, 1987) reported similar characteristics when the impingement plate was placed at z/d=6.7, however, Hussain and Clark (1981) reported that at higher Reynolds numbers there were no such organised periodic structures. Periodicity was observed in this investigation but could not be quantified due to the method of recording results (conventional photography) and the rapid mixing of the smoke.

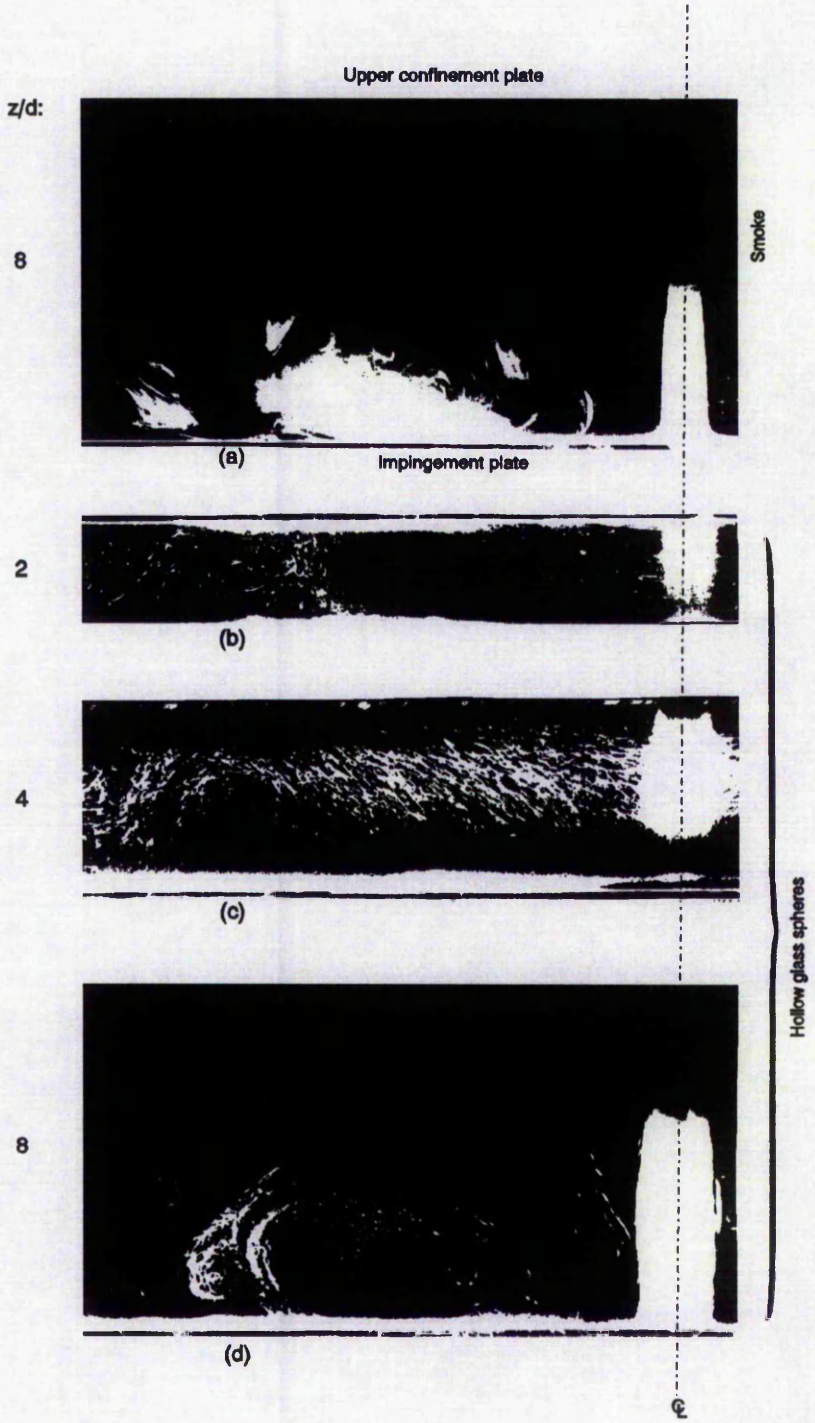

Figure 5.1. Qualitative flow visualisation results; (a) Re = 1200, z/d = 8, (b) Re = 20 000, z/d = 2, (c) Re = 20 000, z/d = 4, (d) Re = 2000, z/d = 8.

Smoke wire tests, where the wire extended across the full width of the jet and upper confinement plate, indicated the severe entrainment at the jet exit. At high Reynolds numbers the fine structures of the jet decrease in size, thereby enhancing local mixing. The lack of a distinct vortex structure can be further explained by the fully developed jet which results in a lower shear, and inability of the particles to follow the turbulent flow. Results are not presented as they could not be captured on film due to the rapid mixing of the flow and low illumination levels. Again, coherent structures could not be discriminated. When the wire was placed close to the impingement plate however, wall eddies were clearly visible, and were attributed by Popiel and Trass (1991), to the impingement of vortices developed upstream, onto the impingement plate. Whether the impingement of these vortices are the sole source of the wall eddies could not be established from the present study.

The flow visualisation results using the hollow glass spheres at a Reynolds number of 20000, for z/d of 2 and 4 are shown in Figures 5.1(b) and 5.1(c) respectively. Flow visualisation results at the laminar Reynolds numbers have been presented in Jambunathan et al. (1990); the flow is dominated by a well defined vortex which occupies the whole cross-section (see above) and a second counter rotating vortex just downstream and close to the impingement plate. As the Reynolds number increases a further recirculation region appears close to the confinement plate which increases in size with Reynolds number. At the higher jet Reynolds number shown here, the flow is characterised by a series of counter rotating vortices. The flow is complex and the boundary layer appears as wavy streamlines between the vortices and the impingement plate. As the nozzle to plate spacing is increased the primary vortex moves further downstream into the wall jet. The results at Re=20000 compare favourably with those of Saripalli (1983) for a semi-confined jet at Re=21 140 and z/d=2.2 and 3, and with a recent tuft deflection study by Lucas et al. (1992). The centre of the primary vortex occurs at approximately 7d from the jet axis.

5.2 Laser-Doppler anemometry

5.2.1 Nozzle exit conditions and symmetry

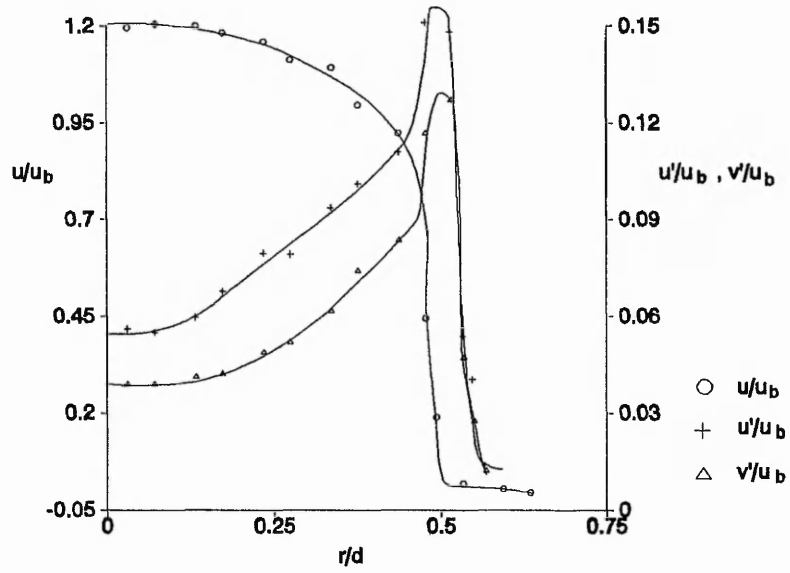

Figure 5.2. Nozzle exit velocity and turbulence characteristics.

The measured nozzle exit velocity and turbulence profiles were used as the inlet boundary conditions in the numerical study and are presented in Figure 5.2. This graph includes data from both sides of the jet axis and demonstrates the symmetry of the jet at the nozzle exit. The difference between readings on opposite sides of the jet lie well within the estimated uncertainty intervals. The radial position of maximum turbulence at r/d=0.47 compares well with recent data discussed in Eggels et al. (1994) for fully developed turbulent pipe flow where maximum turbulence levels were reported at r/d=0.46. The discrepancy is attributed to data in the present study being obtained at 0.03d from the nozzle exit. The fully developed flow profile can be seen and the increase in turbulence as the edge of the jet is approached. The turbulent components of the Reynolds stresses one diameter downstream of the free jet exit are presented in Figure 5.3 and compared with data from Aydore et al.

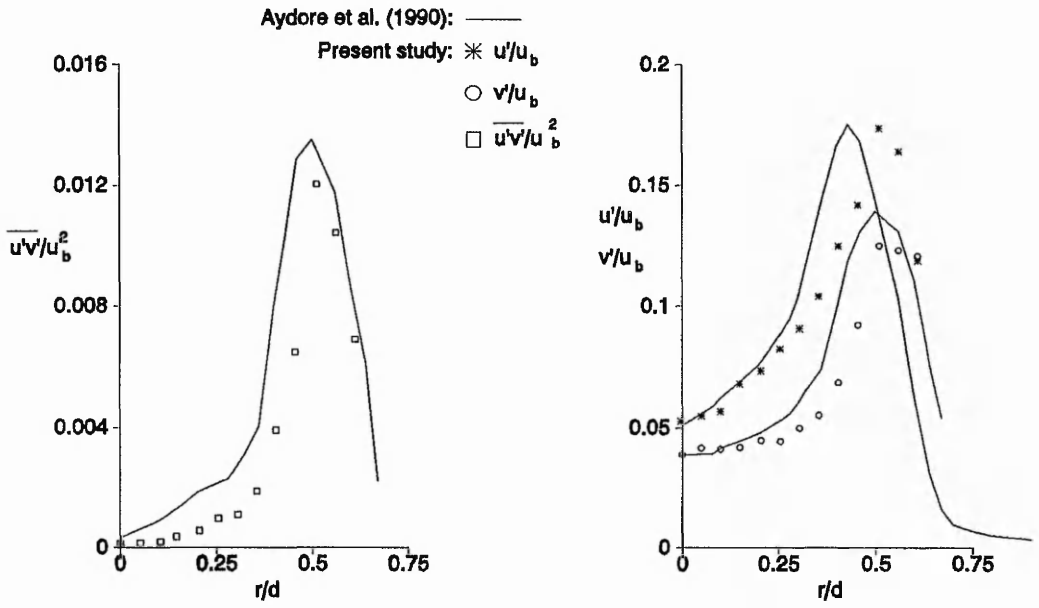

Figure 5.3. Turbulent components of the Reynolds stresses one diameter from the nozzle exit.

(1990), obtained using hot-wire anemometry. Their data was also obtained for a fully developed jet issuing from a long pipe but unconfined and at a slightly higher Reynolds number of 23000. The present results compare well with those of Aydore et al. (1990) with only a small difference occurring within the potential core. As the edge of the jet is approached, all components of the Reynolds stresses increase to a maximum before reducing at further radial distances. The data of Aydore et al. (1990) show higher turbulence on the high velocity side of the shear layer. This can be explained by the further development of the axial turbulent fluctuations than in the present case, due to a nozzle length of 45d, as observed by Obot (1980). Recall that the nozzle length in the present study is 22d.

Symmetry of the flow is further demonstrated in Figure 5.4 where typical profiles of mean velocities and turbulent quantities at r/d=0.5 and r/d=-0.5 are compared. Due to the orientation of the LDA measurement volume and the axisymmetry of the flow, the mean

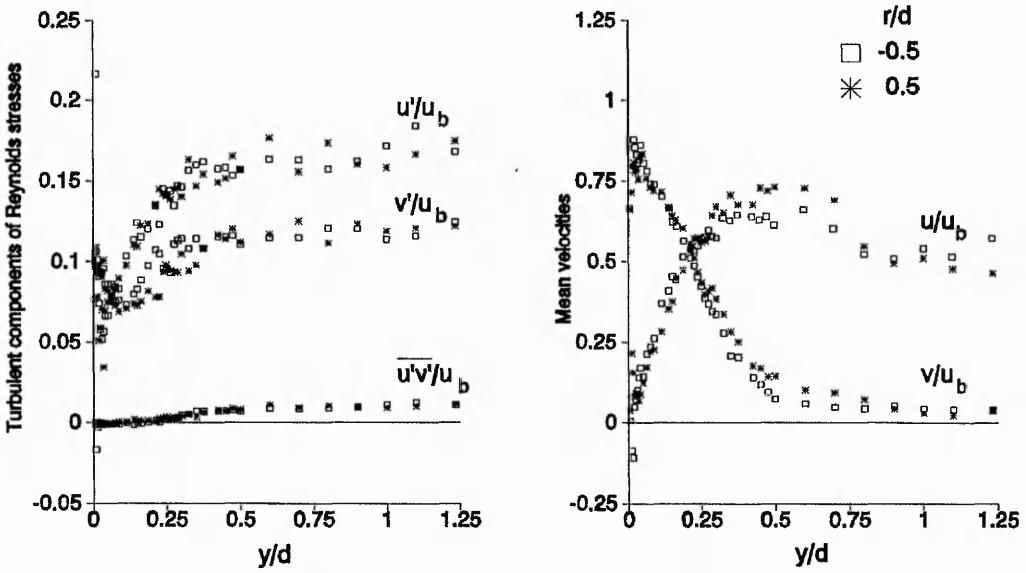

Figure 5.4. Typical symmetry of radial and normal mean velocity and turbulence profiles at r/d=±0.5. z/d=2.

velocity and shear stress component at r/d=-0.5 were of opposite sign to the corresponding components at r/d=0.5. Consequently, the mean velocity and shear stress component have been multiplied by -1, to allow direct comparison of the magnitudes of the quantities. The difference in the profiles of u, v and v' marginally exceed the extremes of the uncertainty intervals discussed in Chapter 3 in the region $0.3<y/d<0.75$. This difference has not been attributed to asymmetry since it will be shown in the next section that this region is associated with intermittency. In the near wall region, $0.02<y/d<0.3$, the differences between the profiles on opposite sides of the jet lie within the uncertainty intervals. The profiles of the other quantities lie within the uncertainty intervals at all values of y/d shown in Figure 5.4.

5.2.2 The probability density functions, skewness and kurtosis

The probability density functions (pdfs) of velocity also provide an insight into the flow

structure. According to Townsend (1976), the velocity pdfs are nearly normal in homogeneous turbulence, depart from the normal in a shear flow and are far from normal near the edge of a free turbulent flow such as a jet. In order to characterise the radial velocity pdfs, the skewness and kurtosis factors are employed. The theoretical values of skewness and kurtosis are 0 and 3 respectively, for a normal or Gaussian distribution. Skewness of the velocity distribution is associated with the convection of turbulent energy; the transfer of energy from regions of large intensity to regions of smaller intensity. Kurtosis is associated with intermittency; near the edge of the fully developed jet the flow alternates between slow fluctuations of low intensity and rapid fluctuations of high intensity. Very large values of kurtosis indicate that the distribution of intensity is 'spotty', Townsend (1976). Thus, the probability density distributions and their associated skewness and kurtosis help to illustrate the nature of intermittent flows.

The change in probability density functions of velocity are presented in Figure 5.5 for the z/d=2 case, at distances from the impingement surface of 0.25d, 1.0d and 1.5d, and at radial stations varying from 0 up to 2.5d. The graphs have been normalised so that the height of the pdfs is almost equal. When $y/d \geq 1.0$ and away from the potential core, $r/d \geq 0.5$, the small velocity fluctuation in both axial and radial directions is indicated by the narrow distribution of the pdfs. The decrease in the mean velocity along the jet axis, r/d=0, can be observed and the slight increase in axial turbulence, indicated by a broadening of the pdfs. There is no increase in radial turbulence for these distances from the surface and the radial velocity on the axis remains at zero as expected. Two regions of high velocity fluctuations are apparent: in the impingement region close to the wall and in the shear layer surrounding the jet.

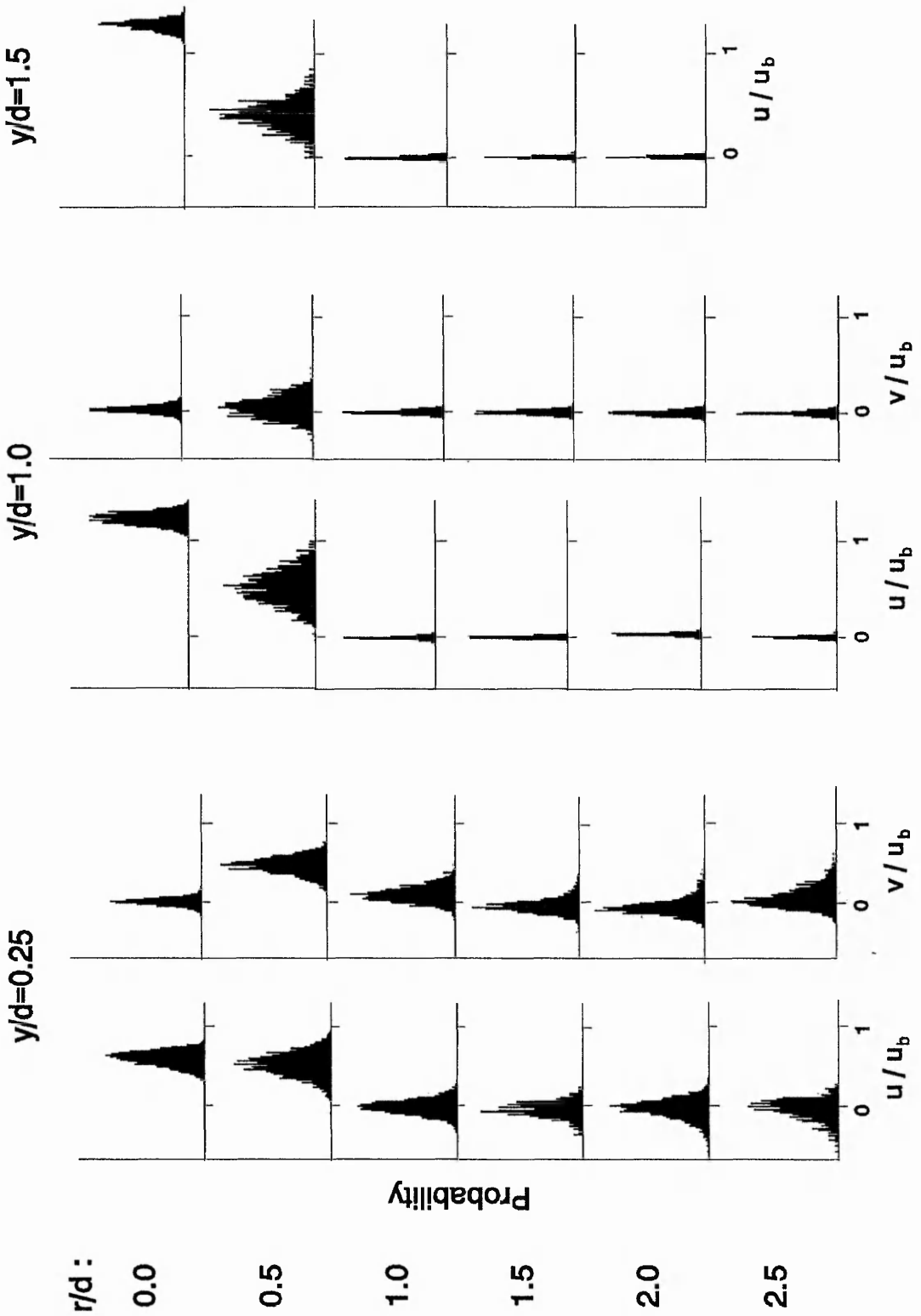

Figure 5.5. Change of probability density functions of velocity. z/d=2.

Further away from the wall at y/d=0.25 and r/d≥1.0, just above the developing wall jet along the surface where the mean velocities are close to zero, the radial velocity pdfs skew on the lower velocity side (positive skew) and the normal velocity pdfs skew on the higher velocity side (negative skew). Positive skew indicates that more than half of the deviations occur left of the mean but that the large deviations are to the right. In other words the low velocities have a higher probability of being measured. The converse is true for negative skew. At y/d=0.25 and r/d=0, where the jet is approaching the impingement plate, the plate restricts positive fluctuations of the axial velocity from the mean value which leads to a negative skewness.

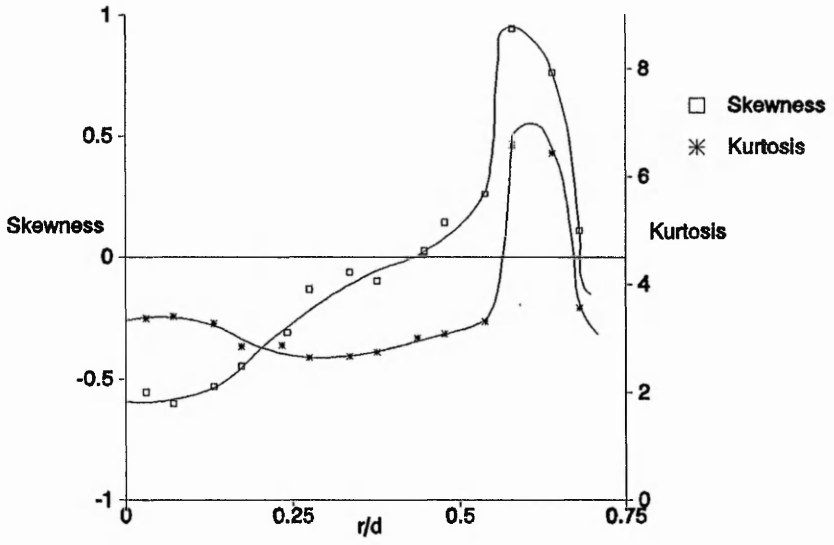

Figure 5.6. Skewness and kurtosis for the axial velocity in the developing jet.

The skewness and kurtosis factors for the developing jet profile are shown in Figure 5.6 at 1d from the nozzle exit. The change in skewness factor as the edge of the jet is approached indicates the shear layer region and comparison of Figure 5.6 with Figure 5.3 shows that increasing skewness occurs in regions of increasing turbulence intensity where high gradients prevail. A negative skewness factor approaching -0.6 is obtained in the central region of the

jet. This factor increases to a maximum positive skewness approaching 1 at the edge of the jet, with the cross-over from negative to positive occurring at r/d≈0.4. In the potential core of the jet, the turbulence is continuous with respect to time and a kurtosis value close to 3 is obtained. As the free boundary of the jet is approached the kurtosis increases to a maximum value of 7 indicating the intermittency of the axial velocity fluctuations.

A more detailed view of skewness and kurtosis associated with the radial velocity measurements can be seen in Figures 5.7 to 5.13. Skewness and kurtosis factors close to 0 and 3 respectively, exist on the fully developed jet axis. Similar values for the axial velocity component occurred (shown typically by Figure 5.6) consistent with values obtained in the fully developed region of free jets by Hetsroni and Sokolov (1971) and more recently by Kimura et al. (1990). At the edge of the jet, r/d=0.5, and in the impingement region, y/d=0.25, a slight negative skewness develops, with a return to zero skewness as the impingement surface is approached. Small changes in skewness and kurtosis factors have been attributed to convection or entrainment as in the above works. At further radial distances however, in the region $0.25<y/d<0.5$ the skewness factor increases in magnitude up to a maximum value of 2.5 at r/d=2.5 followed by a decrease at further radial distances. The positive skewness factors are associated with high values of kurtosis with abnormally high values occurring at r/d=2.5. The greater the difference in sizes between the energy containing and dissipation regions, the larger the kurtosis, Townsend (1976). As will be shown later, these maxima coincide with the largest gradients of mean velocity and turbulence intensity. The full significance of these results is not clear, but they support the conjecture in the previous section that large scale turbulent structures are generated at the jet exit, and are then transported into the impingement region. Although intermittency may be associated with a laminar to turbulent transition, it is apparent from Figure 5.22 that the high values observed here lie well out of the boundary layer.

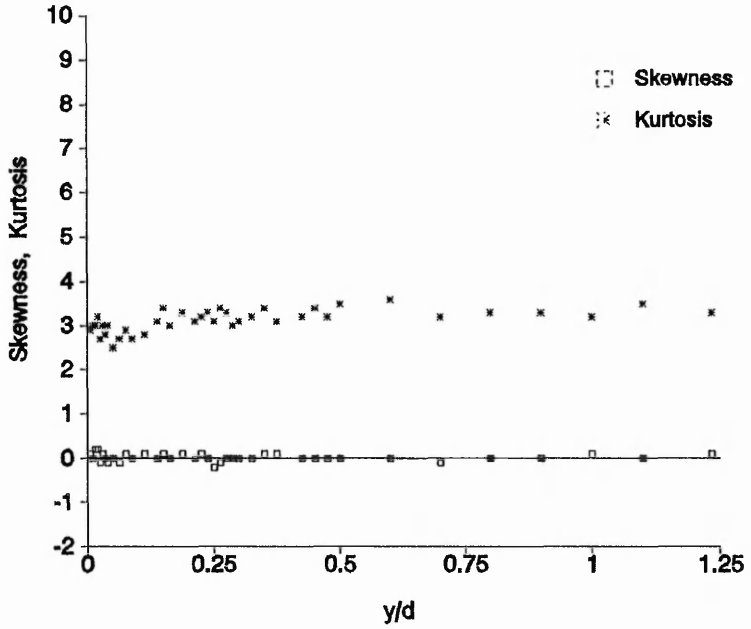

Figure 5.7. Skewness and kurtosis at r/d = 0.

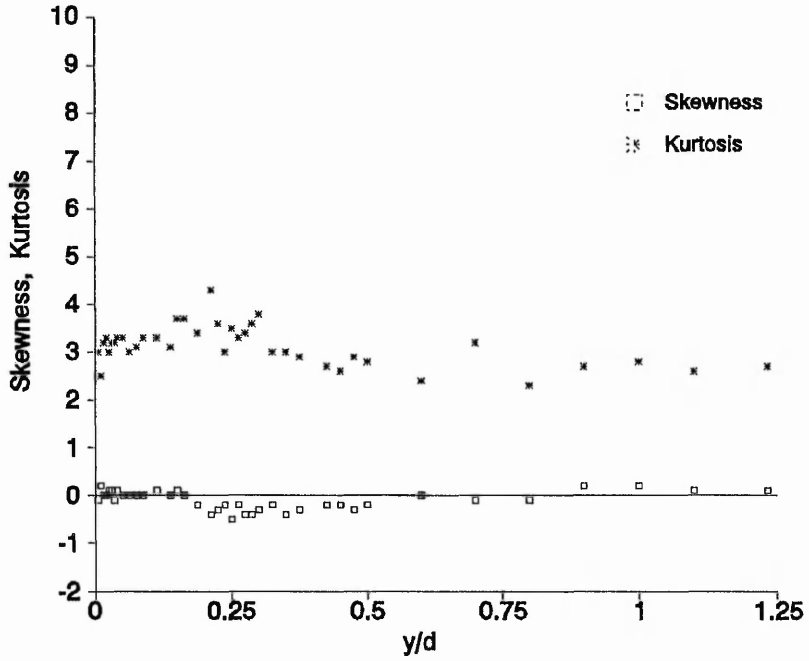

Figure 5.8. Skewness and kurtosis at r/d = 0.5.

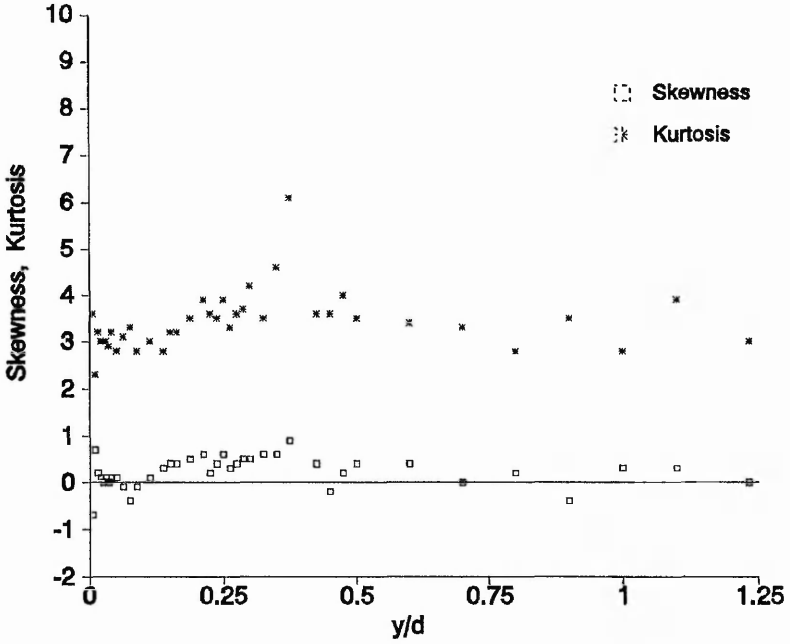

Figure 5.9. Skewness and kurtosis at r/d = 1.0.

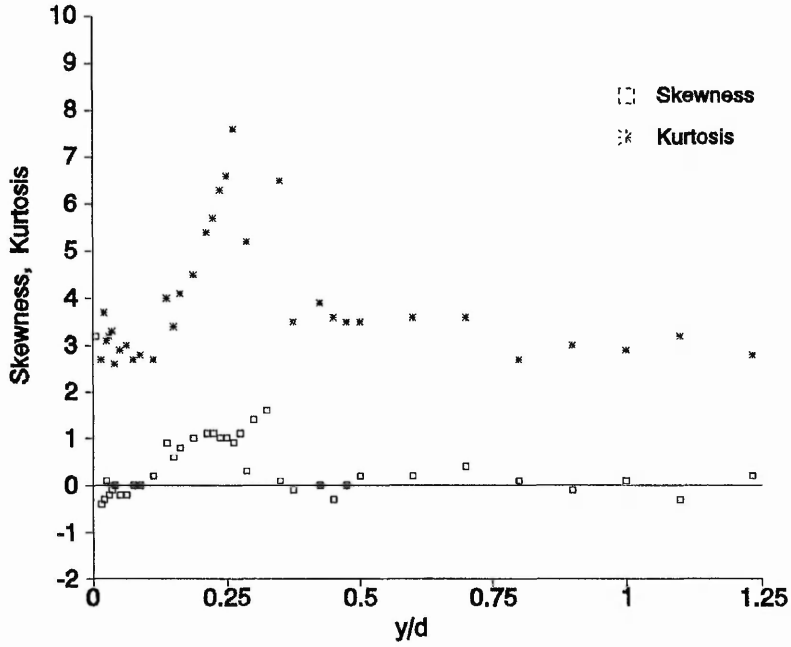

Figure 5.10. Skewness and kurtosis at r/d = 1.5.

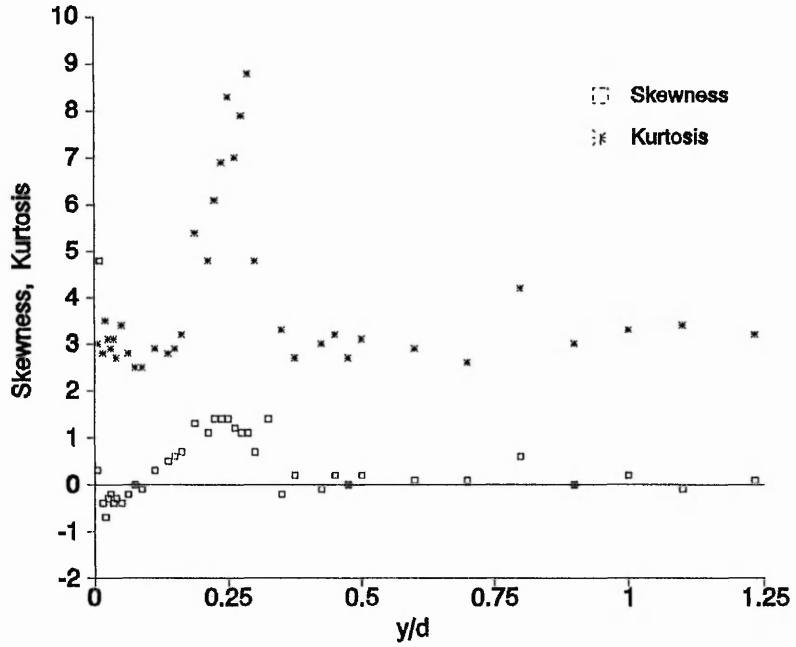

Figure 5.11. Skewness and kurtosis at r/d = 2.0.

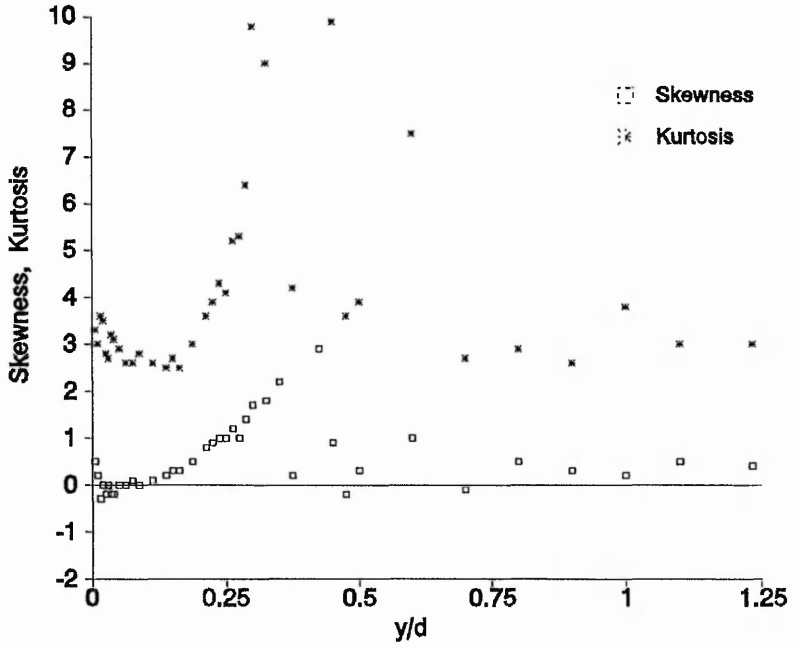

Figure 5.12. Skewness and kurtosis at r/d = 2.5.

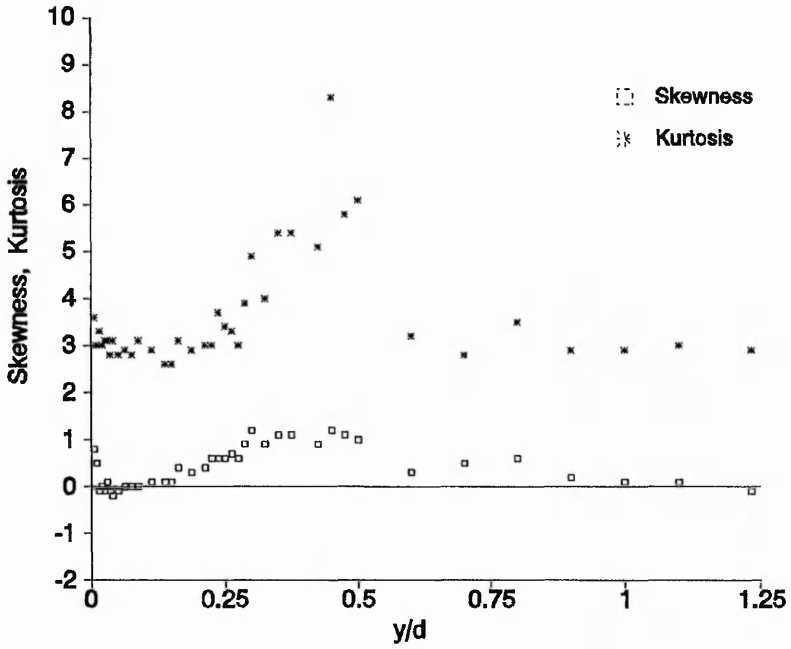

Figure 5.13. Skewness and kurtosis at r/d = 3.0.

5.2.3 Velocity and turbulence along the axis of the free and impinging jet

Figure 5.14 shows the axial velocity decay and turbulence development of the free turbulent jet, fully developed at exit, normalised by the maximum exit velocity, $u_{max,}$ and local velocity, u. Data is plotted from several data sets and demonstrates the consistency of the results. Initially, the central core of the jet is unaffected by the regions of entrainment and shear surrounding it, and the velocity remains constant at the jet exit value. This potential core is commonly defined as the distance from the nozzle exit to where the axial velocity has decreased to 95% of the initial axial velocity. For this geometry this leads to a potential core length of 4.6d. When a 98% criterion is used the potential core extends to 4d. The axial turbulence intensity increases from 6% at the jet exit to over 20% at z/d=10 due to the penetration of turbulence to the axis from the shear layer. The absolute value of axial turbulence increases from the jet exit to a maximum at z/d=8 and then decreases. Although the turbulence level increases on the jet axis, the turbulence maxima occur at the mid-points

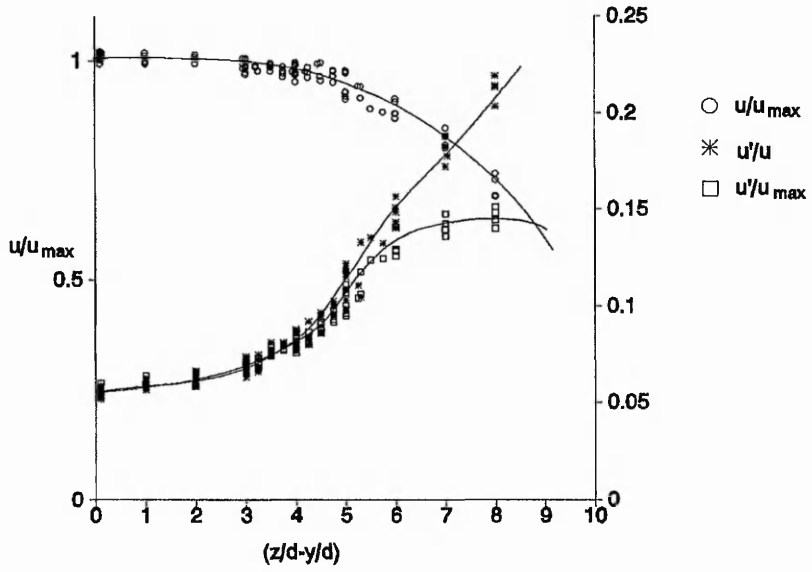

Figure 5.14. Decay of the free jet.

of the shear layer, as seen in Figure 5.3. The above velocity and turbulence characteristics compare well with those of van de Meer (1991) who measured the axial decay of an isothermal jet issuing from a long, slowly tapering burner. The burner arrangement was considered as unconfined but the burner wall thickness of approximately 1.25d would restrict entrainment to some extent, as in the case of semi-confinement. Van de Meer reported an increase of turbulence from 6%-8% at the jet exit to 20% at z/d=10, with a potential core length of 4d (95% criterion).

Figure 5.15 shows the axial velocity decay and turbulence development for the case of the impinging jet, at nozzle to plate spacings of 2d, 4d and 6d. As in the case of the free jet the axial velocity decreases slowly and is unaffected by the wall until approximately 0.8d from the wall when significant axial deceleration takes place. There is clear evidence that for the z/d=6 case the presence of the wall leads to an extension of the potential core; from 4.6d to 4.9d. The axial turbulence also exhibits similar characteristics to the free jet until very

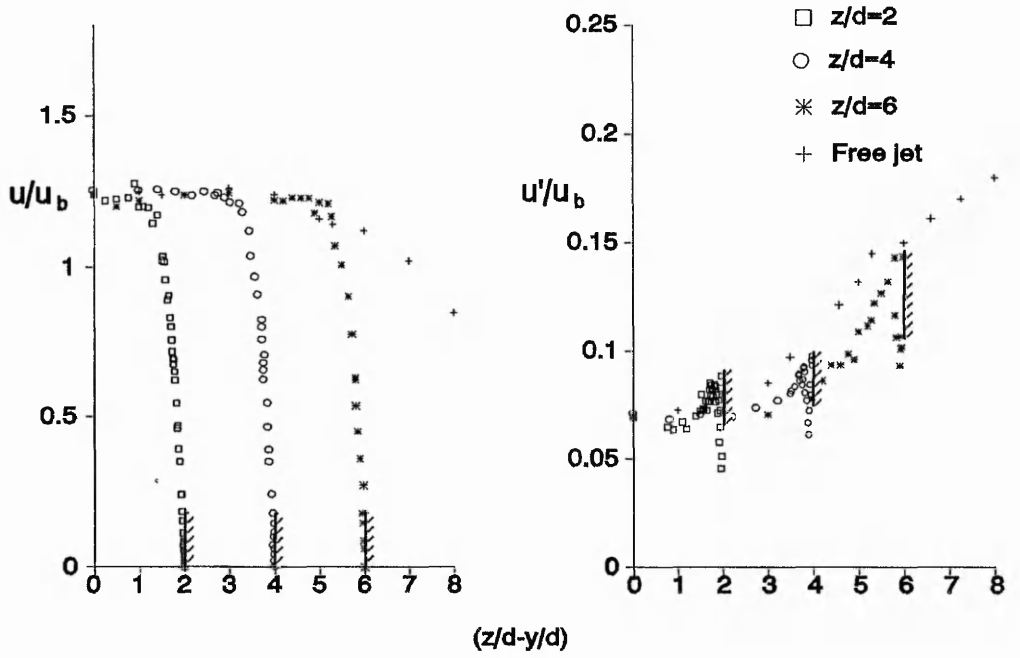

Figure 5.15. Axial velocity decay and turbulence development of the impinging jet.

close to the wall when there is an abrupt reduction in turbulence followed by an abrupt increase. The magnitude of the axial turbulence on impingement is similar for the z/d=2 and z/d=4 case since the wall is positioned within the potential core. This value is much higher for the z/d=6 case due to the further development of the jet before impingement. These turbulence profiles represent the absolute values of turbulence relative to a constant velocity.

In Figure 5.16 the same turbulent profile for the z/d=2 case is compared with the turbulence intensity profile, which is the turbulent fluctuation normalised by the local velocity. Due to the decreasing axial velocity and steady turbulence fluctuation for $0.3<y/d<1.25$, the turbulence intensity also rises steadily. However, the increase in the turbulent fluctuation for $y/d<0.3$, coupled with the decreasing local velocity, gives rise to extremely high values of turbulence intensity.

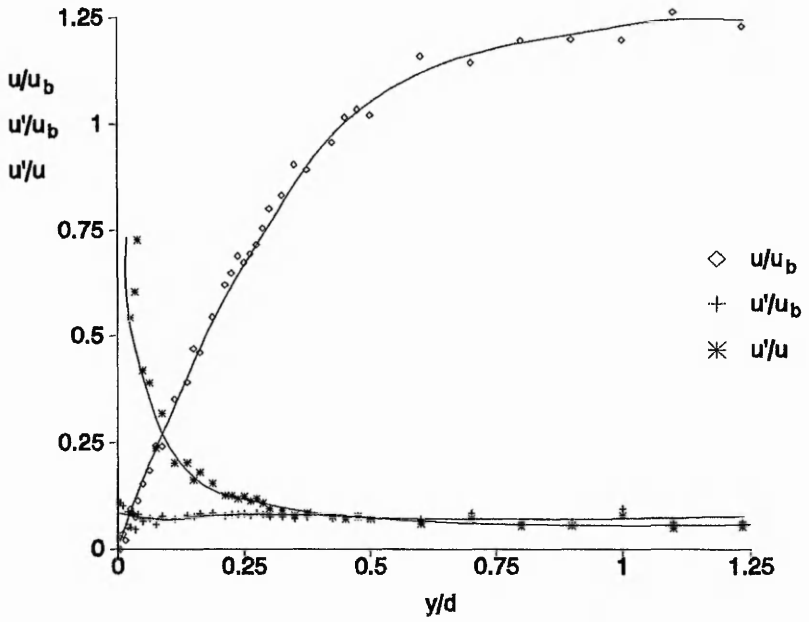

Figure 5.16. Near wall axial turbulence and turbulence intensity. z/d=2.

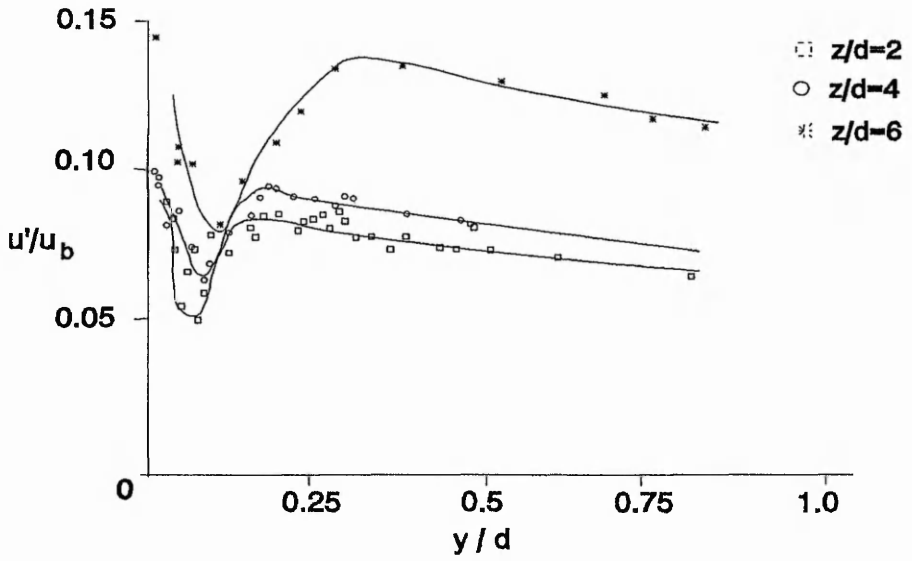

Figure 5.17. Near wall axial turbulence.

In Figure 5.17 the near wall axial turbulence (r/d=0), for all nozzle to plate spacings, is considered in more detail. As the wall is approached, the turbulence increases steadily up to 0.15d, 0.2d and 0.3d for z/d=2, 4 and 6 respectively, due to the diffusion of turbulence from the edge of the jet to the axis. A 50% reduction in turbulence then occurs at y/d=0.075d, 0.09d, and 0.1d for the cases of z/d=2, 4 and 6 respectively, probably due to the wall exerting a damping effect and suppressing the turbulence fluctuations. This data compares, qualitatively, very well with that of Cooper et al. (1993), shown in Figure 5.18.

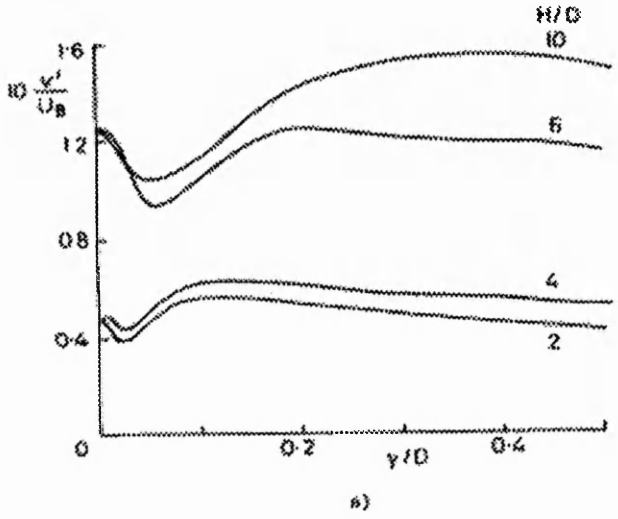

Figure 5.18. Near wall axial turbulence measured by Cooper et al. (1993). *(Reproduced with author's permission).*

The quantitative differences are unlikely to be due to experimental uncertainty but will depend largely on the jet exit conditions, determined by the particular geometry. The level of the turbulent fluctuation u´, increases as the velocity gradient, du/dy, increases until the effect of the wall is felt. Figure 5.19 confirms that the radial velocity gradient is negligible in this region. The subsequent increase in turbulence as the wall is further approached was also observed by Cooper et al. (1993) and was believed to be due to the hot-wire becoming sensitive to radial fluctuations. Here the very near wall increase could be attributed to errors caused by the finite length of the LDA measuring volume and near wall reflections,

as discussed in Chapter 3. The profiles in near wall axial turbulence are similar for all nozzle to plate spacings and in general the magnitude increases with z/d. The z/d=2 and z/d=4 case are of similar orders of magnitude but the z/d=6 case has an axial turbulence level approximately 50% greater than the smaller spacings.

Figure 5.19 shows both components of velocity and the fluctuation velocity component of the normal Reynolds stresses along the axis within the impingement region for the z/d=2 case. The normal velocity decreases to zero and the radial velocity is uniform and zero as expected. The shear stress component $\overline{u'v'}$ is also near zero which is consistent with zero velocity gradients on the axis. The axial turbulent fluctuation is of the order of 50% higher than the radial fluctuation, the difference increasing as the wall is approached, and indicates the anisotropic nature of the jet impingement region.

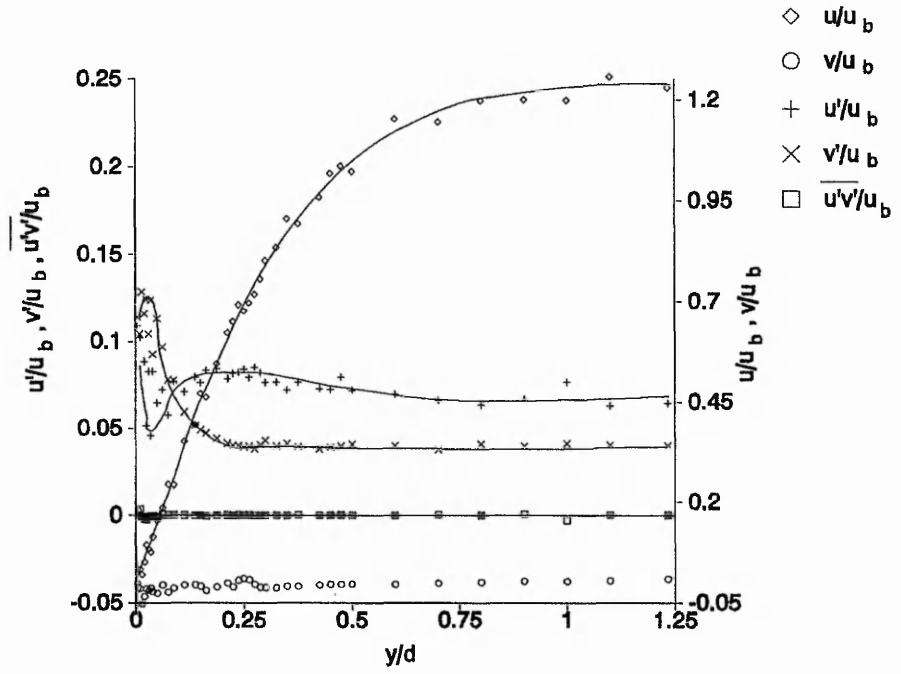

Figure 5.19. Velocity and turbulence characteristics within the stagnation region at r/d =0 for the z/d = 2 case.

5.2.4 Radial velocity and turbulence profiles along the plate

Radial velocity and turbulence profiles are presented in Figures 5.20 and 5.21 respectively, for the z/d=2 case at radial locations varying from r/d=0.5 to r/d=3.0 as a function of non-dimensional distance from the plate y/d, where 0<y/d<1.25. As the wall is approached, y/d≥0.3, the radial velocities are steady with a near zero value, except at r/d=0.5 where the radial velocity increases slightly due to the spreading of the jet. Closer to the wall, y/d<0.3 the development of the velocity profile along the plate from the stagnation region to the wall jet region can be clearly seen. Similarly for the radial turbulence levels, these are low and steady away from the wall, except at r/d=0.5, in the shear layer, where the turbulence level is initially higher but then gradually decreases as the wall is approached.

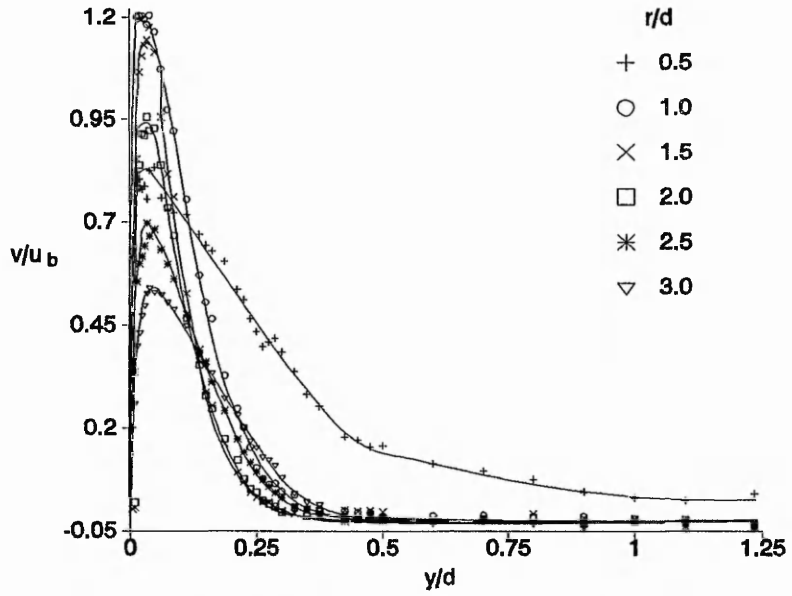

Figure 5.20. Radial velocity profile along the plate. z/d = 2.

Figures 5.22 to 5.27 show the radial velocity profiles and turbulence levels in the near wall region (y/d<0.3 where the mean velocity gradients are largest) in more detail for all of the nozzle to plate spacings considered. In all cases the maximum radial velocity increases up to a maximum at r/d=1, reduces marginally at r/d=1.5, followed by a decrease characteristic

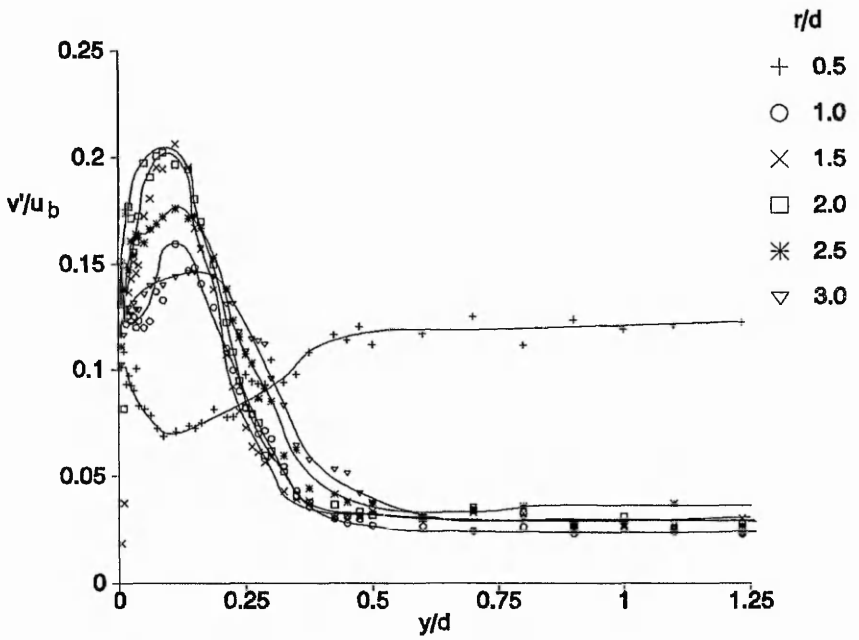

Figure 5.21. Radial turbulence profiles along the plate. z/d = 2.

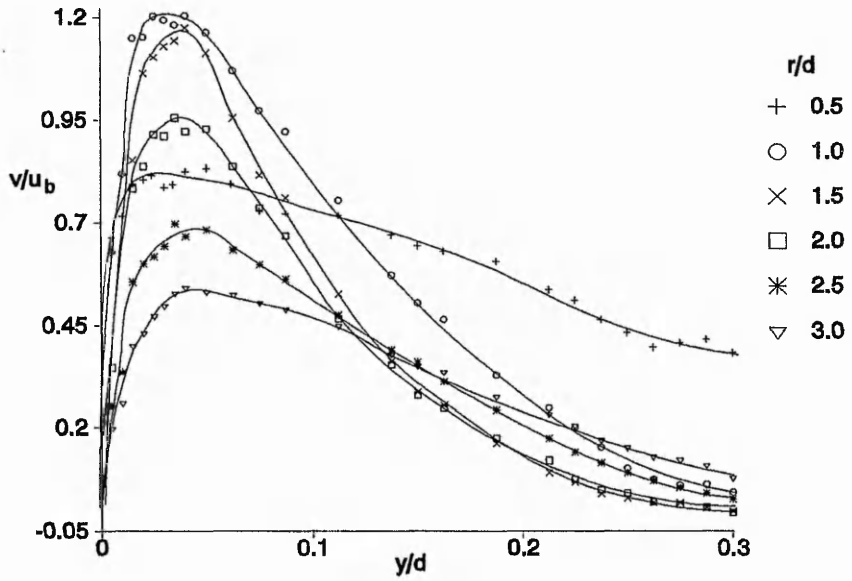

Figure 5.22. Radial velocity profile along the plate, z/d = 2.

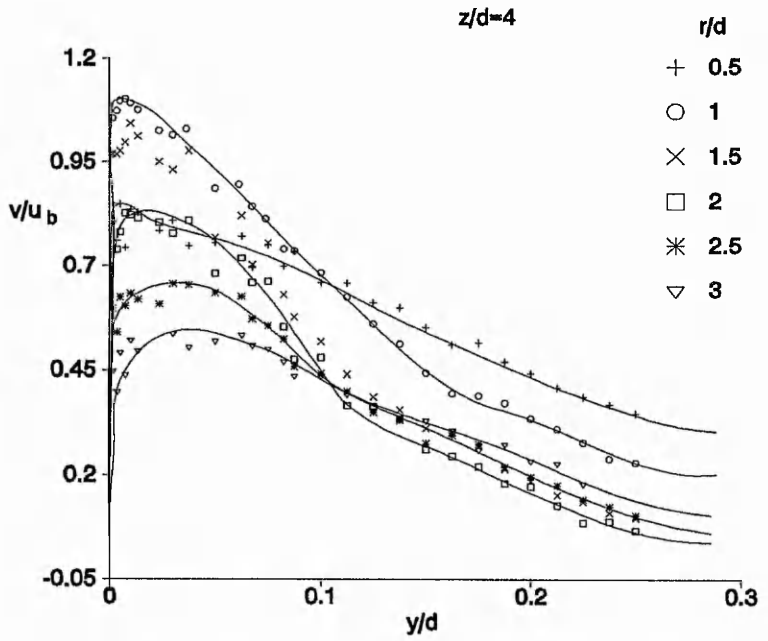

Figure 5.23. Radial velocity profile along the plate, z/d = 4

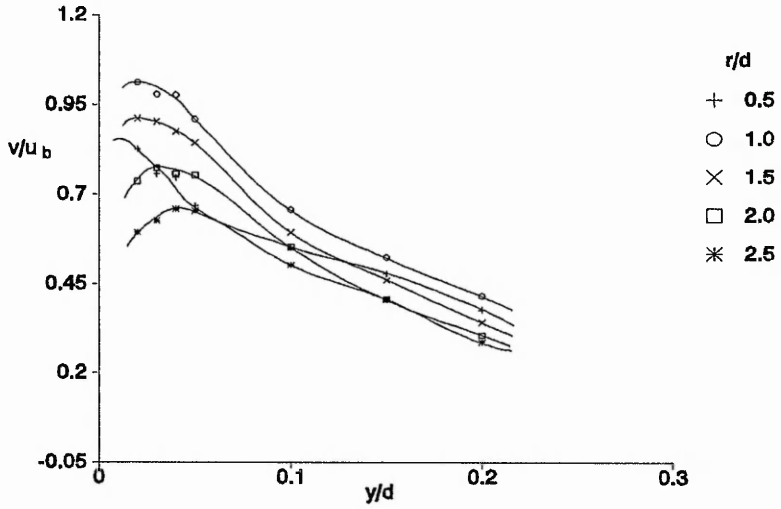

Figure 5.24. Radial velocity profile along the plate, z/d = 6.

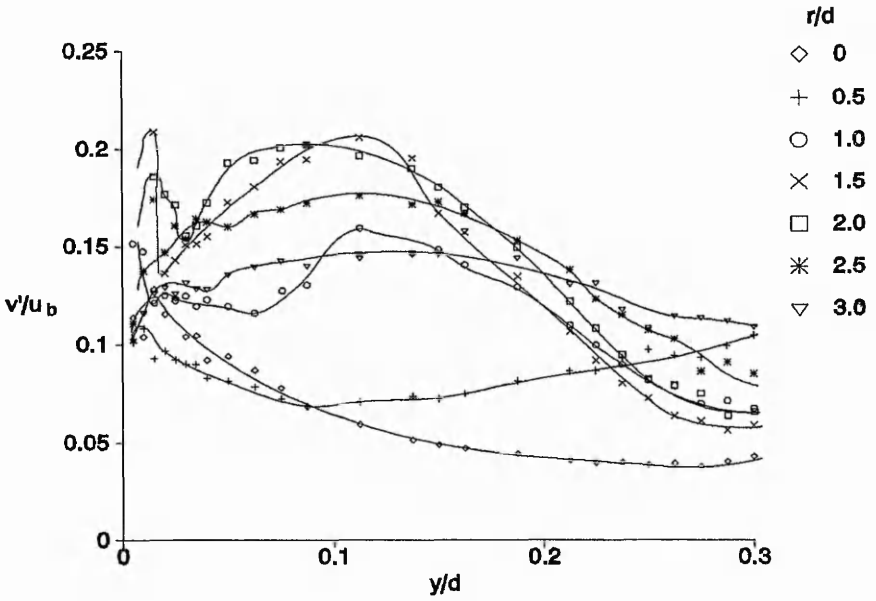

Figure 5.25. Radial component of turbulence profile, z/d = 2.

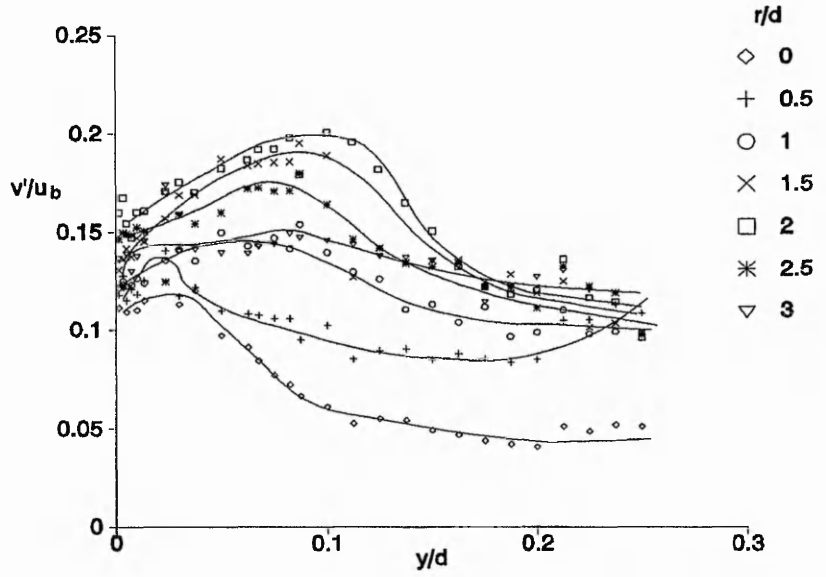

Figure 5.26. Radial component of turbulence profile, z/d = 4.

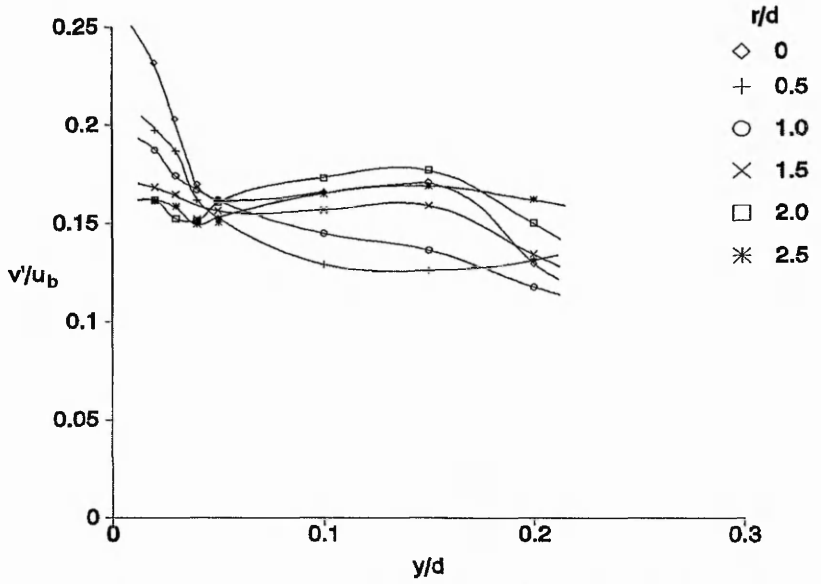

Figure 5.27. Radial component of turbulence profile, z/d = 6.

of a wall jet. The quantitative differences are due to the nozzle to plate spacing, and the consequent development of the axial velocity before impact.

The radial turbulence profiles show similar qualitative behaviour. In all cases and at all radial stations except r/d=0 and r/d=0.5, the turbulence level increases to a maximum at y/d≈0.1 followed by a decrease at y/d≈0.03. At r/d=0, again for all nozzle to plate spacings, v´ remains constant up to y/d=0.2 and then begins to rise steadily as the wall is approached.

At r/d=0.5, v´ decreases to a minimum at y/d≈0.1 and then also increases as the wall is approached. For the z/d=2 case the maximum and minimum levels of turbulence vary between $0.07<v'/u_b<0.21$, at the various radial stations away from the stagnation point. This difference is less pronounced when z/d=4 and $0.08<v'/u_b<0.18$. For z/d=6 the gap closes further, $0.125<v'/u_b<0.175$, and the turbulence levels close to the wall at r/d=0.5 are the same order of magnitude to those at r/d=1.5 and r/d=2.0. This can be attributed to the

development of the jet before impingement where the mixing layers have already spread to the axis. The z/d=2 case exhibited the highest overall levels of near wall turbulence away from the stagnation point, in the region 1.5<r/d<2, despite the fact that the turbulence levels are higher for the z/d=6 case prior to impingement due to the further development of the jet. Since the turbulence levels at r/d=1.5 and r/d=2 were of similar magnitude, further experiments were conducted at r/d=1.75 and r/d=2.25, for the z/d=2 case. In order to locate where the maxima in the measured variables occurred, the maximum radial turbulence is plotted in Figure 5.28, along with the maximum radial velocity, at each radial station, for all the nozzle to plate spacings considered. The maximum velocity in the boundary layer increases up to r/d≈1.1. This radial distance indicates the edge of the stagnation region and compares well with the findings of Schrader (1961), Hrycak (1981) and the theory of Abromavich (1963). The maximum radial turbulence level occurs at r/d≈1.75 and r/d=2 when z/d=2 and z/d=4 respectively. A possible explanation is that the

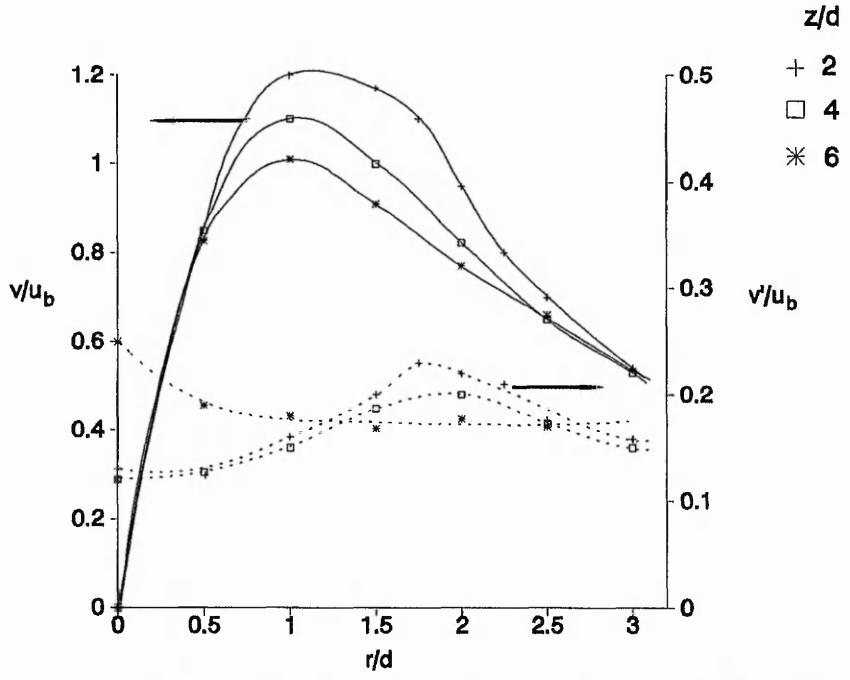

Figure 5.28. Maximum velocity and turbulence along the plate.

large eddies generated in the mixing layer, transported downstream and then deflected due to impingement, penetrate into the wall jet at this radial distance, giving rise to this maximum. This suggestion is supported by the statistical moments presented in Figures 5.7 to 5.13 where the non-Gaussian pdfs suggest a region of discrete oscillations. Reference to the heat transfer data presented in the next section in Figure 5.38, shows that this maximum coincides with a second local maximum in heat transfer. When z/d=6 however, the maximum radial level of turbulence occurs on the jet axis and reduces to a uniform level at further radial distances, which is below that in the region $1.5<r/d<2$ in the case of lower nozzle to plate spacings. Synonymously, the maximum heat transfer occurs at the stagnation point and a secondary peak does not occur. It is interesting to note that when normalised by the local velocity, the turbulence intensity would rise progressively with increasing radial distance.

5.2.5 Normal velocity, normal turbulence and shear stress profiles along the plate

The normal velocity profiles are presented in Figure 5.29 for the z/d=2 case at radial locations varying from r/d=0.5 to r/d=3.0 for $0<y/d<1.25$. At r/d=0.5, the normal velocity initially increases with a shallow gradient as the wall is approached due to the spreading of the jet, but then a sudden increase occurs due to the deflection of the jet followed by a sudden decrease where the axial momentum is transferred into radial momentum. At greater radial distances the normal velocities are near zero for $y/d>0.25$ but develop a relatively small negative velocity profile within the wall jet; the negative velocity reflects the fact that the fluid is moving away from the wall. The largest normal velocity in the wall jet occurs between r/d=1.5 and r/d=2 at approximately 0.1d from the wall.

Similarly, in Figure 5.30 the largest normal turbulence profile occurs around $r/d\approx2$, but the peak levels are only 75% of the radial turbulence levels. At the other radial stations

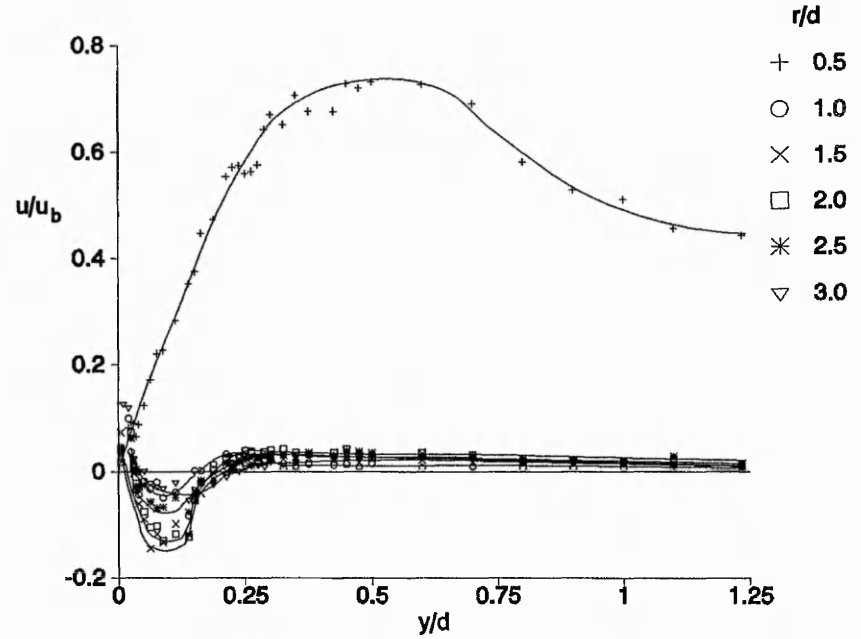

Figure 5.29. Normal velocity profiles. z/d=2.

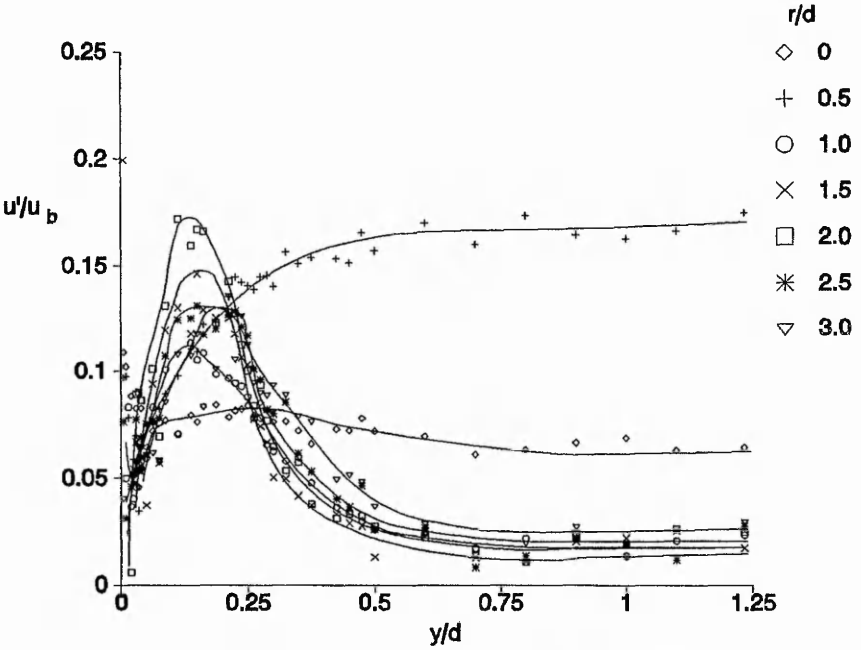

Figure 5.30. Normal turbulence profiles. z/d=2.

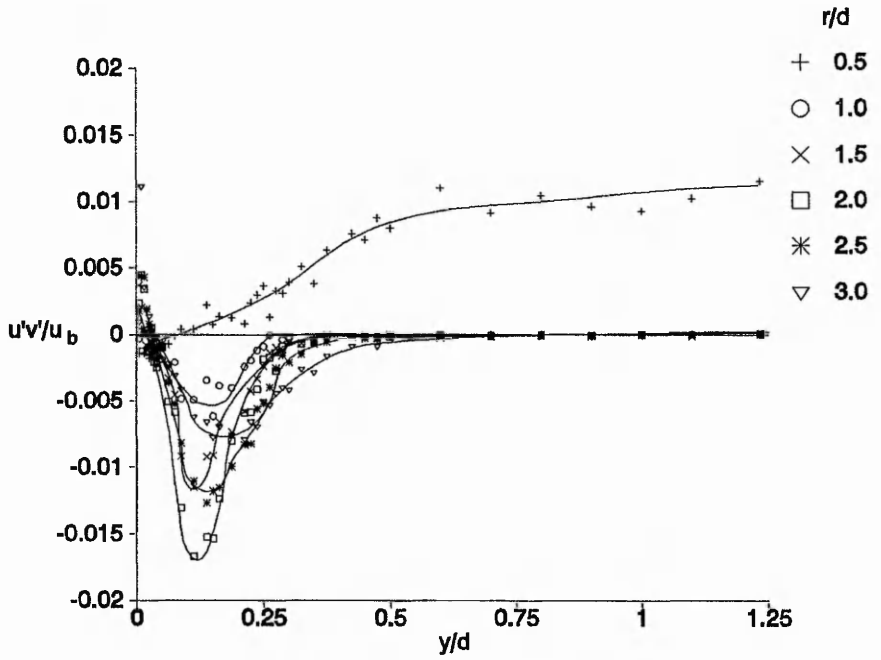

Figure 5.31. Shear stress profiles. z/d=2.

(r/d>0.5) the peak levels of normal turbulence are about 65% of the radial, which is typical of wall bounded thin shear flows. The corresponding levels of the shear stress component are shown in Figure 5.31 and the peak levels occur at the same location as the normal stresses, at r/d≈2. The shear stress is positive at the edge of the jet (r/d=0.5) and increases up to y/d=0.5 from the wall which reflects that in this region the fluid is moving radially outwards, see Ribeiro and Whitelaw (1975). The shear stress within the wall jet is also consistent with the direction of the mean velocity components in that the negative stress indicates that the flow is away from the wall. As the wall jet develops the shear stress component begins to flatten out. This coincides with the reduction in the radial velocity gradient (normal velocity gradient becomes negligible).

Figure 5.32 presents the radial distribution of the maximum levels of the normal and shear stress components close to the wall for z/d=2 and z/d=6. The z/d=2 case has two peaks in the normal stress component which occur at r/d=0.5 and r/d≈2. At r/d≈2 this is

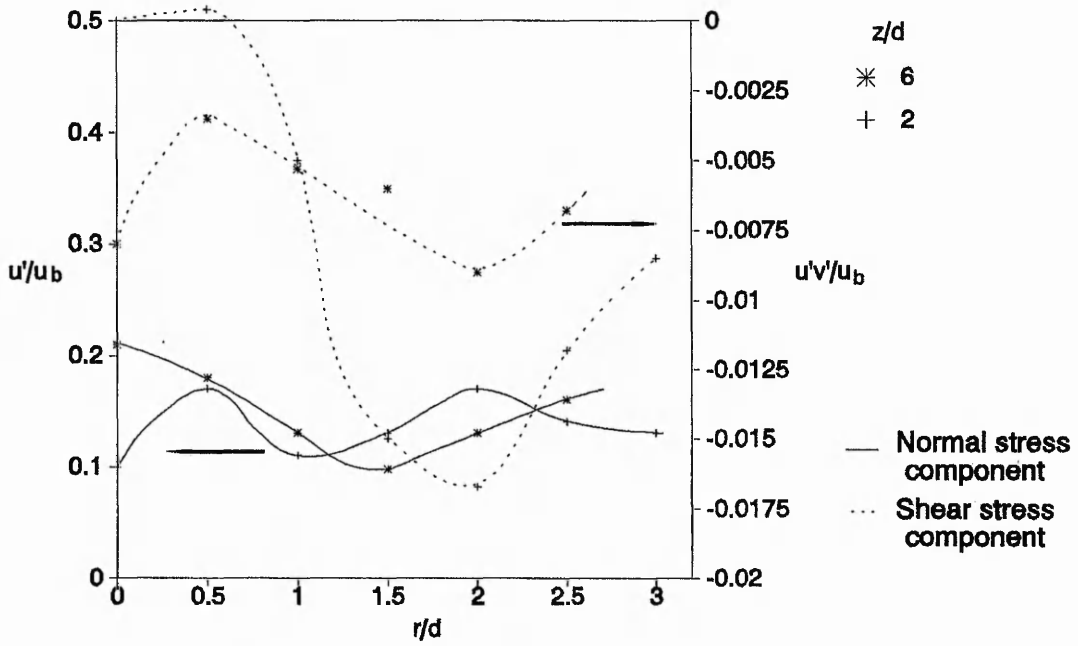

Figure 5.32. Radial distribution of maximum levels of normal and shear stress components.

accompanied by a large negative shear component. The z/d=6 case shows a normal stress component on the jet axis that is twice that in the z/d=2 case, and a minimum at r/d≈1.5. The shear component is larger at the jet axis, but lower than that at r/d≈2, when compared to the z/d=2 results.

Finally, typical profiles of the ratio of the radial stress component to axial stress component, u´/v´ are plotted in Figure 5.33. The anisotropy increases, shown by the increase in u´/v´ as the impingement plate is approached. On the axis u´ reaches twice the value of v´ at y/d≈0.25. This peak occurs for all of the radial stations investigated, but reduces in magnitude with distance from the stagnation point as the wall jet develops and the flow tends to isotropy. In the near wall region there is a linear relationship between u´ and v´ typical of boundary layer flow.

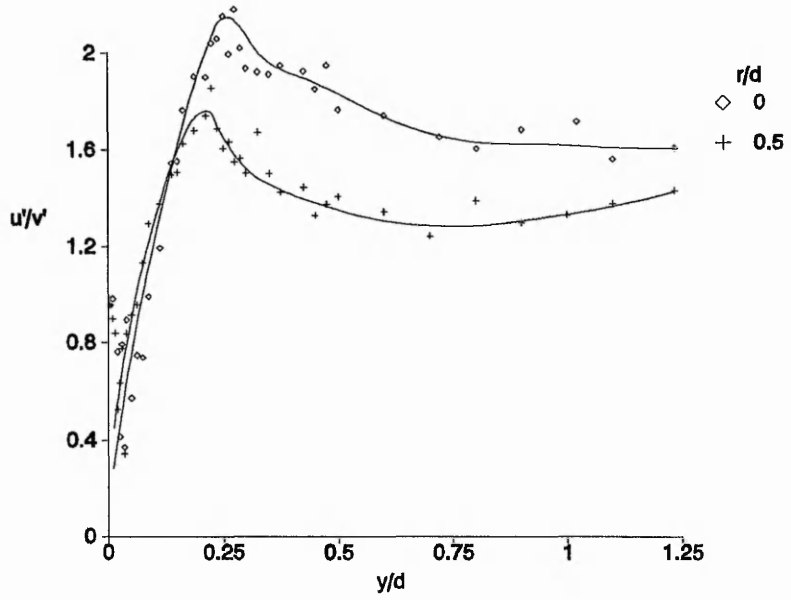

Figure 5.33. Ratio of normal stress components in the stagnation region. z/d=2.

5.3 Heat transfer results and comparison with velocity and turbulence data

The heat transfer data will be introduced by considering the isotherms recorded on video with respect to time. Quantitative results in the close vicinity of the stagnation point, r/d<1, will then be presented and discussed, and finally the results downstream in the developing radial wall jet. Heat transfer data will be related to the velocity and turbulence data presented previously, throughout the discussion where appropriate.

5.3.1 Liquid crystal isotherms

The location where the liquid crystal first changes colour indicates areas of peak heat transfer and the width of the observed isotherms gives an indication of the relative temperature gradient in that area. When z/d≤4 the liquid crystal colour change first appeared over a relatively wide annular band at r/d≈0.5, indicating an area of high heat

transfer but with low temperature gradient. This then divided into two isotherms, one of which moved towards the axis and the other became thinner and moved radially outwards indicating a sharp drop in heat transfer. For z/d=1 and z/d=2 a third isotherm appeared in the region 1.5<r/d<2 indicating a secondary maximum, which also divided into two. One of these moved towards the axis, met the second isotherm and then disappeared, and the other continued to move radially outwards while becoming wider in appearance, thus indicating a decreasing heat transfer coefficient with a shallower temperature gradient. Figures 5.34 and 5.35 present typical series of images used for analysis in the z/d=1 and z/d=6 cases respectively, and also illustrate the excellent axisymmetry, which was observed in all of the liquid crystal tests. Consequently, heat transfer data in the rest of this Chapter is shown only for 0<r/d<4.

An important observation during the tests was the location of the stagnation point. For z/d≤5, as the inner isotherm approached the jet axis before disappearing, its final location coincided with the geometric stagnation point. However, for z/d≥6 an instantaneous stagnation point occurred. Repeat tests confirmed that this phenomenon was not due to the relative location of the jet above the impingement plate. This instantaneous stagnation point was confined within the region -0.5<r/d<0.5. When the isotherm had reached a radial position of r/d≥2.5, the isotherm appeared axisymmetric about the geometric stagnation point, or at least, its deviation from axisymmetry was not discernable. As far as the author is aware, this instantaneous stagnation point has not been reported in other jet impingement heat transfer works. However, Kataoka et al. (1986) in a stroboscopic visualisation of jet impingement, using the hydrogen bubble technique, reported that the impingement region becomes doubly-periodic at the optimal nozzle to plate spacing of impingement heat transfer. They attributed this periodicity to the alternate impingement of fast and slow moving core fluids transported from the mixing layer of the jet. The observed periodicity

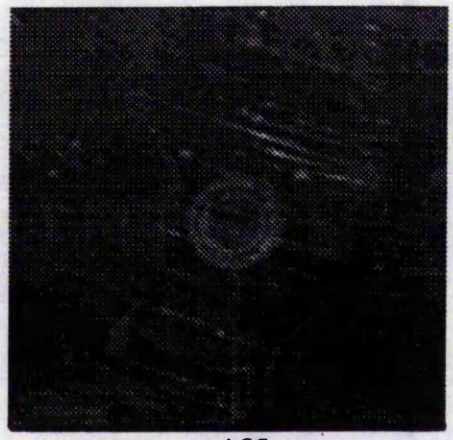

t = 4.25s.

t = 5 s.

t = 7.2 s.

t = 7.8 s.

t = 9 s.

t = 25 s.

Figure 5.34. Series of liquid crystal isotherm images. z/d=1.

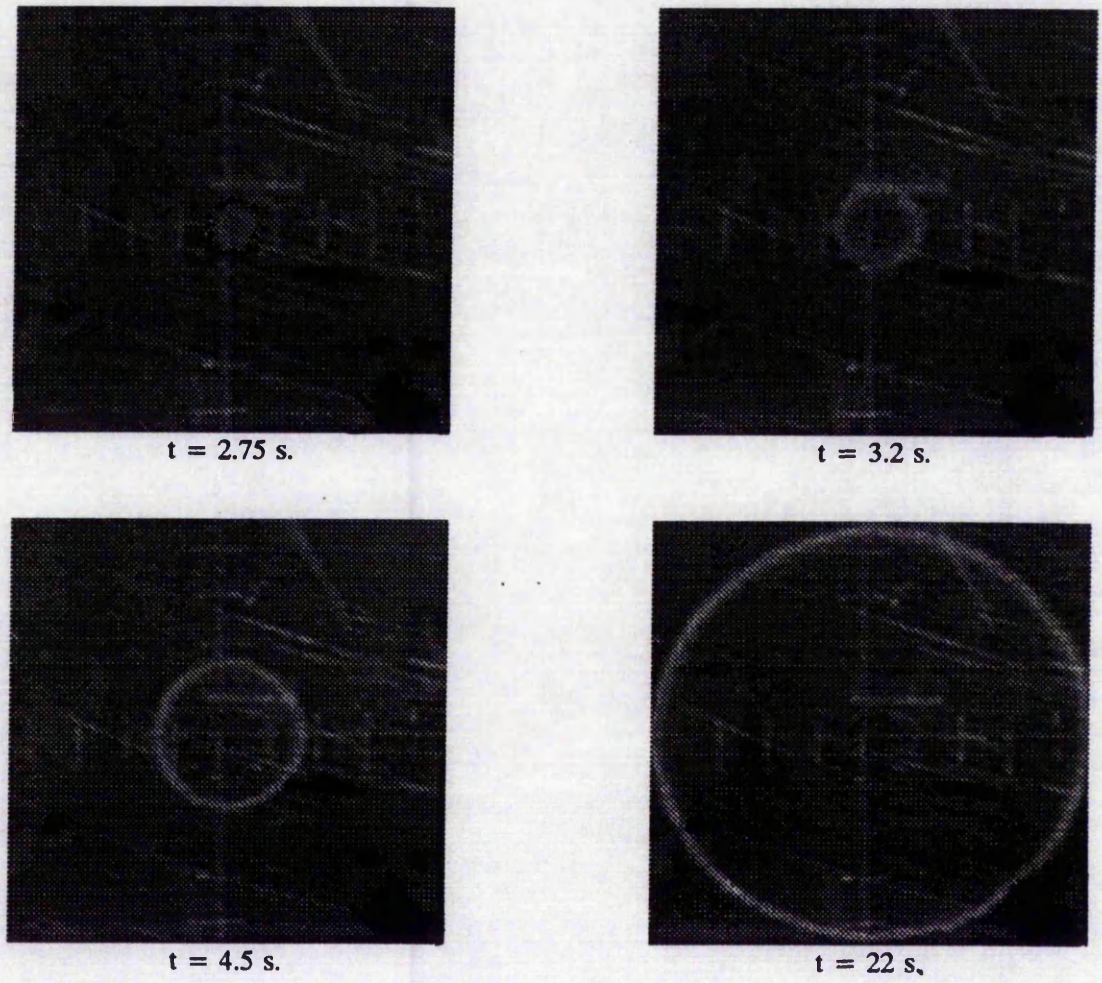

Figure 5.35. Series of liquid crystal isotherm images. z/d=6.

in the heat transfer tests of the present study complements the periodicity observed in the flow visualisation tests, reported earlier in Section 5.1.

5.3.2 Heat transfer distribution in the vicinity of the stagnation point (r/d<1)

In this Section, the effect of the jet effectiveness on stagnation point Nusselt number, Nu_0, will be discussed first followed by the variation of Nu_0 with nozzle to plate spacing. Finally, the radial distribution of the Nusselt number in the region 0<r/d<1 will be discussed.

Effect of the jet effectiveness on stagnation point Nusselt number

Recently, other workers have focused their attention on assessing the effect of the difference between the jet and ambient temperatures, and the subsequent effect on heat transfer. Goldstein et al. (1990) and later Baughn et al. (1991) established that local heat transfer data for an unheated axisymmetric jet can be used for a heated jet with entrainment if the local heat transfer coefficient is defined in terms of the local adiabatic wall temperature. The adiabatic wall temperature, T_{aw}, is the temperature that the heat transfer surface assumes when it is in equilibrium with the jet and is usually measured in a separate experiment. The use of T_{aw} in defining the Nusselt number, as opposed to using T_{jet}, can have a significant effect on the magnitude of Nu. The heat transfer data of Baughn et al. (1991) obtained for heated jets compares well with unheated jets if the above approach is used. They reported a large reduction in effectiveness (dimensionless adiabatic wall temperature) for r/d<2 in the unconfined case. However, Lucas et al. (1992) reported a higher effectiveness in the semi-confined case at low nozzle to plate spacings. The stagnation point adiabatic wall temperature was measured as discussed in Chapter 3, and is presented in terms of the effectiveness, η, in Figure 5.36.

The values of η in the present study are higher than those extracted from Baughn et al. (1991) for z/d>2. This difference can be explained by the difference in the potential core length due to geometry differences as discussed in Ashforth-Frost and Jambunathan (1994). Baughn et al. (1991) used an unconfined jet which would lead to more entrainment and a shorter potential core than in the present study so that the mixing layer would spread to the jet axis sooner, thereby reducing the jet temperature and effectiveness. The difference subsides as the nozzle to plate spacing increases beyond z/d=6 indicating the reduced effect of semi-confinement. The present results are considerably higher (5%-13%) than those of Goldstein et al. (1990) plotted using their correlation for η valid for z/d>2. Goldstein et al.

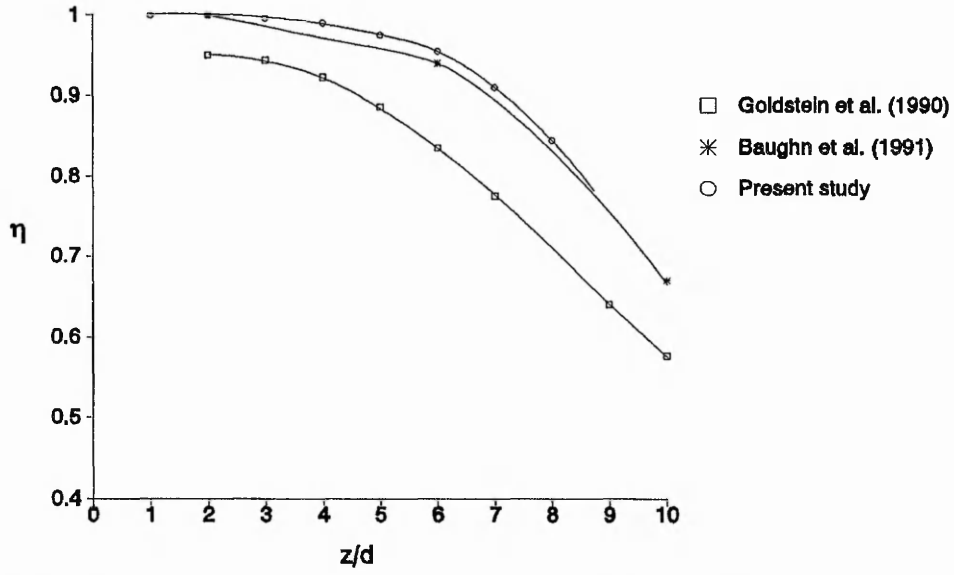

Figure 5.36. Effect of nozzle to plate spacing on the effectiveness. r/d=0.

(1990) used an ASME nozzle which produces a flatter exit velocity profile, leads to higher rates of shear at the edge of the jet, even higher entrainment rates and thus a lower effectiveness.

Variation of stagnation point Nusselt number with nozzle to plate spacing

The present stagnation Nusselt number has been recalculated using the measured adiabatic wall temperature as opposed to the jet temperature and is plotted in Figure 5.37, along with data extracted from Baughn and Shimizu (1989) and Yan et al. (1992) using an isothermal jet, and from Baughn et al. (1991) using a heated jet with Nu_0 defined using T_{aw}. This Figure shows that this definition does indeed have a pronounced effect on the heat transfer data in the present study. For z/d<3 there is less than 2% difference in Nu_0 in the present results, which can be explained by the impingement plate being placed within the potential core where T_{aw} is very close to T_{jet}. As z/d is increased further, and the mixing layer spreads to the axis, so the difference in the results increases to a maximum of 23% at z/d=7.

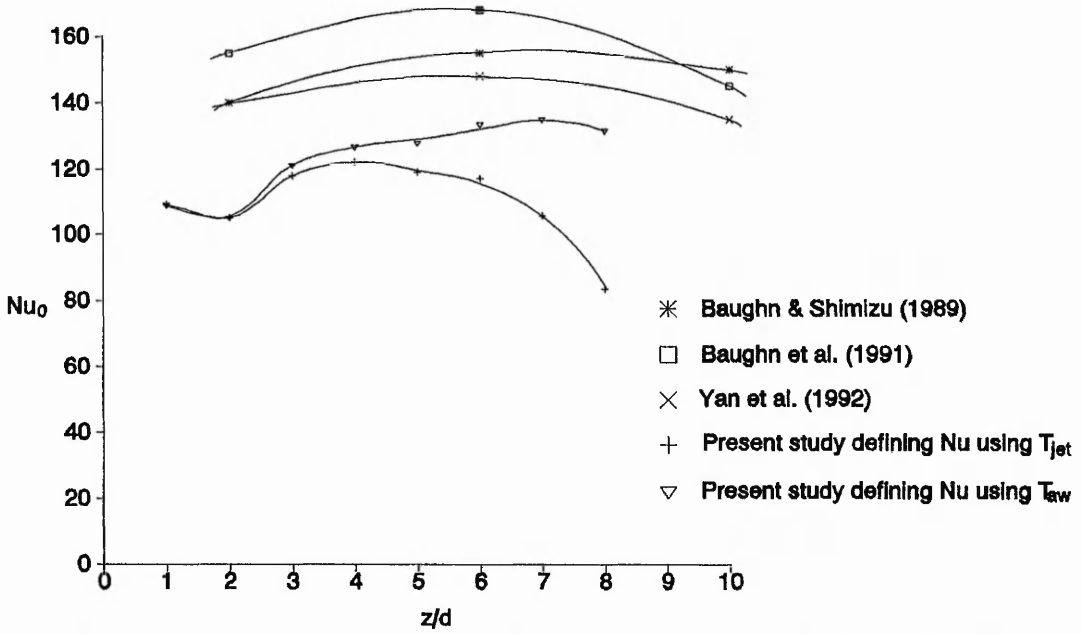

Figure 5.37. Effect of nozzle to plate spacing on stagnation Nusselt number.

As z/d increases further the comparison improves although the present results lie slightly below the other workers, again probably due to semi-confinement.

Referring again to the present results shown in Figure 5.37, as the nozzle to plate spacing is increased from z/d=1 to z/d=2, there is a 7% decrease in the stagnation point Nusselt number, Nu_0. Lytle and Webb (1991) studied unconfined jet impingement for a fully developed jet at Re=23000 and $z/d \leq 1$ and also reported significant increases in Nu as z/d was reduced. This can be attributed to increasing levels of acceleration, especially for $z/d \leq 0.25$ where the outlet area of the jet is equal to, or less than, the circumferential outlet area between the edge of the jet and the confinement plate. They also presented results for z/d=6 which compare well with more recent results by Baughn et al. (1991) and Yan et al. (1992), which strengthens their findings. Ichimiya (1993) also reported high levels of heat transfer when z/d=1.

As z/d is further increased Nu_0 begins to increase to a peak at z/d≈7 which is 30% higher than that at z/d=2. Referring to Figure 5.17, the corresponding near wall peaks of axial turbulence, u'/u_b, for z/d=2, z/d=4 and z/d=6 are 0.08, 0.09 and 0.14 respectively. Cooper et al. (1993) compared their velocity and turbulence data to that of Baughn and Shimizu (1989) and also reported an increase in Nu_0 with increase in axial turbulence levels.

Comparing the present data with that of Baughn and Shimizu (1989), Baughn et al. (1991) and Yan et al. (1992), they all show only a slight dependence of Nu_0 on z/d for $4<z/d<8$, with a peak in Nu_0 at z/d=6. The present data shows a similar dependence in the range $3<z/d<7$, but a much lower value of Nu_0 at z/d=2 that is attributed to the effect of semi-confinement which, at low nozzle to plate spacings, severely limits the amount of entrained air. At z/d=2 Nu_0 of the semi-confined case is only 75% of that of the unconfined case. By z/d=6 the above ratio has increased to 80% and increases further as the nozzle to plate spacing is increased, and the effect of semi-confinement reduces. Obot et al. (1982) also reported a significant difference between heat transfer data for the unconfined and semi-confined cases for a short nozzle up to z/d=8. The peak in Nu_0 towards z/d=7 in the present study as opposed to z/d=6 as observed by the other workers is attributed to the longer potential core caused by the jet impingement geometry.

Radial variation of Nusselt number in the region $0<r/d<1$

Figure 5.38 shows the Nusselt number, defined using T_{jet}, as a function of the radial distance from the stagnation point for $1<z/d<8$. The local peaks in heat transfer lead to high average surface heat transfer coefficients. Despite the dependence of Nu_0 on $Re^{0.5}$ reported by many authors and correlated by Jambunathan et al. (1992) for the region $r/d<0.5$, the flow is not laminar in this region; the turbulence of the flow is illustrated in Figures 5.19 and 5.21 which show clear evidence of near wall turbulence in the stagnation region for z/d=2.

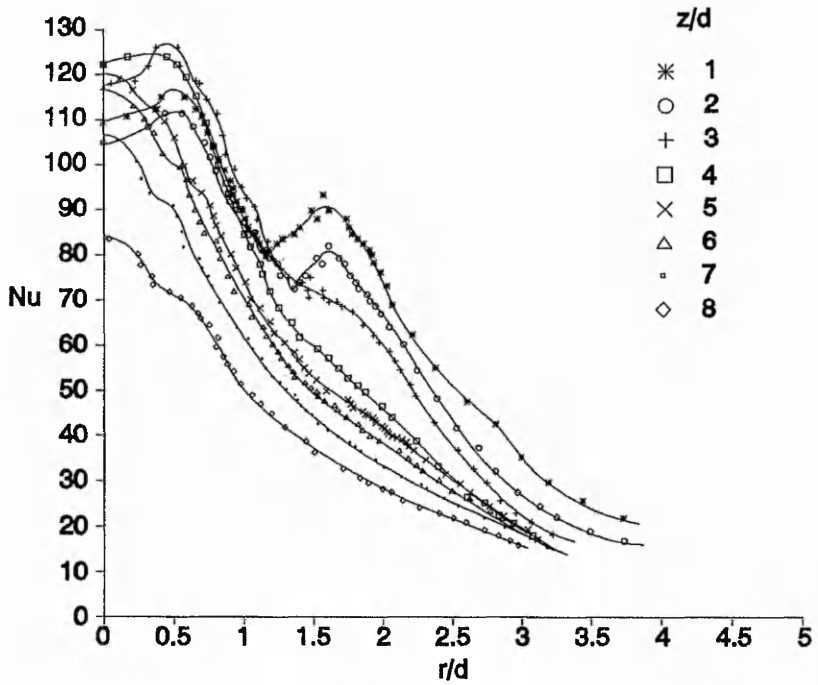

Figure 5.38. Radial distribution of Nusselt number.

The laminar-like dependence on Re can be explained by the thermal boundary layer in the stagnation point being confined within the viscous sublayer, as pointed out by Craft et al. (1993). Any thinning of the boundary layer at r/d=0.5 could not be discriminated from the present results, such that no support can be offered to the theoretical finding of Kezios (1956) that this maximum is due to such a phenomenon. There is however, clear evidence of turbulent motions at this location (see Figure 5.32).

For z/d<5 there is a slight minimum in Nusselt number at the stagnation point accompanied by a maximum at r/d≈0.5. As z/d increases from 1 to 5 this maximum moves towards the axis from r/d=0.5 to r/d=0.1 and then disappears, or at least cannot be differentiated for z/d>5, so that a maximum now occurs at the stagnation point. This coincides with the length of the potential core of the jet discussed previously. From Figures 5.28 and 5.32, in the z/d=2 case, the maximum radial turbulence near the wall at r/d=0.5 is similar to that at r/d=0 but the axial component is 70% larger. The z/d=4 case shows a similar

phenomenon. Conversely, in the z/d=6 case, not only is the axial turbulence high compared to the z/d=2 case at the stagnation point, but the radial turbulence is higher at r/d=0 than at r/d=0.5. This maximum is therefore attributed directly to near wall turbulence. The radial movement of this peak towards the axis can be related to the development of the mixing layer, which for z/d>5 has spread fully to the jet axis. The same phenomenon was not observed by Baughn and Shimizu (1989), Baughn et al. (1991) and Yan et al. (1992) from the same laboratory, for their fully developed (l/d=72) unconfined jet at Re≈23000. Obot et al. (1982) however, reported distinct minima at the stagnation point using a short nozzle (l/d=1) for both the unconfined and semi-confined case. Ichimiya (1993) also studied the semi-confined jet at Re=20000 and z/d=1. The nozzle exit geometry is undefined in this work but the diagram suggests a near fully developed jet exit profile. The heat transfer data is also difficult to interpret due to contour presentation and asymmetry of the jet, but a slight minimum at the stagnation point can be observed, and maxima were reported at r/d=0.5 and r/d=2. This suggests that the present results differ from those of Baughn's, due to the smooth entrance to the nozzle 22d upstream as opposed to the 72d nozzle used by Baughn's research group. This is supported by Obot et al. (1979). Although the maximum nozzle length they investigated only extended to 50d, they showed that the minimum at the stagnation point becomes less pronounced, and less dependent on nozzle entrance geometry, as the length of the nozzle increases. Obot (1980) also showed that the streamwise turbulence intensity in a pipe flow continues to develop long after the mean flow becomes fully developed. The suggestion of Popiel and Trass (1991) that in a short nozzle a laminar layer forms on the wall of the nozzle between the jet and ambient air causing the development of strong vortices, may help to explain this peak at r/d=0.5; as the nozzle length is increased and the jet develops a turbulent boundary layer, thereby generating weaker vortices which will result in less mixing. In Baughn's nozzle, the ratio in turbulence at the axis, to the edge of the jet, may have been higher than in the present case.

Moving radially outwards from r/d≈0.5 up to r/d=1, the Nusselt number decreases monotonically for all nozzle to plate spacings.

5.3.3 Heat transfer distribution downstream of the stagnation point (r/d≥1)

Again referring to Figure 5.38, moving away from the jet axis the Nusselt number begins to decrease. Where the jet impinges onto the plate within the potential core (z/d<4) a secondary maximum in heat transfer occurs. The maximum is largest in magnitude for z/d=1 and is 85% of the corresponding Nu_0. At z/d=2 the peak has reduced but is still 80% of Nu_0. By z/d=3 the peak is noticeable, but has almost disappeared by z/d=4. The peak is unlikely to be due to transition from laminar to turbulent flow as it has already been demonstrated that the flow is turbulent before impingement and in the stagnation region. Prior to the secondary maximum, a local minimum occurs at r/d=1.15 and r/d=1.3 for the cases of z/d=1 and z/d=2 respectively. Referring to Figure 5.25 it can be seen that in the z/d=2 case this minimum coincides with the position of maximum radial velocity along the plate where velocity gradients are shallow and the local turbulence intensity in this area will be relatively low. For the z/d=2 case the secondary peak occurs at r/d≈1.7. We can also see from Figures 5.28 and 5.32, that the maximum radial, normal and shear stress components occur in the range 1.5<r/d<2, again associating the heat transfer distribution and the near wall turbulence stress levels discussed in the earlier sections. In Figure 5.25, the radial turbulence level was presented in smaller radial increments and confirms that the maximum occurs somewhere between r/d=1.5 and r/d=2.

At all nozzle to plate spacings, as the radial distance increases further (r/d>2) the heat transfer profiles decrease monotonically with distance from the stagnation point and by r/d=4 have developed very shallow gradients which corresponds to developed flow. At larger radial distances the heat transfer becomes less dependent on the nozzle to plate

spacing.

5.4 Concluding remarks

Qualitative flow visualisation has been carried out to gain an insight into the semi-confined jet impingement flow field. Quantitative measurements of velocity and turbulence and surface convective heat transfer coefficient have been made using laser-Doppler anemometry and liquid crystal thermography respectively, and provide new data for the semi-confined geometry. The consistency and dependability of the results has been demonstrated by comparison with other authors works.

The flow field of the semi-confined impinging jet at a Reynolds number of 20000 and nozzle to plate spacing of 2d has been characterised using the above data, with comparison with some additional data obtained at higher nozzle to plate spacings where appropriate. Particular attention has been paid to the near wall mean velocity and turbulent components of the Reynolds stresses.

The flow visualisation has shown the semi-confined jet impingement flow at a Reynolds number of 20000 and nozzle to plate spacing of 2d to be characterised by a series of counter rotating vortices, with the centre of the primary vortex occurring at $r/d \approx 7$. As the nozzle to plate spacing is increased the primary vortex moves further downstream into the wall jet.

Periodicity was observed in the flow at nozzle to plate spacings of $z/d \geq 6$ during the flow visualisation tests which would explain the occurrence of an instantaneous stagnation point observed in the liquid crystal tests, again for $z/d \geq 6$.

The nozzle exit conditions have been described and symmetry demonstrated to enable the

tests to be replicated and the results to be used as input boundary conditions to a numerical model, for validation of that model by comparison with the experimental results in the stagnation region.

Probability density functions and skewness and kurtosis have been used to provide a further insight to the flow field by identifying regions of high shear and intermittency, indicated by high values of skewness and kurtosis respectively, which coincide with high gradients of mean velocity and turbulence intensity.

At a nozzle to plate spacing of 6d, the presence of the impingement plate has been shown to lead to an extension of the potential core length from 4.6d to 4.9d, based on a 95% criterion.

The axial and radial near wall distributions of the normal and shear Reynolds stress components have been described in detail. The flow has been shown to be anisotropic in the stagnation region, with a return to isotropy as the wall jet develops. The distribution of the Nusselt number at the same nozzle to plate spacings has been related to the Reynolds stress components and a direct link between turbulence and heat transfer maxima identified.

The Nusselt number can be defined using either the jet temperature or the adiabatic wall temperature, and for $z/d \geq 3$ this definition has a pronounced effect on the magnitude of the Nusselt number. The jet effectiveness (dimensionless adiabatic wall temperature) at the stagnation point has been shown to be marginally higher for the semi-confined jet than the unconfined jet when $z/d \geq 3$ and is attributed to the longer potential core of the present study which is largely dependent on the nozzle length and effect of semi-confinement. Beyond the potential core the difference in the effectiveness subsides and indicates the reduced

effect of semi-confinement. The stagnation point Nusselt number, Nu_0, has been shown to be unaffected by its definition when $z/d \leq 2$, but increasingly affected as z/d increases. When defined by the jet temperature, the maximum value of Nu_0 occurs at $z/d \approx 4$ whereas when the adiabatic wall temperature is used, the maximum value occurs at $z/d \approx 7$.

The Nusselt number distributions at a Reynolds number of 20000 and nozzle to plate spacings in the range $1 \leq z/d \leq 8$ have been described. The connection between the local maxima in heat transfer and the maximum Reynolds stresses will now be summarised. When defined by the adiabatic wall temperature, the maximum stagnation point Nusselt number occurs when the impingement plate is placed downstream of the potential core near to $z/d=7$, and corroborates the well known findings of other authors discussed in Chapter 2. This maximum is attributed to high axial, radial and shear turbulence components of the Reynolds stress. At a nozzle to plate spacing of $z/d=6$, the axial component has been shown to be approximately twice that when $z/d=2$, and the radial component has been shown to be 50% greater than that at $z/d=2$.

The peak stagnation point heat transfer occurs at a larger nozzle to plate spacing than in the unconfined case due to the extended potential core which results from the effect of semi-confinement.

When $z/d<5$ a local minimum in Nu occurs at the stagnation point accompanied by a local maximum at $r/d \approx 0.5$. This peak moves towards the axis as z/d increases until by $z/d=6$ it cannot be differentiated and the maximum Nu now occurs at the stagnation point as described above. The local maximum at $r/d \approx 0.5$ is again related directly to turbulence since the axial component of the Reynolds stresses is 70% higher than that at the stagnation point.

The differences in the heat transfer distributions compared to other authors who have used a fully developed jet (eg. Baughn et al., 1991) have been explained by differences in nozzle and jet impingement geometries, substantiated by the findings of other workers such as Obot et al. (1979, 1982) and a related study by Ashforth-Frost and Jambunathan (1994). The length of the potential core is extended due to the effect of semi-confinement which severely limits entrainment, and a fully developed velocity profile which results in a lower shear and less mixing. In addition, even when the mean velocity profile appears fully developed, the turbulence continues to increase such that a higher level of axial turbulence will develop the longer the nozzle length. This may explain the maximum heat transfer appearing at the stagnation point for a very long nozzle (70d) as opposed to that at $r/d \approx 0.5$ for a shorter nozzle (22d).

For $z/d<4$ a minimum in heat transfer occurred in the region $1.2<r/d<1.5$ followed by a secondary maximum in the region $1.5<r/d<2$. The secondary maximum decreases in magnitude and moves radially outwards as z/d is increased. Despite high absolute values of turbulence, the minimum has been shown to coincide with maximum radial velocities which leads to lower levels of local turbulence intensity. The secondary maximum has been attributed to a laminar to turbulence transition by earlier workers, but the present data has shown clear evidence of near wall turbulence at the stagnation point. This peak is therefore attributed to the maximum values of all of the turbulence components of the Reynolds stresses, which occur in the same region, $1.5<r/d<2$. By $z/d=5$, this peak had disappeared.

At all nozzle to plate spacings, the heat transfer profiles decrease monotonically with distance from the stagnation point ($r/d>2$) and by $r/d=4$ have developed very shallow gradients which corresponds to developed flow.

CHAPTER 6

PRESENTATION AND DISCUSSION OF NUMERICAL RESULTS

In this Chapter the results of the numerical simulation of semi-confined jet impingement at a Reynolds number of 20000 and nozzle to plate spacing of 2d will be discussed and compared to results from the experimental measurements. The inlet boundary conditions to the numerical model were specified using the measured velocity and turbulence profiles presented in Chapter 5. The high Reynolds number version of the kappa-epsilon (k-ϵ) eddy viscosity model of turbulence has been used which is available as a standard option in the commercial software PHOENICS. The k-ϵ model assumes local isotropy and has been described in detail in Chapter 4. Good reviews of various forms of turbulence models have been provided by Rodi (1980) and Abbott and Basco (1984). Reynolds stress models solve transport equations for the individual Reynolds stresses and are said to give anisotropy. However, they are comparatively expensive of computing time. Both the k-ϵ model and Reynolds stress models have predicted a wide variety of flows to reasonable accuracy. However, despite the expectation that the Reynolds stress models would improve the prediction of impinging flows, evidence to date reveals that this only happens when specific near wall models are used, Launder (1991), which at present are not widely available. Consequently, the k-ϵ model is most often adopted due to its simplicity and economy over the second-moment closure models. This combined with the fact that the k-ϵ model was available for several years before the Reynolds stress models, has resulted in it being adopted as a standard option in most commercial packages and subsequent frequent use in both academia and industry. For these reasons, the assessment of the k-ϵ model in predicting turbulent jet impingement was undertaken in this investigation.

6.1 Qualitative results

To gain a qualitative indication of the velocity and turbulent quantities within the simulated flow field, velocity streamlines and contours of the turbulent kinetic energy, k, its dissipation

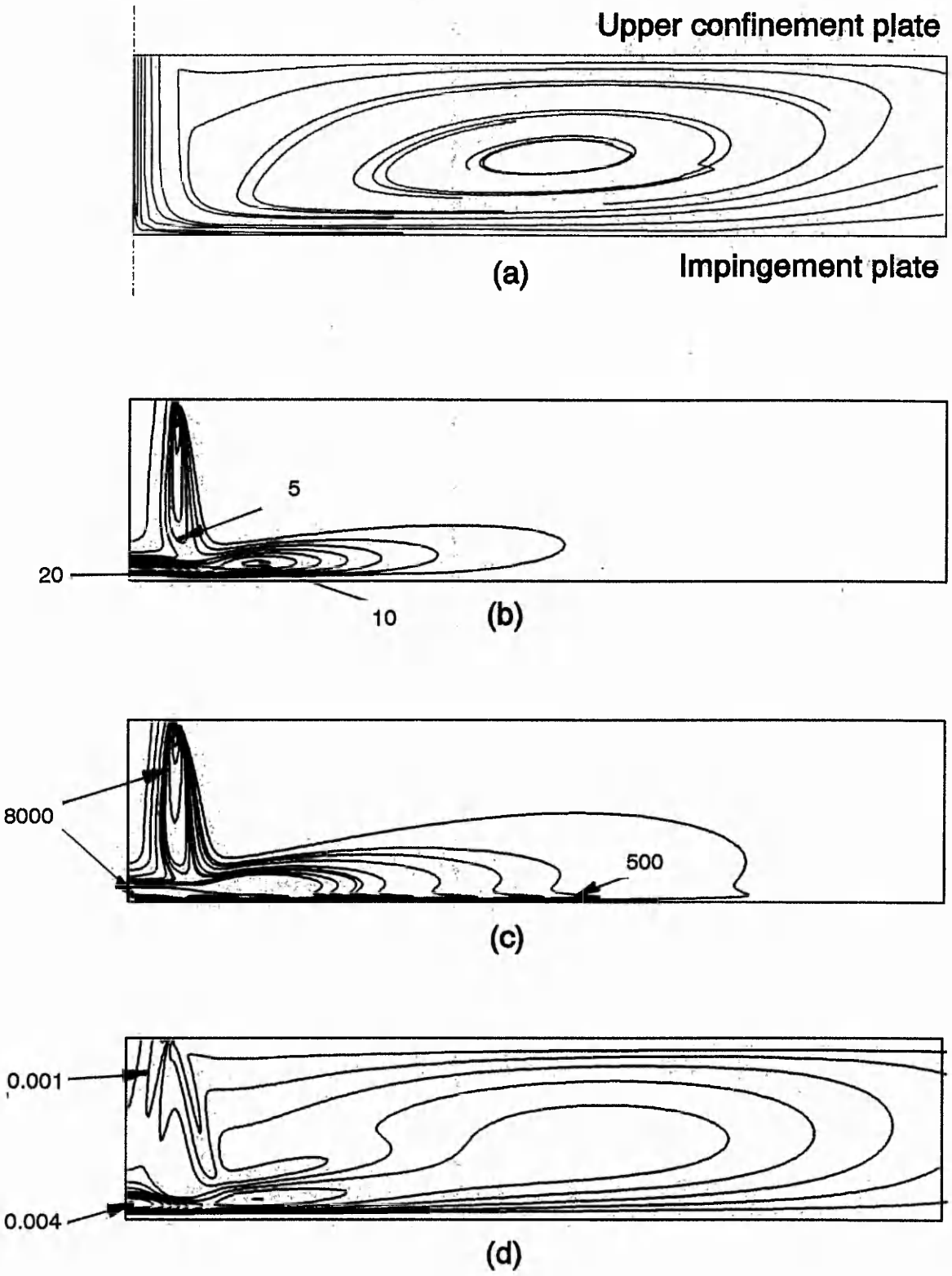

Figure 6.1. Qualitative numerical results: (a) velocity streamlines, (b) turbulent kinetic energy, k, (c) dissipation rate of k, ϵ (d) turbulent kinematic viscosity ν_t.

rate, ϵ and the turbulent kinematic viscosity, ν_t are presented in Figure 6.1.

The position of the centre of the primary recirculation compares well with the experimental results shown in Figure 5.1(b), and the model has shown that it can predict the large scale characteristics of the mean flow well. However, the streamlines in Figure 6.1(a) also show that the numerical model is unable to capture the smaller scale eddies and near wall wavy streamlines.

As to be expected, the highest levels of the turbulent quantities, k, ϵ and ν_t occur in the mixing layer of the impinging jet, directly beneath the impinging jet in the stagnation region, and in the wall jet, close to the wall ($y/d<0.25$), up to $r/d=2$. At a first glance, the model appears to have predicted the qualitative trends satisfactorily. It will be shown in the next Section that the predicted values are excessively high in the stagnation region, which will lead to incorrect prediction of the Reynolds stress components.

6.2 Velocity and turbulence profiles

Figure 6.2 shows the numerical prediction of the decay of the axial velocity compared with experiment. The correlation is excellent along the entire axis.

The turbulent kinetic energy has been calculated using $k=\frac{1}{2}(u'^2+v'^2)$ according to Shaw (1992). The computed turbulent kinetic energy and radial velocity profiles at $r/d=0.5$ and $r/d=2.5$ show agreement with those of several other workers obtained recently using the k-ϵ eddy viscosity model at $z/d=2$ and $Re=23000$, reviewed in Cooper et al. (1993), further indicating the consistency of the present results using this commercial package. The envelope of the predictions reported by Cooper at el. (1993) have been compared with the present results in Figures 6.3 and 6.4.

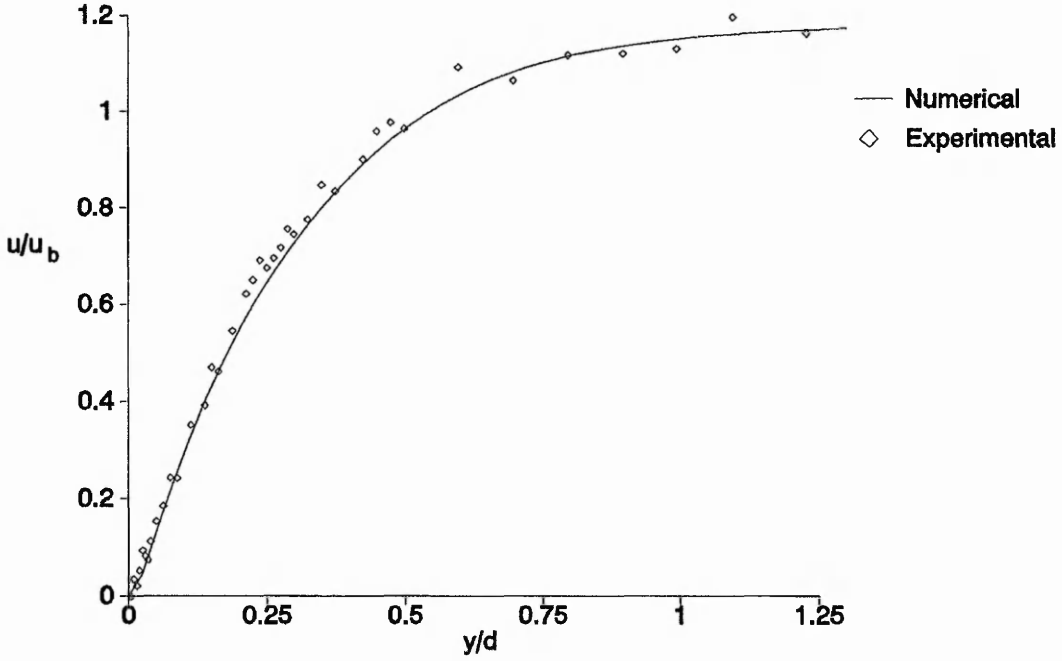

Figure 6.2. Axial velocity decay. Re=20000. z/d=2.

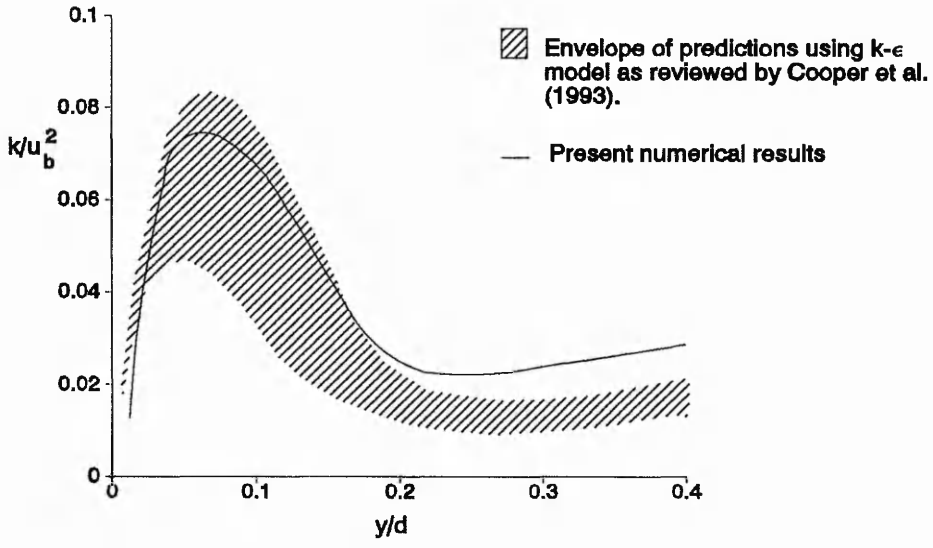

Figure 6.3. Comparison of typical predicted turbulent kinetic energy profile with other authors. r/d=0.5. z/d=2.

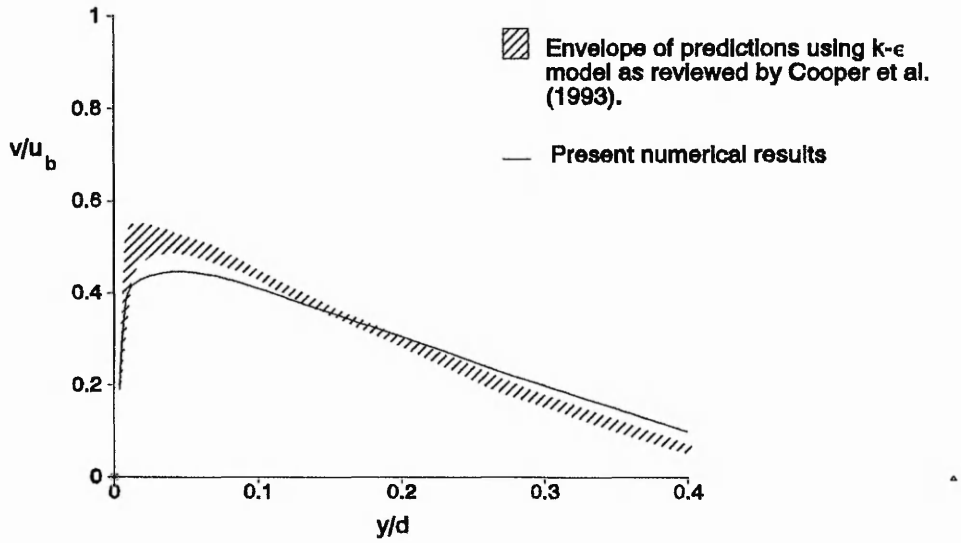

Figure 6.4. Comparison of typical predicted radial velocity profile with other authors. r/d=2.5. z/d=2.

Further comparisons are made of the variation of radial velocity profiles and, axial and radial, turbulent kinetic energy profiles with distance from the plate, in Figures 6.5 to 6.10 and Figures 6.11 to 6.17 respectively.

The numerical model predicts the correct trends in the radial velocity profiles in that the radial velocity develops to a maximum at r/d≈1 and then reduces as the wall jet develops. The near zero radial velocities for y/d>0.75 are also correctly predicted. However, the spreading rate is underpredicted at all radial stations (maximum velocities underpredicted by 12% at r/d=0.5, 25% at r/d=1 and 40% at r/d=2). At r/d=0.5 the computed profile compares reasonably well with the experimental profile, but as the jet develops further the wall jet is too thick; in the experimental results the velocity increases below y/d<0.25 whereas in the numerical results, the velocity begins to increase at y/d≈0.5. For r/d≥2.5 the predicted profiles improve progressively with radial distance; the difference being 25% by r/d=3.

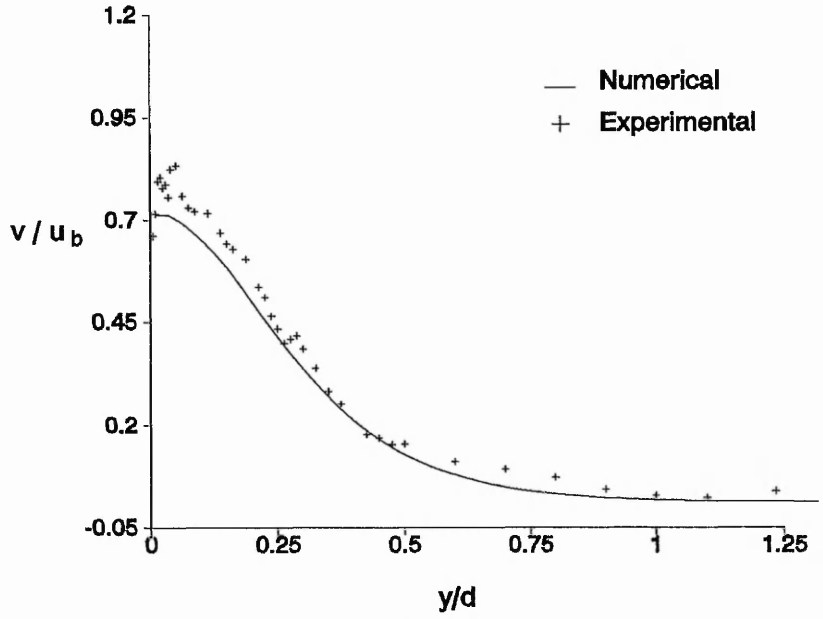

Figure 6.5. Radial velocity profile, r/d = 0.5.

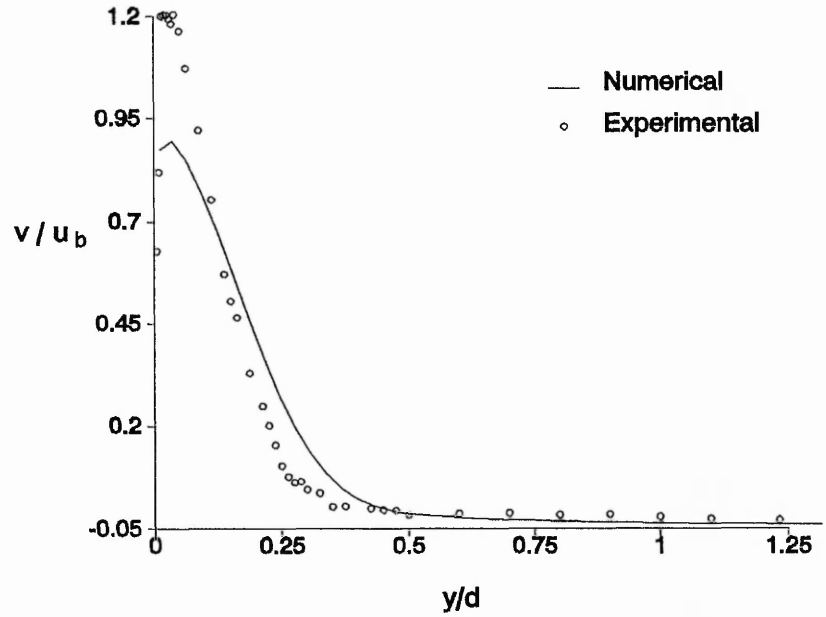

Figure 6.6. Radial velocity profile, r/d = 1.0

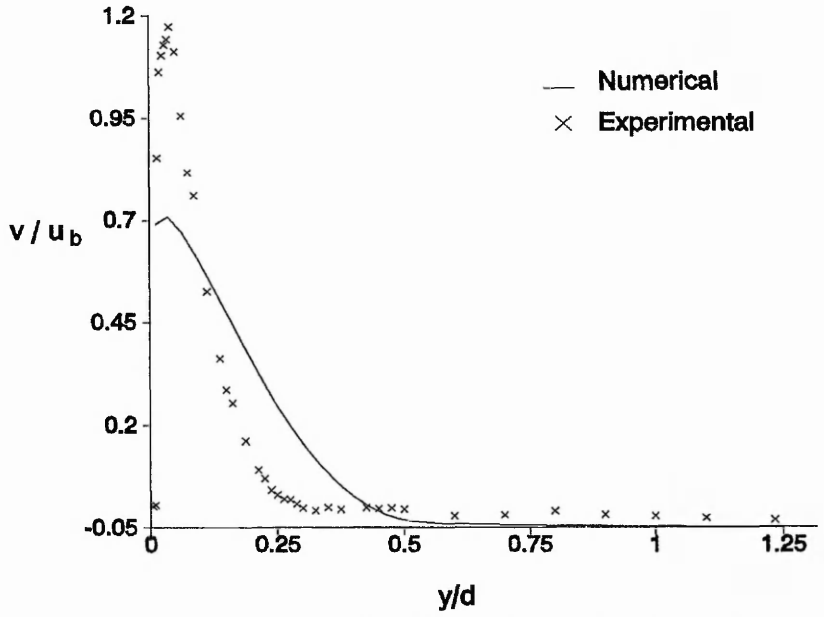

Figure 6.7. Radial velocity profile, r/d = 1.5.

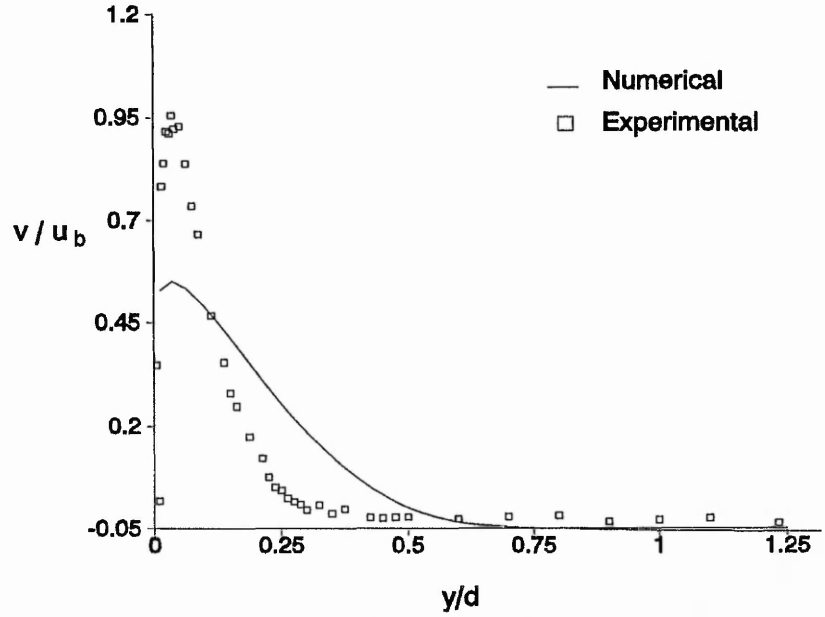

Figure 6.8. Radial velocity profile, r/d = 2.

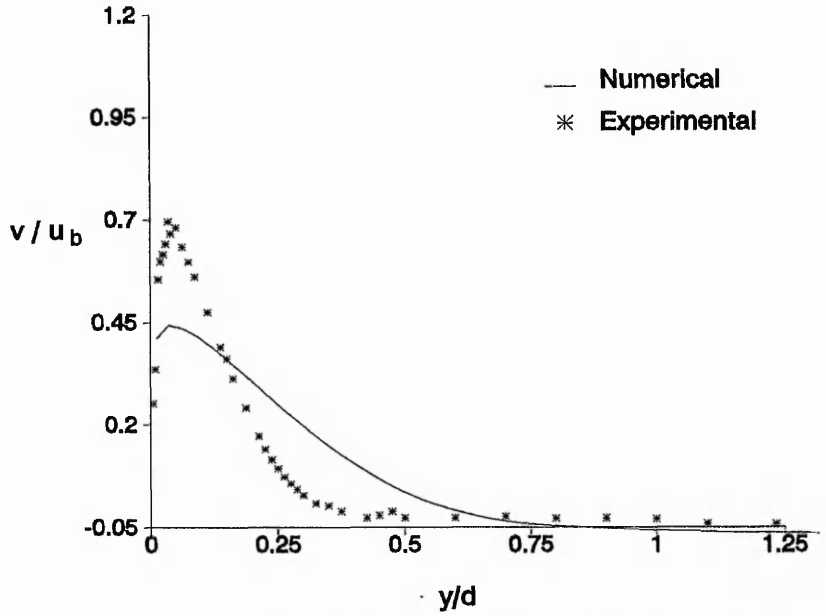

Figure 6.9. Radial velocity profile, r/d = 2.5.

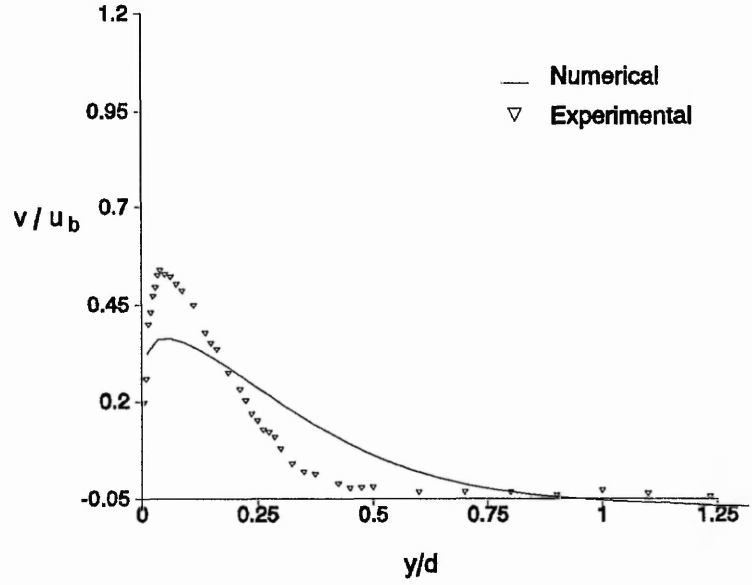

Figure 6.10. Radial velocity profile, r/d = 3.

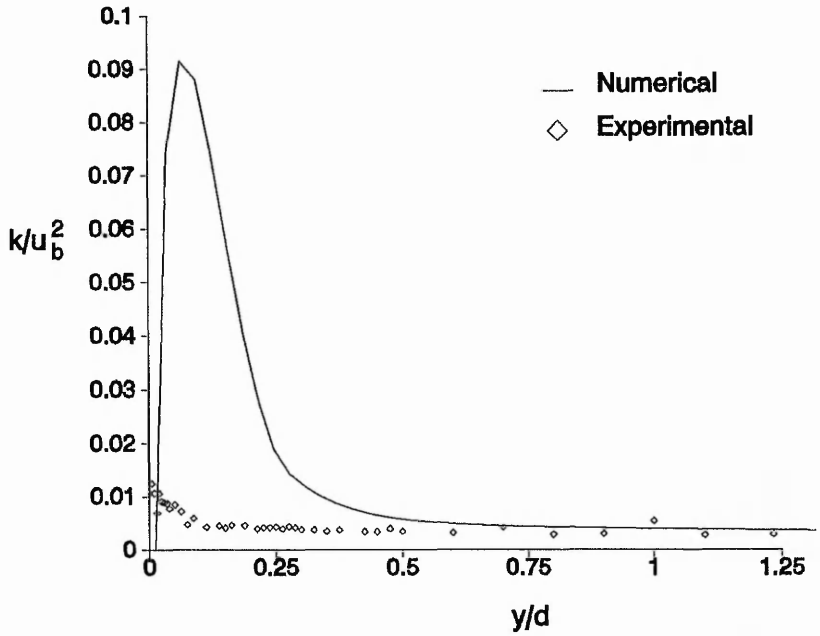

Figure 6.11. Turbulent kinetic energy profile, r/d = 0.

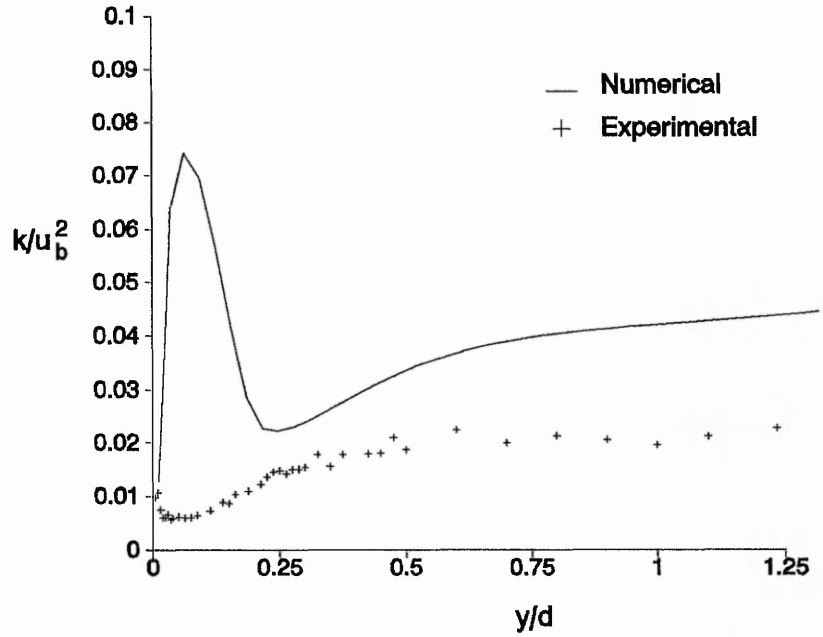

Figure 6.12. Turbulent kinetic energy profile, r/d = 0.5.

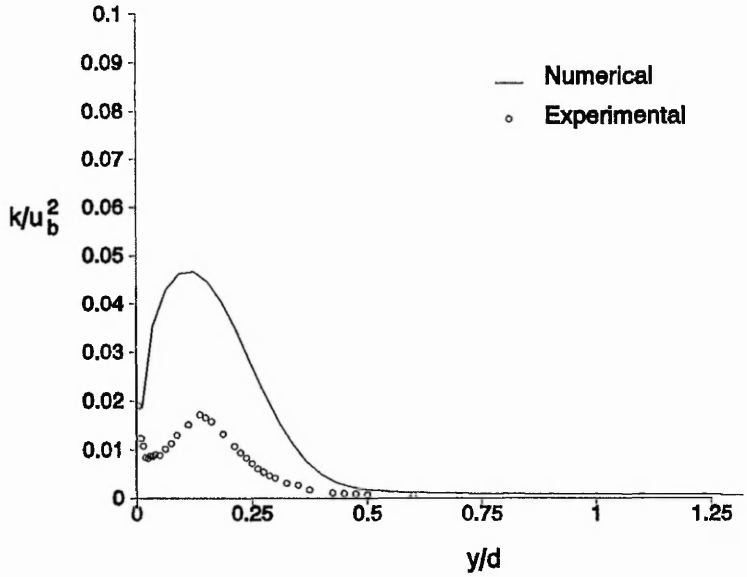

Figure 6.13. Turbulent kinetic energy profile, r/d = 1.

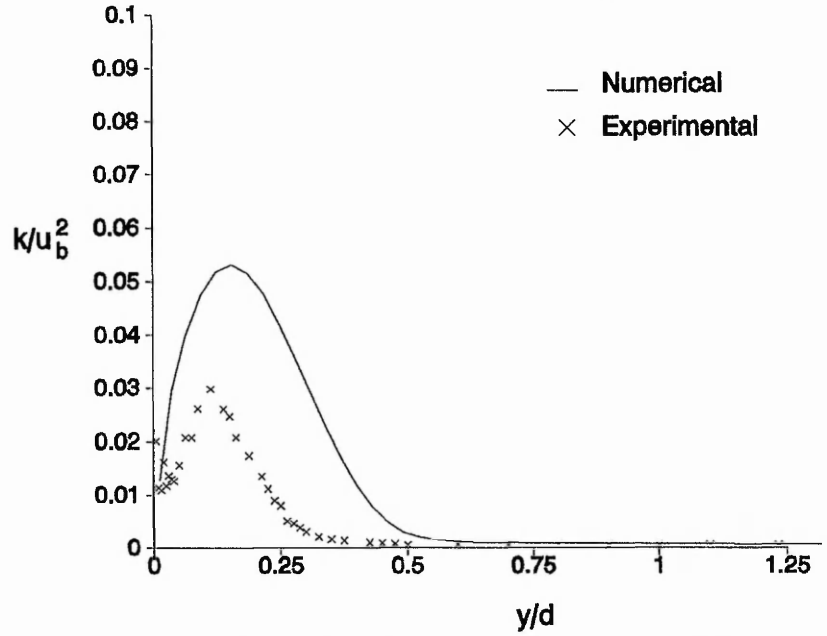

Figure 6.14. Turbulent kinetic energy profile, r/d = 1.5.

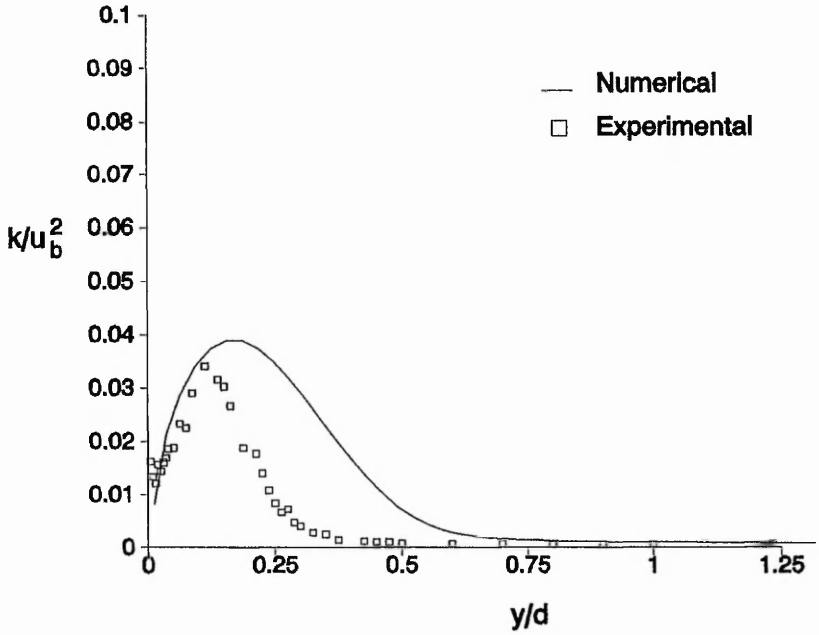

Figure 6.15. Turbulent kinetic energy profile, r/d = 2.

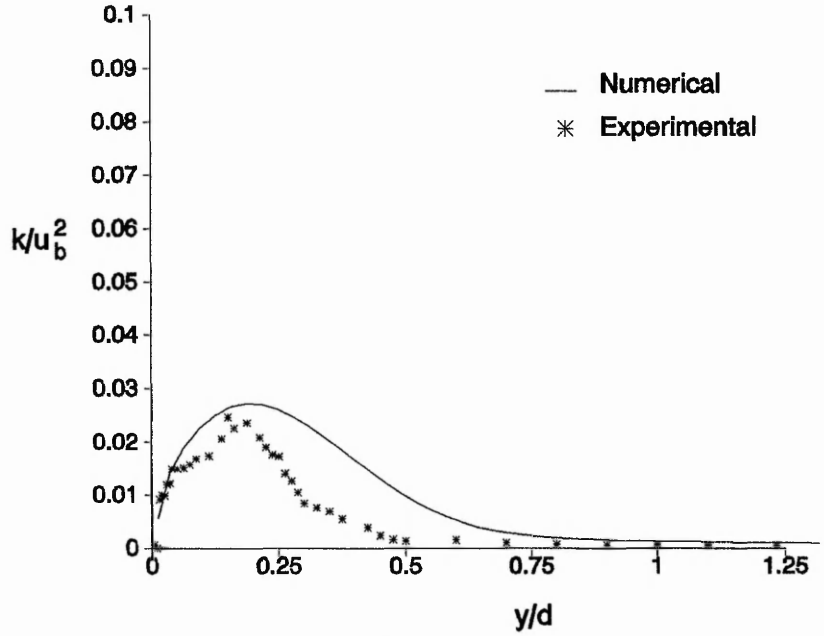

Figure 6.16. Turbulent kinetic energy profile., r/d = 2.5.

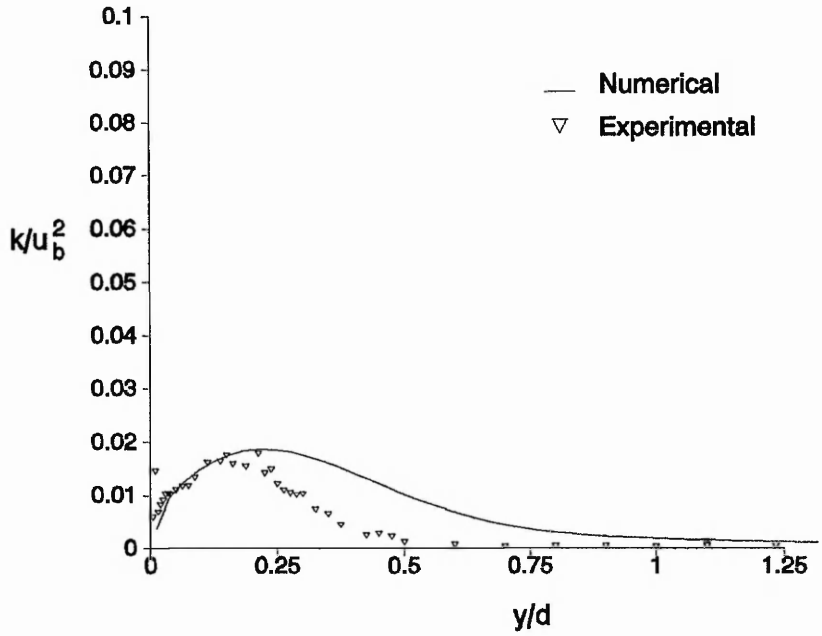

Figure 6.17. Turbulent kinetic energy profile, r/d = 3.

The correct trends in the development of the turbulent kinetic energy, k, are reasonably predicted out of the stagnation region when r/d≥1, and for y/d>0.75 the magnitudes of k are also well predicted. Poor comparison of the numerical and experimental results only occurs in the stagnation region. The turbulent kinetic energy is grossly overpredicted on the jet axis, with the peak computed value being nine times the experimental value. The prediction improves progressively downstream and by r/d=3, a reasonable comparison exists; the peak value being within 10% of experiment. It is this overprediction of k that leads to higher entrainment than is the actual case. This extra entrainment of the free stream fluid leads to the underprediction of the peak radial velocities and the wall jet appears too thick. The overprediction of k will lead to incorrect values of the individual turbulent stresses, since the eddy-viscosity concept described in Chapter 4 is used to calculate all the stress components. Boussinesq's eddy viscosity concept implies that turbulence is isotropic. Inspection of Figure 5.33 shows that in the stagnation region the flow is anisotropic which cannot be accounted for by the numerical model.

6.3 Heat transfer distribution along the plate and the effects of the numerical model

The radial distribution of the computed Nusselt number is compared with experiment in Figure 6.18. In the wall jet, r/d≥3, the Nusselt number is predicted to within 20% of the experimental values. At the stagnation point however, Nu_0 is overpredicted by over 300%. In the developing wall jet (r/d>3) the comparison gradually improves and by r/d=3 the computations compare well with experiment. The turbulence models and wall functions have been developed for flows parallel to walls where isotropy prevails. It has been shown in Chapter 5 that when the flow impinges on the wall, the wall exerts an effect on the distribution of the turbulence levels such that the flow in the stagnation region is anisotropic, with a return to isotropy further downstream. In addition, the k-ϵ model is only valid for high Reynolds numbers so that the flow characteristics near to the wall will not be simulated correctly.

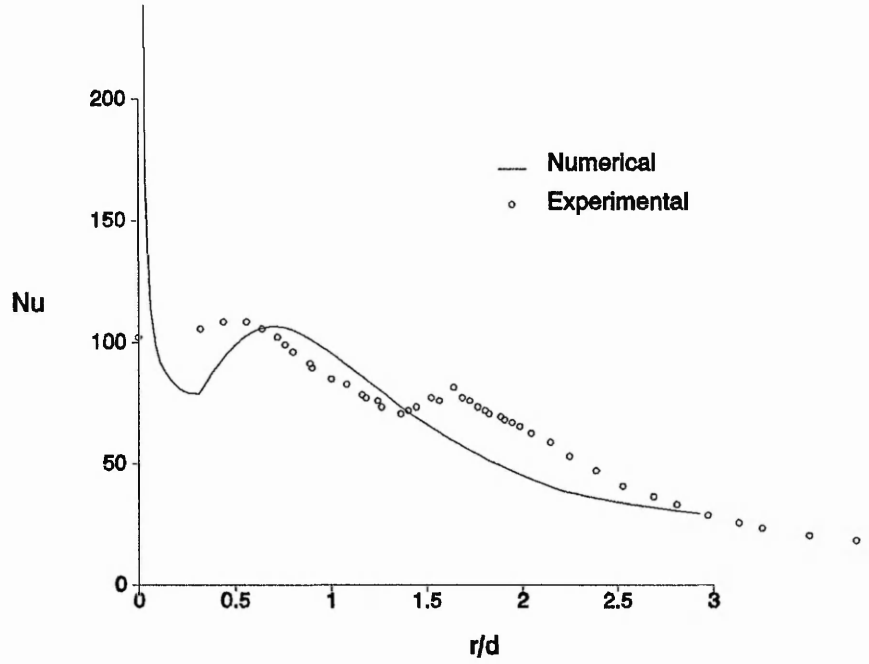

Figure 6.18. Radial distribution of Nusselt number. Re=20000. z/d=2.

It will be shown that the overprediction of heat transfer cannot be attributed solely to the overprediction of the turbulent kinetic energy. For the area between the wall and the near

wall node, k and ϵ are not calculated but are obtained from a universal wall function. Recall from Chapter 3 that the near wall node needs to lie just inside the turbulent region for the wall function to be valid ($y^+ > 11.5$). In the numerical model this distance was based on the experimental measurements at r/d=0.5. Since $y^+ \sim f(Re^{0.5})$ then a near wall Reynolds number greater than 132 is required to allow correct use of the wall function. The near wall Reynolds number calculated at the near wall node (see Appendix G) is plotted in Figure 6.19 and it is clear that, with the present numerical model, the wall function is only valid for r/d>0.3, where the near wall Reynolds number reaches ~132 and which corresponds to the location where a significant improvement in the prediction of Nu is obtained. In the developed wall jet the Reynolds number levels out close to Re≈100 which explains the improvement in the predictions in this region although Re>132 is preferential (and may lead to an improvement in the 20% difference reported above). It is difficult to specify an appropriate value of y_p for the entire length of a computational domain, especially in a developing flow, without prior knowledge of the flow field. The stagnation region of an impinging jet cannot be compared to a fully developed boundary layer for which the wall function is valid. The radial velocity accelerates rapidly from zero at the stagnation point such that the universal wall function is inappropriate, since it was derived for a developed flow.

It has already been stated that the wall function was developed for two-dimensional flow and yet it is widely applied to axisymmetric flow. Considering that the developing radial flow in an axisymmetric geometry is moving into a continually enlarging area it is a reasonable assumption that the flow characteristics in axisymmetric flow will differ from those of two-dimensional flow. This fact is often overlooked and yet Patel and Head (1969) demonstrated that velocity profiles in axisymmetric flow differ from those in two-dimensional flow and more recently Eggels et al. (1994) extended these measurements to

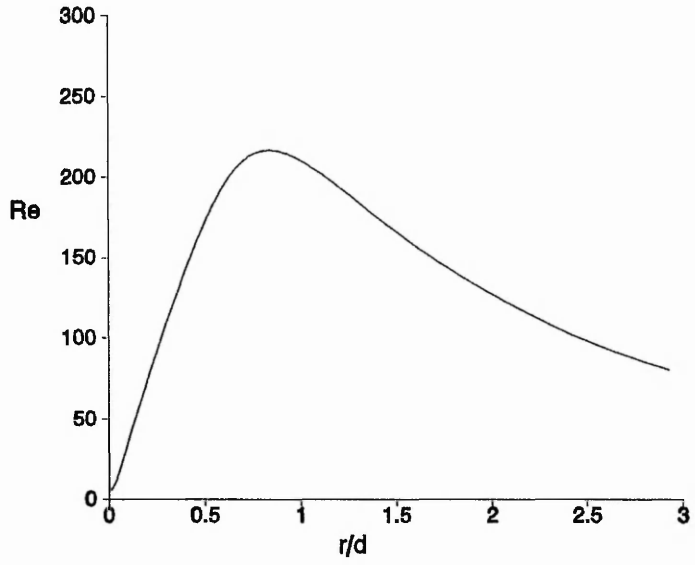

Figure 6.19. Variation of near wall Reynolds number with radial distance. Re=20000, z/d=2.

show that the velocity profile in a pipe flow fails to conform to the accepted law of the wall. This will also contribute to the 20% difference between the measured and predicted Nusselt number in the wall jet, obtained in this investigation. The latter work also describes different characteristics in the higher order statistics (turbulence, skewness and kurtosis).

Craft et al. (1993) have reported a significant improvement in the prediction of jet impingement using a second-closure approach with new schemes which account for the effect of the wall. They obtained reasonable comparison of predictions of Nusselt number with experiment for r/d<0.3, however they found a $Re^{0.6}$ dependence at the stagnation point (as opposed to the $Re^{0.5}$ dependence obtained from experiment) which they also attributed to the use of the eddy-viscosity concept across the sublayer.

6.4 Concluding remarks

By comparison with other authors work, summarised by Cooper et al. (1993), the commercial CFD package PHOENICS has been shown to predict jet impingement to the same level of accuracy as other available codes which use the same turbulence model.

It has been shown that the widely used k-ϵ turbulence model can predict the axial velocity decay in the impinging jet very well and can also predict the qualitative trends of the radial velocity profiles at all radial stations. For $y/d>0.75$ good quantitative agreement is also obtained. The qualitative trends of the radial profiles of turbulent kinetic energy are also predicted well except at $r/d=0$ and $r/d=0.5$ were an overprediction up to nine times the experimental values occurs. Again for $y/d>0.75$ reasonable quantitative agreement is also shown. For $r/d\geq3$ both the radial velocity and turbulent kinetic energy are fairly predicted (given the numerical and experimental uncertainties) and the comparison improves with radial distance; by $r/d=3$ the peak values are within 25% and 10% respectively, of the experimental results.

The overprediction of turbulent kinetic energy, most significantly in the stagnation region, leads to an underprediction of the spreading rate in the wall jet and radial velocity profiles that are too thick, although the trends in the jet development are reasonably predicted. The large scale recirculation which dominates the flow is predicted by the numerical model, but the smaller length scales are not captured.

In the developed wall jet the heat transfer is predicted to within 20% where the turbulent kinetic energy is reasonably predicted by the k-ϵ eddy viscosity model and the universal wall function is valid. However, the stagnation point Nusselt number is overpredicted by ~300%. At the stagnation point the wall function is invalid such that the failure of the simulation

cannot be attributed directly to the overprediction of turbulent kinetic energy alone. It should also be noted that the wall function was derived for developed two-dimensional flows.

It is evident that attention needs to be paid to the near wall predictions. Recent literature has shown that second-moment closures can offer considerable improvement in the prediction of anisotropic flows such that it seems sensible to use a similar approach near the wall, instead of using the eddy viscosity concept. This was suggested by Launder (1989) but as far as the author is aware there have been no publications of such an approach to date.

It should be pointed out that where the ϵ equation in the k-ϵ model is identified as the source of poor performance of the model, the second closure models will not offer any improvement since a similar single length scale equation is solved.

In general, the flow is reasonably predicted, and the numerical model can be used with confidence, where isotropy prevails and the wall function is valid.

CHAPTER 7

SUMMARY OF CONCLUSIONS AND RECOMMENDATIONS

This Chapter commences with a summary of the major findings of this study with reference to the aims specified in Section 1.2. The conclusions are discussed in three sections based on qualitative experimental results, quantitative experimental results and numerical results. Practical applications of these findings are then discussed followed by recommendations for further work.

7.1 Summary of conclusions

An airflow rig and traverse mechanism have been successfully designed and built to facilitate the measurement of velocity, turbulence levels and higher order moments in a two-dimensional plane of a semi-confined round turbulent impinging jet, using forward collection laser-Doppler anemometry. Software has been developed for automatic control of the test rig, data acquisition and data analysis. A relevant literature survey on the effects of turbulence on jet impingement heat transfer has been completed. Particular attention has been paid to the specification of the experimental quantities and procedures to minimise experimental uncertainty and thus ensure the quality of the results. The same airflow rig has been used to obtain surface heat transfer coefficients using liquid crystal thermography with a transient wall heating technique. A preliminary flow visualisation study of the impinging jet provided a useful insight to the flow field.

The present study has provided new data for velocity, Reynolds stress components, skewness and kurtosis for a semi-confined turbulent impinging jet and has corroborated and extended the existing heat transfer data for this configuration. No other similar fluid flow measurements were found in the literature for the semi-confined case.

With reference to the aims specified in Section 1.2, the following conclusions have been

drawn, based on the results presented and discussed in the previous Chapters.

7.1.1 Qualitative experimental results

Full field flow visualisation was carried out over a Reynolds number range 600 to 20000. The flow is dominated by a large recirculation whose size is limited by the nozzle to plate spacing, followed downstream by a further counter rotating recirculation. Much of the spent air from the jet flows back along the upper plate for subsequent entrainment at the jet axis. As the nozzle to plate spacing was increased the primary recirculation moved further downstream. The boundary layer is complex and appears as wavy streamlines between the vortices and the impingement plate.

A distinct vortex structure, initiated at the jet exit, was not observed for the fully developed turbulent impinging jet. The lack of a distinct vortex structure may be explained by the fully developed velocity profile which results in a lower shear, Lepicovsky (1989), and inability of the particles to follow the turbulent flow. Slight periodicity of the large scale motions was observed and at the lower Reynolds numbers a periodic contraction of the impinging jet was also noted. During the liquid crystal tests an instantaneous stagnation point was observed when $z/d \geq 6$ which was contained within the region $-0.5 < r/d < 0.5$. These structures originating at the jet exit are still believed to exist based on the findings of the present, and other studies; namely, the observed periodicity of the flow, the flow visualisation at lower Reynolds numbers, the intermittency observed in the LDA data, the occurrence of an instantaneous stagnation point for $z/d \geq 6$ and the findings of Yokobori et al. (1979), Kataoka et al. (1986) and Popiel and Trass (1991).

It is apparent from the flow visualisation study that the jet is well mixed and turbulent on impingement such that laminar to turbulent transition is unlikely to have taken place and

the secondary maximum in heat transfer may not therefore be due to a transition to turbulence. The measurement of the near wall turbulent quantities using LDA confirms the existence of turbulent motions at the stagnation point.

It is also confirmed that smaller scale vortices are generated at the impingement surface although it is not known where they first appear. It is suggested that these wall eddies are partly responsible for the high local turbulence and heat transfer maxima.

The flow visualisation in the present study has highlighted the danger in specifying the outflow region in numerical studies too close to the jet axis, as this would result in an inflow condition on an outflow boundary, and is partly responsible for model/experiment disagreement reported in other works.

The recorded concentric liquid crystal isotherms clearly demonstrate that for $z/d<4$ a secondary peak in heat transfer occurs and that for $z/d<5$ a local minimum occurs at the stagnation point with the primary maximum occurring at $r/d\approx0.5$.

7.1.2 Quantitative experimental results

The structured nature of the flow field has been documented from the measurement of higher order statistical quantities. Probability density functions, skewness and kurtosis factors have indicated regions of high shear and intermittency within the flow field, which coincide with high gradients of mean velocity and turbulence intensity.

The axial velocity decay of the free and impinging jet has been documented. At a nozzle to plate spacing of 6d, the presence of the impingement plate has been shown to extend the length of the potential core from 4.6d in the free jet to 4.9d in the impinging jet, based on

a 95% criterion.

The axial and radial near wall distributions of the normal and shear Reynolds stress components have been described in detail. The flow has been shown to be anisotropic in the stagnation region with a tendency to isotropic flow further downstream in the wall jet. At a distance of 0.25d from the impingement surface in the stagnation region, the axial turbulence reaches a maximum at twice the value of the radial turbulence.

The stagnation point jet effectiveness (dimensionless adiabatic wall temperature) has been shown to be marginally higher for the semi-confined jet when compared with other authors data of the unconfined jet, in the region $2<z/d<9$. The effectiveness is unaffected when $z/d \leq 2$ where the axial velocity and temperature remain constant in the initial region of the potential core, and the effect subsides at large nozzle to plate spacings beyond the potential core, indicating the reduced effect of the semi-confinement. The use of the adiabatic wall temperature, as opposed to the jet temperature, in the definition of the Nusselt number has a pronounced effect on the magnitude of the Nusselt number for $z/d>2$.

The distribution of the Nusselt number at a Reynolds number of 20000 and nozzle to plate spacings in the range $1<z/d<8$ has been presented and related to the mean velocities and Reynolds stress components and a direct link between turbulence and heat transfer maxima has been identified. When defined by the adiabatic wall temperature, the maximum stagnation point Nusselt number occurs when the impingement plate is placed downstream of the potential core near to $z/d=7$, and corroborates the well known findings of other authors discussed in Chapter 2. The maximum stagnation point heat transfer occurs at a larger nozzle to plate spacing than in the unconfined case due to the extended potential core which results from the effect of semi-confinement. This maximum is attributed to high axial,

radial and shear components of the Reynolds stresses; at a nozzle to plate spacing of z/d=6, the axial turbulence component of the Reynolds stress has been shown to be approximately twice that when z/d=2, and the radial component has been shown to be 50% greater than that at z/d=2.

When z/d<5 a local minimum in Nu occurs at the stagnation point accompanied by a local maximum at r/d≈0.5. This peak moves towards the axis as z/d increases until by z/d=6 it cannot be differentiated and the maximum Nu now occurs at the stagnation point as described above. The local maximum at r/d≈0.5 is again related directly to turbulence since the axial component of the Reynolds stresses is 70% higher than that at the stagnation point, in the present case.

The differences in the heat transfer distributions compared to other authors who have used a fully developed jet (Baughn and Shimizu, 1989, Baughn et al., 1991 and Yan et al., 1992) can be explained by differences in nozzle and jet impingement geometries, substantiated by the findings of other workers such as Obot et al. (1979, 1982) and a related study by Ashforth-Frost and Jambunathan (1994). The Nusselt number for the semi-confined jet lies below that of the unconfined jet at all of the nozzle to plate spacings considered. At radial distances beyond the edge of the jet, r/d>0.5, the results showed the same trends in the profiles of Nusselt number. The difference in magnitude has been attributed directly to the effect of semi-confinement which severely limits entrainment. The local minimum in stagnation point heat transfer observed in the present study at low nozzle to plate spacings, as opposed to a maximum in the above works, has been attributed to the effect of semi-confinement and differences in the turbulence level at the nozzle exit; even when the mean velocity profile appears fully developed, the turbulence continues to increase such that a higher level of axial turbulence will develop the longer the nozzle length. At z/d=2 the

semi-confined stagnation point Nusselt number is only 75% of that of the unconfined case. By z/d=6 the above ratio has increased to 80% and increases further as the nozzle to plate spacing is increased.

For z/d<4 a minimum in heat transfer occurred in the region 1.2<r/d<1.5 followed by a secondary maximum in the region 1.5<r/d<2. The secondary maximum decreases in magnitude and moves radially outwards as z/d is increased. Despite high absolute values of turbulence, the minimum has been shown to coincide with maximum radial velocities which leads to lower levels of local turbulence intensity. The secondary maximum has been attributed to a laminar to turbulence transition by earlier workers, but the present data has shown clear evidence of near wall turbulence at the stagnation point. This peak is therefore attributed to the maximum values of all of the turbulence components of the Reynolds stresses, which occur in the same region, 1.5<r/d<2. By z/d=5, this peak had disappeared.

Whereas two peaks in the turbulent quantities occur at r/d≈0.5 and in the region 1.5<r/d<2 at the lower nozzle to plate spacings, which coincide with the heat transfer maximum unique to these spacings, the peak turbulence for the z/d=6 case occurs in the region of the stagnation point. At r/d=2 the turbulence in the z/d=6 case is lower than that in the z/d=2 case and explains the lack of a secondary peak at the higher nozzle to plate spacings.

There is a 28% increase in the stagnation point heat transfer coefficient when the nozzle to plate spacing is increased from 2d to 6d, which corresponds to an increase in the peak axial turbulence (u'/u_b) from 0.08 to 0.14 respectively, indicating that the increase in heat transfer coefficient is not directly proportional to increase in turbulence. When much of the cited literature proposes such a strong influence of the turbulence level in the approaching flow on stagnation point heat transfer, a much greater increase in heat transfer might be

anticipated. One explanation is that the thermal boundary layer is contained within the viscous sublayer. This was the finding of Craft et al. (1993) based on numerical simulation. In this case, the turbulence levels will not have such a marked effect as in the case where the thermal boundary layer is much thicker.

At further radial distances (r/d>2), the heat transfer profiles decrease monotonically with distance from the stagnation point and by r/d=4 have developed very shallow gradients which corresponds to developed flow.

The nozzle exit conditions have been described and symmetry demonstrated to enable the tests to be replicated and the results to be used as input boundary conditions to a numerical model. The model can then be validated by comparison with the present experimental results in the stagnation region.

7.1.3 Numerical results

By comparison with other authors work, summarised by Cooper et al. (1993), the commercial CFD package PHOENICS has been shown to predict jet impingement to the same level of accuracy as other available codes which use the same turbulence model.

It has been shown that the widely used k-ϵ turbulence model can predict the axial velocity decay in the impinging jet very well and can also predict the qualitative trends of the radial velocity profiles at all radial stations. For y/d>0.75 good quantitative agreement is also obtained. The qualitative trends of the radial profiles of turbulent kinetic energy are also predicted well except at r/d=0 and r/d=0.5 where an overprediction up to nine times the experimental values occurs. Again for y/d>0.75 reasonable quantitative agreement is also shown. For r/d≥3 both the radial velocity and turbulent kinetic energy are reasonably

predicted (given the numerical and experimental uncertainties) and the comparison improves with radial distance; by r/d=3 the peak values are within 25% and 10% respectively, of the experimental results.

The large scale recirculation which dominates the flow is predicted by the numerical model, but the smaller length scales are not captured since only a single length scale equation is solved (ϵ).

In the developed wall jet the heat transfer is predicted to within 20% where the turbulent kinetic energy is reasonably predicted by the k-ϵ eddy viscosity model and the universal wall function is valid. However, the stagnation point Nusselt number is overpredicted by ~300%. The secondary heat transfer maxima at r/d≈2 were not identified. The deficiency in the prediction of the surface heat transfer is attributed to the overprediction of the near wall turbulent kinetic energy by the k-ϵ turbulence model and the improper use of the universal wall function, which incidentally was derived for developed two-dimensional flows. In the computational model the jet penetrates further into the outer stream than is the actual case; the higher values of k lead to higher rates of entrainment of the free stream fluid, which results in the wall jet being too thick ie. the radial velocity is underpredicted. The agreement between computation and experiment improves as the flow tends to isotropy further downstream.

In general, the trends in the flow are reasonably predicted, and the numerical model can be used with confidence, where isotropy prevails and the wall function is valid.

7.2 Practical applications of the results

Maximum heat transfer rates are achieved when the impingement surface is placed at

$6 \leq z/d \leq 7$ for the fully developed jet impinging in a semi-confined space. High average heat transfer rates are obtained when the plate is placed within, and just at the end of, the potential core of the jet. These spacings are recommended for optimal performance but have not taken into account the required pumping power. At larger nozzle to plate spacings jet impingement heat transfer becomes less effective.

The present study has indicated that an unconfined geometry should be used in preference to the semi-confined geometry since higher heat transfer rates can be achieved for the same Reynolds number and nozzle to plate spacing. The full benefit of increasing axial turbulence to increase heat transfer rates is only experienced when the thermal boundary layer thickness is not much smaller than that of the hydrodynamic boundary layer. The selection of the cooling medium, where appropriate, may therefore offer increased performance.

The data produced in the present study will be useful to those modelling turbulent jets and surface heat transfer. The jet is easily characterised by its fully developed exit profile, and the boundary conditions can be specified more easily than in the unconfined configuration.

7.3 Recommendations for further work

The optimal geometry for high average heat transfer coefficients, taking into account the required pumping power, remains to be established.

The wall jet region is well documented but the stagnation region requires substantial attention. In order to fully assess the role of turbulence on heat transfer, knowledge of the thermal boundary layer is needed to complement the hydrodynamic boundary layer data.

This could be achieved in the first instance by traversing a thermocouple through the flow of a much larger scale facility. Ideally, velocity information and temperature should be measured simultaneously. Although still in early stages of development, the use of liquid crystals as a seeding material for Particle Image Velocimetry, Ashforth-Frost and Jambunathan (1993), would enable very useful simultaneous velocity and temperature data at low Reynolds numbers.

Jet impingement seems to be dominated by coherent structures generated at the nozzle exit, but to what extent these are responsible for the turbulent transport to the impingement surface has not, to date, been quantified. A larger scale flow visualisation study would provide further insight into the flow structure. In particular, the generation of wall eddies within, and close to, the stagnation region would help to identify the source of the large near wall turbulence profiles. Further measurements near the wall, using a small measurement volume as in this study, but employing methods to eliminate near wall reflections, such as varying the polarization of the scattered light, Gardavský and Kleine (1988) and traversing in smaller radial increments, would be useful. Performed on a larger scale facility, these measurements would also enable any thinning of the boundary layer at r/d=0.5 to be identified.

The effect of the impingement of these coherent structures on the occurrence of an instantaneous stagnation point needs to be established, and a steady state measurement technique for heat transfer should be used to corroborate the existence of, and quantify, this phenomenon.

The use of microballoons as a seeding medium could be improved by applying a wetting agent to the particles. The larger microballoons (~30m) have been shown to become

damaged during use and filtering is therefore recommended to provide microballoons of size $<20\mu m$.

Based on the aforementioned surmise that the full benefit of jet impingement heat transfer depends on the relative size of the thermal and hydrodynamic boundary layers, the effect of Prandtl number on jet impingement heat transfer needs to be established.

Future development of turbulence models should only be attempted where grid independency is ensured and the boundary conditions can be well defined. Care should also be exercised in avoiding the specification of an inflow region on an outflow boundary. Only in this way, can deficiencies in the results be attributed directly to the model under test.

The present study and other recent studies, for example Craft and Launder (1991) and Craft et al. (1993) have indicated the deficiencies in the k-ϵ turbulence model and second-moment closures in predicting jet stagnating flows. In view of the structure of turbulence in such a flow, the question arises, if a universal model will ever be developed from these approaches. Launder's (1991) suggestion of solving two length scale equations is recommended; one for large scale eddies and one for small scale. With the continual development of computing capabilities, a full solution to the Navier Stokes equations may be the only way forward.

REFERENCES

Abromavich G N, 1963. *The theory of turbulent jets.* MIT Press,

ACT Pulsar Ltd, 1984. *Poly-TRM/VT user guide.* Birmingham, England.

Agarwal R K and Bower W, 1982. Navier-Stokes computations of turbulent compressible two-dimensional impinging jet flow fields. *AIAA Journal*, **20**(5), 577-83.

Akino N, Kunugi T, Ichimiya K, Mitsushiro K and Ueda M, 1989. Improved liquid crystal thermometry excluding human colour sensation. *ASME J. Heat Transfer*, **111**, 558-65.

Amano R S, 1983. Turbulence effect on the impinging jet on a flat plate. *Bulletin of the JSME,* **26**(221), 1891-9.

Amano R S and Brandt H, 1984. Numerical study of turbulent axisymmetric jets impinging on a flat plate and flowing into an axisymmetric cavity. *ASME J. Fluids Eng.*,**106**, 411-7.

Amano R S and Jensen M K, 1982. A numerical and experimental investigation of turbulent heat transport of an axisymmetric jet impinging on a flat plate. *ASME Paper 82-WA/HT-55.*

Amano R S and Neusen K F, 1982. A numerical and experimental investigation of high velocity jets impinging on a flat plate. *6th Int. Symp. on Jet Cutting Technology*, 6-8 April, University of Surrey, UK, 107-22.

Amano R S and Sugiyama S, 1985. An investigation on turbulent heat transfer of an axisymmetric jet impinging on a flat plate. *Bulletin of JSME*, **28**(235), 74-9.

Arganbright D G and Resch H, 1971. A review of basic aspects of heat transfer under impinging air jets. *Wood, Science and Technology*, **5**, 73-94.

Ashforth-Frost S, 1988. Software for remote control of the laser-Doppler anemometry signal processing unit. Internal report, Dept Mech. Eng, Nottingham Polytechnic, England.

Ashforth-Frost S and Jambunathan K, 1993. Flow visualisation using liquid crystals. *Presented at SPIE Annual International Symposium on Optics, Imaging and Instrumentation: Optical Diagnostics in Fluid and Thermal Flow,* San Diego, USA, 11-16 July, 237-45.

Ashforth-Frost S and Jambunathan K, 1994. Effect of nozzle geometry and semi-confinement on the potential core of a turbulent axisymmetric jet. *Presented at The Tenth International Heat Transfer Conference*, Brighton, UK, 14-18 August, Paper no. 63.

Ashforth-Frost S, Wang L S, Jambunathan K, Graham D P and Rhine J M, 1992. Application of image processing to liquid crystal thermography. In: *Optical Methods and Data Processing in Heat and Fluid Flow*. 2-3 April, City University, London, 121-6.

Aydore S, Disimile P J, Tsuei Y G and Behbahani A I, 1990. Flow characteristics in the nearfield of an impinging jet issuing from a long circular pipe. *ASME Fluids Eng. Div.*, **94**, 67-72.

Barata J M M, Durão D F G, Heitor M V and McGuirk J J, 1987. The turbulence characteristics of a single impinging jet through a crossflow. *Proc. 6th Symp. on Turbulent Shear Flows*, Toulouse, France, September, 13.5.1-13.5.11

Barata J M M, Durão D F G, Heitor M V and McGuirk J J, 1988. On the validation of 3-D

numerical simulations of turbulent impinging jets through a crossflow. *Validation of Computational Fluid Dynamics, AGARD-CP-437*, **1**, 35.1-35.10.

Barata J M M, Durão D F G and McGuirk J J, 1989. Numerical study of single impinging jets through a crossflow. *J. Aircraft*, **26**(11), 1002-8.

Barata J M M, Durão D F G and McGuirk J J, 1991. Impingement of single and twin turbulent jets through a crossflow. *AIAA J.*, **29**(4), 595-602.

Bates C J and Hughes T D R, 1977. The effect of both sampling size and sampling rate on the statistical fluid flow parameters in a high Reynolds number, low turbulence intensity flow, In: *5th Biennial Symp. on Turbulence,* October 1977.

Baughn J W, Hechanova A E and Yan X, 1991. An experimental study of entrainment effects on the heat transfer from a flat surface to a heated circular impinging jet. *Proc. ASME/JSME Joint Conf. Thermal Engineering*, Reno, NV, USA, March 17-22, **3**, 143-9.

Baughn J W and Shimizu S, 1989. Heat transfer measurements from a surface with uniform heat flux and an impinging jet. *ASME J. Heat Transfer*, **111**, 1096-8.

Baughn J W and Yan X, 1991. A preheated-wall transient method for measurements of the heat transfer from a surface to an impinging jet. *Proc. Eurotherm Heat Transfer in Single Phase Flows*, Université de Pau et des Pays de l'Adour, France, 8-10 July.

Becko Y, 1976. Impingement cooling - A review. von Karman Inst. for Fluid Dynamics, Lecture Series 83.

Beltaos S and Rajaratnam N, 1974. Impinging circular turbulent jets. *Journal of the Hydraulics Division*, **10**, 1313-28.

Beltaos S and Rajaratnam N, 1977.Impingement of axisymmetric developing jets. *J. Hydraulic Research*, **15**(4), 311-26.

Bird B R, Stewart W E and Lightfoot E N, 1960. *Transport phenomena*. John Wiley & Sons, New York.

Black Box Catalogue Ltd, 1985. Communications interface adapter user manual. Reading, Berkshire, England.

Bonnett P, 1989. *Applications of liquid crystals in aerodynamic testing*. D.Phil Thesis, Oxford University, Dept. Engineering Science.

Bower W W, Kotansky D R and Hoffman G H, 1977. Computations and measurements of two-dimensional turbulent jet impingement flow fields. *Symp. Turbulent Shear Flows*, 18-20 April, Pennsylvania State Univ., 3.1-3.8.

Brison J F and Brun G, 1991. Round normally impinging turbulent jets. *15th Meeting of IAHR Working Group on Refined Flow Modelling*, ECL, Lyon.

BRITISH STANDARDS INSTITUTION, 1983. BS1042: 1983. *The measurement of fluid flow in closed conduit. Section 2.1:Methods using Pitot-static tubes.*

BRITISH STANDARDS INSTITUTION, 1968. BS4311: 1968. *Specification for gauge blocks*

and accessories.

Button B L, 1977. A motorised traverse gear. Report ME398, Lanchester Polytechnic, Coventry, England.

Button B L and Leech J R, 1972. The selection of a contraction design method. Coventry (Lanchester) Polytechnic Internal Report, ME395.

Button B L and Jambunathan K, 1989. Jet impingement heat transfer: a bibliography 1976-1985. *Previews Heat Mass Transfer*, **15**(2), 149-78.

Button B L and Wilcock D, 1978. Impingement heat transfer - a bibliography 1890-1975. *Previews Heat Mass Transfer*, **4**(3), 83-9.

Caruso S C, Ferziger J H and Oliger J, 1985. *Adaptive grid techniques for elliptic fluid-flow problems*. Stanford Univ., CA, Report Thermoscience Div., Part TF23.

Cebeci T and Bradshaw P, 1984. *Physical and computational aspects of convective heat transfer*. Springer-Verlag, New York.

CHAM Ltd, 1990. PHOENICS Instruction Course notes TR/300. CHAM, Wimbledon, London.

Chieng C C and Launder B E, 1980. On the calculation of turbulent heat transport downstream of an abrupt pipe expansion. *Numerical Heat Transfer*, **3**, 189-207.

Clifford R J, Jones T V and Dunne S T, 1983. Techniques for obtaining detailed heat transfer coefficient measurements within gas turbine blade and vane cooling passages. *ASME Paper 83-GT-58.*

Coleman H W and Steele W G, 1989. *Experimentation and uncertainty analysis for engineers*, Wiley, New York.

Cooper D, Jackson D C, Launder B E and Liao G X, 1993. Impinging jet studies for turbulence model assessment - I. Flow-field experiments. *Int. J. Heat Mass Transfer*, **36**(10), 2675-84.

Craft T J and Launder B E, 1991. Comparison of turbulence models in a single impinging jet. *Proc. Workshop on Turbulence Modelling for Impinging Flows*, UMIST, Manchester, 30 October.

Craft T J, Graham L J W and Launder B E, 1993. Impinging jet studies for turbulence model assessment - II. An examination of the performance of four turbulence models. *Int. J. Heat Mass Transfer*, **36**(10), 2685-97.

Data Translation Inc., 1989. User manual for DT2861 and DT2862 UM-0830-A, 4th edition.

Data Translation Inc., 1989. DT-IRIS(TM) User manual SP0215 (Version 1.04), UM-06852-E, 6th edition.

Deighton M O and Sayle A E, 1971. An electronic tracker for the continuous measurement of Doppler frequency from a laser anemometer. *DISA information 12 : Measurement and*

Analysis, 5-10.

Deshpande M D and Vaishnev R N, 1982. Submerged laminar jet impingement on a plane. *J. Fluid Mech.*, **114**, 213-36.

Deshpande M D and Vaishnev R N, 1983. Wall stress distribution due to jet impingement. *ASCE J. Eng. Mech.*, **109**(2), 479-93.

Dietrich C F, 1991. *Uncertainty, calibration and probability (the statistics of scientific and industrial measurement).* 2nd Ed., Adam Hilger, Bristol, UK.

Downs S J and James E H, 1987. Jet impingement heat transfer - A literature survey. *ASME paper 87-H-35.*

Durão D F G and Whitelaw J H, 1974. Measurements in the region of recirculation behind a disc. *Proc. of 2nd Int. Workshop on Laser Velocimetry*, Purdue University, **2**, 413.

Durst F, Melling A and Whitelaw J H, 1981. *Principles and practice of laser-Doppler anemometry.* (London: Academic Press Inc. Ltd).

Durst F and Tropea C, 1981. Turbulent, backward facing step flows in two-dimensional duct and channel flows. *Proc. 3rd Symp. on Turbulent Shear Flows,* September 9-11, Davis, California, USA.

Durst F and Whitelaw J H, 1971. Measurements of mean velocity, fluctuating velocity, and shear stress in air using a single channel optical anemometer. *DISA information* ***12*** *:*

Measurement and Analysis, 11-6.

Edwards R J, 1987. *Enhancement of heat transfer in smooth annular ducts using longitudinal fins or swirling flow.* PhD Thesis, Nottingham Polytechnic, CNAA.

Eggels J G M, Unger F, Weiss M H, Westerweel J, Adrian R J, Friedrich R and Nieuwstadt F T M, 1994. Fully developed turbulent pipe flow: a comparison between direct numerical simulation and experiment. *J. Fluid Mech.*, **268**, 175-209.

El-Genk M S, Huang L and Guo Z, 1992. Heat transfer between a square flat plate and a perpendicularly impinging circular air jet. *ASME Enhanced Heat Transfer*, HTD-Vol. **202,** 33-8.

Emerson and Cumming Inc., 1977. ECOSPHERES IG25, Low density, industrial grade microballoons, technical bulletin 14-2-1C, Emerson and Cumming Inc., Dielectric Materials Division, Canton, Massachussetts.

Fisher E and Jensen E, 1982. *PET/CBM and the IEEE-488 bus (GPIB)*, Osborne/McGraw-Hill, California, USA.

Fletcher C A J, 1988a. *Computational Techniques for Fluid Dynamics. Volume 1 - Fundamental and general techniques.* Springer-Verlag, New York.

Fletcher C A J, 1988b. *Computational Techniques for Fluid Dynamics. Volume 2 - Specific techniques for different flow categories.* Springer-Verlag, New York.

Gardavský J and Kleine R, 1988. Application of polarization reflection suppression in laser-Doppler anemometry. *Int. Symp. on Applications of Laser Doppler Anemometry to Fluid Mechanics,* Lisbon, Portugal.

Gardon R and Akfirat J C, 1965. The role of turbulence in determining heat transfer characteristics of impinging jets. *Int. J. Heat Mass Transfer*, **8**, 1261-72.

Gardon R and Akfirat J C, 1966. Heat transfer characteristics of impinging two-dimensional air jets. ASME J. Heat Trans., February, 101-8.

Gardon R and Cobonpue J, 1962. Heat transfer between a flat plate and jets of air impinging on it. *Int. Developments in Heat Transfer*, **2**, 454-60.

Gauntner J W, Livingood J N B and Hrycak P, 1970. Survey of literature on flow characteristics of a single turbulent jet impinging on a flat plate. *NASA Report TN D-5652.*

Giralt F, Chia C J and Trass O, 1977. Characterization of the impingement region in an axisymmetric turbulent jet. *Ind. Eng. Chem. Fundam.*, **16**(1), 21-8.

Goldstein R J and Franchett M E, 1988. Heat transfer from a flat surface to an oblique impinging jet. J. Heat Trans., **110**, 84-90.

Goldstein R J, Sobolik K A and Seol W S, 1990. Effect of entrainment on the heat transfer to a heated circular air jet impinging on a flat surface. ASME J. Heat Transfer, **112**, 608-11.

Gouldin F C, Schefer R W, Johnson S C and Kollmann W, 1986. Nonreacting turbulent

mixing flows, *Prog. Energy Combust. Sci.* **12**, 257-303.

Gundappa M, Hudson J F and Diller T E, 1989. Jet impingement heat transfer from jet tubes and orifices. *National Heat Transfer Conf.* Philadelphia, PA, 6-9 August, **107**, 43-50.

Hetsroni G, 1988. Particles-turbulence interaction, *In Proc: ASME 3rd Int. Symp. on liquid solid flows*, **75**, 1-12.

Hetsroni G and Sokolov M, 1971. Distribution of mass, velocity and intensity of turbulence in a two-phase jet. *J. Appl. Mech.*, **38**(8), 315-20.

Hollworth B R and Gero S I, 1984. Entrainment effects on impingement heat transfer: Part II - Local heat transfer measurements. ASME J. Heat Trans., **107**, 910-5.

Hoogendoorn C J, 1977. The effect of turbulence on heat transfer at a stagnation point. *Int. J. Heat Mass Transfer*, **20**, 1333-8.

Hrycak P, 1981. Heat transfer from impinging jets: A literature review. *AWAL-TR-81-3054.*

Hrycak P, Lee D T Gauntner W J and Livingood J N B, 1970. Experimental flow characteristics of a single turbulent jet impinging on a flat plate. *NASA Tn D-5690.*

Huang G C, 1963. Investigations of heat transfer coefficients for air flow through round jets impinging normal to a heat transfer surface. *J. Heat Transfer,* **85**, 237-45.

Hussain A K M F and Clark A R, 1981. On the coherent structure of the axisymmetric

mixing layer: a flow visualisation study, *J. Fluid Mech.*, **104**, 263-94.

Ichimiya K, 1993. Heat transfer and flow characteristics of an oblique turbulent impinging jet with confined wall. ASME Proceedings HTD-**246** Heat transfer in Turbulent Flows, 17-24.

Ireland P T and Jones T V, 1985. The measurement of local heat transfer coefficients in blade cooling geometries, *AGARD Conference proceedings* **390**, paper 28.

Ireland P T and Jones T V, 1986. Detailed measurements of heat transfer on and around a pedestal in fully developed passage flow. *Proc. 8th Int. Heat Transfer Conf.*, San Francisco, 975-80.

Ireland P T and Jones T V, 1987. The response time of a surface thermometer employing encapsulated thermochromic liquid crystals. *J.Phys.E: Sci.Instrum.*, **20**.

Jambunathan K, Ashforth-Frost S and Button B L, 1990. Flow visualisation of a laminar jet impinging in a semi-confined space. Presented at: *Fifth International Symposium on Application of Laser Techniques to Fluid Mechanics*. Lisbon, Portugal, 9-12 July.

Jambunathan K, Kapasi S, Button B L and Bland J A, 1989. Numerical study of flow field for confined laminar jet impingement. *3rd Int. PHOENICS User Conf.*, Dubrovnik, Yugoslavia, 28 Aug - 1 Sept.

Jambunathan K, Lai E, Moss M A and Button B L, 1992. A review of heat transfer data for single circular jet impingement. *Int. J. Heat and Fluid Flow*, **13**(2), 106-15.

Jayatilleke C L V, 1969. The influence of Prandtl number and surface roughness on the resistance of the laminar sublayer to momentum and heat transfer. *Progress in Heat and Mass Transfer,* **1**, 198-329.

Johnson P L and Barlow R S, 1989. Effect of measuring volume length on two-component laser velocimeter measurements in a turbulent boundary layer. *Experiments in Fluids,* **8**, 137-44.

Jones T V, Wang Z and Ireland P T, 1992. The use of liquid crystals in aerodynamic and heat transfer experiments. In: *Optical Methods and Data Processing in Heat and Fluid Flow*. 2-3 April, City University, London, 51-65.

Kapasi S, 1994. *A study of heat and mass transfer characteristics of jet impingement.* PhD Thesis, The Nottingham Trent University, Nottingham, UK.

Kasagi N, Moffat R J and Hirata M, 1989. Liquid Crystals. In: *Handbook of Flow Visualisation*. Ed. W J Yang, 105-24.

Kataoka K, 1985. Optimal nozzle-to-plate spacing for convective heat transfer in nonisothermal, variable density impinging jets. *Drying Technol.*, **3**, 235-54.

Kataoka K, Degawa H, Hamada Y and Hamano S, 1987. Modelling turbulent heat transfer in impinging jets, *Proc. 2nd Int. Symp. on Transport Phenomena in Turbulent Flows*, 349-60.

Kataoka K, Mihata I, Maruo K, Suguro M and Chigusa T, 1986. Quasi-periodic large-scale structure responsible for the selective enhancement of impinging jet heat transfer. *Proc. 8th*

Int. Heat Transfer Conf., **3**, 1193-8.

Kataoka K, Suguro M, Degawa H, Maruo K and Mihata I, 1987. The effect of surface renewal due to large scale eddies on jet impingement heat transfer. *Int. J. Mass Transfer*, **30**, 559-67.

Kestin J, Maeder P F and Sogin H H, 1961a. The influence of turbulence on the transfer of heat to cylinders near the stagnation point. *Z. Angew. Math. Phys.*, **12**, 115-31.

Kestin J, Maeder P F and Wang H E, 1961b. Influence of turbulence on the transfer of heat from plates with and without pressure gradient. *Int. J. Heat Mass Transfer.*, **3**, 133-54.

Kezios S P, 1956. *Heat transfer in the flow of a cylindrical air jet normal to an infinite plane.* PhD Thesis, Illinois Institute of Technology, Chicago, Illinois, USA.

Kim T S, 1967. *Analysis of flow characteristics in circular submerged impinging jets*. PhD Thesis, Illinois Institute of Technology, USA.

Kimura M, Ono K and Saima A, 1990. Velocity and concentration fluctuations of turbulent buoyant round jets. *JSME Int. J, Series 2, Fluid Eng.*, **33**(3), 562-8.

Kline S and McClintock, 1953. Describing uncertainties in single sample experiments, Mechanical Engineering, **75**. 3-8.

Kolmogorov A N, 1942. Equations of turbulent motion of an incompressible fluid. Izv. Akad. Nauk. SSSR, Ser. Phys. **6**(1/2), 56-8.

Koopman R N and Sparrow E M, 1976. Local and average transfer coefficients due to an impinging row of jets. *Int. J. Heat Mass Transfer*, **19**, 673-83.

Kreith F and Black W Z, 1980. *Basic heat transfer*, Harper and Row, New York.

Launder B E and Spalding D B, 1972. *Lectures in Mathematical models of turbulence*. Academic Press, London.

Launder B E and Spalding D B, 1974. The numerical computation of turbulent flows, *Comput. Meths. Appl. Mech. Eng.*, **3**, 269-89.

Launder B E, 1991. *Turbulence Modelling for Impinging Flows*. ERCOFTAC UK North Pilot Centre/SERC CFD Community Club Workshop, UMIST, Manchester, UK, 30 October.

Lepicovsky J, 1989. The role of nozzle-exit boundary layer velocity gradient in mixing enhancement of free jets. *Proc. 3rd ASCE/ASME Mechanics Conf.*, San Diego, CA.

Lin C, Jambunathan K and Button B L, 1994. Intelligent liquid crystal applications database. To be published.

Livingood J N B and Hrycak P, 1973. Impingement heat transfer from turbulent air stream jets to flat plates - A literature survey. *NASA TM X-2778*.

Löfdahl L, 1988. Traverse mechanisms for the determination of Reynolds stresses using hot-wire techniques. *Experiments in Fluids*, 46, 352-4.

Lucas M G, Ireland P T, Wang Z and Jones T V, 1992. Fundamental studies of impingement cooling thermal boundary conditions. In Proc: *AGARD Conf. on Heat Transfer and Cooling in Gas Turbines*, **527**, Paper no. 14.

Ludwig J C, Qin H Q and Spalding D B, 1989. *The PHOENICS reference manual* CHAM TR/200.

Lytle D and Webb B W, 1991. Secondary heat transfer maxima for air jet impingement at low nozzle-to-plate spacings. In Proc: *2nd World Conf. on Experimental heat transfer, Fluid Mechanics and Thermodynamics*, 776-83.

Markatos N C, 1986. The mathematical modelling of turbulent flows. *Appl. Math. Modelling*, **10**, 190-220.

Martin H, 1977. Heat and mass transfer between impinging gas jets and solid surfaces, *Adv. Heat Transfer*, **13**, 1-60.

McGuirk J J, 1991. A synopsis of the computational results from Lyon/IAHR Workshop. *Proc. ERCOFTAC UK North Pilot Centre/SERC CFD Community Club Workshop on Turbulence Modelling for Impinging Flows*, UMIST, Manchester, UK, 30 October.

McNaughton K J and Sinclair C G, 1966. Submerged jets in short cylindrical flow vessels. *J. Fluid Mech.*, **25**(2), 367-75.

Merzkirch W, 1987. *Flow visualisation*, Academic Press Inc., London.

Metzger D E and Larson E E, 1986. Use of melting point surface coatings for local convective heat transfer measurements in rectangular channel flows with 90-deg. turns. *ASME J. Heat Transfer*, **108**, 48-54.

Metzger D E, Bunker R S and Bosch G, 1991. Transient liquid crystal measurement of local heat transfer on a rotating disk with jet impingement, *ASME J. Turbomachinery*, **113**, 52-9.

Moffat R J, 1985. Using uncertainty analysis in the planning of an experiment, *J. Fluids Eng.*, **107**, 173-9.

Moffat R J, 1990. Some experimental methods for heat transfer studies, *Experimental Thermal and Fluid Science*, **3**, 14-32.

Mohanty A K and Tawfek A A, 1993. Heat transfer due to a round jet impinging normal to a flat surface. *Int. J. Heat Mass Transfer*, **36**, 6, 1639-47.

Moreno O A, Katyl R H, Jones J D and Moschak P A, 1993. Mass transfer of an impinging jet confined between parallel plates. *IBM. J. Res. Develop.*, **37**, 2, 143-55.

Obi S, Hishida K and Maeda M, 1988. Heat transfer characteristics from a flat plate to a gas-solid two phase flow downstream of a slit injection, *ASME J. Heat Transfer*, **110**, 687-94.

O'Brien J E, Simoneau R J, Lagraff J E and Morehouse K A, 1986. Unsteady heat transfer and direct comparison for steady state measurements in a rotor wake experiment. *Proc. 8th Int. Heat Transfer Conf.*, San Francisco, 1243-8.

Obot N T, 1980. *Flow and heat transfer for impinging round turbulent jets*. PhD Thesis, McGill University, Montreal, Canada.

Obot N T, Majumdar A S and Douglas W J M, 1979. Effect of nozzle geometry on impingement heat transfer under a round turbulent jet. *ASME paper 79-WA/HT-53.*

Obot N T, Majumdar A S and Douglas W J M, 1982. Effect of semi-confinement impingement heat transfer. *Proc. 7th Int. Heat Transfer Conf.*, Munich, 6-10 September, **3**, 395-400.

Pamadi B N and Belov I A, 1980. A note on the heat transfer characteristics of circular impinging jet. *Int. J. Heat Mass Transfer*, **25**(6), 783-7.

Parker Digiplan Ltd, 1987a. *CD20,CD30 and CD40 Stepper motor drives instruction manual.* Poole, Dorset, England.

Parker Digiplan Ltd, 1987b. *Stepping motor drives and control systems processor interface manual.* Poole, Dorset, England.

Patankar S V, 1980. *Numerical heat transfer and fluid flow.* Hemisphere Publishing Co., New York.

Patankar S V and Spalding D B, 1972. A calculation procedure for heat, mass and momentum transfer in three dimensional parabolic flows, *Int. J. Heat Mass Transfer*, **15**, 1787-1805.

Patel V C and Head M R, 1969. Some observations on skin friction and velocity profiles in fully developed pipe and channel flows. *J. Fluid Mech.* **38**, 181-201.

Persen L N, 1986. Concepts of turbulence and CFD applications. *Prog. Aerospace Sci.*, **23**, 167-83.

Polat S, Huang B, Majumdar A S and Douglas W J M, 1989. Numerical flow and heat transfer under impinging jets: a review. *Annual Review of Numerical Fluid Mechanics and Heat Transfer* (Ed. C L Tien & T C Chawla), **2**, 157-97.

Popiel C O and Boguslawski L, 1986. Mass or heat transfer in impinging single, round jets emitted by a bell-shaped nozzle and sharp-ended orifice. *Proc. 8th Int. Heat Transfer Conf.*, San Francisco, CA, 1187-92.

Popiel C O and Boguslawski L, 1988. Effect of flow structure on the heat or mass transfer on a flat plate in impinging round jets. *2nd UK Nat. Conf. on Heat Transfer*, University of Strathclyde, UK, September 14-16, **1**, 663-85.

Popiel C O and Trass O, 1982. The effect of ordered structure of turbulence on momentum, heat and mass transfer of impinging round jets. *Proc. 7th Int. Heat Transfer Conf.*, Munich, Germany, September 6-10, **6**, 141-6.

Popiel C O and Trass O, 1991. Visualization of a free and impinging round jet. *Experimental Thermal and Fluid Science*, **4**, 253-64.

Rao V V and Trass O, 1964. Mass transfer from a flat surface to an impinging turbulent jet.

Can. J. Chem. Eng., **42**, 95-9.

Ribeiro M M and Whitelaw J H, 1975. Statistical characteristics of a turbulent jet. *J. Fluid Mech.*, **70**(1), 1-15.

Rodi W, 1980. Turbulence models and their application in hydraulics - A state of the art review. *IAHR Section on Division II: Experimental and Mathematical Fluid Dynamics*.

Rosten H I and Worrell J K, 1988. Generalised wall functions for turbulent flow. *PHOENICS Journal of CFD and its applications*, 1(1), 81-109.

Saad N R, Douglas W J M and Majumdar A S, 1977. Prediction of heat transfer under an axisymmetric laminar impinging jet. *Ind. Eng. Chem. Fundam.*, **16**, 148-54.

Saripalli K R, 1983. Visualisation studies of jet impingement flows at McDonnell Douglas Research Laboratories, *Flow Visualisation III*, 6-9 September, Ann Arbor, USA, 503-9.

Savory E and Toy N, 1984. Microcomputer of wind tunnel instrumentation with on-line data acquisition and analysis. *Software and Microsystems,* 43, (4), 93-7.

Schlicting H, 1968. *Boundary layer theory*. McGraw Hill, New York.

Schlünder E U and Gnielinski V, 1967. Heat and mass transfer between surfaces and impinging jets. *Chem. Ing. Tech.*, **39**, 578-84 (Translation held by BLDSC).

Scholtz M T and Trass O, 1970. Mass transfer in a nonuniform impinging jet. *AIChemE J.*,

16, 82-96.

Schrader H, 1961. Drying of moist surfaces by means of hot air jets: flow characteristics and mass transfer. *Forschungsh. Ver. Dtsch. Ing,* **484.**

Schultz D L and Jones T V, 1973. Heat transfer measurements in short-duration hypersonic facilities. *AGARD 165.*

Shayesteh M V and Bradshaw P, 1987. Microcomputer-controlled traverse gear for three-dimensional flow explorations. *J.Phys.E:Sci. Instrum.* 420, 320-2.

Shaw C T, 1992. *Using Computational Fluid Dynamics*. Prentice Hall Int. (UK) Ltd.

Sibulkin M, 1952. Heat transfer near the forward stagnation point of a body of revolution. *Journal of the Aeronautical Sciences*, August, 570-1.

Sikmanovic S, Oka S and Koncar-Djurdjevic S, 1974. Influence of the structure of turbulent flow on heat transfer from a single cylinder in cross flow. *5th Int. Heat Transfer Conf.*, Tokyo, 320-4.

Smirnov V A, Verevochkin G E and Brdlick P M, 1961. Heat transfer between a jet and a held plate normal to flow. *Int. J. Heat Mass Transfer,* **2,** 1-7.

Sparrow E M, Goldstein R J and Rouf M A, 1975. Effect of nozzle-surface separation distance on impingement heat transfer for a jet in a crossflow. *J. Heat Transfer,* **97**(4), 528-33.

Srikantaiah D V, Philip T and Wilson W W, 1988. Dedicated microprocessor system to control laser Doppler velocimetry measurements and to reduce data. *Rev.Sci.Instrum*, **459**(5), 793-6.

Tennekes H and Lumley J L, 1972. *A first course in turbulence*. MIT Press, Cambridge, Mass.

Townsend A A, 1976. *The structure of turbulent shear flow*. Cambridge University Press.

Tropea C, 1986. A practical aid for choosing the shift frequency in LDA. *Experiments in Fluids*, **4**, 79.

Vallis E A, Bacon D H and Patrick M A, 1979. The application of a two equation model of turbulence to the prediction of flows in regions of recirculation and impingement. *Symp. on Thermodynamics and Heat Transfer*, Leicester Polytechnic, 13-14 Nov. 27-35.

van den Berg B, 1990. Turbulence modelling: survey of activities in Belgium and the Netherlands; an appraisal of the status and a view on the prospects. Presented at the *AGARD Fluid Dynamics panel Technical Status Review on Appraisal of the suitability of turbulence models in flow calculations*. 26 April, Friedrichshafen. NTIS PB92-202365.

van der Meer T H, 1991. Stagnation point heat transfer from turbulent low Reynolds number jets and flame jets. *Experimental and Thermal Fluid Science*, **4**, 115-26.

Vickers J M F, 1959. Heat transfer coefficients between fluid jets and normal surfaces. *Ind. Eng. Chem.*, **51**(8), 967-72.

Yan X, Baughn J W and Mesbah M, 1992. The effect of Reynolds number on the heat transfer distribution from a flat plate to an impinging jet. *ASME Heat Transfer Division: Fundamental and Applied Heat Transfer Research for Gas Turbines Engines,* **226**,1-7.

Yanta W J and Smith R A, 1973. Measurements of turbulent-transport properties with a laser-Doppler velocimeter, *AIAA paper 73-169*, 1-9.

Yianneskis M, 1988. Thermal monitoring by liquid crystals. *Journal of Condition Monitoring*, **2**, 139-51.

Yoshida H, Suenaga K and Echigo R, 1988. Turbulence structure and heat transfer of a two-dimensional impinging jet with gas-solid suspensions, *Proc. ASME National Heat Trans. Conf.*, Houston, USA, **96**, 461-7.

Yokobori S, Kasagi N, Hirata M, Nakamaru M and Haramura Y, 1979. Characteristic behaviour of turbulence and transport phenomena at the stagnation region of an axi-symmetrical impinging jet. *2nd Symp. on Turbulent Shear Flow*, London, 4.12-4.17.

Bibliography

Cebeci T and Bradshaw P, 1984. *Physical and computational aspects of convective heat transfer.* Springer-Verlag, New York.

Coleman H W and Steele W G, 1989. *Experimentation and uncertainty analysis for engineers,* Wiley, New York.

Durst F, Melling A and Whitelaw J H, 1981. *Principles and practice of laser-Doppler anemometry.* (London: Academic Press Inc. Ltd).

Fisher E and Jensen E, 1982. *PET/CBM and the IEEE-488 bus (GPIB),* Osborne/McGraw-Hill, California, USA.

Fletcher C A J, 1988. *Computational Techniques for Fluid Dynamics. Volume 1 - Fundamental and general techniques.* Springer-Verlag, New York.

Fletcher C A J, 1988. *Computational Techniques for Fluid Dynamics. Volume 2 - Specific techniques for different flow categories.* Springer-Verlag, New York.

Hinze J O, 1959. *Turbulence.* McGraw-Hill, New York.

Kreith F and Black W Z, 1980. *Basic heat transfer,* Harper and Row, New York.

Launder B E and Spalding D B, 1972. *Lectures in Mathematical models of turbulence.* Academic Press, London.

Ludwig J C, Qin H Q and Spalding D B, 1989. *The PHOENICS reference manual* CHAM TR/200.

Patankar S V, 1980. *Numerical heat transfer and fluid flow.* Hemisphere Publishing Co., New York.

Schlicting H, 1968. *Boundary layer theory.* McGraw Hill, New York.

Spalding D B, 1989. *The PHOENICS beginners guide*, CHAM TR/100.

White F M, 1976. *Fluid Mechanics*. McGraw-Hill, New York.

APPENDICES

Appendix A - Profile coordinates of plenum contraction.

Inlet width, D1=80 mm

Outlet width D2=20 mm

EPSILON = 0.57165

Q(inlet) = -2.1683

Q(outlet) = 2.1683

TRUE LENGTH =144.61

REF.	XA VALUE	YA VALUE
1	0	10
2	3.098	10.017
3	6.197	10.073
4	9.296	10.182
5	12.398	10.369
6	15.507	10.684
7	18.634	11.201
8	21.808	12.047
9	25.109	13.415
10	28.730	15.576
11	33.107	18.815
12	35.805	20.864
13	38.986	23.139
14	42.731	25.534
15	47.064	27.910
16	51.944	30.133
17	57.278	32.108
18	62.959	33.793
19	68.883	35.186

20	74.972	36.315
21	81.167	37.216
22	87.430	37.927
23	93.735	38.485
24	100.066	38.919
25	106.413	39.254
26	112.771	39.509
27	119.134	39.699
28	125.500	39.836
29	131.869	39.929
30	138.239	39.983
31	144.610	40.000

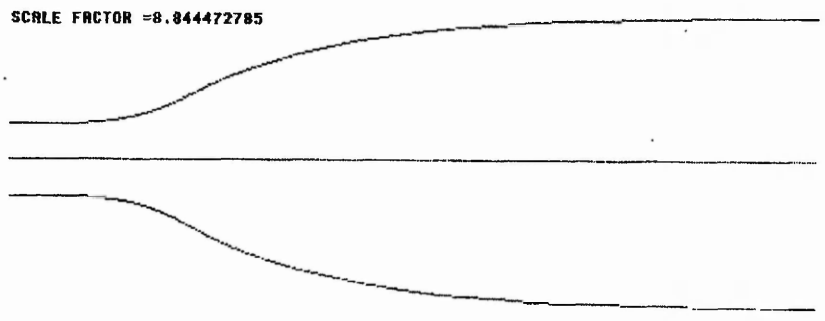

Appendix B - Design of traverse mechanism and software for control of measurement system.

B.1 Background

At the commencement of this project a traverse mechanism with minimum flow interference was required to position the measurement volume of the LDA system operating in forward scatter mode. With the large number of measurement stations required for the detailed LDA investigation, the amount of data to be collected and data processing required at each of these stations, this was clearly an ideal application for microcomputer control. It was desired to commission the traverse and instrumentation system at a lower cost as possible.

Commercially available traverse systems on offer by both LDA manufacturers and independent companies were considered but the necessary modifications for this application resulted in quotations far in excess of the allowed budget. The traverse was therefore designed and built as part of this project. The method of approach and experience gained are likely to be applicable to laboratory scale traversing gears.

Data is obtained while traversing the LDA system along one coordinate (X) while keeping the other coordinate (Z) fixed. The range of X and Z is 0.5 m and 0.25 m respectively.

In the first instance a literature review was conducted to establish if a suitable system had already been designed elsewhere. Very few detailed relevant descriptions were found in the archived literature. Various types of instrumentation and their interface to a desk-top microcomputer for wind tunnel applications have been previously recorded by Savory and Toy (1984) but are only described in brief. A detailed account of microcomputer controlled traverse gear for three dimensional flow explorations has been described by Shayesteh and Bradshaw (1987) for flow measurement devices requiring a smaller scale traverse system, for example, Pitot tubes and hot-wire probes. A further paper by Löfdahl (1988) addressed the

fundamental problems of controlling movement of the sensor rather than details of the traverse system. Button (1977) described the design and calibration of a two-dimensional traverse system, with both axis in the horizontal plane for small probes, which provided some useful suggestions, especially in the testing of the completed system. Srikantaiah et al. (1988) used a similar approach to this instrumentation system using different hardware for communication with counter processors and integrated with a portable TSI Inc. LDV system. Consequently the developed software is considerably different.

B.2 The traversing gear

The main constraint on the design of the traverse was the need to minimise interference with the flow field and to be able to traverse the LDA transmission and collection optics simultaneously in a vertical direction, on opposite sides of the flow field. A central traverse unit was adopted, to carry both the transmission and collection optics, as opposed to obtaining simultaneous motion by traversing the optics using separate mechanisms or by gearing system. The main concern was then to minimise any vibration caused by the motors which would be amplified to the optics via the supporting frame structure, which was essentially a cantilever arrangement mounted directly on the horizontal traverse mechanism.

Figure B.1 shows the general arrangement of the traverse mechanism. The flow straightening section (1) and jet impingement arrangement (2) were supported from the floor by an outer frame structure (16). The complete traverse assembly was positioned on a surface plate (17), which was also supported by the outer frame (16). The LDA transmission optics (3) were mounted on a small manual traverse (4) with resolution of 0.02 mm to facilitate small positional adjustments of the optics in the Y direction. A once only adjustment is necessary in this direction during initial set-up or when the optics are tilted to make one of the laser beams parallel with a surface, for example, when making near wall

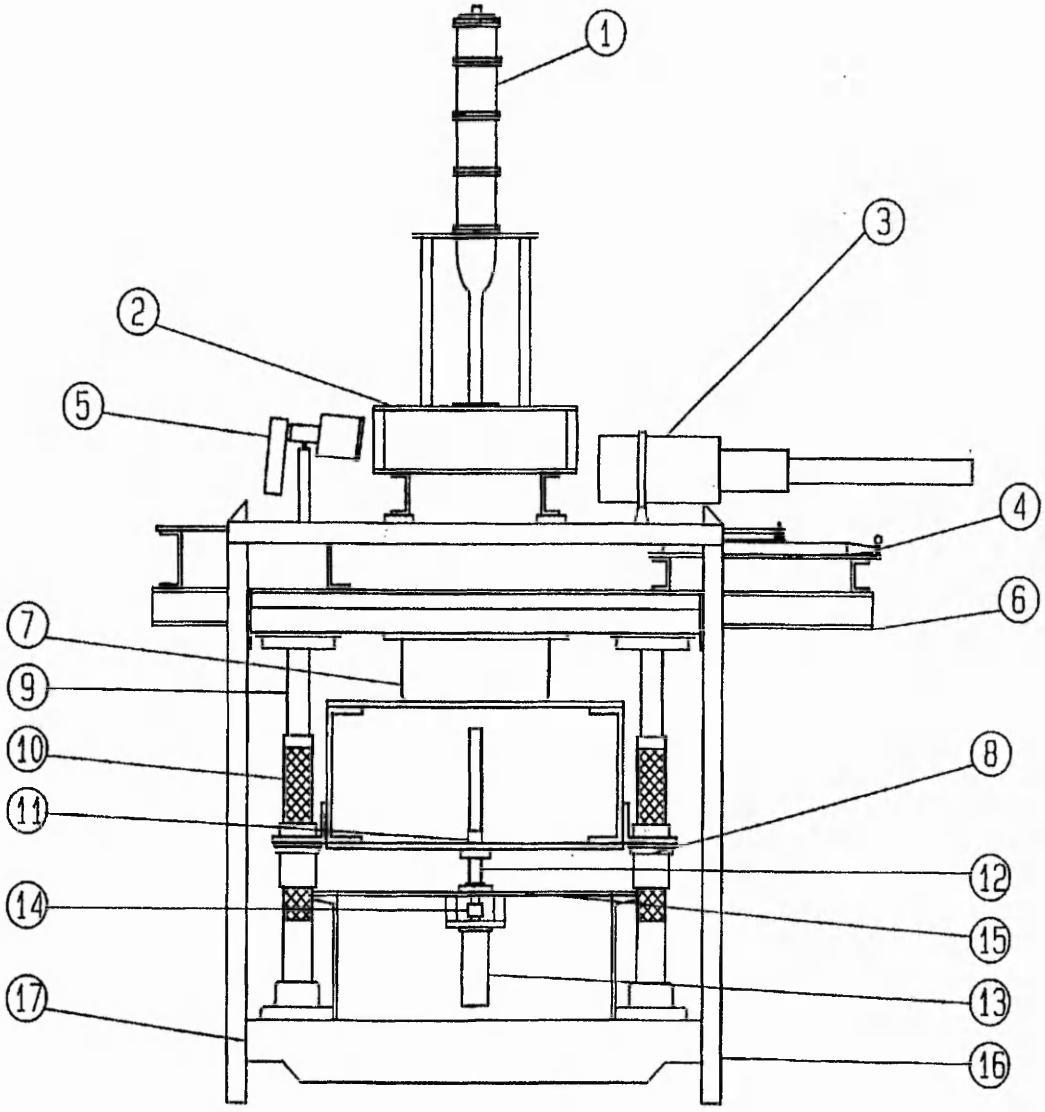

Figure B.1 General arrangement of traverse mechanism.

measurements. The transmission optics (3) and collection optics (5) were mounted on a further frame structure (6) which was supported by the X-direction drive unit (7). The linear X motion was provided by driving this framework (6) along two slideways by means of a lead screw connected to a digital stepper motor (not drawn), which was fixed to the X-direction drive unit. This drive unit was mounted on the upper square plate of the Z axis carriage, which was fixed to four ball bearing bushes (8). The carriage was guided

throughout the vertical traverse by four telescopic bearing arrangements consisting of a guide pillar (9) fixed to the surface plate (17), ball cage (10) and ball bearing bush (8). The structure was driven in the Z-direction by means of a ball nut attached to the plate (11) and lead screw (12) connected to another stepper motor (13), and supported by the axial thrust bearing assembly (14). The motor was secured to the support structure (15). Both lead screws were made from induction hardened thread rolled bar. The lead screw pitch was 5 mm with pitch accuracy of 50 μm/300 mm. The complete assembly was mounted on vibration isolated feet.

The X and Z stepper motors were controlled by CD20 and CD30 bipolar drives respectively, from Parker Digiplan Ltd. (1987a and 1987b). The motors gave 400 steps/revolution yielding an achievable resolution of 12.5 μm. The unit has the facility to datum to a point near to the extreme of each axis, provided by an inductive proximity switch. The switch was approached at high speed in the negative direction and over-travelled. The drive was then reversed and the switch approached in the positive direction at slow speed. The datum has then been approached in the same direction as the measurement stations to counter backlash. Emergency stops were also provided at the very extreme of the axes by reed proximity switches.

Tests were made to check the mechanical accuracy of the traverse system under measurement conditions. This was to determine the accuracy of the leadscrew pitch, to examine for incremental and periodic errors and to obtain backlash values at various stations along the leadscrews. Controlled by the computer, the traverse was moved to equi-spaced stations, selected at random, and then moved in 5 mm steps, forwards and backwards, for this purpose. The axes were set to their datum at the start of each test. The errors were measured using a linear variable differential transducer (LVDT) and a dial test indicator

(DTI). The maximum backlash found was 0.01 mm in axis X and 0.05 mm in axis Z. The positional errors varied between ±0.015 mm along axis X and ±0.085 mm along axis Z. To ensure complete removal of backlash, measurement points were always approached in the positive direction. If travelling back to a point, it would be over travelled and the drive reversed to approach the point in the positive direction. The motor speeds are program controlled in steps/s and are variable up to a mechanical restriction of 5000 steps/s, although the electronics are capable of speeds far in excess of this.

B.3 Computing facility and software

A schematic arrangement of the complete measurement system was presented in Figure 3.6. The computer was a Commodore 4032-PET micro-computer with the associated peripherals available such as disk drive, cassette player, plotter and paper printer. The traversing unit and signal processor were controlled, and data read from the processor via an IEEE-488 Standard Bus Interface. The operating system was BASIC 4.0. In order to use the IEEE-488 bus on the PET at maximum speed, it was necessary to use machine language rather than BASIC statements for data transfer. The routine presented here for data collection was based on an article by Cooke (see Fisher and Jenson, 1982). His IEEE handshake procedure, implemented in assembly language, produced transfers on the GPIB of up to 5000 bytes/s as opposed to 75 readings/s achieved using standard CBM statements. The routine was stored within the main program using DATA statements. The BASIC program, Ashforth-Frost (1988) sends the traverse to datum then positions the measurement volume of the LDA system at some predetermined position. The user then selects frequency range, filter bandwidth, frequency shift, number of batches of data to be collected, calibration factor and traverse speed, acceleration and increment to the next measurement station. The program checks user input variables and processor status before allowing data collection to proceed. This has been implemented to avoid the collection of non-valid data.

Five bytes of data are read from the processor which contain values of the parameters input by the user, status of the processor and frequency information. The read values of range and bandwidth are checked against those input by the user, the lock status is checked for the 'in-lock' condition and the frequency shift calculated. This information is deduced from the bytes using the BASIC AND function. 256 samples of data over a variable number of batches, selected by the user, are then collected. Data is only processed by the microcomputer or transmitted to store if the frequency out lies within the relevant code range of the processor. Batch results and cumulative results of mean velocity and turbulence intensity are displayed on screen and printed, if required. Data can be stored using the CBM 2031 disk drive or transferred to an ACT Apricot allowing later communication with the VAX 4600 computer.

B.4 Interfacing

The IEEE-488 interface allows the CBM computer to communicate with the external peripherals and other devices. This standard bus, permitting interchange of data between devices, is described in the IEEE document IEEE-488 published in 1978 and based on a 1975 standard. Any devices, subject to certain limitations become plug-compatible and able to transmit and receive ASCII (American Standard Code on Information Interchange) data. The bus consists of sixteen lines, eight of which are bi-directional data lines, each carrying one bit of data, for transfer between the CBM and selected device; the result is often described 'bit parallel', as opposed to 'byte serial' transmission of the RS-232, which operates with two lines only. The CBM relies on the IEEE's,secondary address feature to identify which device is to be addressed. Files can be opened to tape, disk, printer, signal processor, frequency shifter, traverse controller, oscilloscope or any IEEE device. Using the BASIC OPEN and PRINT# statements the CBM can distinguish between several files open at one time.

Transfer of data to the ACT Apricot involves the conversion of bit parallel data to byte serial. Assuming a hardware interface exists to convert IEEE-488 to RS-232, a file can be opened as usual, and also control characters sent to alter spacing, line separation or other feature.

The transfer of data from the PET IEEE port to the Apricot serial port is performed using a Black Box communications interface adapter (CIA), Black Box Catalogue Ltd. (1985). This device provides three input and three output ports providing any combination of input/output of RS-232, Centronics and IEEE-488. Valid data is input from the IEEE port and stored in a First-In-First-Out (FIFO) buffer providing a limited amount of temporary storage up to 256 Kbytes long. When any characters are present in this buffer the CIA will output data via the active port, RS-232. If transmission is inhibited, or the rate at which characters are received consistently exceeds the rate at which they are re-transmitted, the FIFO buffer will fill until no more characters can be received. Further character input is then determined by the output rate. For this application the maximum data transfers of input and output ports are IEEE-488 3000 chars/s and RS-232 19200 baud. The ASCII code is largely followed by CBM equipment, but there are some differences and care should be taken in using this device without first transforming the data to be transferred into true ASCII. One major difference is the use of the high bit as a parity bit. CBM's version of ASCII has no parity bit. For this application transformation has not been necessary since the numeric data to be transferred is the same in both cases.

Data is received at the Apricot using poly-TRM/VT software, ACT Pulsar Ltd. (1984). This is a simple to use menu driven program which allows the ACT Apricot to emulate an asynchronous ASCII terminal.Settings needed for serial communication are easily defined to meet the requirements of the peripherals. The transmission format is defined as follows;

number of data bits, 7, number of stop bits, 1 and parity bit, none. The baud rate is set to 2400 baud and the handshaking is set to Xon/Xoff to control the flow of information. This option causes Xoff commands to temporarily halt,the flow of characters from the Apricot to prevent character overruns. The same poly-TRM/VT software allows the data stored by the Apricot to be transferred to a VAX 4600 computer.

B.5 Machine language routine for data transfer

The IEEE bus handshake procedure in machine language - fully commented.

MAIN PROGRAM:

Memory location (Hex)	Memory location (Dec)	Machine Code (Hex)			Machine Code (Dec)			Instruction (Assembler)	Comments
1800	32256	A2	00		162	000		LDX#00	Load X with 00. Prepare index register
1802	32256	A9	FB		169	251		LDA#FB	Set ATN out low. Bytes sent to device to be treated as a command not data
1804	32260	2D	40	E8	045	064	232	ANDE840	Perform logical AND memory with accumulator.
1807	32263	8D	40	E8	141	064	232	STAE840	Store result back in address referenced by the opcode
180A	32266	A9	4C		169	076		LDA#4C	CBM acting as controller sends address 4C (76 decimal) to the tracker. C inicates device 12 and 4 that it is to be a talker.
180C	32268	85	01		133	001		STA01	Store in $0001
181C	32270	20	80	7E	032	128	126	JSR 7E80	Jump to new address 7E80
181F	32273	A9	FD		169	253		LDA#FD	Set NRFD out low
1821	32275	2D	40	E8	045	064	232	ANDE840	
1824	32278	8D	40	E8	141	064	232	STAE840	
1827	32281	A9	F7		169	247		LDA#F7	Set NDAC out low
1829	32283	2D	21	E8	045	033	232	ANDE821	
182C	32286	8D	21	E8	141	033	232	STAE821	
182F	32289	A9	04		169	004		LDA#04	Set ATN out high
1831	32291	0D	40	E8	013	064	232	ORAE840	Send data not IEEE commands.
1834	32294	8D	40	E8	141	064	232	STAE840	
1837	32297	A0	00		160	000		LDY#00	Y to count 256 bytes
1839	32299	20	B0	7E	032	176	126	JSR7EB0	Jump to new address 7EB0
183C	32302	A5	02		165	002		LDA02	Load accumulator with contents of $0002
183E	32304	9D	00	7F	157	000	127	STA7F00,X	Store value in $7F00+X - CBM memory location 32512+X
1841	32307	E8			232			INX	Increment X
1842	32308	88			136			DEY	Decrement Y
1843	32309	D0	F4		208	244		BNE1839	Branch (jump back) if Y is not zero.(Z flag=1)
1845	32311	A9	FB		169	251		LDA#FB	Set ATN out low.
1847	32313	2D	40	E8	045	064	232	ANDE840	Send IEEE commands not data.
184A	32316	8D	40	E8	141	064	232	STAE840	
184D	32319	A9	02		169	002		LDA#02	Set NRFD out high
184F	32321	0D	40	E8	013	064	232	ORAE840	
1852	32324	8D	40	E8	141	064	232	STAE840	
1855	32327	A9	08		169	008		LDA#08	Set NDAC out high
1857	32329	0D	21	E8	013	033	232	ORAE821	
185A	32332	8D	21	E8	141	033	232	STAE821	

Main program continued...

```
185D  32335  A9  5F        169  095        LDA#5F    UNT. $5F transferred as
                                                     a primary address causes
                                                     untalk command to be
                                                     issued
185F  32337  85  01        133  001        STA01     Store in $0001
1861  32339  20  80  7E     032  128  126   JSR7E80   Jump to new address 7E80
1864  32342  A9  04        169  004        LDA#04    Set ATN out high
1866  32344  0D  40  E8     013  064  232   ORAE840
1869  32347  8D  40  E8     141  064  232   STAE840
186C  32350  60             096             RTS       Return to BASIC program.
```

SUBROUTINE - 7E80 - **Handshake into bus**

```
1880  32384  AD  40  E8     173  064  232   LDAE840   NRFD?
1883  32387  29  40        041  064        AND#40    Wait until NRFD in is
                                                     high
1885  32389  F0  F9        240  249        BEQ1880   Branch if Z flag=0
1887  32391  A5  01        165  001        LDA01     Get data byte from $01.
                                                     In m/c code the data is
                                                     EORed with $FF before
                                                     transmission. The CBM
                                                     output register is $E822
1889  32393  49  FF        073  255        EOR#FF    Complement it
188B  32395  8D  22  E8     141  034  232   STAE822   Send data to bus.
188E  32398  A9  F7        169  247        LDA#F7    Set DAV out low
1890  32400  2D  23  E8     045  035  232   ANDE823
1893  32403  8D  23  E8     141  035  232   STAE823
1896  32406  AD  40  E8     173  064  232   LDAE840   NDAC?
1899  32409  29  01        041  001        AND#01    Wait until NDAC in is
                                                     high
189B  32411  F0  F9        240  249        BEQ1896   Branch if Z flag=0 ie
                                                     accepted
189D  32413  A9  08        169  008        LDA#08    Set DAV out high
189F  32415  0D  23  E8     013  035  232   ORAE823
18A2  32418  8D  22  E8     141  034  232   STAE823
18A5  32421  A9  FF        169  255        LDA#FF    255 into bus. ie. output
                                                     register is set null
18A7  32423  8D  22  E8     141  034  232   STAE822
18AA  32426  60             096             RTS       Return to MAIN.
```

SUBROUTINE - 7EB0 - **Handshake from bus**

```
18B0  32432  A9  02        169  002        LDA#02    Set NRFD out high
18B2  32434  0D  40  E8     013  064  232   ORAE840
18B5  32437  8D  40  E8     141  064  232   STAE840
18B8  32440  AD  40  E8     173  064  232   LDAE840   DAV?
18BB  32443  29  80        041  128        AND#80    Wait until DAV in is
                                                     high
18BD  32445  D0  F9        208  249        BNE18B8   Branch if Z flag=0
```

Handshake from bus continued...

18BF	32447	AD	20	E8	173	032	232	LDAE820	Get character from input register
18C2	32450	49	FF		073	255		EOR#FF	Complement it.
18C4	32452	85	02		133	002		STA02	Store in $0002
18C6	32454	A9	FD		169	253		LDA#FD	Set NRFD out low
18C8	32456	2D	40	E8	045	064	232	ANDE840	
18CB	32459	8D	40	E8	141	064	232	STAE840	
18CE	32462	A9	08		169	008		LDA#08	Set NDAC out high
18D0	32464	0D	21	E8	013	033	232	ORAE821	
18D3	32467	8D	21	E8	141	033	232	STAE821	
18D6	32470	AD	40	E8	173	064	232	LDAE840	DAV?
18D9	32473	29	80		041	128		AND#80	Wait until DAV in is high
18DB	32475	F0	F9		240	249		BEQ18D6	Branch if Z flag=0 ie. DAV is high
18DD	32477	A9	F7		169	247		LDA#F7	Set NDAC out low
18DF	32479	2D	21	E8	045	033	232	ANDE821	
18E2	32482	8D	21	E8	141	033	232	STAE821	
18E5	32485	A9	FF		169	255		LDA#FF	255 into bus. ie. output register is set null.
18E7	32487	8D	22	E8	141	034	232	STAE822	
18EA	32490	60			096			RTS	Return to MAIN.

IEEE bus handshake routine listing:

CBM memory location	Machine code (decimal)							
	(Main program)							
32256	162	000	169	251	045	064	232	
32263	141	064	232	169	076	133	001	
32270	032	128	126	169	253	045	064	232
32278	141	064	232	169	247	045	033	232
32286	141	033	232	169	004	013	064	232
32294	141	064	232	160	000	032	176	126
32302	165	002	175	000	127	232	136	
32309	208	244	169	251	045	064	232	
32316	141	064	232	169	002	013	064	232
32324	141	064	232	169	008	013	033	232
32332	141	033	232	169	095	133	001	
32339	032	128	126	169	004	013	064	232
32347	141	064	232	096				
	(Handshake to bus)							
32384	173	064	232	041	064	240	249	
32391	165	001	073	255	141	034	232	
32398	169	247	045	035	232	141	035	
32406	173	064	232	041	001	240	249	
32413	169	008	013	035	232	141	035	232
32421	169	255	141	034	232	096		
	(Handshake from bus)							
32432	169	002	013	064	232	141	064	232
32440	173	064	232	041	128	208	249	
32447	173	032	232	073	255	133	002	
32454	169	253	045	064	232	141	064	232
32462	169	008	013	033	232	141	033	232
32470	173	064	232	041	128	240	249	
32477	169	247	045	033	232	141	033	232
32485	169	255	141	034	232	096		

B.6 BASIC software for data collection on PET 4032

```
100 REM            PROGRAM TO REMOTELY CONTROL
120 REM             THE LASER-DOPPLER ANEMOMETRY
130 REM         FREQUENCY TRACKER SIGNAL PROCESSOR
135 REM
140 REM           BY S A ASHFORTH-FROST (1990)
145 REM
150 REM        (C) NOTTINGHAM POLYTECHNIC,NOTTINGHAM.
160 REM
170 REM
180 REM ********IEEE 488 BUS HANDSHAKE:
190 REM  ***MAIN PROGRAM
200 DATA 162,000,169,251,045,064,232
210 DATA 141,064,232,169,076,133,001
220 DATA 032,128,126,169,253,045,064,232
230 DATA 141,064,232,169,247,045,033,232
240 DATA 141,033,232,169,004,013,064,232
250 DATA 141,064,232,160,000,032,176,126
260 DATA 165,002,157,000,127,232,136
270 DATA 208,244,169,251,045,064,232
280 DATA 141,064,232,169,002,013,064,232
290 DATA 141,064,232,169,008,013,033,232
300 DATA 141,033,232,169,095,133,001
310 DATA 032,128,126,169,004,013,064,232
320 DATA 141,064,232,096
330 REM ***HANDSHAKE TO BUS
340 DATA 173,064,232,041,064,240,249
350 DATA 165,001,073,255,141,034,232
360 DATA 169,247,045,035,232,141,035,232
370 DATA 173,064,232,041,001,240,249
380 DATA 169,008,013,035,232,141,035,232
390 DATA 169,255,141,034,232,096
400 REM ***HANDSHAKE FROM BUS
410 DATA 169,002,013,064,232,141,064,232
420 DATA 173,064,232,041,120,208,249
430 DATA 173,032,232,073,255,133,002
440 DATA 169,253,045,064,232,141,064,232
450 DATA 169,008,013,033,232,141,033,232
460 DATA 173,064,232,041,128,240,249
470 DATA 169,247,045,033,232,141,033,232
480 DATA 169,255,141,034,232,096
500 RESTORE
510 REM
520 REM
530 REM ***START OF IEEE-488 HANDSHAKE INSTALLATION
540 REM ***INSERT MAIN PROGRAM TO MEMORY
550 FOR I=1TO95
560 READ ML%
570 IR=32255+I
580 POKE IR,ML%
590 NEXTI
600 REM ***INSERT SUBROUTINE FOR HANDSHAKE INTO BUS
610 FOR I=1TO43
620 READ ML%
630 IR=32383+I
640 POKE IR,ML%
650 NEXTI
660 REM ***INSERT SUBROUTINE FOR HANDSHAKE FROM BUS
670 FOR I=1TO59
680 READ ML%
690 IR=32431+I
```

```
700 POKE IR,ML%
710 NEXT I
720 REM ***MAKE SPACE IN CBM MEMORY FOR PROCEDURE
750 POKE 48,254
760 POKE 49,125
770 POKE 50,255
780 POKE 51,125
790 POKE 52,255
800 POKE 53,125
810 REM ***END OF IEEE-488 HANDSHAKE PROCEDURE AND INSTALLATION
820 REM
830 REM ***READ ALL VARIABLES
840 REM
845 DIM MR(7),DR%(5),DT$(5),FD(256,16)
846 MR(1)=10./256
847 MR(2)=33./256
848 MR(3)=100./256
849 MR(4)=333./256
850 MR(5)=1000./256
851 MR(6)=3333./256
852 MR(7)=10000./256
855 PRINT"□"
860 PRINT"    PROGRAM TO REMOTELY CONTROL"
861 PRINT
862 PRINT"      LASER-DOPPLER ANEMOMETRY"
863 PRINT
864 PRINT"FREQUENCY TRACKER SIGNAL PROCESSOR"
865 PRINT
866 PRINT
867 PRINT"BEFORE PROCEEDING, ENSURE THAT THE"
868 PRINT
869 PRINT"PROCESSOR IS OPERATING IN REMOTE"
871 REM****INPUT TRAVERSE PARAMETERS
872 Z=0:X=0:INC=0:MOVES=0
874 PRINT:PRINT
875 PRINT"ENTER START COORDINATES:"
876 PRINT
878 PRINT"REMEMBER TO TAKE OFF 10MM & APPLY"
879 PRINT"CORRECTION TO LVDT DISPLAY FOR Z READING"
887 INPUT" Z (MM FROM PLATE)";Z
888 INPUT" X (MM FROM AXIS)";X
890 INPUT" X INCREMENT (STEPS)";INC
891 PRINT"INCREMENT MUST BE IN LINE# 2316"
892 INPUT" NUMBER OF INCREMENTS TO X";MOVES
898 INPUT" TITLE AND DATE OF DATA FILE";NAME$
920 REM
926 PRINT
1070 A$="7"
1080 RA%=ASC(A$)-48
1090 B$="4"
1120 BW%=ASC(B$)-49
1130 REM
1140 REM ***WRITE RANGE, BANDWIDTH & ADDRESS TO PROCESSOR
1160 CW$=CHR$(128+BW%*8+RA%)
1170 OPEN 5,44: REM PROCESSOR LISTEN ADDRESS 44
1180 PRINT# 5,CW$;
1190 CLOSE 5
1200 REM
1210 REM ***READ MODE, LOCK STATUS, BANDWIDTH, RANGE & FREQUENCY SHIFT
1230 FOR I=1TO50:NEXT I:REM ***WAIT 0.5SEC
1240 OPEN 5,76: REM PROCESSOR TALK ADDRESS 76
1250 FOR I=1TO5
```

```
1260 : GET# 5,DT$(I)
1270 : DR%(I)=0
1280 : IF LEN(DT$(I))=1THEN DR%(I)=ASC(DT$(I))
1290 NEXT I
1300 CLOSE 5
1310 REM
1320 REM ***CALCULATE FREQUENCY SHIFT
1330 XX=DR%(1)AND127
1340 E=(DR%(1)AND48)/16
1350 M=DR%(1)AND15
1360 M=15-M
1370 IF(E>0ANDE<4ANDM>0ANDM<10)OR(E=3ANDM=0)THEN FS=M*10↑E
1380 IF XX>63 THEN FS=-1*FS: IF XX<64THEN FS=FS
1390 PRINT"■"
1400 PRINT"FREQUENCY SHIFT=";FS;"KHZ"
1402 REM ***CHECK STATUS
1405 IF(DR%(1)AND128)=128 THEN PRINT"LOCK READ FROM THE TRACKER":PRINT
1406 IF (DR%(1)AND128)=0 THEN PRINT"LOCK ASSUMED":PRINT
1410 REM ***CHECK IF IN LOCK
1420 IF(DR%(4)AND32)=32THEN PRINT"■";"TRACKER IN LOCK"
1430 IF(DR%(4)AND32)=32THEN1530
1440 IF(DR%(4)AND32)=0 THEN PRINT"■";"TRACKER NOT IN LOCK"
1450 PRINT"■■■■"
1520 GOTO 1140
1530 REM
1540 REM ***CHECK RANGE AND BANDWIDTH READ FROM PROCESSOR TO THAT
1560 REM ***INPUT BY THE USER
1570 RBW%=(DR%(4)AND24)/8
1580 IF RBW%=BW% GOTO1600
1590 PRINT "BANDWIDTH SETTING ERROR":GOTO 0930
1600 RRA%=(DR%(4)AND7)
1610 IF RRA%=RA% GOTO1630
1620 PRINT"RANGE SETTING ERROR":GOTO 0930
1625 REM
1630 REM ***LOOK AT MODE OF OPERATION
1640 IF(DR%(4)AND128)=128 THEN PRINT"INHIBIT SELECTED"
1645 PRINT
1650 IF(DR%(4)AND64)=64 THEN PRINT"TRANSMISSIONS DO NOT AWAIT DR SIGNAL"
1660 PRINT"■":PRINT"STATUS OK"
1700 REM ***CONTINUOUS FREQUENCY READING
1710 REM ***USING MACHINE CODE:
1770 REM
1825 NB%=12
1830 PRINT"■"
1840 PRINT NB%;"BATCHES OF DATA TO BE COLLECTED"
1860 OPEN3,6
1865 PRINT#3,CHR$(10)
1870 PRINT#3,CHR$(10)
1880 PRINT#3,MOVES;CHR$(10)
2012 OPEN4,4
2014 PRINT#4,NAME$;MOVES
2040 REM
2045 FOR K=0 TO MOVES
2050 REM ***CALL HANDSHAKE ROUTINE FOR IEEE
2060 REM
2080 SUM=0:MV=0:N=0
2160 REM
2170 PRINT:  PRINT "COLLECTING DATA":PRINT
2175 FOR J=1TO NB%
2180 SYS(32256)
2185 I=0
2186 REM **READ & SUM DATA
2190 FOR I=1 TO 256
```

```
2200 : ID%=PEEK(32511+I)
2201 : IF ID%<19 THEN FD(I,J)=9999.99
2202 : IF ID%<19 THEN 2270
2220 : FD(I,J)=(ID%*MR(RA%))-FS
2230 : SUM=SUM+FD(I,J)
2250 : N=N+1
2270 NEXT I
2275 NEXT J
2300 REM******TRAVERSE ROUTINE
2304 REM
2308 IF K>MOVES OR K=MOVES THEN 2350
2312 OPEN9,9
2316 PRINT#9,"X+80$"
2320 REM****CHECK MOTION COMPLETE
2324 OPEN6,9,0
2328 GET#6,A$,X$,X$
2330 IF(ST<>0)THEN2328
2331 R=ASC(A$)
2332 IF(RAND8)=8 THEN2328
2335 CLOSE6
2350 MV=(SUM/N)*6.34/1000
2400 PRINT"WRITING DATA TO APRICOT"
2410 PRINT#3,X;Z;N;MV;CHR$(10)
2430 FOR J=1 TO NB%
2440 I=0
2450 FOR I=1 TO 256
2460 IF(INT(I/13)-(I/13))=0 THEN PRINT#3,CHR$(10)
2470 IF FD(I,J)=9999.99 GOTO 2485
2480 PRINT#3,FD(I,J);
2485 NEXT I
2490 NEXT J
2496 PRINT#3,CHR$(10)
2500 REM
2505 PRINT: PRINT"RESULTS AT THE FOLLOWING POSITION ARE":PRINT
2506 PRINT "X COORDINATE=";X;"MM"
2507 PRINT "Z COORDINATE=";Z;"MM":PRINT
2510 PRINT"V-MEAN(M/S)=";MV
2540 PRINT"SAMPLES N=  ";N
2570 REM
2602 PRINT#4,X;Z;N;MV
2620 X=X+INC*25.4/2000
2666 REM****CHECK FAULT STATUS
2670 OPEN7,9,4
2675 GET#7,A$,X$,X$
2680 IF(ST<>0) THEN2675
2685 R=ASC(A$)
2690 CLOSE7
2695 IF(RAND15)=0 THEN 2720
2700 IF(RAND1)=1 THEN PRINT"DATA FAULT"
2705 IF(RAND2)=2 THEN PRINT"EMERGENCY STOP"
2710 IF(RAND4)=4 THEN PRINT"DRIVE FAULT"
2715 IF(RAND8)=8 THEN PRINT"STALL FAULT"
2720 REM****CHECK POSITION
2725 OPEN7,9,8
2730 INPUT#7,B$
2735 IF(ST<>0)THEN 2730
2740 CLOSE7
2745 B=0
2750 FOR XX=(LEN(B$)-1) TO 0 STEP-1
2755 S=LEN(B$)-XX
2760 W$=MID$(B$,S,1)
2765 IF W$<"A" GOTO 2775
2770 B=B+16↑XX*(ASC(W$)-55):GOTO 2780
```

```
 2775 B=B+16↑XX*(VAL(W$))
 2776 REM PRINT"W$=";W$
 2777 REM PRINT "B=";B
 2780 NEXT XX
 2790 REM*****IF ALL STEPS COMPLETED THEN CONTINUE
 2800 IF B=0 THEN 2840
 2810 REMFXCO=X0+(INC-B)*25.4/2000
 2820 REMPRINT"DISTANCE FROM AXIS=",FXCO
 2830 GOTO 5000
 2840 REM
 2860 CLOSE9
 2900 NEXT K
 3000 CLOSE3:CLOSE4
 3900 PRINT
 4000 PRINT"REMEMBER TO SAVE DATA TO DISK"
 4010 PRINT
 5000 END
READY.
```

B.7 FORTRAN software for data analysis on VAX 4600

```
      PROGRAM ANALYSIS

      Character Word*250
      Character DOCh*12
      Character DOChp*12
      Character DOChm*12
c     Character DOCOUT*12
      DIMENSION FD(2560,250),N(250),FS(250),XCO(250),ZCO(250),VM(50)
      DIMENSION SM(250),EXC(250),skEW(250),RMS(250),VELY(250),DIFF(250)
      DIMENSION Umean(50),Vmean(50),uv(50),u2(50),v2(50)

c     Program to read DATA sent from pet via apricot
C     LOC=MOVES+1=number of radial locations; N=total number of DATA (ie.2560)
C     XCO,ZCO=X,Z coordinates; FD=Doppler Frequency; FI=Instantaneous Frequency
C     Calibration factor=6.34 ms-1/MHz.
C


      WRITE(6,*) 'Enter name of HORIZONTAL input file: eg. h0_4.dat'
      READ(5,4) DOCh
      WRITE(6,*) 'Enter name of PLUS input file: eg. hp0_4.dat'
      READ(5,4) DOChp
      WRITE(6,*) 'Enter name of MINUS input files: eg. hm0_4.dat'
      READ(5,4) DOChm
      VSh=19.175
      VShm=19.175
      VShp=19.175
      VSh=VSh*0.805
      VShm=VShm*0.805
      VShp=VShp*0.805
      VSm=(VSh+VShm+VShp)/3

4     FORMAT (3(A12))
C
c     Co-ordinate axes of Reynolds stress equations differ from
c     those used for LDA data collection, such that data saved in
c     hp?.dat must be used as hm?.dat and vice versa in RE.FOR.
c     Note that this is done by making unit 15 hm?.dat instead of
c     unit 13 etc.
c
C     Absolute values of results files:
```

```
      OPEN(UNIT=25,FILE='re.out',STATUS='UNKNOWN',ACCESS='APPEND')

OPEN(UNIT=22,FILE='hM.out',STATUS='UNKNOWN',ACCESS='APPEND')
      OPEN(UNIT=23,FILE='hP.out',STATUS='UNKNOWN',ACCESS='APPEND')
      OPEN(UNIT=24,FILE='h.out',STATUS='UNKNOWN',ACCESS='APPEND')
c     Results non-dimensionalised with bulk jet exit velocity

OPEN(UNIT=14,FILE='reND.out',STATUS='UNKNOWN',ACCESS='APPEND')


OPEN(UNIT=16,FILE='hpND.out',STATUS='UNKNOWN',ACCESS='APPEND')

OPEN(UNIT=17,FILE='hmND.out',STATUS='UNKNOWN',ACCESS='APPEND')
      OPEN(UNIT=18,FILE='hND.out',STATUS='UNKNOWN',ACCESS='APPEND')

      open(unit=11,file=DOCh,defaultfile='.dat',status='UNKNOWN')
      open(unit=13,file=DOChm,defaultfile='.dat',status='UNKNOWN')
      open(unit=15,file=DOChp,defaultfile='.dat',status='UNKNOWN')
c     open(unit=11,file='H4.DAT',status='UNKNOWN')
c     open(unit=15,file='HP4.DAT',status='UNKNOWN')
c     open(unit=13,file='HM4.DAT',status='UNKNOWN')
      open(unit=12,file='data.dat',status='unknown',ACCESS='APPEND',RECL=250)


c  ****Remove carriage returns included from ftp transfer to VAX

10    read(11,15,end=30) Word
15    format(A250)
      if (Word(1:7).eq.'9999.99') then
            write(12,15) Word(8:250)
      else
            write(12,15) Word(1:250)
      endif
      goto 10
30    CLOSE(11)

610   read(13,15,end=630) Word
      if (Word(1:7).eq.'9999.99') then
            write(12,15) Word(8:250)
      else
            write(12,15) Word(1:250)
      endif
      goto 610
```

```
630     CLOSE(13)

710     read(15,15,end=730) Word
        if (Word(1:7).eq.'9999.99') then
                write(12,15) Word(8:250)
        else
                write(12,15) Word(1:250)
        endif
        goto 710
730     CLOSE(15)

        CLOSE(12)
        WRITE(6,*) 'Raw data read & <CR> removed'

C       Read data from Apricot file transferred via drive e:

        open(unit=21,file='data.dat',status='unknown')

        LOC=0
        LOCLAST=0
        DO 40 J=1,3
        MOVES=0
        READ(21,*) MOVES
        WRITE(6,*) 'MOVES=',MOVES
        LOCLAST=LOC+1
        LOC=LOC+MOVES+1
        DO 2 L=LOCLAST,LOC
        READ(21,*) XCO(L),ZCO(L),N(L),VM(L)
        WRITE(6,*) L,N(L),XCO(L),ZCO(L),VM(L)
        I=1
        READ(21,*) (FD(I,L),I=1,N(L))
2       CONTINUE
40      CONTINUE
C
c       Analyse data
        DO 3 L=1,LOC
        SUM=0
        VELY(L)=0
        SM(L)=0
        SKEW(L)=0
        EXC(L)=0
C       Sum data to find mean
        DO 33 I=1,N(L)
```

```
      SUM=SUM+FD(I,L)
33    CONTINUE
      VELY(L)=SUM/N(L)
C     Subtract mean from instantaneous data to find RMS(L) and other
c     statistical quantities.
      DO 333 I=1,N(L)
      FI=FD(I,L)-VELY(L)
      SM(L)=SM(L)+FI**2
      SKEW(L)=SKEW(L)+FI**3
      EXC(L)=EXC(L)+FI**4
333   CONTINUE
      RMS(L)=SQRT(SM(L)/N(L))
      SKEW(L)=SKEW(L)/(N(L)*(RMS(L)**3))
      EXC(L)=EXC(L)/(N(L)*(RMS(L)**4))
      RMS(L)=RMS(L)/1000*6.34
      VELY(L)=VELY(L)/1000*6.34
c     Check that mean velocity calculated equals that recorded from PET
      DIFF(L)=(VM(L)-VELY(L))*100/VELY(L)
3     CONTINUE

C     Calculate Reynolds stress components where THETA=45 degrees.
c     U, u', V, v' are axial and radial, mean and rms velocities respectively.
c     INC is number of locations per velocity component ie. U, U+ and U-.
c     RMS=rms velocity by direct measurement in radial direction
c     VELY=mean velocity by direct measurement in radial direction
c     Umean=mean velocity by measurement of U+ and U- in axial direction
c     Vmean=mean velocity by measurement of U+ and U- in radial direction

      INC=LOC/3
      DO 50 L=1,INC
      Vmean(L)=(VELY(INC+L)+VELY(L+2*INC))/(2*0.70710678)
      Umean(L)=(VELY(INC+L)-VELY(L+2*INC))/(2*0.7071068)
      v2(L)=((RMS(INC+L)+RMS(L+2*INC))**2)/(4*(0.70710678**2))
      u2(L)=((RMS(INC+L)**2)+(RMS(L+2*INC)**2)-
     1 2*((RMS(L)**2)*(0.70710678**2)))/(2*(0.7071068**2))
      uv(L)=(RMS(INC+L)**2-RMS(L+2*INC)**2)/(4*0.7071068*0.70710678)
50    CONTINUE

C     Output all data:
c
      L=0
      DO 9999 L=1,LOC
```

```
c       Output Reynolds stress components:
        IF(L.LE.INC) THEN
          WRITE(25,20) XCO(L),ZCO(L),VELY(L),RMS(L)**2,SKEW(L),
     1   EXC(L),Vmean(L),Umean(L),v2(L),u2(L),uv(L)
          WRITE(14,25) XCO(L),ZCO(L),VELY(L)/VSm,RMS(L)**2/(VSm**2),
     1   SKEW(L),EXC(L),Vmean(L)/VSm,Umean(L)/VSm,
     2   v2(L)/(VSm**2),u2(L)/(VSm**2),uv(L)/(VSm**2)
20        FORMAT( F5.1,X,F5.2,2(X,F6.2),2(X,f5.1),5(X,F7.3))
25        FORMAT( F5.1,X,F5.2,X,F7.4,X,F8.5,X,2(X,f4.1),
     1   2(X,F7.4),3(X,F9.6))

c       Output statistical data for individual files:
          WRITE(24,200) XCO(L),ZCO(L),N(L),VELY(L),RMS(L)**2,SKEW(L),
     1   EXC(L)
          WRITE(18,250) XCO(L),ZCO(L),N(L),VELY(L)/VSm,RMS(L)**2/(VSm**2)
     1   ,SKEW(L),EXC(L)
200       FORMAT( F5.1,X,F5.2,i5,2(X,F6.2),2(X,F5.1))
250       FORMAT( F5.1,X,F5.2,i5,2(X,F7.4),2(X,F5.1))
        endif

        IF(L.GT.INC .AND. L.LE.(2*INC)) THEN
          WRITE(22,200) XCO(L),ZCO(L),N(L),VELY(L),RMS(L)**2,SKEW(L),
     1   EXC(L)
          WRITE(16,250) XCO(L),ZCO(L),N(L),VELY(L)/VShp,
     1   RMS(L)**2/(VShp**2),SKEW(L),EXC(L)
        endif

        IF(L.GT.(2*INC) .AND. L.LE.LOC) THEN
          WRITE(23,200) XCO(L),ZCO(L),N(L),VELY(L),RMS(L)**2,SKEW(L),
     1   EXC(L)
          WRITE(17,250) XCO(L),ZCO(L),N(L),VELY(L)/VShm,
     1   RMS(L)**2/(VShm**2),SKEW(L),EXC(L)
        endif

9999    CONTINUE

        IF (ABS(DIFF(L)).GT.1)THEN
          WRITE(6,*) '*ERROR**Mean velocity from PET differs from VAX by ',
     1    diff,' %'
        endif

        CLOSE(21,status='delete')
        CLOSE(14)
```

```
      CLOSE(16)
      CLOSE(17)
      CLOSE(18)
      CLOSE(22)
      CLOSE(23)
      CLOSE(24)
      CLOSE(25)
      WRITE(6,*) 'Results written to file  re.out, h.out, hp.out
     1and hm.out and non-dimensionalised in reND.out, hND.out,
     2hp.out and hm.out'
      STOP
      END
```

Appendix C - Data reduction equations and propagation of uncertainty for the measurement of Reynolds stress components.

Consider rotation of the LDA optics by an angle $\pm\theta$ about the principal velocity axis, in this case, the radial velocity as shown in Figure 3.11.

By resolving parallel to the measured velocity components at $\pm\theta$, equations for the principal velocities and the Reynolds stress components can be derived.

Consider the mean velocity components:

$$\begin{aligned} v_{\theta^+} &= v\cos\theta + u\sin\theta \\ v_{\theta^-} &= v\cos\theta - u\sin\theta \end{aligned} \tag{C.1}$$

Addition and re-arrangement of these equations leads to

$$\begin{aligned} v &= \frac{v_{\theta^+} + v_{\theta^-}}{2\cos\theta} \\ u &= \frac{v_{\theta^+} - v_{\theta^-}}{2\sin\theta} \end{aligned} \tag{C.2}$$

Similarly, for the stress components

$$\begin{aligned} v' &= \frac{v'_{\theta^+} + v'_{\theta^-}}{2\cos\theta} \\ u' &= \frac{v'_{\theta^+} - v'_{\theta^-}}{2\sin\theta} \end{aligned} \tag{C.3}$$

Hence

$$\overline{v'^2} = \frac{(v'_{\theta^+} + v'_{\theta^-})^2}{4\cos^2\theta} \tag{C.4}$$

$$\overline{u'^2} = \frac{(v'_{\theta^+} - v'_{\theta^-})^2}{4\sin^2\theta} \tag{C.5}$$

$$\overline{u'v'} = \frac{\overline{v'^2_{\theta^+}} - \overline{v'^2_{\theta^-}}}{4\cos\theta\sin\theta} \tag{C.6}$$

Since the radial component of velocity, v, is measured directly, only the uncertainties

propagated through Equations (C.5) and (C.6) need to be considered. The product $v'_{\theta+}v'_{\theta-}$ can be eliminated from the expansion of Equation (C.5), leading to

$$\overline{u'^2} = \frac{\overline{v'^2_{\theta^+}} + \overline{v'^2_{\theta^-}} - 2\overline{v'^2}\cos^2\theta}{2\sin^2\theta} \qquad \textbf{(C.7)}$$

Kline and McClintock (1953) showed that the uncertainty interval of a result $r=f(x_1,x_2.....x_n)$ is given by

$$\delta r = \left[\left(\frac{\partial r}{\partial x_1}\delta x_1\right)^2 + \left(\frac{\partial r}{\partial x_1}\delta x_1\right)^2 + ...\left(\frac{\partial r}{\partial x_1}\delta x_n\right)^2\right]^{0.5} \qquad \textbf{(C.8)}$$

where δx_i are the uncertainties in the measured variables x_i. All intervals must be based on the same interval width of the normal distribution.

Applying this uncertainty analysis procedure to Equations (C.6) and (C.7) leads to equations from which the uncertainties in the indirectly measured Reynolds stresses components can be evaluated based on directly measured components. Consider the shear stress component:

$$(\delta\overline{u'v'})^2 = \left[\left(\frac{\partial(\overline{u'v'})}{\partial\overline{v'^2_{\theta^+}}}\,\delta\overline{v'^2_{\theta^+}}\right)^2 + \left(\frac{\partial(\overline{u'v'})}{\partial\overline{v'^2_{\theta^-}}}\,\delta\overline{v'^2_{\theta^-}}\right)^2 + \left(\frac{\partial(\overline{u'v'})}{\partial\theta}\,\delta\theta\right)^2\right]^{0.5} \qquad \textbf{(C.9)}$$

The partial derivatives are:

$$\frac{\partial(\overline{u'v'})}{\partial\overline{v'^2_{\theta^+}}} = \frac{1}{4\cos\theta\sin\theta}$$

$$\frac{\partial(\overline{u'v'})}{\partial\overline{v'^2_{\theta^-}}} = \frac{-1}{4\cos\theta\sin\theta} \qquad \textbf{(C.10)}$$

$$\frac{\partial(\overline{u'v'})}{\partial\theta} = -\frac{\overline{u'v'}\cos 2\theta}{\cos\theta\sin\theta}$$

Substitution of these derivatives into Equation (C.9) leads to

$$(\delta\overline{u'v'})^2 = \left(\frac{\delta(\overline{v'^2_{\theta^+}})}{4\cos\theta\sin\theta}\right)^2 + \left(\frac{-\delta(\overline{v'^2_{\theta^-}})}{4\cos\theta\sin\theta}\right)^2 + \left(\frac{\overline{u'v'}\cos 2\theta\,\delta\theta}{\cos\theta\sin\theta}\right)^2 \qquad \text{(C.11)}$$

Since the radial and $\pm\theta$ components are measured directly then

$$\delta(\overline{v'^2}) = \delta(\overline{v'^2_{\theta^+}}) = \delta(\overline{v'^2_{\theta^-}}) \qquad \text{(C.12)}$$

and

$$(\delta\overline{u'v'})^2 = \frac{(\delta\overline{v'^2})^2}{8\cos^2\theta\sin^2\theta} + \left(\overline{u'v'}\frac{\cos 2\theta}{\cos\theta\sin\theta}\delta\theta\right)^2 \qquad \text{(C.13)}$$

Applying Equation (C.8) to the uncertainty in the normal stress component yields

$$(\delta\overline{u'^2})^2 = \left(\frac{\partial\overline{u'^2}}{\partial\overline{v'^2}_{\theta^+}}\delta\overline{v'^2}_{\theta^+}\right)^2 + \left(\frac{\partial\overline{u'^2}}{\partial\overline{v'^2}_{\theta^-}}\delta\overline{v'^2}_{\theta^-}\right)^2 + \left(\frac{\partial\overline{u'^2}}{\partial\overline{v^2}}\delta\overline{v'^2}\right)^2 + \left(\frac{\partial\overline{u'^2}}{\partial\theta}\delta\theta\right)^2 \qquad \text{(C.14)}$$

The partial derivatives are:

$$\frac{\partial\overline{u'^2}}{\partial\overline{v'^2}_{\theta^+}} = \frac{1}{2\sin^2\theta}$$

$$\frac{\partial\overline{u'^2}}{\partial\overline{v'^2}_{\theta^-}} = \frac{1}{2\sin^2\theta} \qquad \text{(C.15)}$$

$$\frac{\partial\overline{u'^2}}{\partial\overline{v'^2}} = -\frac{\cos^2\theta}{\sin^2\theta}$$

$$\frac{\partial\overline{u'^2}}{\partial\theta} = \frac{2\cos\theta}{2\sin^3\theta}\left(2\overline{v'^2}\sin^2\theta - [\overline{v'^2_{\theta^+}} + \overline{v'^2_{\theta^-}} - 2\overline{v'^2}\cos^2\theta]\right) = \frac{2(\overline{v'^2} - \overline{u'^2})}{\tan\theta}$$

which leads to

$$(\delta\overline{u'^2})^2 = \frac{(\delta\overline{v'^2})^2(1+2\cos^4\theta)}{2\sin^4\theta} + \left(\frac{2(\overline{v'^2} - \overline{u'^2})\delta\theta}{\tan\theta}\right)^2 \qquad \text{(C.16)}$$

Appendix D - Software for determination of Nusselt number.

```
c       Program to find the analytical solution to the transient conduction
c       equation for a semi-infinite solid subjected to a convection boundary
c       condition, using simple iteration.
c       By S Ashforth-Frost, The Nottingham Trent University, November 1992.
c
        DIMENSION R_D(80),TIME(80),HC(80)
        DIMENSION HCt(80),Tg0(80)

      OPEN(UNIT=26,STATUS='UNKNOWN',FILE='lcDIA.out',ACCESS='APPEND')
        OPEN(UNIT=27,STATUS='UNKNOWN',FILE='nolabel.DAT')
        OPEN(UNIT=28,STATUS='UNKNOWN',FILE='zd1con.DIA')
        OPEN(UNIT=29,STATUS='UNKNOWN',FILE='zd2con.DIA')
        OPEN(UNIT=30,STATUS='UNKNOWN',FILE='zd3con.DIA')
        OPEN(UNIT=31,STATUS='UNKNOWN',FILE='zd4con.DIA')
        OPEN(UNIT=32,STATUS='UNKNOWN',FILE='zd5con.DIA')
        OPEN(UNIT=33,STATUS='UNKNOWN',FILE='zd6conR.DIA')
        OPEN(UNIT=34,STATUS='UNKNOWN',FILE='zd7con.DIA')
        OPEN(UNIT=35,STATUS='UNKNOWN',FILE='zd8con.DIA')
        OPEN(UNIT=36,STATUS='UNKNOWN',FILE='zd2conr.DIA')

        WRITE(26,*) '   R/D   ','   HCT   ','   Nu   ','  Numf'
        DO 40 K=27,36
c       WRITE(6,*)  'K=',K,'    Z/D =',(K-27)
        READ(K,*) Tg,T0,Tlc,CALIB,DATA
        CALIB=54.6/CALIB

        READ(K,*) ((TIME(I),R_D(I),Tg0(I)),I=1,DATA)
        WRITE(6,*) 'z/d=',(k-27),Tg,T0,(tg-t0),time(1)
        DO 3 I=1,DATA
C       WRITE(6,*) TIME(I),R_D(I),Tg0(I)

3       CONTINUE
        DENSITY=1180.0
        TK=0.2
        CP=1585.5
        ALPHA=1.069E-7
        X=(DENSITY*CP*TK)**0.5

        DO 2 I=1,DATA
        R_D(I)=R_D(I)*CALIB/20
C       Initial guess for HC
        HCt(I)=10
        COUNT=0
```

```
      Ts=0
      DO 20, WHILE (ABS(Tlc-Ts).GT.0.01)
      Told=Ts
c     Non-dimensional time (B)
      B=0
      ETA=0
      ERF=0

      B=HCt(I)*(TIME(I)**0.5)/X
c     Gauss error function for (B)
      ERF=(B-(B**3)/3+(B**5)/10-(B**7)/42+(B**9)/216-(B**11)/1320
     1 +(B**13)/9360-(B**15)/75600+(B**17)/685440)*1.12838
c     Solution for surface temp based on estimation of heat transfer coefficient
      Ts=(1-((EXP(B**2))*(1-ERF)))*(Tg0(I)-T0)+T0
C
      COUNT=COUNT+1
C

C     WRITE(6,*) R_D(I),ETA,B,ERF,Ts,(Tlc-Ts),COUNT
C     WRITE(6,*) I,R_D(I)
      STEP=10.0
      IF (ABS(Tlc-Ts).LT.(2.5)) STEP=2.5
      IF (ABS(Tlc-Ts).LT.(1.5)) STEP=1.0
      IF (ABS(Tlc-Ts).LT.(0.75)) STEP=0.5
      IF (ABS(Tlc-Ts).LT.(0.1)) STEP=0.1
      IF (ABS(Tlc-Ts).LT.(0.05)) STEP=0.05
      IF ((Tlc-Ts).LT.0) STEP=-1*STEP
C     write (6,*) step
      HCt(I)=HCt(I)+step
20    CONTINUE
C     WRITE(6,*) I,R_D(I),HCt(I)
2     CONTINUE

c     WRITE(6,*) '     R/D    ',
c    1 '      Nu     ','Nut_meanfilm'
      WRITE(26,*) ' '
      WRITE(26,*)  'Z/D=',(K-27)
      WRITE(26,*) ' '
      DO 1000 I=1,DATA
      TKair=0
      eNut=0
c     Interpolate to find Kair
      TKair=((((0.5*(TG0(I)+Tlc)+273)-325)*0.00748)+2.816)/100
```

```
C       Calculate Nusselt number
        eNut=HCt(I)*0.02/TKair
c       WRITE(6,*)  R_D(I),eNut

C       WRITE(26,*)  R_D(I),HCt(I),eNut
        WRITE(26,*)  R_D(I),eNuT
1000    CONTINUE
40      CONTINUE

C
        STOP
        END
```

Appendix E - Data reduction equation and propagation of uncertainty for the determination of heat transfer coefficient.

Equation (3.25) gives the solution to the one-dimensional transient conduction equation subject to the described boundary and initial conditions, as

$$\frac{T(0,t)-T_0}{T_\infty-T_0} = \theta = 1 - e^{\eta}(1-erf(\sqrt{\eta})) \tag{E.17}$$

$$\textit{where} \qquad \eta = \frac{h^2\alpha t}{k^2} = \frac{h^2 t}{k\rho c} \tag{E.18}$$

simplifying Equation (E.17) by putting $\gamma=\sqrt{\eta}$ leads to

$$\theta = 1 - e^{\gamma^2}(1-erf(\gamma)) \tag{E.19}$$

Applying the procedure of Kline and McClintock (1953) to obtain the error in h propagated through these equations, gives

$$(\delta h) = \left[\left(\frac{\partial h}{\partial t}\delta t\right)^2 + \left(\frac{\partial h}{\partial(\sqrt{\rho ck})}\delta(\sqrt{\rho ck})\right)^2 + \left(\frac{\partial h}{\partial T_{(0,t)}}\delta T_{(0,t)}\right)^2 + \left(\frac{\partial h}{\partial T_\infty}\delta T_\infty\right)^2 + \left(\frac{\partial h}{\partial T_0}\delta T_0\right)^2 \right]^{0.5} \tag{E.20}$$

The partial derivatives with respect to t and $\sqrt{(\rho ck)}$ can be found directly by differentiating Equation (E.18):

$$\frac{\partial h}{\partial t} = -\frac{\gamma\sqrt{\rho ck}}{2t^{1.5}} = -\frac{h}{2t}$$
$$\frac{\partial h}{\partial(\sqrt{\rho ck})} = \frac{\gamma}{\sqrt{t}} = \frac{h}{\sqrt{\rho ck}} \tag{E.21}$$

However, re-arrangement of Equation (E.17) does not allow its solution in terms of h, so that the following procedure is used to find the partial derivatives with respect to the

measured temperatures:

$$\frac{\partial h}{\partial T_{(0,t)}} = \frac{\partial \theta}{\partial T_{(0,t)}} \frac{\partial h}{\partial \theta}$$

$$\frac{\partial h}{\partial T_\infty} = \frac{\partial \theta}{\partial T_\infty} \frac{\partial h}{\partial \theta} \qquad \textit{where} \quad \frac{\partial h}{\partial \theta} = \frac{\partial \gamma}{\partial \theta} \frac{\partial h}{\partial \gamma} \tag{E.22}$$

$$\frac{\partial h}{\partial T_0} = \frac{\partial \theta}{\partial T_0} \frac{\partial h}{\partial \theta}$$

To find $\partial\gamma/\partial\theta$:

$$\begin{aligned} \frac{\partial \theta}{\partial \gamma} &= \frac{\partial}{\partial \gamma}\left(1 - e^{\gamma^2}[1 - erf(\gamma)]\right) \\ &= \frac{2}{\sqrt{\pi}} - 2\gamma e^{\gamma^2}[1 - erf(\gamma)] \\ &= \frac{2 - 2\sqrt{\pi}\gamma(1 - \theta)}{\sqrt{\pi}} \end{aligned} \tag{E.23}$$

$$\textit{Hence} \quad \frac{\partial \gamma}{\partial \theta} = \frac{\sqrt{\pi}}{2 - 2\sqrt{\pi}\gamma(1 - \theta)}$$

Differentiating θ with respect to the measured temperatures leads to:

$$\frac{\partial \theta}{\partial T_{(0,t)}} = \frac{1}{T_\infty - T_0}$$

$$\frac{\partial \theta}{\partial T_\infty} = -\frac{(T_{(0,t)} - T_0)}{(T_\infty - T_0)^2} \tag{E.24}$$

$$\frac{\partial \theta}{\partial T_0} = \frac{T_{(0,t)} - T_\infty}{(T_\infty - T_0)^2}$$

Substituting the partial derivatives into Equation (E.21) leads to

$$\frac{\partial h}{\partial T_{(0,t)}} = \frac{h}{\beta(T_\infty - T_0)}$$

$$\frac{\partial h}{\partial T_\infty} = \frac{-h(T_{(0,t)} - T_0}{\beta(T_\infty - T_0)^2} \qquad \textit{where} \quad \beta = 2\gamma(\pi^{-0.5} - \gamma(1 - \theta)) \qquad \textbf{(E.25)}$$

$$\frac{\partial h}{\partial t_0} = \frac{h(T_{(0,t)} - T_\infty)}{\beta(T_\infty - T_0)^2}$$

Substituting these derivatives into Equation (E.20), dividing by h and replacing γ with $\sqrt{\eta}$ yields:

$$\frac{\delta h}{h} = \left[\left(\frac{\delta t}{2t}\right)^2 + \left(\frac{\delta(\sqrt{\rho ck})}{\sqrt{\rho ck}}\right)^2 + \left(\frac{1}{\beta(T_\infty - T_0)}\right)^2\left(\delta T_{(0,t)}^2 + (\theta - 1)^2\delta T_0^2 + \theta^2\delta T_\infty^2\right)\right]^{0.5}$$

$$\textit{where} \quad \beta = 2\sqrt{\eta}\left(\pi^{-0.5} - \sqrt{\eta}(1 - \theta)\right) \qquad \textbf{(E.26)}$$

Appendix F - Measurement of the thermal conductivity of perspex

Commercially available thermal conductivity apparatus supplied by G Cussons Ltd. was used to measure the coefficient of thermal conductivity of perspex. A selection of 25 mm diameter by 1 mm thick Perspex specimens were manufactured from the perspex sheet. The specimen was clamped between two copper cylinders of the same cross-sectional area. Good contact was ensured by polishing the contact surfaces and by applying a thin smear of high conductivity fluid (silicone grease) at the interfaces. This arrangement was enclosed in a sealed vessel to ensure negligible loss of heat. Heat was applied at the top of the arrangement by contact with a thermostatically controlled heater block, and cooled at the base of the arrangement by contact with a water cooled calorimeter. The heat delivered to the sample was controlled by regulating the current supplied to the heater block. The heat transmitted through the specimens was easily calculated from the measurement of water flow and temperature rise of the water. To determine the temperature gradient along the copper cylinders, four pre-calibrated thermocouples were inserted into small holes in the cylinders at known distances from the heater. Again, silicone grease was applied to ensure good contact. The temperature difference between the faces of the perspex specimen were determined by extrapolation of the derived temperatures of the copper cylinders.

The heat supplied to the calorimeter is given by

$$\dot{Q} = \frac{Jm(W_2 - W_1)}{t}$$

where J=specific heat capacity of water (4816 J/kg°C)

m=mass of water collected (kg)

W_1= water inlet temperature (°C)

W_2= water outlet temperature (°C)

t=time to collect m kg of water (s)

The thermal conductivity is then

$$k = \dot{Q}\frac{\ell}{A(T_2 - T_1)}$$

where ℓ=thickness of the specimen (m)

A=cross-sectional area of the specimen/copper cylinders (m^2)

$T_{1,2}$= specimen interface temperatures (°C).

The perspex was not allowed to attain a temperature above 110°C at any time during the tests. This was to avoid any softening of the material which, according to the manufacturers (ICI Technical Services) begins at 114°C. The thickness and diameter of the specimen was measured before and after heating and no change in dimensions was observed. A total of sixteen sets of readings were obtained, using different specimens from the same sheet as the test plate, to monitor repeatability of the results. Applying the analysis procedures described in Chapter 3, the uncertainty in k can be found from

$$\frac{\delta k}{k} = \left[\left(\frac{\delta m}{m}\right)^2 + \left(\frac{\delta \ell}{\ell}\right)^2 + \left(\frac{\delta W_1}{W_2 - W_1}\right)^2 + \left(\frac{\delta W_2}{W_2 - W_1}\right)^2 + \left(\frac{2\delta d}{d}\right)^2 + \left(\frac{\delta t}{t}\right)^2 + \left(\frac{\delta T_1}{T_2 - T_1}\right)^2 + \left(\frac{\delta T_2}{T_2 - T_1}\right)^2\right.$$

The mean value of thermal conductivity was established as 0.2 ±0.015 W/mK. Typical published values of k are in the range 0.18 - 0.2 W/mK.

The typical values of the measured quantities and uncertainty intervals used establishing this value are given overleaf:

Measured quantity		Typical Value	Uncertainty Interval
Mass		0.1	2×10^{-3} kg
Thickness		0.98	0.02 mm
Temperature	W_1	19.7	0.2 °C
	W_2	23.7	0.2 °C
	T_1	27.1	0.1 °C
	T_2	106.5	0.1 °C
Diameter		25	0.1 mm
Time		256	1 s

There was an approximate temperature difference of 80°C across the perspex specimen. It is not known how the thermal conductivity of the material varies with temperature. This is extremely difficult to establish since the material deteriorates at higher temperatures. Performing the experiment with a smaller temperature difference across the specimen would lead to a very small value of (W_2-W_1) and much higher overall uncertainty.

Appendix G - PHOENICS data input file, Q1.dat, and GROUND coding for calculation of Nusselt number and extraction of numerical data.

G.1 Q1.dat

```
TALK=F;RUN(1,1);VDU=3
   LG(20)=T

   GROUP 1. Run title and other preliminaries
TEXT(Semi-confined fully developed jet impingement, z/d=2)
   RE=20000
   INTEGER(JM1)
REAL(WIN,WMAX,RAD,TKEIN,EPSIN,GFRAC,GYDIS)
WMAX=19;RAD=0.01

   GROUP 2. Transience; time-step specification

   GROUP 3. X-direction grid specification
CARTES=F

   GROUP 4. Y-direction grid specification
SUBGRD(Y,1,20,0.01,1.0)
SUBGRD(Y,21,40,0.006,1.0)
SUBGRD(Y,41,60,0.01,1.0)
SUBGRD(Y,61,80,0.02,1.0)
SUBGRD(Y,81,120,0.25,1.25)

   GROUP 5. Z-direction grid specification
   ***Near wall cell is 0.02d ie out of laminar layer
SUBGRD(Z,1,1,0.001,1.0)
SUBGRD(Z,2,5,0.003,1.0)
SUBGRD(Z,6,65,0.0354,1.0)
SUBGRD(Z,66,67,0.0016,1.0)
SUBGRD(Z,68,68,0.001,1.0)

   GROUP 6. Body-fitted coordinates or grid distortion

   GROUP 7. Variables stored, solved & named
+       SOLUTN(P1,Y,Y,Y,N,N,N)
+       SOLUTN(V1,Y,Y,N,N,N,N)
+       SOLUTN(W1,Y,Y,N,n,N,N)
```

```
+       SOLUTN(H1,Y,Y,y,N,N,N)
+       STORE(ENUT)
+       TURMOD(KEMODL)
+       STORE(C1,C2,C3)

   GROUP 8. Terms (in differential equations) & devices
+       TERMS(H1,N,Y,Y,N,Y,N)
DIFCUT=0.5

   GROUP 9. Properties of the medium (or media)
ENUL=1.514E-5
RHO1=1.20268
PRNDTL(H1)=0.7
PRT(H1)=0.9

   GROUP 10. Inter-phase-transfer processes and properties

   GROUP 11. Initialization of variable or porosity fields
+      FIINIT(W1)=READFI
+      FIINIT(V1)=READFI
+      FIINIT(P1)=READFI
+      FIINIT(H1)=READFI
+      FIINIT(EP)=READFI
+      FIINIT(KE)=READFI
+      FIINIT(ENUT)=READFI
       FIINIT(W1)=Wmax/10.0
       FIINIT(V1)=Wmax/100.0
       FIINIT(EP)=EPSIN/2
       FIINIT(KE)=TKEIN/2
       FIINIT(H1)=25.0
       FIINIT(P1)=WMAX*RHO1/100


   GROUP 12. Convection and diffusion adjustments

   GROUP 13. Boundary conditions and special sources
   **Fully developed velocity profile
   GYDIS=distance to cell centre from jet axis
   GFRAC=YFRAC(JJ-1)
GFRAC=0;GYDIS=0
   MESGM(JJ YFRAC GFRAC GYDIS WIN YVLAST
DO JJ=1,20
GYDIS=YVLAST*(YFRAC(JJ)-((YFRAC(JJ)-GFRAC)/2))
```

```
PATCH(JET:JJ:,LOW,1,NX,:JJ:,:JJ:,1,1,1,1)
WIN=WMAX*((RAD-GYDIS)/RAD)**0.15373
   **Calculation of TKEIN
TKEIN=2*0.5*(0.4/25*(GYDIS*1000)**2+0.85)**2
   **Calculation of EP (where lmix=0.1xd)
EPSIN=0.163*(TKEIN**1.5)/2.0E-3
   MESG(:JJ:,:YFRAC(JJ)*1000:,:GFRAC*1000:,:GYDIS*1000:,:WIN:,:YVLAST:
COVAL(JET:JJ:,P1,FIXFLU,WIN*RHO1)
COVAL(JET:JJ:,W1,ONLYMS,WIN)
COVAL(JET:JJ:,KE,ONLYMS,TKEIN)
COVAL(JET:JJ:,EP,ONLYMS,EPSIN)
COVAL(JET:JJ:,H1,ONLYMS,55.0)
GFRAC=YFRAC(JJ)
ENDDO
   **Use CELL to define top confinement plate**
PATCH(TPLATE,CELL,1,NX,21,NY-1,1,1,1,1)
COVAL(TPLATE,W1,FIXVAL,0.0)
COVAL(TPLATE,V1,FIXVAL,0.0)
COVAL(TPLATE,H1,FIXVAL,21.0)
COVAL(TPLATE,KE,FIXVAL,0.0)
COVAL(TPLATE,EP,FIXVAL,0.0)
   ** Wall functions**
PATCH(CON,LWALL,1,NX,21,NY-1,2,2,1,1)
COVAL(CON,V1,GRND2,0.0)
COVAL(CON,W1,GRND2,0.0)
COVAL(CON,KE,GRND2,GRND2)
COVAL(CON,EP,GRND2,GRND2)
COVAL(CON,H1,GRND2,21.0)
   **Use CELL to define impingement plate**
PATCH(IPLATE,CELL,1,NX,1,NY-1,NZ,NZ,1,1)
COVAL(IPLATE,W1,FIXVAL,0.0)
COVAL(IPLATE,EP,FIXVAL,0.0)
COVAL(IPLATE,KE,FIXVAL,0.0)
COVAL(IPLATE,V1,FIXVAL,0.0)
COVAL(IPLATE,H1,FIXVAL,21.0)
   **Wall functions
PATCH(IMP,HWALL,1,NX,1,NY-1,NZ-1,NZ-1,1,1)
COVAL(IMP,V1,GRND2,0.0)
COVAL(IMP,W1,GRND2,0.0)
COVAL(IMP,KE,GRND2,GRND2)
COVAL(IMP,EP,GRND2,GRND2)
COVAL(IMP,H1,GRND2,21.0)
   **Outflow**
```

```
PATCH(OUTLET,NORTH,1,NX,NY,NY,1,NZ,1,1)
COVAL(OUTLET,P1,FIXP,0.0)
COVAL(OUTLET,H1,ONLYMS,SAME)
COVAL(OUTLET,V1,ONLYMS,SAME);COVAL(OUTLET,W1,ONLYMS,SAME)
COVAL(OUTLET,KE,ONLYMS,SAME);COVAL(OUTLET,EP,ONLYMS,SAME)
```

GROUP 14. Downstream pressure for PARAB=.TRUE.

GROUP 15. Termination of sweeps

```
**Number of total sweeps after this run=
LSWEEP=100
RESREF(W1)=1.E-8
RESREF(V1)=1.E-8
RESREF(P1)=1.E-8
RESREF(KE)=1.E-8
RESREF(EP)=1.E-8
RESREF(H1)=1.E-8
ISWC1=LSWEEP/6
```

GROUP 16. Termination of iterations

GROUP 17. Under-relaxation devices

```
+     RELAX(P1,LINRLX,0.8)
+     RELAX(V1,linrlx,0.8)
+     RELAX(W1,linrlx,0.8)
+     RELAX(EP,linrlx,0.8)
+     RELAX(KE,linrlx,0.8)
+     RELAX(H1,LINRLX,0.8)
+     RELAX(ENUT,linrlx,0.8)

      RELAX(P1,LINRLX,0.8)
      RELAX(V1,falsdt,10)
      RELAX(W1,falsdt,10)
      RELAX(EP,falsdt,10)
      RELAX(KE,falsdt,10)
      RELAX(H1,LINRLX,0.5)
      RELAX(ENUT,falsdt,0.1)

     ******patchWISE FALSE-TIME-STEP RELAXATION
     ******For W1:
     ******For KE:
      PATCH(RELKE,PHASEM,1,NX,20,60,2,NZ-1,1,1)
      COVAL(RELKE,KE,300,SAME)
```

```
      COVAL(RELKE,EP,300,SAME)

      PATCH(RELKE2,PHASEM,1,NX,60,75,NZ-32,NZ-1,1,1)
      COVAL(RELKE2,KE,300,SAME)
      COVAL(RELKE2,EP,300,SAME)

   KELIN=2

   GROUP 18. Limits on variables or increments to them
VARMAX(H1)=55.0
VARMIN(H1)=21.0
VARMAX(W1)=WMAX
VARMIN(W1)=-1*WMAX
VARMAX(V1)=WMAX
VARMIN(V1)=-1*WMAX
VARMAX(EP)=1.0E4
   VARMIN(EP)=0.0
   VARMAX(KE)=0.66*WMAX
   VARMIN(KE)=-0.66*WMAX


   GROUP 19. Data communicated by satellite to GROUND

   GROUP 20. Preliminary print-out
+     ECHO=T
   UWATCH=T
   USTEER=T

   GROUP 21. Print-out of variables
+    OUTPUT(P1,Y,Y,Y,Y,Y,Y)
+    OUTPUT(V1,Y,Y,Y,Y,Y,Y)
+    OUTPUT(W1,Y,Y,Y,Y,Y,Y)
+    OUTPUT(H1,Y,Y,Y,Y,Y,Y)
     OUTPUT(ENUT,Y,Y,Y,Y,Y,Y)
INIFLD=T

   GROUP 22. Spot-value print-out
IXMON=1;IYMON=20;IZMON=66
   NPRMON=50

   GROUP 23. Field print-out and plot control
NYPRIN=5;NZPRIN=5
   IZPRL=5
```

```
   IYPRL=60
NPLT=5
   NPRINT=500
PATCH(WALDEP,PROFIL,1,NX,1,80,NZ-1,NZ-1,1,1)
PLOT(WALDEP,P1,0.0,0.0)
PLOT(WALDEP,V1,0.0,0.0)
PLOT(WALDEP,H1,0.0,0.0)
PLOT(WALDEP,W1,0.0,0.0)
PLOT(WALDEP,KE,0.0,0.0)

PATCH(AXISDEP,PROFIL,1,NX,1,1,2,NZ-1,1,1)
PLOT(AXISDEP,W1,0.0,0.0)
PATCH(DEPke,PROFIL,1,NX,20,20,NZ-25,NZ-1,1,1)
PLOT(DEPke,ke,0.0,0.0)
PATCH(VDEP,PROFIL,1,NX,20,20,NZ-25,NZ-1,1,1)
PLOT(VDEP,v1,0.0,0.0)
PATCH(EXIT,PROFIL,1,NX,1,20,2,2,1,1)
PLOT(EXIT,W1,0.0,0.0)
PLOT(EXIT,KE,0.0,0.0)
PATCH(KEFIELD,CONTUR,1,1,1,80,2,NZ-1,1,1)
PLOT(KEFIELD,KE,0.0,10)
PLOT(KEFIELD,EP,0.0,10)
PLOT(KEFIELD,P1,0.0,10)


   GROUP 24. Dumps for restarts
SAVE=T;AUTOPS=F
RESTRT(ALL)
STOP
```

G.2 Extract from GROUND.FOR for the calculation of Nusselt number

```
C************************************************************
      SUBROUTINE GROUND
      INCLUDE 'PHOINC:SATEAR'
      INCLUDE 'PHOINC:GRDLOC'
      INCLUDE 'PHOINC:GRDEAR'
      INCLUDE 'PHOINC:GRDBFC'
CXXXXXXXXXXXXXXXXXXXXXXXXXXXXXXXXXXXXXXXXXX USER SECTION
STARTS:
C
C 1   Set dimensions of data-for-GROUND arrays here. WARNING: the
C     corresponding arrays in the MAIN program of the satellite
C     and EARTH must have the same dimensions.
      PARAMETER (NLG=20, NIG=20, NRG=100, NCG=10)
      DIMENSION GSTAN(200,20),GREYN(200,20)
      DIMENSION GH1(200,20),GHH1(200,20),GQ1(200,20),GHTC(200,20)
C        ,GSKIN(200,20)
C        ,GYPLUS(200,20)
C

COMMON/LGRND/LG(NLG)/IGRND/IG(NIG)/RGRND/RG(NRG)/CGRND/CG(NCG)

      LOGICAL LG
      CHARACTER*4 CG
C
C 2   User dimensions own arrays here, for example:
C     DIMENSION GUH(10,10),GUC(10,10),GUX(10,10),GUZ(10)
C
C 3   User places his data statements here, for example:
C     DATA NXDIM,NYDIM/10,10/
C
C 4   Insert own coding below as desired, guided by GREX examples.
C     Note that the satellite-to-GREX special data in the labelled
C     COMMONs /RSG/, /ISG/, /LSG/ and /CSG/ can be included and
C     used below but the user must check GREX for any conflicting
C     uses. The same comment applies to the EARTH-spare working
C     arrays EASP1, EASP2,....EASP20. In addition to the EASPs,
C     there are 10 GRound-earth SPare arrays, GRSP1,...,GRSP10,
C     supplied solely for the user, which are not used by GREX. If
C     the call to GREX has been deactivated then all of the arrays
C     may be used without reservation.
C
```

```
      EQUIVALENCE (IZ,IZSTEP)
       PARAMETER(MX=2)

     IXL=IABS(IXL)
     IF(IGR.EQ.13) GO TO 13
     IF(IGR.EQ.19) GO TO 19
     GO TO (1,2,3,4,5,6,25,8,9,10,11,12,13,14,25,25,25,25,19,20,25,
    125,23,24),IGR
  25 CONTINUE
     RETURN
C*********************************************************************
C
C--- GROUP 1. Run title and other preliminaries
C
    1 GO TO (1001,1002),ISC
1001    CONTINUE

C
C     User may here change message transmitted to the VDU screen or
C     batch-run log file.
      IF(IGR.EQ.1.AND.ISC.EQ.1) THEN
       CALL WRYT40('GROUND file is GROUND.FTN of:    110191 ')
       CALL WRYT40('PHOENICS version number is :    1.6    ')
       CALL WRYT40('October 1992 heat transfer code S Ashforth-Frost')
      ENDIF
C
      RETURN
1002  CONTINUE
      RETURN
C*********************************************************************
C
C--- GROUP 2. Transience; time-step specification
C
    2 CONTINUE
      RETURN
C*********************************************************************
C
C--- GROUP 3. X-direction grid specification
C
    3 CONTINUE
      RETURN
C*********************************************************************
C
```

```
C--- GROUP 4. Y-direction grid specification
C
   4 CONTINUE
     RETURN
C*********************************************************************
C
C--- GROUP 5. Z-direction grid specification
C
   5 CONTINUE
     RETURN
C*********************************************************************
C
C--- GROUP 6. Body-fitted coordinates or grid distortion
C
   6 CONTINUE
     RETURN
C*********************************************************************
C   * Make changes for this group only in group 19.
C--- GROUP 7. Variables stored, solved & named
C*********************************************************************
C
C--- GROUP 8. Terms (in differential equations) & devices
C
   8 GO TO (81,82,83,84,85,86,87,88,89,810,811,812,813,814,815)
    1,ISC
  81 CONTINUE
C   * ----------SECTION  1 ----------
C    For U1AD.LE.GRND--- phase 1 additional velocity. Index VELAD
     RETURN
  82 CONTINUE
C   * ----------SECTION  2 ----------
C    For U2AD.LE.GRND--- phase 2 additional velocity. Index VELAD
     RETURN
  83 CONTINUE
C   * ----------SECTION  3 ----------
C    For V1AD.LE.GRND--- phase 1 additional velocity. Index VELAD
     RETURN
  84 CONTINUE
C   * ----------SECTION  4 ----------
C    For V2AD.LE.GRND--- phase 2 additional velocity. Index VELAD
     RETURN
  85 CONTINUE
C   * ----------SECTION  5 ----------
```

```
C    For W1AD.LE.GRND--- phase 1 additional velocity. Index VELAD
     RETURN
  86 CONTINUE
C   * ------------------SECTION  6 -------------------------
C    For W2AD.LE.GRND--- phase 2 additional velocity. Index VELAD
     RETURN
  87 CONTINUE
C   * ------------------SECTION 7 ---- Volumetric source for gala
     RETURN
  88 CONTINUE
C   * ------------------SECTION 8 ---- Convection fluxes
     RETURN
  89 CONTINUE
C   * ------------------SECTION 9 ---- Diffusion coefficients
C   * ----------GROUP 8  SECTION 9 --- DIFFUSION COEFFICIENTS
C--- Entered when UDIFF =.TRUE.; block-location indices are LAE
C    for east, LAW for west, LAN for north, LAS for
C    south, LD11 for high, and LD11 for low.
C    User should provide INDVAR and NDIREC IF's as above.
C
     RETURN
 810 CONTINUE
C   * ------------------SECTION 10 --- Convection neighbours
     RETURN
 811 CONTINUE
C   * ------------------SECTION 11 --- Diffusion neighbours
     RETURN
 812 CONTINUE
C   * ------------------SECTION 12 --- Linearised sources
     RETURN
 813 CONTINUE
C   * ------------------SECTION 13 --- Correction coefficients
     RETURN
 814 CONTINUE
C   * ------------------SECTION 14 --- User's solver
     RETURN
 815 CONTINUE
C   * ------------------SECTION 15 --- Change solution
     RETURN
C
C   * See the equivalent section in GREX for the indices to be
C     used in sections 7 - 15
C
```

```
C   * Make all other group-8 changes in GROUP 19.
C*********************************************************************
C
C--- GROUP 9. Properties of the medium (or media)
C
C   The sections in this group are arranged sequentially in their
C   order of calling from EARTH. Thus, as can be seen from below,
C   the temperature sections (10 and 11) precede the density
C   sections (1 and 3); so, density formulae can refer to
C   temperature stores already set.
    9 GO TO (91,92,93,94,95,96,97,98,99,900,901,902,903,904,905),ISC
C*********************************************************************
  900 CONTINUE
C   * ------------------SECTION 10 -------------------------
C     For TMP1.LE.GRND---------phase-1 temperature Index TEMP1
      RETURN
  901 CONTINUE
C   * ------------------SECTION 11 -------------------------
C     For TMP2.LE.GRND---------phase-2 temperature Index TEMP2
      RETURN
  902 CONTINUE
C   * ------------------SECTION 12 -------------------------
C     For EL1.LE.GRND---------phase-1 length scale Index LEN1
      RETURN
  903 CONTINUE
C   * ------------------SECTION 13 -------------------------
C     For EL2.LE.GRND---------phase-2 length scale Index LEN2
      RETURN
  904 CONTINUE
C   * ------------------SECTION 14 -------------------------
C     For SOLVE(TEMP1)-------------------------phase-1 specic heat
      RETURN
  905 CONTINUE
C   * ------------------SECTION 15 -------------------------
C     For SOLVE(TEMP2)-------------------------phase-2 specic heat
      RETURN
   91 CONTINUE
C   * ------------------SECTION  1 -------------------------
C     For RHO1.LE.GRND--- density for phase 1       Index DEN1
      RETURN
   92 CONTINUE
C   * ------------------SECTION  2 -------------------------
C     For DRH1DP.LE.GRND--- D(LN(DEN))/DP for phase 1
```

```
C                                          Index D1DP
      RETURN
   93 CONTINUE
C   * ------------------SECTION  3 -------------------------
C     For RHO2.LE.GRND--- density for phase 2       Index DEN2
      RETURN
   94 CONTINUE
C   * ------------------SECTION  4 -------------------------
C     For DRH2DP.LE.GRND--- D(LN(DEN))/DP for phase 2
C                                          Index D2DP
      RETURN
   95 CONTINUE
C   * ------------------SECTION  5 -------------------------
C     For ENUT.LE.GRND--- reference turbulent kinematic viscosity
C                                          Index VIST
      RETURN
   96 CONTINUE
C   * ------------------SECTION  6 -------------------------
C     For ENUL.LE.GRND--- reference laminar kinematic viscosity
C                                          Index VISL
      RETURN
   97 CONTINUE
C   * ------------------SECTION  7 -------------------------
C     For PRNDTL( ).LE.GRND--- laminar PRANDTL nos., or diffusivity
C                                          Index LAMPR
      RETURN
   98 CONTINUE
C   * ------------------SECTION  8 -------------------------
C     For PHINT( ).LE.GRND--- interface value of first phase
C                                          Index FII1
      RETURN
   99 CONTINUE
C   * ------------------SECTION  9 -------------------------
C     For PHINT( ).LE.GRND--- interface value of second phase
C                                          Index FII2
      RETURN
C*****************************************************************
C
C--- GROUP 10. Inter-phase-transfer processes and properties
C
   10 GO TO (101,102,103,104),ISC
  101 CONTINUE
C   * ------------------SECTION  1 -------------------------
```

```
C    For CFIPS.LE.GRND--- inter-phase friction coeff.
C                                        Index AUX(INTFRC)
     RETURN
  102 CONTINUE
C   * ------------------SECTION  2 -------------------------
C    For CMDOT.EQ.GRND- inter-phase mass transfer  Index AUX(INTMDT)
     RETURN
  103 CONTINUE
C   * ------------------SECTION  3 -------------------------
C    For CINT( ).EQ.GRND--- phase1-to-interface transfer coefficients
C                                        Index COI1
     RETURN
  104 CONTINUE
C   * ------------------SECTION  4 -------------------------
C    For CINT( ).EQ.GRND--- phase2-to-interface transfer coefficients
C                                        Index COI2
     RETURN
C*****************************************************************
C
C--- GROUP 11. Initialization of variable or porosity fields
C                                        Index VAL
   11 CONTINUE
     RETURN
C*****************************************************************
C
C--- GROUP 12. Convection and diffusion adjustments
C
   12 CONTINUE
     RETURN
C*****************************************************************
C
C--- GROUP 13. Boundary conditions and special sources
C                                  Index for Coefficient - CO
C                                  Index for Value       - VAL
   13 CONTINUE
     GO TO (130,131,132,133,134,135,136,137,138,139,1310,
    11311,1312,1313,1314,1315,1316,1317,1318,1319,1320,1321),ISC
  130 CONTINUE
C------------------SECTION  1 ------------ coefficient=GRND
     RETURN
  131 CONTINUE
C------------------SECTION  2 ------------ coefficient=GRND1
     RETURN
```

```
 132 CONTINUE
C------------------SECTION  3 ------------ coefficient=GRND2

C       WRITE(6,*) 'ITCTRL=',ITCTRL
        IF (INDVAR .EQ. 14 ) THEN

c       Create storage for required variables
c       GSTAN=St*u; GHTC=calculated heat transfer coefficient
c       GREYN=calculated near wall Reynolds number
c       GHTC=heat transfer coefficient, then Nusselt number
c       GH1=near wall node temperature
c       GHH1=wall temperature
        CALL GETYX(C1,GSTAN,NY,MX)
        CALL GETYX(C2,GHTC,NY,MX)
        CALL GETYX(C3,GREYN,NY,MX)
        CALL GETYX(H1,GH1,NY,MX)
        CALL GETYX(HIGH(H1),GHH1,NY,MX)

c       Access required quantities from EARTH
        LOCO=L0F(CO)
        LOSK=L0PVAR(PVSKIN,IREG,0)
        LORLVL=L0PVAR(PVRLVL,IREG,0)
        LOMUDD=L0F(LD11)
        IPLUS=(IXF-2)*NY
        J=0
c       DO 13211 IX=IXF,IXL
              IPLUS=IPLUS+NY
              DO 13211 IY=IYF,IYL
              I=IY+IPLUS
              J=J+1

c       Calculate heat flux:
c       Qdot=St*deltaH*u*rho1 where deltaH is change in enthalpy
c       Remember St has been stored by gxwall.for as STAN*f(L0RLVL+J) ie. St*u
        GSTAN(IY,1)=F(LOCO+I)
        GQ1(IY,1)=(GSTAN(IY,1)*(GH1(IY,1)-GHH1(IY,1))*1.2)
C       WRITE(6,*) IY,IZ,'     GHH1=',GHH1(IY,1)

c       Calculate htc based on T_jet as opposed to Tnear-wall-node:
        GHTC(IY,1)=0
c       Calculate Nusselt number:
        GHTC(IY,1)=GQ1(IY,1)/(55.0-GHH1(IY,1))
        GHTC(IY,1)=GHTC(IY,1)*0.02/0.0299
```

```
c       Calculate yplus
        GYPLUS(IY,1)=((F(LOSK+J))**0.5)*F(LORLVL+J)/(F(LOMUDD+I)+TINY)

c       Access skin friction s
c       GSKIN(IY,1)=F(LOSK+J)

c       Calculate near wall Reynolds number
        GREYN(IY,1)=F(LORLVL+J)/(F(LOMUDD+I)+TINY)

c       Output results at next but last sweep
        IF (ISWEEP. GE. LSWEEP-1) THEN
        IF (IY. LE. 10) THEN
        WRITE(6,*) 'S=',ISWEEP,IY,IZ,' h=',GHTC(IY,1),' RE=',GREYN(IY,1)
C       WRITE(6,*) 'HTC USING T_jet =',GHTC(IY,1)
        ENDIF
        ENDIF
13211   CONTINUE

c       Set variables C1 to C4 to user variables to allow access from
c       phida.dat for plotting.
        CALL SETYX(C1,GSTAN,NY,MX)
        CALL SETYX(C2,GHTC,NY,MX)
        CALL SETYX(C3,GREYN,NY,MX)


        ENDIF

    RETURN
  133 CONTINUE
C-------------------SECTION  4 ------------ coefficient=GRND3
    RETURN
  134 CONTINUE
C-------------------SECTION  5 ------------ coefficient=GRND4
    RETURN
  135 CONTINUE
C-------------------SECTION  6 ------------ coefficient=GRND5
    RETURN
  136 CONTINUE
C-------------------SECTION  7 ------------ coefficient=GRND6
    RETURN
  137 CONTINUE
C-------------------SECTION  8 ------------ coefficient=GRND7
    RETURN
```

```
  138 CONTINUE
C------------------SECTION  9 ------------ coefficient=GRND8
      RETURN
  139 CONTINUE
C------------------SECTION 10 ------------ coefficient=GRND9
      RETURN
 1310 CONTINUE
C------------------SECTION 11 ------------ coefficient=GRND10
      RETURN
 1311 CONTINUE
C------------------SECTION 12 ------------------value=GRND
      RETURN
 1312 CONTINUE
C------------------SECTION 13 ------------------value=GRND1
      RETURN
 1313 CONTINUE
C------------------SECTION 14 ------------------value=GRND2
      RETURN
 1314 CONTINUE
C------------------SECTION 15 ------------------value=GRND3
      RETURN
 1315 CONTINUE
C------------------SECTION 16 ------------------value=GRND4
      RETURN
 1316 CONTINUE
C------------------SECTION 17 ------------------value=GRND5
      RETURN
 1317 CONTINUE
C------------------SECTION 18 ------------------value=GRND6
      RETURN
 1318 CONTINUE
C------------------SECTION 19 ------------------value=GRND7
      RETURN
 1319 CONTINUE
C------------------SECTION 20 ------------------value=GRND8
      RETURN
 1320 CONTINUE
C------------------SECTION 21 ------------------value=GRND9
      RETURN
 1321 CONTINUE
C------------------SECTION 22 ------------------value=GRND10
      RETURN
C*************************************************************
```

```
C
C--- GROUP 14. Downstream pressure for PARAB=.TRUE.
C
  14 CONTINUE
     RETURN
C*************************************************************
C* Make changes for these groups only in GROUP 19.
C--- GROUP 15. Termination of sweeps
C--- GROUP 16. Termination of iterations
C--- GROUP 17. Under-relaxation devices
C--- GROUP 18. Limits on variables or increments to them
C*************************************************************
C
C--- GROUP 19. Special calls to GROUND from EARTH
C
  19 GO TO (191,192,193,194,195,196,197,198),ISC
 191 CONTINUE
C   * ------------------SECTION 1 ---- Start of time step.
     RETURN
 192 CONTINUE
C   * ------------------SECTION 2 ---- Start of sweep.
     RETURN
 193 CONTINUE
C   * ------------------SECTION 3 ---- Start of iz slab.
     RETURN
 194 CONTINUE
C   * ------------------SECTION 4 ---- Start of iteration.

     RETURN
 195 CONTINUE
C   * ------------------SECTION 5 ---- Finish of iteration.
     RETURN
 196 CONTINUE
C   * ------------------SECTION 6 ---- Finish of iz slab.

      RETURN
 197  CONTINUE
C   * ------------------SECTION 7 ---- FINISH OF SWEEP.



C   * ------------------SECTION 7 ---- Finish of sweep.
     RETURN
```

```
  198 CONTINUE
C   * ------------------SECTION 8 ---- Finish of time step.
C
      RETURN

C*************************************************************
C
C--- GROUP 20. Preliminary print-out
C
   20 CONTINUE
      RETURN
C*************************************************************
C* Make changes for these groups only in GROUP 19.
C--- GROUP 21. Print-out of variables
C--- GROUP 22. Spot-value print-out
C*************************************************************
C
C--- GROUP 23. Field print-out and plot control
   23 CONTINUE
      RETURN
C*************************************************************
C
C--- GROUP 24. Dumps for restarts
C
   24 CONTINUE
      END
C*************************************************************
      SUBROUTINE SPECGR
      CALL WRIT40('Dummy subroutine SPECGR  called.        ')
      CALL WAYOUT(2)
      END
C*************************************************************
      SUBROUTINE SPC1GR
      CALL WRIT40('Dummy subroutine SPC1GR called.         ')
      CALL WAYOUT(2)
      END
C*************************************************************
      SUBROUTINE SPC2GR
      CALL WRIT40('Dummy subroutine SPC2GR called.         ')
      CALL WAYOUT(2)
      END
C*************************************************************
      SUBROUTINE SPC3GR
```

```
      CALL WRIT40('Dummy subroutine SPC3GR called.        ')
      CALL WAYOUT(2)
      END
C*************************************************************
      SUBROUTINE QUIZ
C--- This subroutine is used by CHAM for de-bugging
      END
```

G.3 Coding used to obtain data for error estimation using Richardsons extrapolation technique

G.3.1 Extract from GROUND.FOR

```
C*************************************************************
C$DIR**GROUND
      SUBROUTINE GROUND
      INCLUDE 'SATEAR'
      INCLUDE 'GRDLOC'
      INCLUDE 'GRDEAR'
      EQUIVALENCE (IZ,IZSTEP)
CXXXXXXXXXXXXXXXXXXXXXXXXXXXXXXXXXXXXXXXXXX USER SECTION
STARTS:
C 1   Set dimensions of data-for-GROUND arrays here. WARNING: the
C     corresponding arrays in the MAIN program of the satellite
C     and EARTH must have the same dimensions.
      COMMON/LGRND/LG(20)/IGRND/IG(20)/RGRND/RG(100)/CGRND/CG(10)
      LOGICAL LG
      CHARACTER*4 CG
C 2   User dimensions own arrays here.
      DIMENSION GP1(200,1),GV1(200,1),GW1(200,1)
      DIMENSION YCOOR(200,1),ZCOOR(200)
      PARAMETER (MX=1)
C
      IXL=IABS(IXL)
         IF(IGR.EQ.1) GO TO 1
         IF(IGR.EQ.19) GO TO 19
C      GO TO (1,2,3,4,5,6,24,8,9,10,11,12,13,14,24,24,24,24,19,20,24,
C     124,23,24),IGR
       RETURN
C*************************************************************
C--- GROUP 1. Run title and other preliminaries
    1 GO TO (1001,1002),ISC
 1001 CONTINUE
c**       Activate storage for Y and Z coordinates.
      CALL MAKE(YG2D)
      CALL MAKE(ZGNZ)
      RETURN
 1002 CONTINUE
      RETURN
C*************************************************************
C--- GROUP 19. Special calls to GROUND from EARTH
   19 GO TO (191,192,193,194,195,196,197,198),ISC
  191 CONTINUE
```

```
C   * ------------------SECTION 1 ---- START OF TIME STEP.
      RETURN
  192 CONTINUE
C   * ------------------SECTION 2 ---- START OF SWEEP.
      RETURN
  193 CONTINUE
C   * ------------------SECTION 3 ---- START OF IZ SLAB.
      RETURN
  194 CONTINUE
C   * ------------------SECTION 4 ---- START OF ITERATION.
      RETURN
  195 CONTINUE
C   * ------------------SECTION 5 ---- FINISH OF ITERATION.
      RETURN
  196 CONTINUE
C   * ------------------SECTION 6 ---- FINISH OF IZ SLAB.

C*******PRINT V1,W1,P1 TO A DATA FILE**************
      IF (ISWEEP.NE.LSWEEP-1) GOTO 1969

c*****If first sweep open output file. Data not required at Z=1.
      IF (IZ.NE.1) GOTO 19617
      OPEN(UNIT=41,STATUS='UNKNOWN',FILE='FINEP1.DAT')
      GOTO 1969

C*****Output coords and pressures to a data file. Do not
c     output values at last slab.
19617 IF (IZ.EQ.NZ) GOTO 1969

C*****Put EARTH variables in local arrays
      CALL GETYX(P1,GP1,IY,MX)

C*****Put Y (at cell centre) and Z (at cell centre & face)
C***** coordinates in local system.
      CALL GETYX(YG2D,YCOOR,IY,MX)
      CALL GETZ(ZGNZ,ZCOOR,NZ)
      DO 19637 IY=1,NY
      WRITE (41,*) GP1(IY,1)
19637 CONTINUE
1969  RETURN
  197 CONTINUE
C   * ------------------SECTION 7 ---- FINISH OF SWEEP.
      RETURN
  198 CONTINUE
C   * ------------------SECTION 8 ---- FINISH OF TIME STEP.
      RETURN
```

```
      END


C*************************************************************
      SUBROUTINE SPECGR
      CALL WRIT40('DUMMY SUBROUTINE SPECGR  CALLED.      ')
      CALL WRIT40('PLEASE ATTACH SPECGR  OBJECT AT LINK. ')
      CALL WAYOUT(2)
      RETURN
      END
C*************************************************************
      SUBROUTINE SPC1GR
      CALL WRIT40('DUMMY SUBROUTINE SPC1GR CALLED.       ')
      CALL WRIT40('PLEASE ATTACH SPC1GR OBJECT AT LINK.  ')
      CALL WAYOUT(2)
      RETURN
      END
C*************************************************************
      SUBROUTINE SPC2GR
      CALL WRIT40('DUMMY SUBROUTINE SPC2GR CALLED.       ')
      CALL WRIT40('PLEASE ATTACH SPC2GR OBJECT AT LINK.  ')
      CALL WAYOUT(2)
      RETURN
      END
C*************************************************************
      SUBROUTINE SPC3GR
      CALL WRIT40('DUMMY SUBROUTINE SPC3GR CALLED.       ')
      CALL WRIT40('PLEASE ATTACH SPC3GR OBJECT AT LINK.  ')
      CALL WAYOUT(2)
      RETURN
      END
C*************************************************************
      SUBROUTINE QUIZ
      RETURN
      END
```

G.3.2 FORTRAN program for bi-linear interpolation of output from the fine grid

```
C     Program to interpolate between cell centres to provide data at
C     other locations that correspond to a grid point of a grid
C     with half the number of cells.
      DIMENSION P1(200,200)
      DIMENSION P(200,200)
      DIMENSION P2(200,200)

c     Read values of quantity (V1,W1,P1,etc.) at each grid point of fine
c     grid. FineP1.dat is output by GROUND.  See error.for also.
      OPEN(UNIT=10,FILE='FINEP1.DAT',STATUS='UNKNOWN')
      NY=140
      NZ=54
      DO 100 IZ=2,NZ-1
      DO 200 IY=1,NY
      READ (10,*) P1(IY,IZ)
200   CONTINUE
100   CONTINUE
      CLOSE(10)

c     Interpolate in Y direction:
      J=0
      DO 300 IZ=2,NZ-1
      I=0
      J=J+1
      DO 400 IY=1,NY,2
      I=I+1
      P2(I,J)=(P1(IY,IZ)+P1(IY+1,IZ))/2
400   CONTINUE
300   CONTINUE
      LI=I
      LJ=J

c     Interpolate in Z direction and output results.
      OPEN(UNIT=12,FILE='FINOUT.DAT',STATUS='UNKNOWN')
      DO 500 J=1,LJ,2
      DO 600 I=1,LI
      P(I,J)=(P2(I,J)+P2(I,J+1))/2
      WRITE (12,*) P(I,J)
600   CONTINUE
500   CONTINUE
      CLOSE(12)
      STOP
      END
```

G.3.3 FORTRAN program for calculation of errors using the Richardson extrapolation technique

```
C  *****Program to compute the difference in cell centre values of
C  *****quantities from two different grids.
      DIMENSION P(200,200)
      DIMENSION P2(200,200)
      DIMENSION X(200,200),Y(200,200)
      DIMENSION ERR(200,200)

C     Set values of NZ and NY in Q1 file here:
      NZ=28
      NY=70

c     Read coords of medium mesh and point values of
c     V1,W1 or P1, omitting first and last Z since these
c     represent the impingement walls. Medcoor has been
c     output by GROUND.
      OPEN(UNIT=10,FILE='MEDCOOR.DAT',STATUS='UNKNOWN')
      DO 100 J=2,NZ-1
      DO 200 I=1,NY
      READ(10,*) X(I,J),Y(I,J),P(I,J)
200   CONTINUE
100   CONTINUE
      CLOSE(10)

c     Read interpolated (by Interpol.for) values of this
c     quantity at the same points, but generated by the
c     fine mesh.
      OPEN(UNIT=20,FILE='FINOUT.DAT',STATUS='UNKNOWN')
      DO 300 J=2,NZ-1
      DO 400 I=1,NY
      READ(20,*) P2(I,J)
400   CONTINUE
300   CONTINUE
      CLOSE(20)

c     Compute the % error in the quantity at each grid point.
      OPEN(UNIT=30,FILE='CONME.DAT',STATUS='UNKNOWN')
      WRITE (30,*) NY,(NZ-2)
      DO 500 J=NZ-1,2,-1
      DO 600 I=1,NY
      ERR(I,J)=(P(I,J)-P2(I,J))*100/P2(I,J)
      ERR(I,J)=((ERR(I,J))**2)**0.5
      IF(ERR(I,J).LT.0.1) THEN
     ERR(I,J)=0.1
```

```
      END IF

c     Output results to a datafile for contour plotting in PHOTON
      WRITE (30,*) X(I,J)*1000,(Y(I,J)*1000),ERR(I,J)
600   CONTINUE
500   CONTINUE
      CLOSE(30)
      STOP
      END
```

PUBLICATIONS

Lasers and Electro-Optics, San Jose, CA, USA.

An Experimental Study of the Counter and Tracker Signal Processors used in Fluid Measurements.

Thakker A. & Frawley P.
University of Limerick
Dept. of Mechanical and Production Engineering
Ireland.

Jambunathan K. & Ashforth-Frost S.
Nottingham Polytechnic
Dept. of Mechanical Engineering
England.

Abstract

The aim of the project in question is to evaluate the performance of the Counter and Tracker signal processors. In order to achieve this aim, measurements are carried out on the plane of a laminar, fully developed pipe flow. To facilitate duplicate measurements on both the photomultiplier signal is fed to the frequency shifter and the mixer out signal is then simultaneously passed to both signal processors. To insure that both processors are operating on the same gain only the voltage adjust to the photomultiplier is varied. To validate the results obtained by both Tracker and Counter, a comparison is carried out with the solution obtained by the Navier-Stokes equation. The results show good correlation. The major source of observable error occurs at the edge of the jet. In this region entrainment takes place - so the measuring volume cannot be fully seeded. The measuring volume itself is 0.367 mm in length, so a bias in measurement will occur towards the velocity with the highest density of particles. This ultimately leads to higher measured velocities. The turbulence intensity values are also compared for both processors. In taking measurements two things are noted : (1) that the ratio of low pass filter frequency to high pass filter frequency has a great effect on the measurement. The reason for this is that by reducing the frequency ratio, random noise will occasionally provide a sufficiently coherent signal to pass the validation criteria on the instrument. (2) The gain has to be kept at an adequate setting. As the optical gain is increased an increase is also detected in the measured turbulence intensity. The Counter obtains adequate results over the complete range. In the entrainment there is a sharp increase in the turbulence intensity and the Tracker becomes unreliable. Overall, good correlation exists between the Counter and Tracker signal processors.

1.0 Description of Signal Processors

1.1 Counter

The Counter is basically an 'electric stop watch' which measures the time it takes for a particle to cross a known number of interference fringes in the measuring volume. The distance between fringes is known from the geometry of the optical beams and the wavelength of the laser light. The light scattered from the particle is detected, and the result is a frequency modulated current burst from the detector. The frequency of the modulation is the doppler frequency.

$$Fd = \frac{2\ Ux\ \sin(Q/2)}{\lambda} \qquad [1]$$

The doppler burst frequency is detected by measuring the time for a certain number of zero-crossings of the amplified and high and low pass filtered detector signal.

Particle Velocity : $V = \frac{n}{\partial t}\ \delta_f$

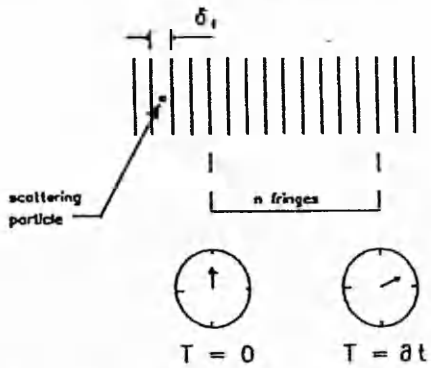

Fig. 1 LDA Counter Principle

1.2 Frequency Tracker

A tracker type processor uses a bandpass filter and frequency discriminator to 'track' the frequency changes in the photomultiplier output. Looking at fig. 3 the signal passing through the filter is fed into

$$\text{Fringe Spacing } \delta_f = \frac{\lambda}{2 \sin \theta}$$

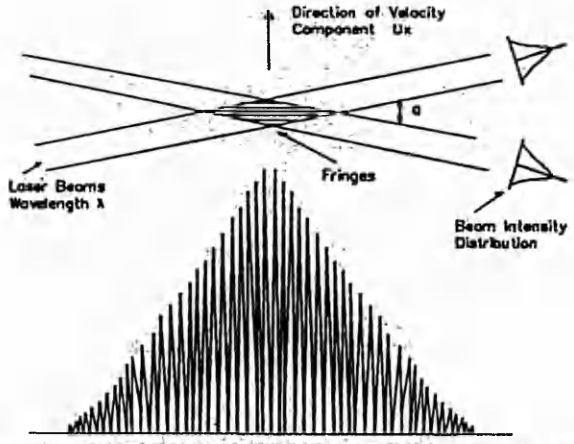

Fig. 2 Intersection of Beams

a frequency discriminator to provide frequency to voltage conversion. The voltage information from the discriminator is integrated and applied to the input of a voltage controlled oscillator whose output is adjusted by this voltage according to the velocity variations. The oscillator is combined with the signal frequency in the mixer to yield an output frequency, which when the loop is operating agrees with the centre frequency of the band pass filter. The frequency of the oscillator and the corresponding voltage input are measures of the signal frequency.

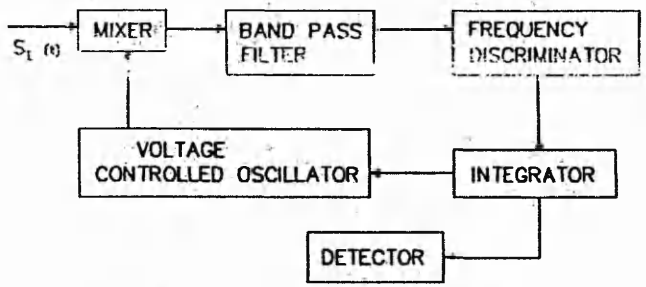

Fig. 3 Frequency Tracking Demodulator

2.0 Experimental Set-Up

2.1 Air Flow

A line diagram of the experimental arrangement is shown in fig. 4. The pipe flow measurements are carried out in the exit plane of a 10 mm inside diameter seamless stainless steel tube of length 850 mm. The Reynold's No. based on diameter was 1220. For fully developed laminar pipe flow, the required length of pipe is given by L = 0.057 x Re x Dia.. For this case the required length, L = 695.4 mm; thus the velocity profile in the exit plane was laminar and fully developed.

The air was seeded with atomised 1:1 water:glycerin solution using a Dantec 55L18 seeding generator. The particle concentration could be adjustment of the by-pass valve and the nozzle supply valve. Particle sizes were in the range 2-3 microns.

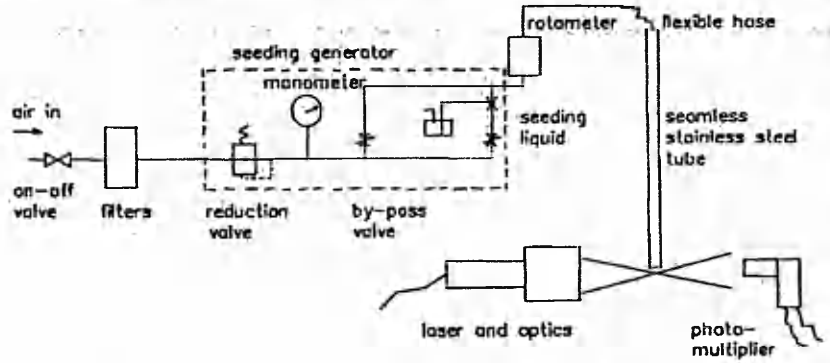

Fig. 4 Air Supply used in Experimentation.

2.2 LDA System

A block diagram of the apparatus is given in fig. 5. To facilitate duplicate measurements on both Counter and Tracker, the photomultiplier signal is fed to the frequency shifter and the mixer out signal is then simultaneously passed to both Tracker and Counter. The doppler signal from both Counter and Tracker is monitored on a digital storage oscilloscope (DSO Gould Model 1604). An indication as to whether the Tracker is 'in-lock' is provided by the lock out signal which is also monitored here. To ensure that both processors are operating gain only

the voltage adjustment to the photomultiplier is varied. So that a valid comparison could be made the Counter was operated in fixed mode - used for continuous signals - and high density seeding was applied to the flow.

Certain criteria were stipulated before data collected. Only when 'in-lock' would the Tracker transfer 1280 samples to the 4032 CBM computer for data processing via the IEEE488 interface. The Comp. Accuracy of the counter was set to 1.5 % on the counter - this ensures that the measurement of frequency for five and eight fringes is less than 1.5 %. Only when the % validated exceeds 10 % on the Counter was data transferred to an Apple 11e computer via an IEEE488 interface. The output from both computers consisted of mean velocity, turbulence intensity and a histogram of the no. samples vs. velocity.

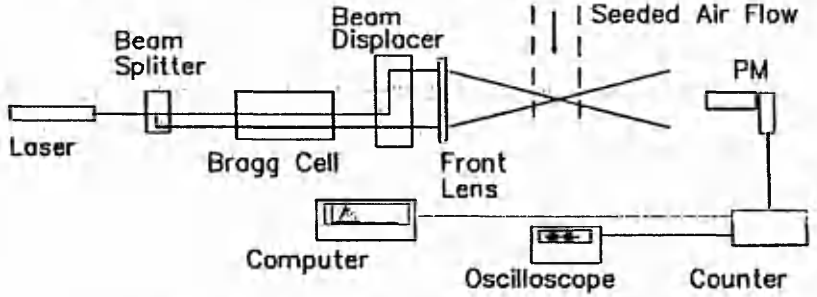

Fig. 5 Laser Doppler Anemometry System

The Tracker was operated on the range 333 KHz - 3.33 MHz with the widest bandwidth setting to accommodate as large a turbulence intensity as possible. The Counter was operated on the range 256 KHz - 4 MHz. It was discovered that the ratio of low pass filter frequency to high pass filter frequency had a great effect on the measurement of the turbulence intensity by the Counter. A ratio of about 10:1 between low and high pass filters is suggested, the reason being that by reducing the frequency ratio, random noise will occasionally provide a sufficiently coherent signal to pass the validation criteria on the instrument.

As the signal-to-noise ratio was high, the threshold window was not increased, since this would only result in a smaller data rate. A constant frequency shift of 1 MHz was applied.

The photomultiplier is mounted so as to be operated in side scatter. There are two reasons for this :

(1) The laser used is a Hughes Aircraft Co. laser type 3227H-PC and has a power rating of only 8 mW. Although it could have been operated in back scatter it would result in lower signal-to-noise ratios.

(2) Fringe spacing may not be constant and may result in measuring errors. This imprecision would be significantly reduced when using side scatter optics which focus on a much shorter length of the probe volume.

3.0 Discussion

3.1 Velocity Measurements

To validate the results obtained by both Tracker and Counter, The measurements are compared with a solution obtained by the Navier-Stokes equation :

$$U = -\frac{1}{4}\frac{dP}{dx}\frac{(R^2-r^2)}{\mu} \qquad [2]$$

It can be seen from fig. 6 that good correlation exists. The only source of observable error occurs at the edge of the jet. In this region entrainment takes place. This leads to low seeding and it becomes increasingly difficult for the Tracker to obtain an 'in-lock' signal. The Counter has no such problems. Since entrainment takes place, the measuring volume cannot be uniformly seeded. The measuring volume itself is 0.3673 mm in length so a bias in measurement will occur towards the velocity of the higher density of particles. This will ultimately lead to higher measured velocities.

The airflow was increased and measurements were taken of the core velocity. The Tracker is accurate up to approximately 16 M/s after which it is impossible to obtain lock. This may have been due to the seeding generator capabilities, as the Tracker should be capable of measuring velocities of almost twice this magnitude. The Counter had no problems following the flow parameters at high velocities.

Although Counter is more susceptible to measurement error in the case of low SNR - under 10 dB - in this situation the SNR played no

major role as the SNR was sufficient. In cases of low SNR, the Tracker is clearly more useful, and can operate with any SNR higher than 3 dB.

3.2 Turbulence Intensity Measurements

The measurements of turbulence intensity are shown in fig. 7. As can be seen, the turbulence ranges from 0.9% to 20%. The counter obtains adequate results over the complete range provided care is taken to keep the gain at an adequate setting. As the optical gain is increased an increase is also detected in turbulence intensity measurements. This aspect has been discussed in the Dantec Monthly. It should be noted that the tracking ability of the counter could have been increased by increasing the value of the comp. accuracy - the setting we imposed of 1.5% is the most rigorous applicable, and should only be applied for low turbulence measurements. The equations substantiating this statement can be checked in Cheng [1].

$$Rm = 2\,C\,(1\text{-}C)\,f1 \,/\, (N2 + N1\,C) \qquad [3]$$

where Rm is the dynamic tracking ability, C the comp. accy. setting, f1 the average freq. of first N1 cycles, N1 the no. of cycles of the first cycle count and N2 the no. of cycles of the last cycle count of the signal.

The results obtained by the frequency tracker are not as satisfactory. It is seen that as the turbulence intensity increased near the edge of the jet, the tracker became less reliable. Although this phenomena had been expected -Durst [2] observed that the max. Turbulence Intensity measurable by trackers can be obtained by the following equation :

$$\frac{df^{2}_{max}}{f_{opt}} = \frac{(R-1)}{3\,(R+1)}$$

where R = f2/f1 = 6.5 for Dantec Tracker

When this equation is applied to the Dantec Tracker it is found that the maximum measurable turbulence intensity is 25% -, it is noted that the maximum reliable reading in this case was approx. 12.5%. This may be due to:

(a) the fact that seeding in this area was not uniform and not of high density

(b) the velocity of the flow in this region is very small and approaches zero. This means the doppler frequency will also be small. From equation 1 it can be seen that velocity and doppler frequency are linerally dependant. The slewing rate for trackers is approximately Wn, since it can change its frequency in 1/Wn seconds. A reasonable value for Wn is 3% of the highest anemometer frequency expected. By increasing the frequency sift, we can increase the doppler frequency and consequently the tracking ability of the frequency tracker. In so doing it was possible to obtain much higher reliable turbulence intensity measurements.

4.0 Conclusions

The experiment indicates good correlation between both tracker and counter signal processors.

It highlights errors that can occur in measurement due to :

a) a bad ratio between high and low pass filter frequencies
b) a high setting used for optical gain
c) non-uniform seeding of the measuring volume

The paper shows that the measuremets of turbulence intensity can be obtained with greater accuracy by :

a) increasing the frequency shift for the Tracker
b) increasing the value of comp. accy. for the Counter

5.0 References

[1] Cheng Y., and Lee S., 1987, "On the dynamic tracking ability of digital counters used in laser doppler anemonetry", Third Int. Symposium on Laser Anemometry, Winter Meeting, MA, USA.

[2] Durst F., 1975, "Electronic Processing of Optical Anemometer signals", Proc. of the LDA Symposium, Copenhagen, Denmark.

Acknowledgements

The authors wish to thank two organisations for their support. Firstly, Dantec for advive on equipment and its operation and secondly, Erasmus for providing the interchange of ideas and personnell between University of Limerick and Nottingham Polytechnic.

AXIAL VEL. ACROSS A JET

TRACKER Vs. COUNTER

Fig. 6

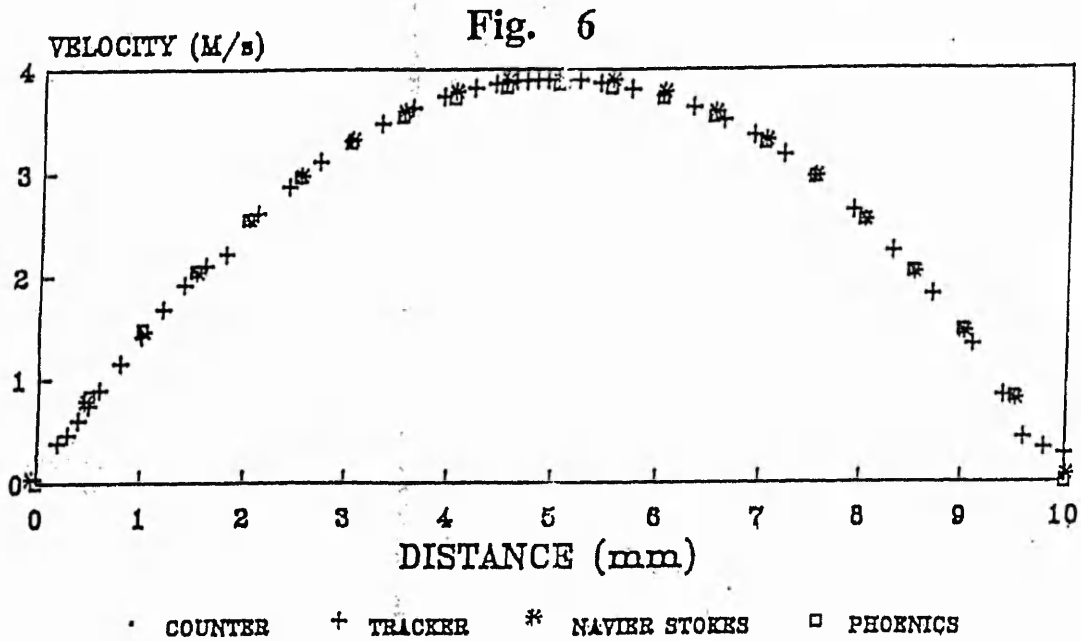

TURBULENCE INT. JET

TRACKERS Vs. COUNTERS

Fig. 7

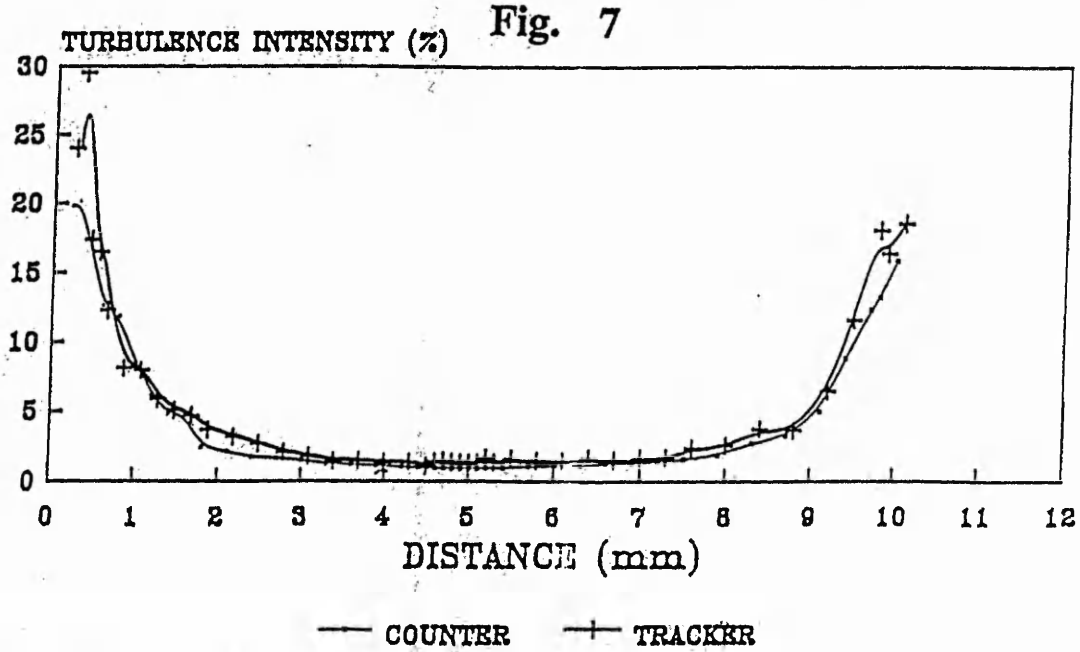

FLOW VISUALISATION OF A LAMINAR JET IMPINGING IN A SEMI-CONFINED SPACE

by

K. Jambunathan, S.A. Ashforth-Frost and B.L. Button.

Department of Mechanical Engineering
Faculty of Engineering
Nottingham Polytechnic
Nottingham NG1 4BU, England.

ABSTRACT

Experimental measurements of averaged velocities in the flow field created by a laminar semi-confined impinging air-jet from a 10mm diameter nozzle have been made using laser-Doppler anemometry at a Reynolds number of 1200 and nozzle to plate spacing of 4. Radial velocities near the wall have been numerically predicted over a Reynolds number range 600 to 1800 and the maximum values agree with measurements within ten percent. The flow is dominated by a recirculating vortex, the size of which increases with Reynolds number, together with a secondary vortex closer to the impingement plate.

The conclusions are supported by whole field flow visualisation using a laser sheet technique.

NOMENCLATURE

d	Nozzle diameter (m)
h	Distance from impingement plate (m)
N	Number of data samples
r	Radial distance from jet axis (m)
Re	Reynolds number
Y	Dimension of cell in radial direction (m)
z	Jet to plate spacing (m)
Z	Dimension of cell in axial direction (m)

INTRODUCTION

Jet impingement flows are frequently used in industrial practice for their excellent heat and mass transfer characteristics. Most of the experimental work so far has concentrated on high Reynolds numbers. The case of laminar impinging flow for both round and slot jets has received some attention in numerical prediction (Deshpande and Vaishnav, 1982, Law and Masliyah, 1984, Rizk and Menon, 1986, Jambunathan et al., 1989) but lesser attention in experimental measurement. To provide complementary experimental information, measurements of averaged velocities in the flow field created by a laminar semi-confined impinging jet have been made using laser-Doppler anemometry. The results are supported by whole field flow visualisation using a low cost laser sheet method. A commercially available finite volume software has been used to numerically model the geometry.

JET CONFIGURATION

Figure 1. shows a schematic diagram of the jet facility and LDA optics. The 10mm diameter air-jet was produced by a wind tunnel comprising a four section settling chamber leading to a seamless stainless steel nozzle through a smooth contraction, providing a fully developed velocity profile at the nozzle exit. Each section of the settling chamber was separated by a fine wire mesh screen, selected according to the criteria of Bradshaw (1968), to remove velocity non-uniformities. The profile coordinates for the contraction were calculated using a computer program by Button and Leech (1972).

The impingement plate and top confinement plate extended to 20 diameters on either side of the jet centreline. The flow rate was controlled by a rotameter and the velocity monitored by pressure tappings, in the settling chamber, connected to a micromanometer with resolution of 0.01mm.

THE LDA SYSTEM

A 10mW He-Ne single component modular LDA system (Dantec 55X) was used for the mean velocity measurements. A Bragg cell was included in the system to provide direction sensitivity and a 3x beam expander to reduce the size of the measurement volume thereby increasing the relative light intensity. A 600mm focal length front lens was used to focus the split laser beams. The beam separation was fixed at 60mm by the optics such that the beam intersection angle was 5.72°. Artificial seeding was provided by a seeding generator (Dantec 55L18). Liquid particles (50% water/50% glycerin) approximately 2um in size are generated and carried into the air flow. In order to avoid unequal seeding concentrations due to entrainment of the ambient air, the outflow region of the flow field was also seeded.

The signal from the photomultiplier (positioned in an off-axis forward location) is analysed by a frequency tracker in conjunction with an interfaced micro-computer.

The LDA system is positioned by an automated traverse mechanism. The maximum backlash found in the horizontal axis was 0.01mm and in the vertical, 0.05mm. Positional errors varied between ±0.015mm and ±0.085mm respectively.

COMPUTERISED DATA ACQUISITION AND PROCESSING FACILITY

A block diagram of the complete measurement system is provided in Figure 2. An 8-bit micro-computer controls the signal processing, traverse mechanism and other peripherals through the IEEE-488 interface and provides limited storage and data reduction capability. Data is transferred to a VAX 785 computer for storage and rapid post-processing via a communications interface adaptor. Although the micro-computer is best restricted to data collection only, on-line data reduction and analysis can be used for a preliminary examination of the Doppler frequencies. This enables suitable range, frequency shift and other software parameters to be set since the accuracy of the measurement using LDA depends upon the correct choice of these parameters. A minimum of 10 batches of 256 samples of data were collected at each measurement station. The flow field was mapped by a series of discrete measurements at intervals of 0.1 to 10mm; the smaller intervals being in regions of high velocity gradient.

QUALITATIVE FLOW VISUALISATION

In order to obtain a visual perception of the flow field a low cost facility was set-up and is shown in Figure 3. A simple lens arrangement was used to generate a thin light sheet by expanding a 10mW He-Ne laser beam in one plane between the two matt black plates. A single lens reflex (SLR) camera and a 80-200mm F4 zoom lens was used with a 1000 ASA red-sensitive film (Kodak 2475). Exposure times were of the order 1/8 s, determined by trial and error. Several seeding mediums were thought suitable for this application. Oil smoke, cigarette smoke, water/glycerin particles, talc and hollow glass spheres were all investigated. A summary of the size, properties of the seeding materials and seeding method is provided in Table 1. Hollow glass spheres (Figure 4) were finally chosen due to their excellent light reflection properties and were introduced into the flow using a simple nebuliser arrangement. The mean diameter of the glass spheres used was 11.5um with standard deviation of 4.5μm. A detailed discussion of these seeding materials and their suitability for this arrangement is given by Braid (1989).

Although the results were favourable they must be considered with reservation since it is not yet understood how well these particles follow the fluid flow. Previous work in this area has been carried out on hollow glass spheres with larger mean diameter. Yoshida et al. (1988) investigated turbulent jet impingement using hollow glass spheres of mean diameter 48.9 μm. They showed that particles rebound from the impinging plate to move upstream against the oncoming flow. Obi et al. (1988) considered larger particles in the range 68.6 to 148μm concluding that the particles promote turbulence of the fluid in a flow with low turbulence and suppress turbulence in a strongly turbulent flow.

Table 1. Comparison of seeding particles.

	Size (μm)	Density (kg/m^3)	Shape	Scattering ability	Seeding method
Cigarette smoke[1]	0.2	1000	nearly spherical	good	plenum chamber
Mineral oil smoke[2]	1-5	860	assumed spherical	good	smoke generator
Glycerin /water	2-5	1100	assumed spherical	poor	seeding generator
Talc[3]	10	278.	flakes	fair	nebuliser
Hollow glass spheres	20-40	228	spherical	excellent	nebuliser

1 Chen and Emrich (1963)
2 Shell Ondina Oil 17
3 Merzkirch (1987)

NUMERICAL MODELLING

The computations were carried out using the PHOENICS computer code which uses the algorithm 'SIMPLEST' of Spalding (1980). The finite difference equations are formulated using an upwind differencing scheme. A non-uniform grid of 56 nodes in the axial direction and 200 nodes in the radial direction was used for the z/d=4 case, and 36 by 200 nodes for z/d=2. This grid was adopted after comparing the results obtained with various mesh densities and near-wall cell sizes. The nodes were concentrated in regions of large gradients; namely, near the walls and the jet axis.

As the size of the near wall cell was reduced from 0.5mm to 0.01mm the effect on the profiles of pressure and velocity gradient at the impingement surface can be seen in Figure 5. The profiles converge to a solution

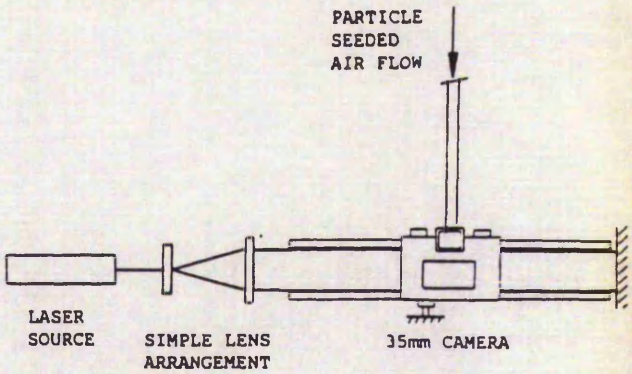

Figure 3. Schematic diagram of the flow visualisation facility.

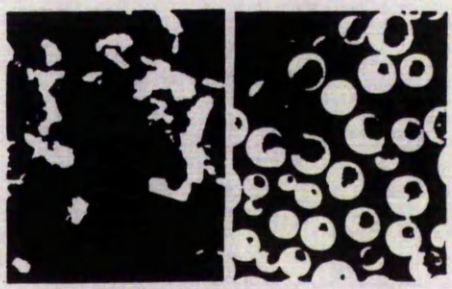

Figure 4. Electron microscope photographs of talc and hollow glass spheres.

where further reduction in the near wall cell size provides no further improvement in the results. A cell size of 0.05mm was adopted since further reduction in the cell size lead to differences in calculated dependent variables not exceeding 3%.

The effect of varying mesh density over the whole domain was also investigated. No appreciable improvemen in the prediction of the near wall velocity gradient, pressure or velocity profiles in the impingement region were detected. However, radial velocity profiles in the

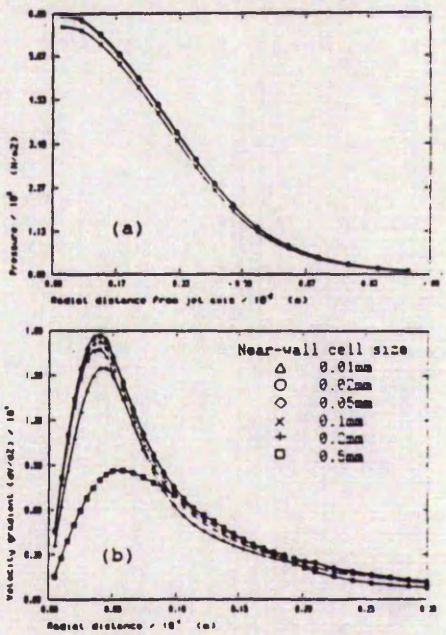

Figure 5. (a) Pressure and (b) velocity gradient at impingement surface for different near wall cell sizes.

outflow region varied considerably. This was thought to be due to the relatively large cell aspect ratio (Y/Z) of 25 in this region. Previous experience and comparison with experiment suggested that an aspect ratio of less than 12.5 is necessary to avoid such errors.

The elliptic nature of the flow field requires that boundary conditions be specified on all sides of the solution domain. Measured values of the jet exit velocity using LDA were specified at the inlet of the domain. Zero velocities were specified at the solid surfaces and a standard laminar wall function activated. A fixed zero pressure was specified at the outlet boundary and the computed pressures are relative to it. The independent variables were monitored for convergence. Iterations were stopped when the velocity residuals were reduced to 10^{-3} and the absolute volumetric error over the whole domain was reduced to 10^{-4}.

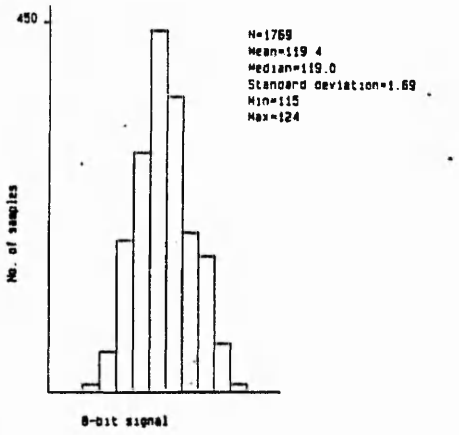

Figure 6. Typical histogram with descriptive statistics.

RESULTS AND DISCUSSION

The validity of the LDA data was checked in several ways. The distribution of the LDA measurements are required to be nearly Gaussian. Consequently, the distribution of the LDA measurements were monitored at various stations. A typical histogram of the raw valid data (obtained in the potential core of the jet) transmitted from the 8-bit processor is shown in Figure 6 with its descriptive statistics. Repeatability of the ensemble averaged mean velocity readings was ensured. The available ranges on the tracker processor overlap such that valid results could be obtained in two ranges with the same frequency shift. Only small differences of the mean velocity were observed with change of tracker range and the results were independent of small changes in frequency shift. In order to avoid any differences all data were taken on one range (0.33-3.3MHz), with a fixed frequency shift (1MHz).

The experimental and numerical radial velocity profiles at various radial stations are compared in Figure 7 for Re=1200 and z/d=4 as a function of the dimensionless distance from the plate h/d, and both show the development of the boundary layer. Up to r/d=1 from the stagnation point the flow is clearly restricted to the wall. The maximum radial velocity increases up to r/d=0.5, decreases slowly up to r/d=1, and then decreases rapidly after r/d=1 which corresponds to the outer edge of the jet. In the stagnation zone (r/d<1) the boundary layer thickness increases only slightly. At further r/d distances there is greater mixing due to the recirculating vortex and the boundary layer thickens more rapidly. Further flattening of the profiles occurs up to about r/d=12, which corresponds to the separation point at the plate, and the beginning of the counter-rotating vortex. The experimental results show the flow more restricted to the wall and higher maximum radial velocities upto r/d=4 when compared with the numerical results, the largest difference in the numerical results being less than 10% of the experimental. At larger radial distances from the stagnation point the radial velocity profiles compare well with the experimental.

The streamline plots obtained from numerical predictions for Reynolds numbers 600, 900, 1200, 1500 and 1800 and z/d=2 and z/d=4 are presented in Figure 8 and show good correlation with experimental flow visualisation pictures carried out for Reynolds numbers of 600 and 1200 and z/d=2 and 4. The experimental flow visualisation was very useful in providing an insight into the flow field of jet impingement as a preliminary investigation for LDA, but near wall information was inhibited by the reflection of the laser beams on the solid surface. The results show that the flow is dominated by a recirculating vortex, whose size is limited by the domain, and a secondary vortex closer to the impingement plate. This secondary motion is of opposite sense to the primary.

Increasing Reynolds number causes the vortices to enlarge and move downstream up to Re=1200. At Re=1500 and z/d=4 a further recirculation region appears close to the confinement plate which increases in size with Reynolds number, the primary vortex now moving radially inwards towards the axis. This occurs at Re=1800 for z/d=2. Increasing the z/d ratio from 2 to 4 leads to a large movement downstream of the recirculating regions.

Separation is shown by the numerical results to occur at approximately r/d=12 for Re=1200 and z/d=4 where the primary vortex lifts off the impingement plate and the secondary counter-rotating vortex begins. This corresponds with the LDA results previously discussed. Re-attachment occurs at r/d=18.

CONCLUSIONS

Flow visualisation experiments have been conducted in air to study a laminar semi-confined impinging jet, and have been correlated with numerical results using a commercially available finite volume package. The experimental conditions and equipment used have been described with validation methods and associated uncertainties where appropriate. The effects of varying near-wall cell sizes and the cell density over the whole domain have been presented for the numerical work.

The quantitative numerical results compare favourably with the LDA results (obtained for one geometrical configuration, Re=1200, z/d=4) except close to the plate in the impingement region where velocity gradients and maximum radial velocity profiles are underpredicted. The development of the boundary layer to separation is clearly seen from plotted radial velocity profiles.

The simple, low cost, whole field visualisation technique using a laser sheet with hollow glass spheres as seeding particles has been found to be successful in describing jet impingement flows. Excellent correlation between numerical and experimental qualitative flow visualisation has been obtained. Points of separation and re-attachment are clearly indicated. Based on numerical results and supported by experiment, the response of the flow field to Reynolds number at two nozzle to plate distances has been characterised. The flow is dominated by a recirculating vortex limited by the confinement plates, which increases in size (and hence moves downstream) with an increase in Reynolds number, together with a secondary counter-rotating vortex closer to the impingement plate. As the Reynolds number is increased further, a third recirculation zone appears close to the top confinement plate, reducing the momentum of the primary vortex. Consequently the primary vortex moves closer to the jet axis. The Reynolds number at which this phenomenon occurs depends on the nozzle to plate spacing.

ACKNOWLEDGEMENTS

The authors wish to thank Nottingham Polytechnic for providing the facilities to carry out this work and the National Advisory Body for funding one of the authors, Mrs S A Ashforth-Frost, as a research assistant.

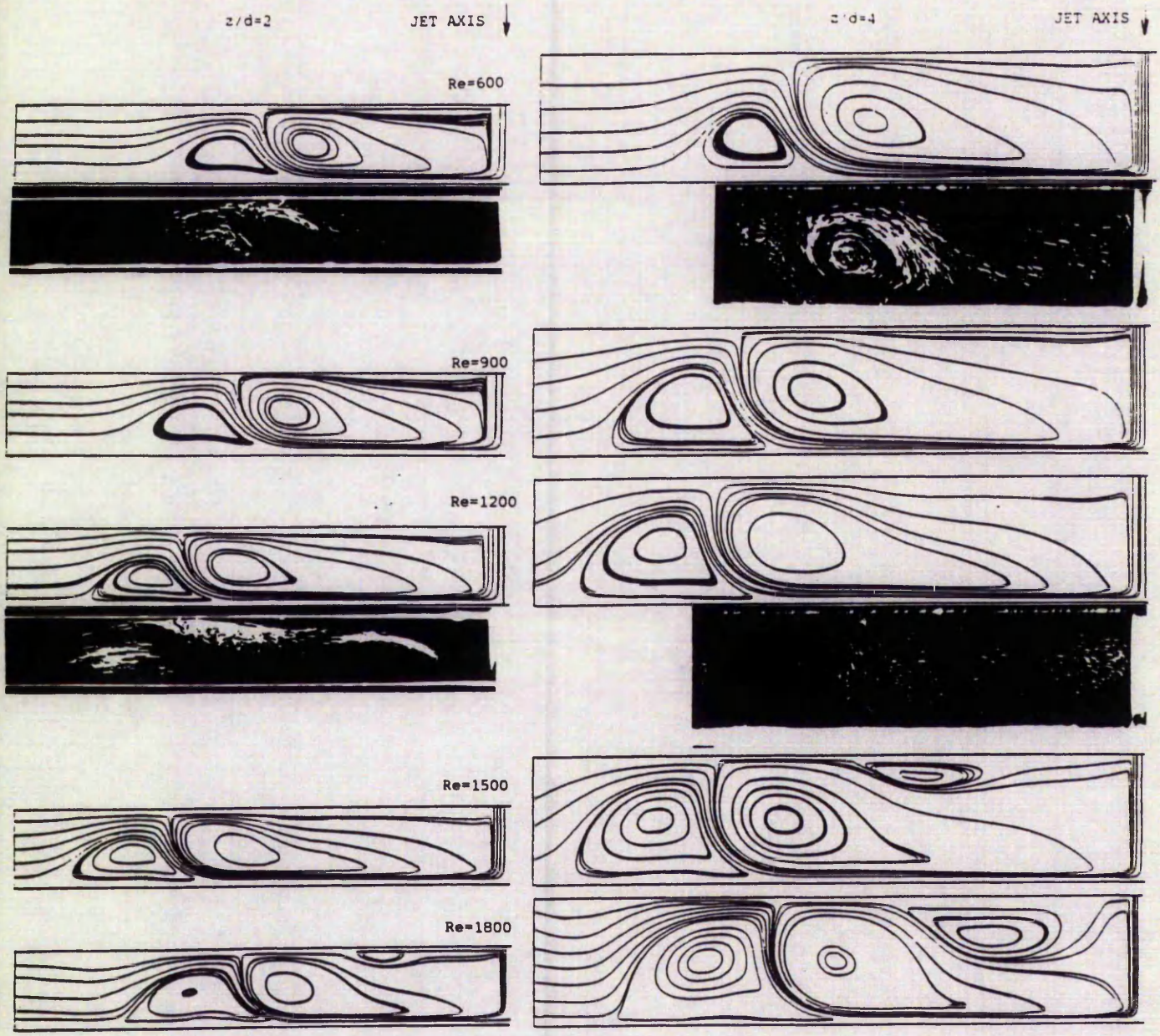

Figure 8. Comparison of numerical results with available experimental.

REFERENCES

Bradshaw, P. 1968 Simple wind tunnel design. *NPL Aero report 1258.*

Braid, S. 1989 Qualitative flow visualisation of jet impingement. *BEng Report*, Dept. Mech. Eng., Nottingham Polytechnic, NG1 4BU.

Button, B.L. & Leech, J.R. 1972 The selection of a contraction design method. *Report No. ME 395.* Dept. Mech. Eng.,Lanchester Polytechnic, Coventry.

Chen, C.J. & Emrich, R.J. 1963 *The Physics of Fluids*, 16, 1-9.

Deshpande, M.D. & Vaishnav, R.M. 1982 Submerged laminar jet impingement on a plane. *J. Fluid. Mech.* 114, 213-236.

Jambunathan, K., Kapasi, S., Button, B. & Bland, J. 1989 Numerical study of the flow field for confined laminar jet impingement. Presented at the *Third International PHOENICS User Conference, Dubrovnik, Yugoslavia.*

Law, H.-S. & Masliyah, J.H. 1984 Numerical prediction of the flow field due to a confined laminar two-dimensional submerged jet.*Computers and Fluids* 12, 3, 199-215.

Merzkirch, W. 1987 *Flow Visualisation*. Academic Press Inc. (London) Ltd.

Obi, S., Hishida, K. & Maeda, M. 1988 Heat transfer characteristics from a flat plate to a gas-solid two-phase flow downstream of a slit injection. *ASME J. Heat Transfer*, 110, 687-694.

Rizk, M.H. & Menon, S. 1986 Numerical simulation of impinging jets. Presented at the *AIAA 24th Aerospace Sciences Meeting*, Nevada, USA.

Spalding, D. B. Mathematical modelling of fluid mechanics, heat transfer and chemical reaction processes. A lecture course, CFDU report, HTS/80/1.

Yoshida, H., Suenaga, K. & Echigo, R. 1988 Turbulence structure and heat transfer of a two-dimensional impinging jet with gas-solid suspensions. *ASME J. Heat Transfer*, 96, 461-467.

Effect of nozzle geometry and semi-confinement on the potential core of a turbulent axisymmetric jet.

S Ashforth-Frost and **K Jambunathan**

Department of Mechanical Engineering, Faculty of Engineering and Computing,
The Nottingham Trent University, Burton Street, Nottingham, NG1 4BU.

Abstract

Maximum heat transfer due to jet impingement is achieved when the impingement plate is placed at the end of the apex of the potential core of the jet, and various recommendations exist in the literature for the optimal spacing. In this paper, the effect of nozzle geometry and semi-confinement on the length of the potential core of the jet at a Reynolds number of 20 000 is reported. The potential core lengths of an unconfined flat jet, a semi-confined flat jet, an unconfined fully developed jet and a semi-confined fully developed jet have been quantified. Mean velocity and turbulence profiles were measured using laser-Doppler anemometry and the optimal nozzle to plate spacing, for each configuration, established using liquid crystals as the temperature indicator. It was found that the potential core of the jet is longer for a fully developed jet exit profile, and is further extended due to the effect of semi-confinement. Semi-confinement was found to reduce the stagnation point heat transfer by up to 10% at the optimal spacing.

1 Introduction

The jet exit height is important in many impinging flow fields; it has been long established that maximum heat transfer due to jet impingement is achieved when the impingement plate is placed at the end of the apex of the potential core of the jet, and various recommendations exist in the literature for the optimal spacing. The potential core extends from the nozzle and is the central portion of the flow in which the velocity remains constant and equal to the jet exit velocity. It is formed as a result of turbulent mixing which originates near the nozzle exit. Turbulence is generated at the jet boundary and diffuses towards the axis such that the width of the mixing zone increases with downstream distance, leaving the potential core region. Some authors state that the potential core length is dependent on Reynolds number while others state that it is independent of Reynolds number but dependent on the velocity profile. The latter view is supported by Abromavich (1963). The velocity profile on impingement will depend on the shape, velocity distribution and turbulence intensity at the nozzle exit. According to Gauntner et al. (1970) the length of the potential core generally lies in the region 4.7d to 7.7d. Gauntner et al. (1970) and Sparrow et al. (1975) suggest a nozzle to surface spacing of 6.1d if the value is unknown. Beltaos and Rajaratnam (1977) recommend 6.1d to 6.3d.

Much of the early jet impingement works related only to unconfined configurations and mostly using converging nozzles or orifices. There is only a limited amount of work which addresses the effect of nozzle geometry and confinement. Obot et al. (1979) carried out an extensive investigation into the effect of nozzle inlet shape and nozzle length to diameter ratio on unconfined impingement heat transfer. In all of their tests they reported similar shapes in the radial Nusselt number distribution but significant differences in their magnitudes. Nozzles with a sharp edged inlet produced much higher heat transfer than contoured nozzles and the difference was more pronounced the shorter the nozzle length. A more conclusive study could be achieved by adjusting the nozzle to plate spacing in smaller increments to allow for the variation in the development of the velocity profiles and subsequent effect on the potential core length.

Lepicovsky (1989) discussed how the nozzle geometry affects the boundary layer thickness at the nozzle exit, which in turn controls the rate of jet mixing and spreading. Applying these findings to jet impingement, the jet mixing will affect the decay of the jet and the length of the potential core and consequently the heat transfer distribution. Lepicovsky (1989) demonstrated that a thin nozzle exit laminar boundary layer resulted in a shorter potential core than in the case of a thick turbulent nozzle exit boundary layer.

Finally, Obot et al. (1982) studied heat transfer distributions where the nozzle was an integral part of a flat surface parallel to the impingement surface (ie.

10th International Heat Transfer Conference, Brighton, UK, 14-18 August 1994.

semi-confined) for 18000<Re<50000. Comparison with the unconfined case showed that semi-confinement reduced the heat transfer, the most significant difference occurring for z/d=2 and the least difference occurring for z/d=6.

Many investigators have omitted details of the nozzle configurations in their reported work. In addition, in some cases where the length of the potential core has been established, the criterion on which the measurement was based is not stated. For these reasons, it is difficult to establish the effect of the nozzle geometry and confinement on the potential core, and the subsequent effect on impingement heat transfer, from existing literature.

In this paper, the effect of nozzle geometry and semi-confinement on the length of the potential core of the jet at a Reynolds number of 20 000 is reported, and the subsequent effect on stagnation point heat transfer discussed.

2 The experimental arrangement

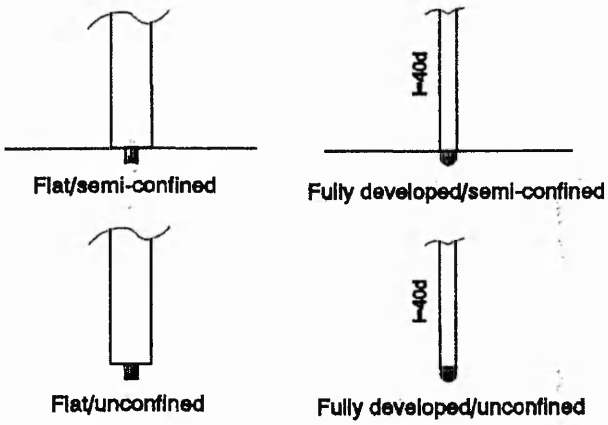

Figure 1. Jet impingement geometries investigated.

Four different jet impingement configurations were investigated, shown schematically in figure 1. Two nozzles were used to provide a flat and a fully developed velocity profile, respectively. To achieve a flat velocity profile, a chamber of 25.4 mm diameter was used leading to a 10 mm orifice. To achieve fully developed flow, a sharp-edged nozzle of 10 mm internal diameter was used and was made from seamless stainless steel tubing with a nominal wall thickness of 1.5 mm. A nozzle length of 40d was used to provide a fully developed velocity profile. According to Obot et al. (1979) a nozzle length of at least 20d is necessary to attain fully developed flow to within 5% and to ensure that the nozzle entry has a small influence on the jet exit velocity. The jet exit profile was compared to that computed from the empirical equation of Schlicting (1968):

$$\frac{u}{u_{max}} = \left(\frac{y}{R}\right)^{\frac{1}{n}}$$

where y is given as the distance from the pipe wall and n=6.5 at Re=20000. The maximum velocity (at the axis) was evaluated from

$$\frac{u_b}{u_{max}} = \frac{2n^2}{(n+1)(2n+1)}$$

Air from a dedicated compressor passed through two filtering systems (25 μm and 5μm) followed by a high precision regulator prior to the nozzles. For the LDA measurements, olive oil particle seeding was provided by a Dantec seeding generator. The centreline jet exit velocity was found to be steady over long time periods. Maximum observed variations in the mean and fluctuating velocities over a typical continuous four hour period were 1% and 5% respectively.

The impingement and confinement plates used extended to 20 diameters on either side of the jet centreline.

A 10mW He-Ne single component modular LDA system (DANTEC 55X) was used for the mean velocity and turbulence measurements. A Bragg cell provided directional sensitivity and a 3x beam expander reduced the size of the measurement volume. The signal from the photomultiplier (positioned in an off-axis forward scatter location) was analysed by a frequency tracker in conjunction with an interfaced micro-computer. The complete system is described in Ashforth-Frost (1994). The LDA optics were tilted by half the intersection angle, relative to the semi-confinement plate, to allow the jet velocity profiles to be measured as close as 0.1d from the nozzle exit. The uncertainty is expected to be negligible since the angle is very small. The uncertainties in the mean velocity and turbulence component were estimated to be less than 5% and 7% respectively. Spatial uncertainty was estimated as 1% of the nozzle diameter.

To assess the effect of the semi-confinement on heat transfer, the nozzle to plate spacing at which maximum stagnation point heat transfer occurred was established using liquid crystal thermography by traversing the impingement plate relative to the jet exit. The constant heat flux impingement plate consisted of a sheet of transparent perspex onto which was sprayed a thin layer of micro-encapsulated liquid crystals followed by a thin layer of black paint, to improve colour resolution. Thin metal foil (25 μm) was attached to the top of the plate using double sided tape and provided the constant heat flux boundary condition via a DC power supply. The

back of the impingement plate was maintained at the liquid crystal change temperature to minimise conduction losses, as described by Goldstein and Franchett (1988). Combined losses due to radiation and conduction were considered small. Details of this technique and the design of surface heaters can be found in Jambunathan et al. (1993) and Jambunathan et al. (1994) respectively. Based on the procedure proposed by Kline and McClintock (1953), the uncertainty in the heat transfer coefficient was less than 8%. Under constant ambient conditions, the relative magnitudes of heat transfer for each configuration were indicated by the power required to locate the liquid crystal isotherm in the vicinity of the stagnation point.

3 Presentation and discussion of results

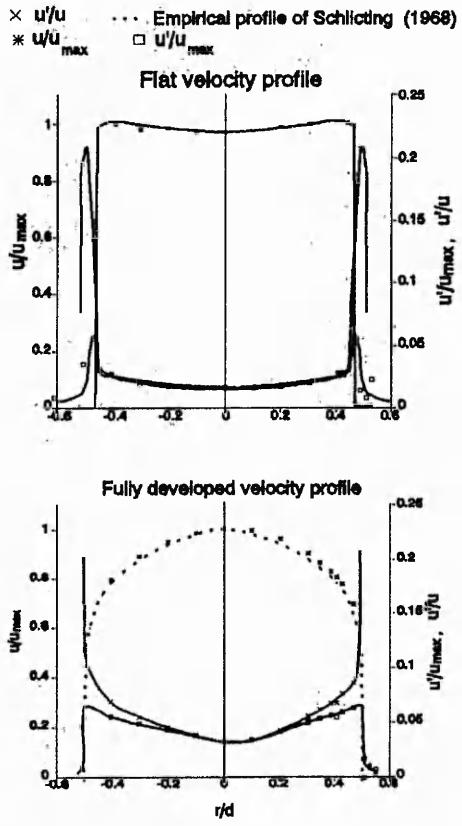

Figure 2. Effect of nozzle exit profile and semi-confinement on the potential core of a free jet. Re = 20 000.

The exit velocity and turbulence characteristics of the long nozzle and orifice are shown in figure 2. The data is non-dimensionalised with the maximum jet exit velocity, u_{max}. The exit velocity and turbulence profiles were shown to be symmetric within the estimated uncertainty intervals. The turbulence levels at the exit of the pipe were higher than those from the orifice, except as the edge of the jet was approached. The axial turbulence intensity of the fully developed jet (3%) is approximately twice the magnitude of the flat jet and is due to the development of the flow in the nozzle. The turbulence increases as the edge of the jet is approached, reaching 20% at the edge of the nozzle. The velocity profile from the long nozzle compares with the fully developed empirical profile of Schlicting (1968) to within 5%. The velocity profile exiting the orifice showed a slight increase as the edge of the jet was approached and was attributed to the effects of a vena contracta.

The axial development of mean velocity and local turbulence intensity for all of the geometries considered is shown in figure 3, and allows the effect of nozzle exit velocity profile and semi-confinement on the length of the potential core to be assessed. Initially, the central core of the jet is unaffected by the regions of entrainment and shear surrounding it, and the velocity remains constant at the jet exit value. This potential core is commonly defined as the distance from the nozzle exit to where the axial velocity has decreased to 95% of the initial axial velocity. Based on a 95% criterion, the potential core lengths for the geometries considered are 4.5d, 4.8d, 5.3d and 5.8d for the flat unconfined jet, the fully developed unconfined jet, the flat semi-confined jet and the fully developed semi-confined jet, respectively. The potential core is extended by up to 10% due to the fully developed velocity profile which corroborates the findings of Lepicovsky (1989). This can be attributed to the higher shear which prevails at the edge of the flat jet due to higher velocity gradients, which in turn leads to more entrainment and the mixing layer spreading to the jet axis sooner than in the fully developed exit profile. This is despite the axial level of turbulence being higher initially in the fully developed jet. This phenomenon is also reflected in the level of turbulence intensity which increases much more rapidly for the flat jet in the initial region (x/d<2), than for the fully developed jet. It is interesting to note that for a fully developed semi-confined jet with an initial axial turbulence intensity of 6%, Ashforth-Frost (1994) reported a potential core length of 5d, as opposed to the present 5.8d, indicating the extension of the potential core due to lower levels of initial turbulence, for a given geometry.

The length of the potential core is further extended, by up to 20%, due to the effect of semi-confinement, and is directly attributed to the semi-confinement plate limiting entrainment. The largest increase occurs for the fully developed exit profile, due to the lower rates of shear at the edge of the jet which already limit entrainment when compared to the flat jet.

As the distance from the nozzle exit increases, the above effects become less significant and the difference between the velocity profiles subsides.

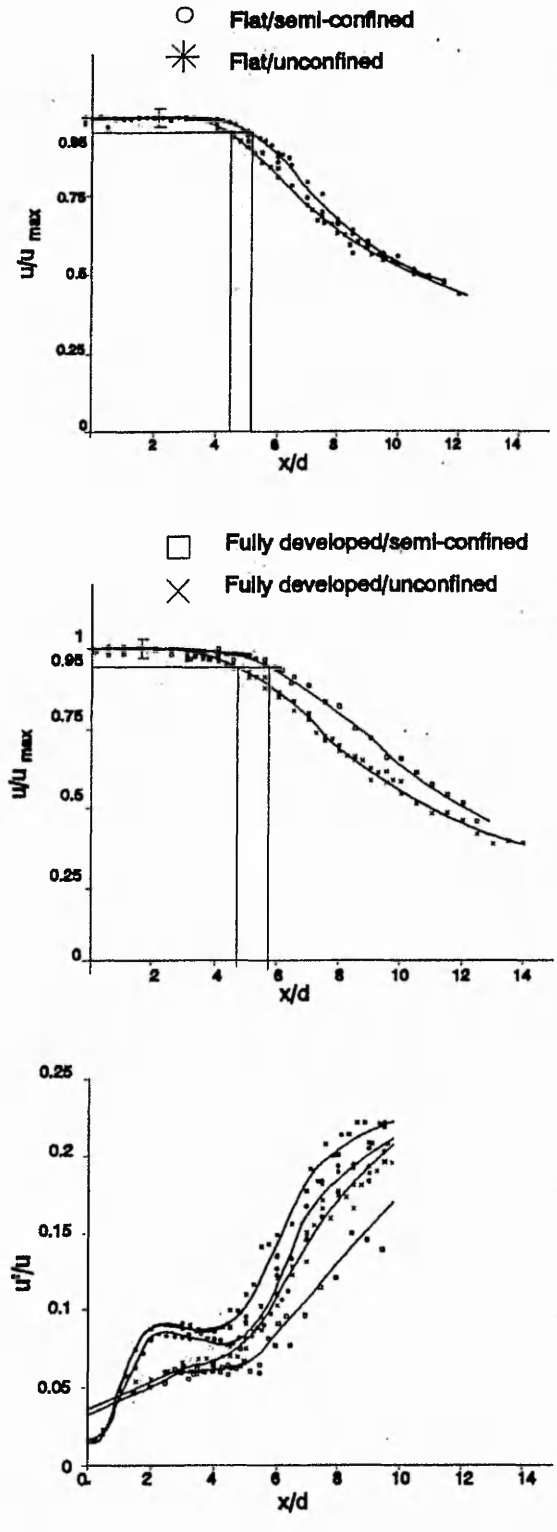

Figure 3. Effect of nozzle exit profile and semi-confinement on the potential core of a free jet. Re = 20 000.

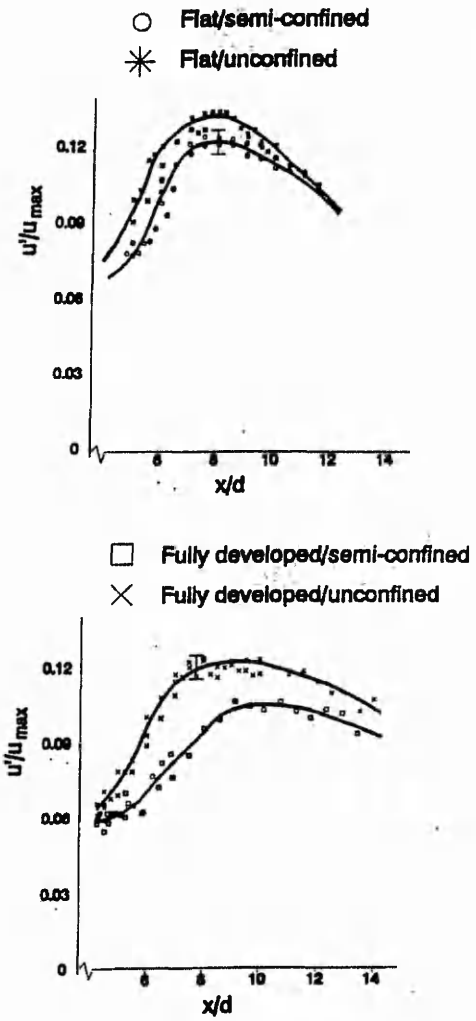

Figure 4. Effect of nozzle exit velocity profile and semi-confinement on the axial development of turbulence within a free jet.

The downstream development of the axial turbulence is shown in figure 4. For both jet exit velocity profiles a lower axial turbulence level develops with semi-confinement. The maximum axial turbulence occurs at x/d≈8 and x/d≈9.5 for the flat and fully developed velocity profiles respectively. This phenomenon is again attributed to the effect of the velocity profile limiting entrainment in the fully developed case. The turbulence level in the flat jets is higher than in the fully developed jets. As x/d is increased further, beyond x/d=12, the difference in the profiles decreases. In terms of turbulence intensity, by x/d=14, a level of 25% turbulence intensity prevails.

The nozzle to plate spacing at which maximum stagnation point heat transfer occurred was difficult to establish since high heat transfer was observed over a distance of several diameters. This was also observed by Baughn and Shimizu (1989) and Yan et al. (1992). However, the location where the highest heat transfer rates first occurred coincided with the length of the

potential core, based on a 95% criterion, to within 10% of the measured potential core length. For both jet exit profiles, semi-confinement was found to reduce the stagnation point heat transfer, at the optimal nozzle to plate spacing, by up to 10%. This reduction is attributed directly to the lower levels of axial turbulence generated as a result of reduced entrainment due to the presence of the semi-confinement. The fully developed jet exit profile provided marginally higher heat transfer than the flat profile at the optimal nozzle to plate spacings.

4 Conclusions

Laser-Doppler anemometry and liquid crystal thermography have been used in a preliminary study to assess the effect of nozzle geometry and semi-confinement on the potential core of a turbulent axisymmetric jet at a Reynolds number of 20 000, and the subsequent effect on the magnitude and axial location of the optimal convective surface heat transfer coefficient due to jet impingement. The potential core lengths, and turbulence levels, in an unconfined flat jet, a semi-confined flat jet, an unconfined fully developed jet and a semi-confined fully developed jet have been quantified. The jet potential core is up to 10% longer for the fully developed jet exit profile when compared to the flat jet exit profile. Semi-confinement has the effect of further extending the potential core by up to 20%, and reducing the stagnation point heat transfer by up to 10% at the optimal nozzle to plate spacing. The maximum stagnation point heat transfer occurs when the impingement plate is placed at the end of, and just downstream from, the potential core, based on a 95% criterion.

5 References

Abromavich G N, 1963. *The theory of turbulent jets.* MIT Press.

Ashforth-Frost S A. *Flow visualisation of semi-confined jet impingement.* PhD Thesis, The Nottingham Trent University. Submitted June 1994.

Baughn J W AND Shimizu S, 1989. Heat transfer measurements from a surface with uniform heat flux and impinging jet. *ASME J. Heat Transfer*, **111**, 1096-8.

Beltaos S and Rajaratnam N, 1977. Impingement of axisymmetric developing jets. *J. Hydraulic Research*, **15**(4), 311-26.

Gauntner J W, Livingood J N B and Hrycak P, 1970. Survey of literature on flow characteristics of a single turbulent jet impinging on a flat plate. *NASA Report TN D-5652.*

Goldstein R J and Franchett M E, 1988. Heat transfer from a flat surface to an oblique impinging jet. *J. Heat Transfer*, **110**, 84-90.

Jambunathan K, Ashforth-Frost S and Whitney C F, 1993. Heat transfer from a flat plate by a semi-confined impinging slot jet. *Proc. EUROTHERM 32 Seminar*, Oxford University, UK, 5-7 July, 93a-94.

Jambunathan K, Ashforth-Frost S and Whitney C F, 1994. Design of surface heaters for liquid crystal thermography. *IMechE Seminar on Optical Methods and Data Processing in Heat and Fluid Flow*, City University, London, 14-15 April, 43-7.

Lepicovsky J, 1989. The role of nozzle exit boundary layer velocity gradient in mixing enhancement of free jets. *Proc. 3rd ASCE/ASME Mechanics Conf.*, San Diego, CA.

Obot N T, Majumdar A S and Douglas W J M, 1979. Effect of nozzle geometry on impingement heat transfer under a round turbulent jet. *ASME Paper 79-WA/HT-53.*

Obot N T, Majumdar A S and Douglas W J M, 1982. Effect of semi-confinement impingement heat transfer. *Proc. 7th Int. Heat Transfer Conf.*, Munich, 6-10 September, **3**, 395-400.

Schlicting H, 1968. *Boundary layer theory.* McGraw Hill, New York.

Sparrow E M, Goldstein R J and Rouf M A, 1975. Effect of nozzle-surface separation distance on impingement heat transfer for a jet in a crossflow. *J. Heat Transfer*, **97**(4), 528-33.

Yan X, Baughn J W and Mesbah M, 1992. The effect of Reynolds number on the heat transfer distribution from a flat plate to an impinging jet. *ASME Heat Transfer Division: Fundamental and Applied Heat Transfer Research for Gas Turbine Engines*, **226**, 1-7.

OPTICAL METHODS AND DATA PROCESSING IN HEAT AND FLUID FLOW

Papers presented at a seminar organised
by the Energy and Thermofluid
Mechanics Group,
on 2nd and 3rd April 1992

The Institution of Mechanical Engineers
LONDON

Application of Image Processing to Liquid Crystal Thermography

S Ashforth-Frost, L S Wang and **K Jambunathan.** Department of Mechanical Engineering, Faculty of Engineering, Nottingham Polytechnic NG1 4BU. **D P Graham** and **J M Rhine.** British Gas plc, Midlands Research Station, Solihull B91 2JW

Abstract

Menu-driven software packages for the automatic analysis of liquid crystal thermographs have been developed. Digital image processing techniques are used to extract colour change data from liquid crystal coated test specimens, either in real time or from a video recording. The inferred temperature distribution can then be used in the determination of the local, steady state convective heat transfer coefficient. The calculation method is chosen to suit the experimental technique; either a one dimensional transient conduction model or a simple energy balance over the thickness of the specimen. This development has substantially reduced the time required for the analysis of thermographic data and has eliminated the subjective interpretation of colour change information. With the added advantage of automatic interpretation using image processing techniques, liquid crystal thermography is a very powerful, yet simple, measurement tool for the determination of quantitative heat transfer data.

Nomenclature

A	area of heated surface (m^2)
h	heat transfer coefficient (W/m^2K)
i	integer
k	thermal conductivity (W/m K)
$\dot{Q}$	supplied power / heat transfer rate (W)
t	time (s)
T	temperature (K)
x	specimen thickness (m)
X	relative area of binarised image
α	thermal diffusivity (m^2/s)

Subcripts:

a	air
b	water bath
lc	liquid crystal
0	zeroth frame buffer
1	first frame buffer

1 Introduction

Moffat (1990) has recently reviewed available methods of heat transfer/ temperature measurement and their applications. Liquid crystals are identified as a convenient measurement method offering satisfactory accuracy and resolution. Providing both qualitative and quantitative results of surface temperature, they are low in cost, non-intrusive, easy to use, versatile, reversible and can replace extensive thermocoupling in complex geometries providing that optical access can be obtained. Until recently, the liquid crystal colour thermographs were processed manually. This allowed uncertainties to be introduced in to the results by human error and individual interpretation of colour. In addition, the method was time consuming if a detailed distribution of surface temperature was required. Surface temperature information can be obtained automatically from liquid crystal thermographs by either chromatic or mono-chromatic interpretation. Kasagi et al. (1989) provide a detailed discussion of chromatic interpretation. A later paper by Gomiciaga et al. (1991)

*Research Assistant from the Department of Modern Mechanics, University of Science and Technology of China.

describes the development of a similar automatic system. The current development is based on mono-chromatic interpretation at a single wavelength. A similar approach was used by Kasagi et al. (1987) and a further variation by Akino et al. (1989a) who used a set of band-pass optical filters; for a steady liquid crystal thermograph the filters were inter-changed until a series of mono-chromatic images had been obtained. Further work by Akino et al. (1989b) looks at surface temperature visualisation based on the method of multiple regression between colour and temperature.
This paper describes the development of a single wavelength mono-chromatic digital image processing system for liquid crystal thermography in both transient and steady-state processes and outlines the experimental techniques.

2 Liquid crystal thermography

2.1 Thermochromic liquid crystals

Cholesteric liquid crystals reflect light at a specific wavelength (colour) for a given temperature and possess the most suitable optical properties for temperature indication. They have been used extensively for surface temperature (leading to heat transfer) measurement. A good general paper and review of liquid crystals in fluid mechanics and heat transfer has been provided by Kasagi et al. (1989). More recently, Lin et al. (1991) have carried out an extensive literature review on the applications of liquid crystals in several industries. A typical narrow band liquid crystal formulation changes colour through the whole spectrum over a bandwidth of 1 deg C starting at approximately 35 deg C and is colourless below and above this range. The micro-encapsulated liquid crystals are supplied in a water soluble binder which when sprayed onto a surface dries as a paint. A layer 30-50 μm is applied over a thin layer of water soluble black paint which improves the colour resolution by absorbing unreflected light. Single event calibration is normally carried out. Bright green has been used by the authors which corresponds to a narrow band filter of wavelength 5286 Å and half bandwidth of 73 Å. Both the illumination and viewing angles are fixed during calibration and experiment. Change in calibration temperature is considered negligible or at least cannot be discriminated when repeated after the tests. The liquid crystal can be calibrated to within 0.1 deg C and its time response is reported by Ireland and Jones (1987) to be within a few milliseconds. Due to the very thin layer of liquid crystals on the specimen surface the thermal resistance is considered to be negligible.

2.2 Experimental technique

2.2.1 Transient analysis

The transient wall heating technique requires measurement of the elapsed time to increase the surface temperature of the liquid crystal coated test specimen from a known initial temperature to a predetermined value. The rate of heating is recorded by monitoring the colour change patterns of the liquid crystal with respect to time. If the specimen is made from a material of low thermal diffusivity and chosen to be sufficiently thick, then the heat transfer process can be considered to be one dimensional into a semi-infinite medium. Numerical and analytical techniques can be used to solve the one dimensional transient conduction equation:

$$\frac{\partial T}{\partial t} = \alpha \frac{\partial^2 T}{\partial x^2}$$

Jambunathan et al. (1987) replace the above equation with finite difference approximations and use an explicit numerical solution method which is also employed here. Ireland and Jones (1985) describe alternative solutions using the Gauss error function.

2.2.2 Steady state analyses

i) Constant flux method

This method has been considered in detail by Rhine and Tucker (1991). Uniform heating of the test specimen surface is required which limits the range of geometries to which the method can be applied. The electrically heated specimen is exposed to a cool flow field. Current is increased to the surface until the liquid crystal reflects the required colour at the desired measurement position. The liquid crystal thermograph is recorded and the above procedure is repeated for other positions. Newton's law of cooling is used to obtain the heat transfer coefficient:

$$\dot{Q} = h\ A\ (T_{lc} - T_a)$$

where $\dot{Q}$ is obtained as the product of current through and voltage across the heater, less losses due to radiation and conduction. Losses are estimated by conducting a 'no flow' experiment in which the test surface is heated to a constant temperature and the heat loss due to natural convection (calculated using an appropriate empirical equation) is deducted from the measured heat flux. By repeating this process for a series of power inputs, and plotting a graph of losses against surface temperature, the losses can be estimated at any measurement position. Alternatively, the losses can be calculated using the well known Stefan-Boltzmann law and Fouriers conduction equation.

ii) Constant temperature method

The liquid crystal coated test specimen forms one side of a constant temperature water bath and is exposed to a cool air flow. The resulting thermograph is recorded on video and further measurement positions are obtained by adjusting the water bath temperature. This method is more time consuming due to the large volume of water that needs to be heated. The use of a water bath also limits the types of geometries that can be investigated. In this case the heat transfer coefficient is determined by equating convection to the conduction at the surface:

$$h\ A\ (T_{lc} - T_a) = \frac{k\ A}{x}\ (T_b - T_{lc})$$

2.3 Experimental uncertainty

All results are critically dependent on the calibration of the liquid crystals. There are several other sources of uncertainty in the temperature measurement, for example, non-uniformities in the liquid crystal layer, non-uniform heating, camera response etc. but these are small in comparison to other factors. The thermal conductivity of insulating materials used as substrates can be difficult to measure. Uncertainty in the estimation of heat losses, measurement of input power and surface area must be considered. Suitable choice of the liquid crystal formulation and test working temperatures must be made to ensure that temperature differences in the calculations $(T_{lc} - T_a)$ are not too small to cause unreasonable errors. Careful consideration of the above factors during the planning of the experiment can lead to an uncertainty in the value of the heat transfer coefficient of the order of 10%, Baughn et al. (1988), Akino et al. (1989a) and Hollingsworth et al. (1989).

3 Image processing facility

3.1 Hardware capabilities

A schematic diagram of the image processing arrangement is shown in figure 1. A CCD camera (756 x 581 resolution, 0.5 lux sensitivity) fitted with a mono-chromatic narrow band filter (5286 Å) is used to record the liquid crystal thermographs on a U-matic video recorder. The image processing system employs an IBM compatible 386 personal computer with a Data Translation® (1989) on board

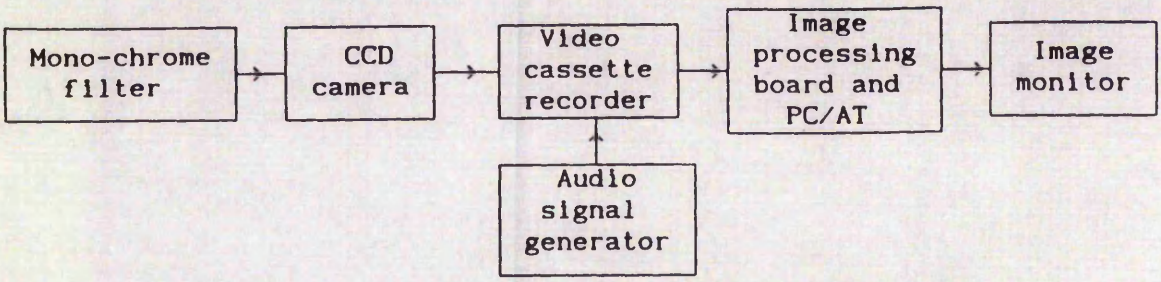

Figure 1. Block diagram of image processing system.

arithmetic frame grabber and associated software, and an A/D card to enable the detection of an audio signal, used to determine the start time of an experiment. Four images of resolution 512 x 512 pixels x 8-bit (256 grey levels) can be stored simultaneously such that four data recordings can be extracted and processed during a single run of the developed program. Potentially up to sixty-four additional frame buffers can be allocated from the available system memory by the dedicated software. A monitor connected to the video camera facilitates focussing and monitoring during the test. A high resolution (850 line) mono-chrome monitor is used to carry out spatial calibration and view both the recorded and binarised images. Typical recorded and binarised images are shown in figure 2 for annular swirling flow. Frames can be analysed at intervals of 40 ms, determined by the video rate (25 frames/s).

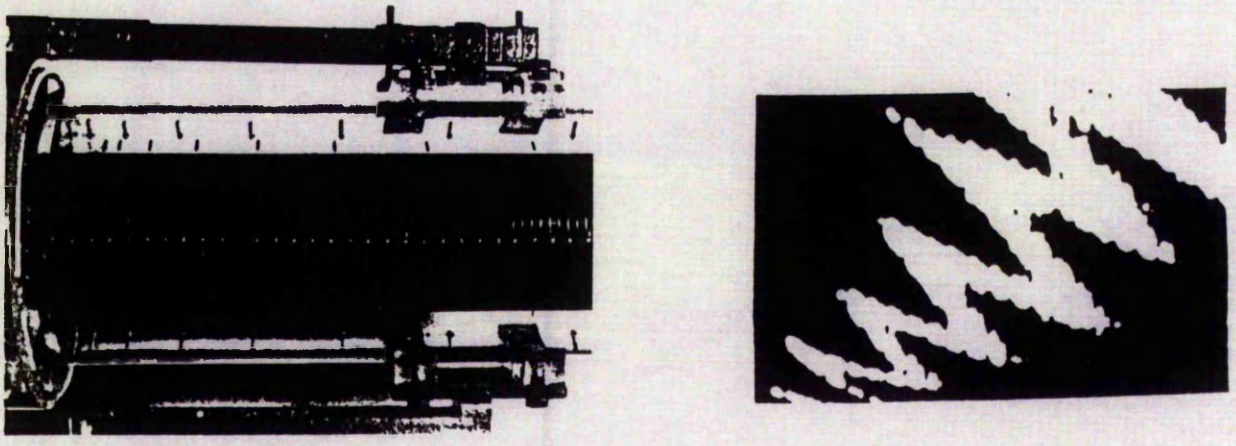

(a) (b)

Figure 2. Typical images for annular swirling flow: (a) liquid crystal thermograph, (b) enlarged binarised image.

3.2 Software environment

The system operates on a command line arguments basis with a series of user friendly multi-layer menu-driven prompts. It has been developed under Microsoft MS-DOS 3.3. The source code is written and compiled using Microsoft C version 5.1. Standard image processing routines from Data Translation® are called from DT-IRIS version 1.04. Program linking was performed using Microsoft overlay LINK version 3.65.

3.3 System operation

For both the steady-state and transient processes the image is collected by the video camera to be analysed 'in situ', or recorded on video for later analysis, by the image processing system. The black/white composite video camera signal is directed to the video cassette recorder. The generated analogue video signal is grabbed by the video frame grabber of the computer. The zeroth stored image is

usually of the geometry before the liquid crystal test commences (ie. background of the specimen). The subsequent images stored in the buffers contain liquid crystal thermographs on the specimen surface.
In the transient case three further images are stored according to a preset time interval. In the steady state case only two buffers are used; the areas of the isotherms from consecutive frames after binarisation are compared until the difference between them lies within a preset tolerance. A steady state is regarded as being achieved if the following equation is satisfied

$$|X_1 - X_0| < 0.5(X_1 + X_0)(\text{tolerance})$$

A pixel by pixel analysis of the intensity of the signal is carried out by the image processing board and associated software. An 8-bit integer, i, between 0 and 255 is assigned to each pixel and stored in computer memory. The zeroth image is subtracted from each of the other images and the resulting images are binarised. A threshold, T, is controlled manually and the binarisation procedure is carried out according to the criterion below:

$$\text{if } i \leq T \text{ then } i = 0$$
$$\text{if } i > T \text{ then } i = 255.$$

Careful selection of the threshold value ensures that relevant information is maintained in the image. A facility for geometrical spatial correction when viewing the liquid crystal isotherms through a transparent wall and/or slightly off-axis is also provided in the software. Noise reduction can be carried out by removing isolated pixels (to reduce background noise in the binarised image) or by median filtering based on a 3 x 3 matrix, although the latter increases the processing time considerably. A potential development which can increase the execution speed is proposed by Karaman and Onural (1989).
Spatial calibration is achieved by locating the cursor on reference markers, a known distance apart, placed on the test specimen surface. The absolute coordinates of one of these points must be known. The cursor can be positioned to within one pixel. As the cursor is moved over the markers, the pixels with the highest intensity are taken to represent the marker positions, and the spatial calibration is complete.
The stored images can be scanned line by line (512 in total) but it is usually more convenient to select a limited number of rows where the heat transfer information is required; for example, on the specimen axis. The position of the liquid crystal isotherms are obtained by scanning the selected lines and checking the grey levels of all the pixels of the binarised image on these lines. By comparing the grey level of each pixel with that of its neighbours, the edges and coordinates of the isotherm can be detected. This process is carried out for each stored image. The inferred temperature distribution can then be used in the determination of the local steady state heat transfer coefficient. The calculation method is chosen to suit the experimental technique as discussed in the previous section, that is, either a one dimensional transient conduction model or a simple heat balance over the thickness of the specimen.
In the transient mode of operation, the start time of the experiment is recorded when the specimen is introduced into the flow field. The audio signal function of the video cassette recorder and a computer controlled analogue to digital convertor are used to facilitate this procedure, with simple direct current circuitry providing the audio signal in the form of an electrical pulse. A temporal resolution of 0.01s is attainable.

4 Conclusions

A software package based upon digital image processing techniques has been developed for the automatic analysis of two dimensional steady state convective heat transfer phenomena, either in real time or from a video recording. The development has substantially reduced the time required for the analysis of

liquid crystal thermographic data and has eliminated the subjective interpretation of colour change information. The mono-chrome image processing facility can presently store up to four images with a resolution of 512 x 512 x 8-bit (256 grey levels). Frame processing and noise reduction are accomplished automatically. Median filtering has been found useful for reducing background noise while maintaining the location of isotherm edges, although it is relatively time consuming. Spatial calibration, relating the digitised images to the real specimen co-ordinate system geometry, is performed interactively. The added advantage of automatic interpretation renders liquid crystal thermography a very powerful, yet simple, measurement tool.

Acknowledgements

Thanks are due to Nottingham Polytechnic and British Gas plc for the financial support given to the work reported here.

References

Akino N, Kunugi T, Ichimiya K, Mitsushiro K and Ueda M, 1989a. Improved liquid crystal thermometry excluding human colour sensation. *ASME Journal of Heat Transfer*, **111**, 558-565.

Akino N, Kunugi T, Ueda M and Kurosawa A, 1989b. A study on thermo-camera using Liquid Crystals (Method of multiple regression between colour and temperature). *Nat. Heat Transfer Conf: Heat Transfer Measurement, Analysis and Flow Visualisation*, **112**, 115-122.

Baughn J W, Ireland P T, Jones T V and Saniei N, 1988. A comparison of the transient and heated-coating methods for the measurement of local heat transfer coefficients on a pin fin. *ASME Paper no. 88-GT-180.*

Data Translation® Inc., 1989. User manual for DT2861 and DT2862 UM-0830-A, fourth edition.

Gomiciaga R, Lee K C and Yianneskis M, 1991. Development of a liquid crystal thermographic technique using video image processing. *IChemE HT'91 Developments in Heat Transfer Symposium*, Nottingham University, England.

Hollingsworth D K, Boehman A L, Smith E G and Moffat R J, 1988. Measurement of temperature and heat transfer coefficient distributions in a complex flow using liquid crystal thermography and true-colour image processing. *HTD Vol. 123, Collected Papers in Heat Transfer.*

Ireland P T and Jones T V, 1985. Heat transfer and cooling in gas turbines. *AGARD 390*, Paper 28.

Ireland P T and Jones T V, 1987. The response time of a surface thermometer employing encapsulated thermochromic liquid crystals. *J.Phys.E:Sci.Instrum*, **20**.

Jambunathan K, Edwards R J and Button B L, 1987. Convective heat transfer coefficients: the colour-change paint technique. *Applied Energy*, **28** (2), 137-152.

Karaman M and Onural L, 1989. New radix-2-based algorithm for fast median filtering. *Electronics Letters*, **25**, 11, 723-4.

Kasagi N, Hosoya K, Hirata M and Suzuki Y, 1987. The effects of free stream turbulence on full-coverage film cooling. *Proc. Tokyo Int. Gas Turbine Congress*, Tokyo, Japan, **3**, 217-222.

Kasagi N, Moffat R J and Hirata M, 1989. Liquid crystals. *In: Handbook of Flow Visualisation*, Ed: W J Yang, 105-124.

Lin C C, Jambunathan K and Button B L, 1991. Intelligent liquid crystal applications database. To be published.

Moffat R J, 1990. Some experimental methods for heat transfer studies. *Experimental Thermal and Fluid Science*, **3**, 14-32.

Rhine J M and Tucker R J, 1991. *Modelling of gas fired furnaces and boilers.* British Gas plc, McGraw-Hill Book Company.

Schultz D L and Jones T V, 1973. Heat transfer measurements in short-duration hypersonic facilities. *AGARD 165.*